2013

# Design and experimental validation of 328 ft (100 m) tall wind turbine towers utilizing high strength and ultra-high performance concrete

Grant M. Schmitz
*Iowa State University*

**Design and experimental validation of 328 ft (100 m) tall wind turbine towers utilizing high strength and ultra-high performance concrete**

by

**Grant M. Schmitz**

A thesis submitted to the graduate faculty

in partial fulfillment of the requirements for the degree of

MASTER OF SCIENCE

Major: Civil Engineering (Structural Engineering)

Program of Study Committee:
Sri Sritharan, Major Professor
Fouad S. Fanous
Lester W. Schmerr
Jennifer Shane

Iowa State University
Ames, Iowa
2013

# TABLE OF CONTENTS

# LIST OF TABLES

## LIST OF FIGURES

## ACKNOWLEDGMENTS

The research presented herein was made possible through the sponsorship of the Grow Iowa Value Fund. Additional support was provided by the project's company partners. Clipper Windpower, Inc. provided valuable insight into the tower design as well as information pertaining to their 2.5 MW Liberty turbine. Coreslab Structures, of Omaha, NE, provided all of the precast concrete components used for laboratory testing. Lafarge North America supplied all of the Ultra-High Performance Concrete (UHPC) material used in the study. In addition to the company partners, support was also received from numerous other companies. Dywidag-Systems International provided the post-tensioning anchorage equipment, Hayes Industries supplied the strand wedges, General Technologies, Inc. provided the post-tensioning duct, and Sumiden Wire Products Corporation supplied the post-tensioning strand. The author would like to thanks these companies for not only providing generous financial support, but also for their willingness to provide technical assistance when needed.

The author would like to thank Dr. Sritharan for the opportunity to work on the project and for the valuable guidance he provided over the course of this project. The author would also like to thank Dr. Aaleti for his continued support, as well as, Dr. Fanous, Dr. Shane, and Dr. Schmerr for serving as his committee members.

The author would like to thank Doug Wood and Owen Steffens for their valued support in the lab. Additionally, the author would like to recognize Aaron Shelman, James Nervig, Brad Petersen, Wenjun He, Maryam Nazari, Ryan Beck, Zhao Cheng, and the countless others who provided assistance over the projects duration.

Finally, the author would like to thank his family, especially his parents Steve and Jane Schmitz and fiancée Randi DuVall for their continued support and guidance throughout his education.

## ABSTRACT

With today's global capacity exceeding 280 GW, windpower has proven to be a formidable source of renewable energy worldwide. In order to keep pace with the growing demand, the wind industry will need to overcome challenges associated with low alternative energy costs without depending upon any form of government subsidy. A major research effort has been focused on reducing the capital, production, and maintenance costs through the use of taller wind turbine towers. Today's turbines often consist of 262 ft (80 m) steel towers. As taller towers become more desirable, material and transportation costs associated with steel tower designs grow significantly. The increase from 262 ft (80 m) to 328 ft (100 m), allows turbines to access the improved wind conditions that exist at higher elevations.

A new tower concept has been developed using Ultra-High Performance Concrete (UHPC) and other high strength concrete materials that would allow taller wind turbine towers to be transported to wind farm sites easily within the current transportation limitations. Three tower designs, consisting of precast UHPC and high strength concrete segments, have been completed for potential field implementation. By utilizing different combinations of these materials, each design offers unique benefits related to costs, tower weight, connection design, etc.

In order to verify the design of each of the three towers, experimental testing was completed using full-scale precast components. Each was found to be the most critical tower component at the governing load case thorough the use of a finite element modeling. The tests provided insight into the performance of the various panel, and precast connection designs specifically developed for each wind turbine tower. By assessing the performance at both the operational and extreme limit states, it was concluded that each specimen responded exceptionally well. In addition to verifying the capacity of each tower, observations made during construction offered insight into future construction practices. Using the results of these tests, appropriate modifications were made to the design making it suitable for full-scale implementation in the wind industry.

# CHAPTER 1. INTRODUCTION

## 1.1 The Widespread Impact of Wind Energy

From the mid part of the 19th century to today, fossil fuels have provided the power necessary to complete many of society's most basic tasks worldwide. The abundant supply allowed prices to stay low even as demand accelerated throughout the years, minimizing the influence of many other forms of energy production. Over the last few years, a number of factors have led to growing concern about future sources of energy. Some of the more prevalent concerns involve fossil fuels and their impact on the environment as well as the diminishing supply. This has forced many nations to rethink their energy portfolios, including options that may have been previously ignored.

Wind energy has experienced a 25% annual growth rate globally since 1990. Today, it represents 13% of all renewable energy produced in the United States. In 2006, the U.S. Department of Energy (DOE) took a major step towards altering the future of its energy resources by setting the ambitious goal of reaching 20% wind energy by 2030 (DOE, 2008). This would require an estimated 305 gigawatts (GW) of installed capacity in the year 2030, which is nearly five times the available capacity installed by the end of 2012. The industry saw the greatest annual increase in total installed capacity during 2012 at nearly 13,000 MW nationally. In order to reach the 20% scenario, installations will need to reach 16,000 MW per year and continue at that rate through 2030. Reaching this scenario with today's technology could prove to be challenging. Innovations need be made to reduce the cost of wind energy, and make it more cost competitive with other energy alternatives.

The federal Production Tax Credit (PTC) has supported the growth of large, utility scale wind turbines since their beginning in the early 1980s. It provides a 2.2 cent/kilowatt-hour benefit for the first ten years of energy production. The impact of the PTC is well known throughout the industry. It has allowed wind energy to consistently compete with other forms of energy production such as coal and natural gas. Unfortunately, many of the most difficult challenges the industry has faced can also be contributed to the PTC. In the past, it has been allowed to expire on three separate occasions, each time dramatically reducing the installed capacity of the following year (Figure 1.1). In order to meet the 20% by 2030 scenario, advancements need to be made that reduce or even eliminate the need for the PTC. This

would provide a much more stable environment in which wind turbine manufacturers and developers could increase their investments and continue to grow the industry.

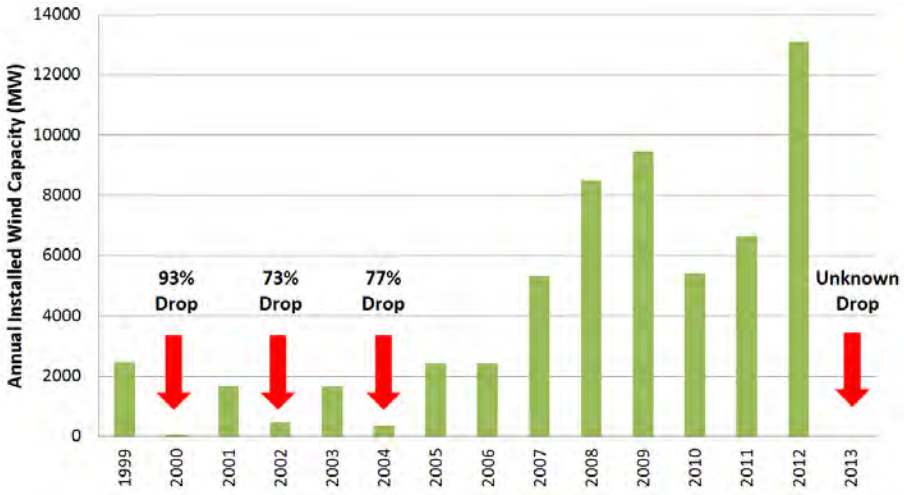


**Figure 1.1: Historic Impact of the PTC Expiration on Annual Wind Installation**

## 1.2 Taller Towers

Many of the components making up today's wind turbines have seen significant improvements over the years; each time, making the system more cost-effective. Many times these improvements are small in terms of increasing the total energy production of the turbine. Taller wind turbine towers, however, have the potential to significantly increase the energy production of each turbine. The power generated from the wind is a function of the cube of wind velocity. This means that even small increases in wind velocity can significantly improve the power output of the turbine. It is well documented that at higher elevations, faster and more sustainable winds exist. Many of the current tower designs provide hub heights of 262 ft (80 m). A number of factors, which will be discussed later in this chapter, have limited towers to this height. Recently, however, the need for greater energy production has encouraged wind turbine manufacturers to begin pushing for taller tower designs.

As the idea of taller towers has become more widespread, more wind resource data has been acquired to verify the potential increases in energy output. Data from the Iowa Energy Center shows that at 328 ft (100 m), wind flows 4.5% faster than it does at 262 ft (80 m). This would result in an increase in power output of approximately 14%. Similar results were

found in a series of charts compiled by NREL that estimated the total wind resource potential in the United States. Figure 1.2 illustrates the relationship between potential energy production in the U.S. for a range of gross capacity factors for both 262 ft (80 m) and 328 ft (100 m) elevations. The difference between the two elevations was found to be 15-20% for the lower spectrum of gross capacity factors.

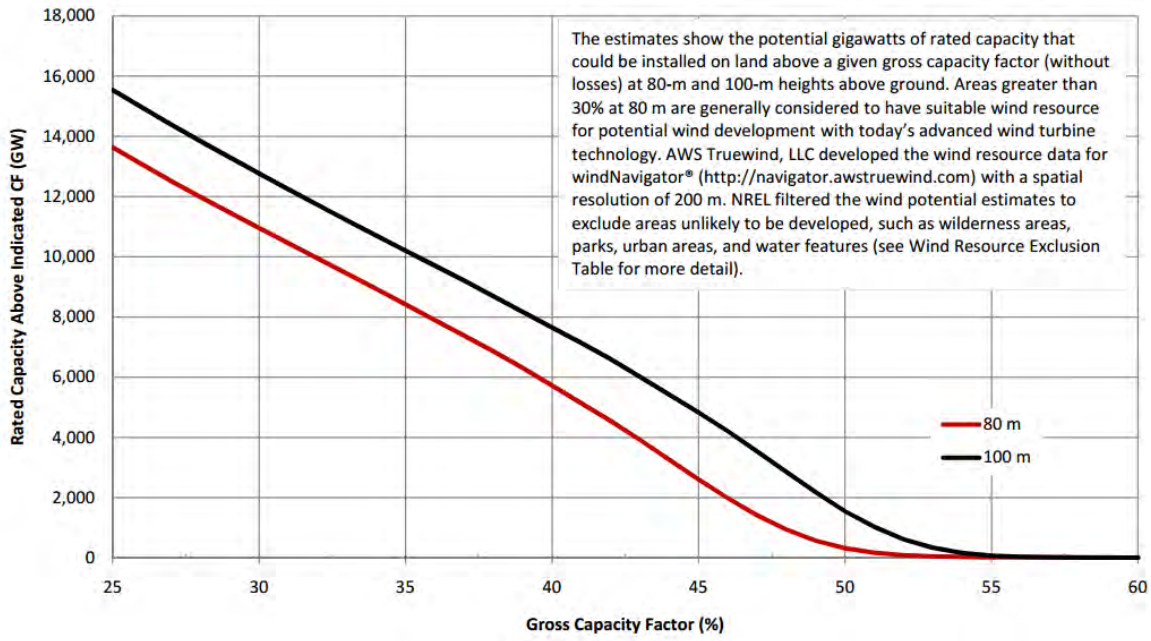


**Figure 1.2: United States Wind Resource Potential (NREL, 2010)**

Many of the transportation challenges associated with increasing tower heights from 262 ft (80 m) to 328 ft (100 m) no longer exist when considering elevations beyond 328 ft (100 m) because segmented tower designs are often used. For this reason, current taller tower designs range from 308 ft (94 m) to 436 ft (133 m). Data provided by Advanced Tower Systems (ATS), shows similar increases in energy output from 328 ft (100 m) to 436 ft (133 m) as those seen from 262 ft (80 m) to 328 ft (100 m). Given the higher output, ATS estimates the additional cost of their tower can be recovered in approximately four years, providing sixteen years of increased revenue over the twenty year service life of the tower. A study completed at Iowa State University, also investigated the potential increase in energy production at higher elevations by instrumenting existing communication towers between 164 ft (50 m) and 656 ft (200 m). When considering the current generator capacity limitations, energy production increases by 9.62% from 262 ft (80 m) to 328 ft (100 m) and

8.59% from 328 ft (100 m) to 492 ft (150 m). When generator capacity limitations are no longer considered, these values increase to 24.74% and 43.92% over the same elevation intervals (Zhang et al., 2013).

When considering the impact of taller towers on large wind farms, which can often consist of one-hundred or more turbines, the difference in combined output becomes even more prevalent. Figure 1.3 shows the increase in power output associated with larger turbines, which become more feasible at higher elevations.

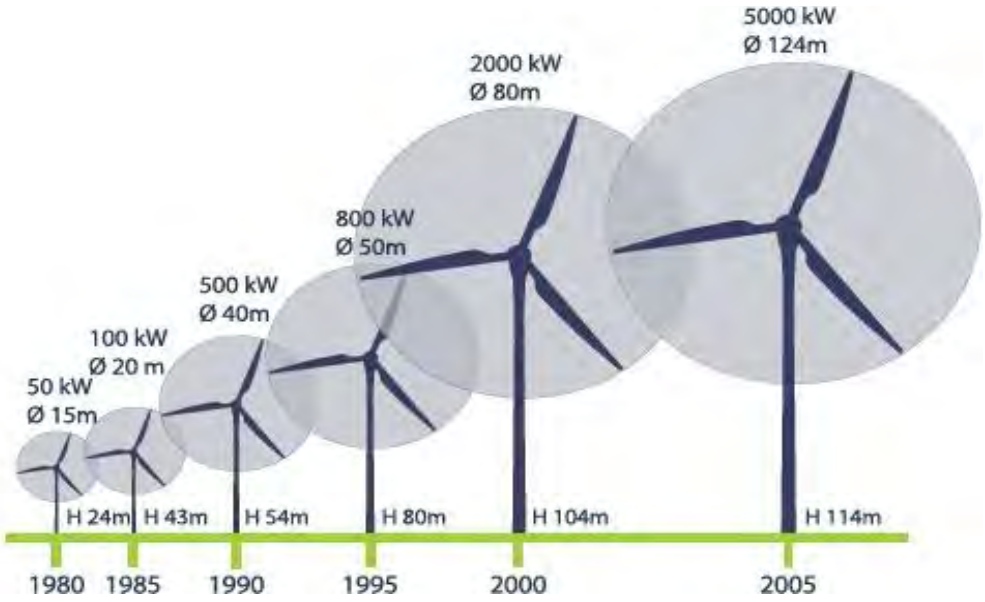


**Figure 1.3: Relationship between Power and Turbine Size (EG-Blog, 2010)**

## 1.3 Current Wind Turbine Tower Designs

Three distinct categories of utility-scale towers have emerged that encompass nearly all existing and current designs: steel towers, concrete towers, and hybrid towers. Each has its own advantages and disadvantages over one another. For this reason the wind turbine industry is often divided on the subject of future wind turbine towers. 328 ft (100 m) prototypes from each of the three above-mentioned categories either have been, or are currently being constructed around the world to further examine the benefits of each. Because this report focuses on the development of concrete wind turbine towers, this overview will only touch on towers that utilize concrete in their design. For more information

regarding steel and hybrid tower designs and applications, may be found in Lewin and Sritharan (2010).

The use of concrete as the primary material for large-scale wind turbine towers is a relatively new concept that has come about as a result of the hub height elevations currently being targeted by turbine manufacturers for the potential economic benefits. To this day, nearly all erected utility-scale turbines use steel towers. These towers are transported to site in three segments, where they are then bolted together. As tower heights increase, the steel segment making up the bottom of the tower reaches a limit at which it is no longer feasible to transport on the highway system due to width restrictions. The maximum allowable tower base diameter corresponds to a 262 ft (80 m) tall tower, which makes up a majority of the newly constructed turbines today. The challenges associated with further dividing steel segments have opened the door for concrete solutions to begin taking hold. These designs address many of the limitations facing steel towers in addition to providing other added benefits.

**Figure 1.4: Transportation of steel tower segments and associated challenges (Karkos, 2010)**

### 1.3.1 Segmental Concrete Towers Being Explored Today

Segmental concrete towers utilize precast technology to simplify construction procedures and reduce the on-site erection times. A large portion of the concrete used in the tower is placed off site in a controlled environment. This minimizes formwork and allows segments to be constructed year-round. A majority of concrete designs utilize this technology given the benefits it provides. One of the more popular segmental concrete towers being used today is produced by the Spanish company Inneo. The tower consists of nine tower segments that are connected together on site using wet joints, which are discussed further in Chapter 2. The

small number of segments allows the tower to be erected within one day, once the pre-assembly process has been completed. Figure 1.5 shows the transportation and erection processes used to construct this tower. Unlike many of the other concrete tower designs, it does not utilize prestressing. Although eliminating prestressing can reduce the material and labor costs, it requires the tower to have an increased base diameter of up to 26 ft (7.8 m) and shell elements thicknesses near 8-in. (20 cm). This, in-turn, increases the overall weight of the tower, escalating transportation costs and potentially foundation costs. Clearance between the tip of the blade and tower can also limit the types of turbines used. If large tower diameters exist at the lower elevations of the blade swept area, many turbines currently being used in conjunction with steel towers many not suitable. This may also be the case for concrete towers utilizing a low level of prestressing.


**Figure 1.5: Transportation and Erection of Inneo Wind Tower (Grupo Inneo, 2008)**

Another tower design, utilizes precast concrete rings three to four meters in height to construct the wind turbine tower. The rings are delivered to the site in two or three segments

to simplify the transportation process. After assembling the rings at the base of the tower and erecting them, the tower is post-tensioned to provide additional strength and rigidity. Details of the tower are illustrated in Figure 1.6. Erection times would increase when compared to non-prestressed towers, however, the use of prestress would allow for reduced section sizes and overall tower diameter.

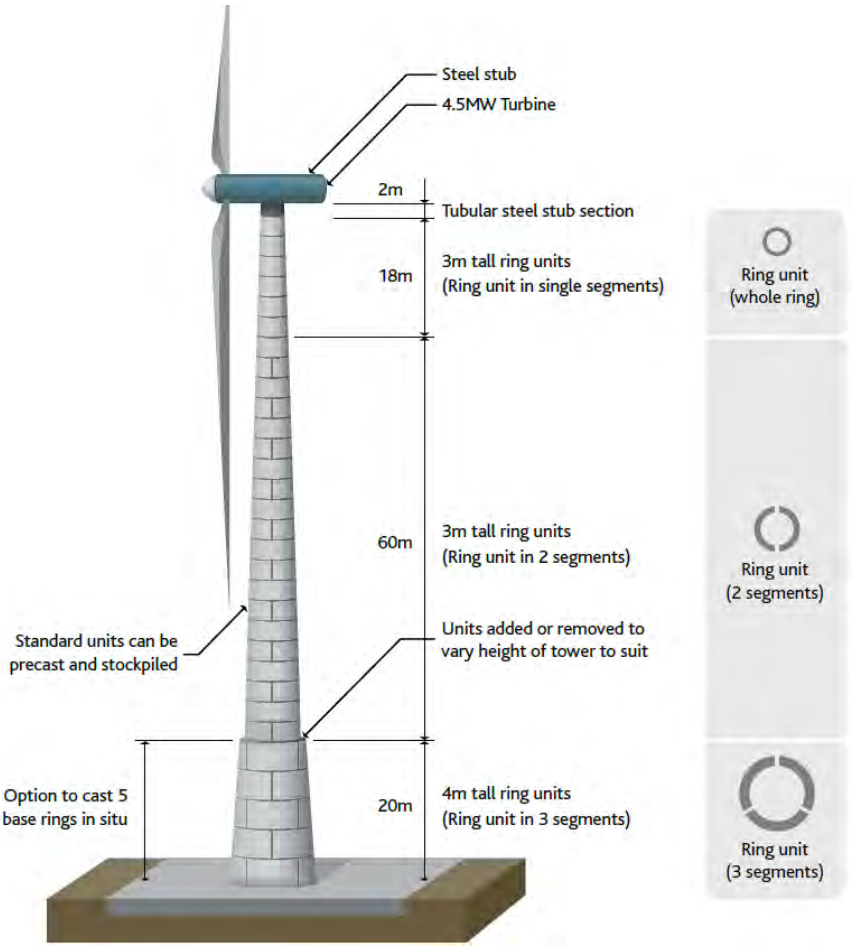


**Figure 1.6: Details of Precast Concrete Towers (The Concrete Centre, 2005)**

### 1.3.2 In-situ Slipformed Concrete Towers

Slipforming is the process of casting concrete in a continuously moving form. The process has been around for many years and is typically used for tall structures such as core walls, silos, and pylons. Slipformed towers provide a number of advantages over alternative concrete designs. They eliminate the need for connections between precast segments, and do not require a crane for assembly. The final product is a monolithically cast structure that can

be prestressed to improve its capacity if desired. The process could be most useful in remote locations where transportation of large precast sections would be difficult (The Concrete Centre, 2005). Figure 1.7 illustrates structures similar to wind turbine towers that have been constructed using a slipform technology. In order to provide a consistent supply of concrete in remote locations, an on-site mix plant would need to be erected. This could cause potential problems if space and geography constraints are present. The slipform jacking rate is vital to completing the tower in a short period of time. Jacking rates typically vary between one-half foot and two feet per hour. Even at a higher jacking rate and around the clock casting, a 328 ft (100 m) tower would take nearly seven days to complete. Today, there are no known wind turbine towers in existence that have been erected using a slipform process; however, FWS Technologies of Winnipeg, Manitoba has produced designs up to 460 ft (140 m).

**Figure 1.7: Slipforming Process for Concrete Towers (The Concrete Centre, 2005)**

## 1.4 Scope of Research

Phase I of this study was completed by Lewin and Sritharan (2010). They investigated a number of potential designs for a 328 ft (100 m) wind turbine tower. Using precast UHPC components in conjunction with post-tensioning, they were able to develop a new design concept that minimized transportation costs and reduced the overall tower weight. The successful development of a 328 ft (100 m) tall precast UHPC Lattice Tower by Lewin and Sritharan (2010) provided the necessary stepping stones for the second phase of the tower development. The objectives of this report include the following:

- Further investigate the source and magnitude of loads acting on the tower through industry partnerships; allowing for the enhancement of the tower proposed by Lewin and Sritharan (2010);
- Reduce the overall cost of the tower to make it more competitive with alternative designs;
- Develop suitable connections between the precast components of the tower that allow it to behave monolithically when loaded;
- Isolate critical regions of the tower based on loads defined for operational and extreme limit states, and experimentally verify their performance; and
- Verify the design of the precast tower components and connections at each limit state, making any necessary refinements.

## 1.5 Report Layout

This report is comprised of six chapters that focus on the advancement of the original 328 ft (100 m) tall precast UHPC Lattice Tower design. A brief description of each chapter can be seen in the following.

- Chapter 1 - Introduction: A brief introduction into the history and future direction of wind energy development, including the benefits and current designs of concrete towers.
- Chapter 2 - Literature Review: A review of the Lewin and Sritharan (2010) segmental UHPC tower design and development of load cases used for the

purposes of design modifications; as well as the material behavior of UHPC and current precast concrete connections

- Chapter 3 - Development of Segmental Concrete Wind Tower: Detailed description of the design process used for each of the three segmental concrete towers developed
- Chapter 4 - Laboratory Testing of Wind Turbine Tower Components: A description of the development, construction, testing, and results of each of the three in-plane tests conducted.
- Chapter 5 - Modeling of the Wind Turbine Towers and Test Units: An overview of the procedures used to create finite element models for the complete towers and their corresponding test units. Results from the models are also presented.
- Chapter 6 - Summary and Conclusions: A summary of the overall performance of each of the three test specimens and the potential for future research

# CHAPTER 2. LITERATURE REVIEW

## 2.1 Introduction

This chapter is a discussion regarding the development of the 328 ft (100 m) tall UHPC Lattice Tower previously completed by Lewin and Sritharan (2010). It summarizes the loads used for design as well as the general tower properties. The material properties of UHPC as well as some of the more recent applications have also been covered to highlight the benefits and substantial differences that exist between UHPC and normal concrete. A significant portion of this study focuses on the connections between the precast concrete segments. A number of possibilities exist that are both commercially available and developmental. An overview of current practices as well as results from studies of similar applications will be examined.

## 2.2 UHPC Lattice Tower

The concept of an Ultra-High Performance Concrete (UHPC) Lattice tower was first developed by Lewin and Sritharan (2010). It was believed that the use of high performance materials in combination with post-tensioning would provide a cost-effective solution for towers extending to 328 ft (100 m) and above. The tower is comprised of six exterior columns along with bracing elements that would allow the columns to act as a composite structure. Two different types of bracing elements were proposed by Lewin and Sritharan (2010). The first consisted of truss like elements that would give the tower a lattice configuration (Figure 2.1). The second utilized panels to transfer the load between the columns. The latter concept would give the tower a completely enclosed interior as seen in Figure 2.2. Ultimately, the lattice tower concept was chosen over the panel concept because it was believed that the wind resistance could be reduced with an open design (Lewin and Sritharan (2010). The purpose of this report is to continue the work completed by Lewin and Sritharan (2010) in order to provide a more commercially applicable design. The following offers a brief description of the UHPC Lattice tower details outlined in Lewin and Sritharan's report.

**Figure 2.1: Proposed Lattice Tower with Horizontal Bracing (Lewin and Sritharan, 2010)**

**Figure 2.2: Proposed Panel Bracing for UHPC Tower (Lewin and Sritharan, 2010)**

### 2.2.1 Tower Loading Criteria

Predicting the loads the wind turbine tower will experience throughout the duration of its service life is one of the most challenging aspects of the design. The lack of unified specifications in the United State requires designers to choose from a number of different sources. Structures in the United States are typically designed using ASCE7, which provides information on wind, seismic, snow, and live loads, in addition to a number of others. In the case of wind turbines, however, ASCE7 does not provide adequate information in terms of the power rating of the turbine and the effects different designs have on the resulting loads. For this reason, IEC 61400-1 is often used. This standard is published by the International Electrotechnical Commission (IEC), founded in London, UK. It provides detailed information regarding the applicable wind models used in the design of a wind turbine (IEC, 2007).

Two distinct load groups make up a majority of the loads acting on the wind turbine. The first encompasses all those acting on the top of the tower. This includes loads on the nacelle, hub, and blades. The second load group is comprised of loads acting directly on the tower. Generally, this type of loading is a result of wind loads, whereas the tower top loads can often be a result of mechanical operations or failures in addition to wind generated loads.

The loads used in the design of the 328 ft (100 m) UHPC Lattice Tower were all determined using the IEC 61400-1. The magnitude of these loads acting on the tower top, however, were obtained through various reports due to the proprietary nature of wind turbine designs. This included a report published by the National Renewable Energy Laboratory (NREL) in 2005, in which three separate 328 ft (100 m) designs were presented. Along with the details of the towers, some load data was provided for the tower top loads. Although limited, it was the best source of reliable load data at the time. The fifty year extreme wind (EWM50) and extreme operating gust (EOG50) models were presented in the report. It included tower top loads resulting from 1.5, 3.6, and 5 MW wind turbines. These values can be seen in Table 2.1.

**Table 2.1: WindPACT Operational Load Envelope at Tower Top, Vector Summations (Lewin and Sritharan, 2010)**

| | | **Thrust** | **Moment** | **Tower Axial Force (causing tower compression)** | **Torsional Moment (about tower longitudinal axis)** |
|---|---|---|---|---|---|
| | | $F_T$, kips (kN) | $M_T$, kip-ft (kN-m) | $F_z$, kip (kN) | $M_z$, kip-ft (kN-m) |
| 1.5 MW | EWM50 | 86.3 (384) | 2810 (3805) | 187.0 (832) | 1450 (1966) |
| | EOG50 | 90.6 (403) | 1083 (1468) | 187.0 (832) | 171.1 (232) |
| 3.6 MW | EWM50 | 244 (1,086) | 12,370 (16,767) | 709 (3155) | 4397 (5961) |
| | EOG50 | 270 (1,199) | 7310 (9913) | 703 (3129) | 1178 (1597) |
| 5 MW | EWM50 | 129.9 (578) | 21,070 (28,568) | 1124 (4998) | 4300 (5834) |
| | EOG50 | 239 (1065) | 14,260 (19,337) | 1097 (4879) | 2740 (3714) |

The turbine used in the Lewin and Sritharan (2010) designs, was an ACCIONA AW-109/3000. This is a 3 MW machine that was designed for a 328 ft (100 m) hub height. Because the NREL report did not provide loads specifically for a 3 MW machine, a best fit

line was created using the three provided load demands. From this, load data for an equivalent 3 MW machine was determined. With the addition of some weight modifications to account for the AW-109/3000, the tower top loads presented in Table 2.2 and Table 2.3 were used for the design of the towers. The NREL report also provided damage equivalent loads for the three turbine sizes. These loads were used for the purpose of evaluating fatigue in the tower and can be seen in Table 2.4.

**Table 2.2: Turbine Top Loads at Operational Estimated for a 3 MW ACCIONA AW-109/3000 Wind Turbine (Lewin and Sritharan, 2010)**

| | | | | | |
|---|---|---|---|---|---|
| **EWM50** | $V_{Tx}$ kip (kN) | $V_{Ty}$ kip (kN) | $M_{Tx}$ kip-ft (kN-m) | $M_{Ty}$ kip-ft (kN-m) | $M_z$ kip-ft (kN-m) |
| | 144.6 (643) | 191.9 (854) | 8120 (11,020) | 4440 (6030) | 3930 (5330) |
| **EOG50** | $V_{Tx}$ kip (kN) | $V_{Ty}$ kip (kN) | $M_{Tx}$ kip-ft (kN-m) | $M_{Ty}$ kip-ft (kN-m) | $M_z$ kip-ft (kN-m) |
| | 245 (1092) | 15.00 (65.5) | 2530 (3420) | 4380 (6820) | 727 (985) |

**Table 2.3: Turbine Axial Loads at Operational Estimated for a 3 MW ACCIONA AW-109/3000 Wind Turbine (Lewin and Sritharan, 2010)**

| | |
|---|---|
| Weight/blade*, kip (kN) | 25.4 (113.2) |
| Nacelle+hub*, kip (kN) | 340 (1510) |
| Additional axial compression, kip (kN) | 70.0 (311) |
| Total axial turbine load, kip (kN) | 486 (2160) |

**Table 2.4: Estimated Damage Equivalent Loads at Tower Top (Lewin and Sritharan, 2010)**

| | |
|---|---|
| $\Delta V_{Tx,fat}$, kip (kN) | 26.8 (119.2) |
| $\Delta M_{Ty,fat}$, ft-kip (kN-m) | 1210 (1640) |

Note: The subscript "fat" refers to fatigue

For loads acting directly on the tower, Lewin and Sritharan (2010) were able to determine magnitudes based on wind speeds calculated from IEC 61400-1. Only the (EWM50) and (EOG50) were used, however, given the available tower top loads from the NREL report. Once the appropriate wind speeds were determined, ASCE 7 was used to calculate the resulting forces based on the geometric properties of the tower (Table 2.5).

**Table 2.5: Estimated Direct Wind Force Loads at Mid-height and Base of the 322 ft (98.2 m) UHPC Lattice Tower at Operational (Lewin and Sritharan, 2010)**

| | | | | |
|---|---|---|---|---|
| **EWM50** | **$V_{Mx}$ kip (kN)** | **$M_{My}$ ft-kip (kN-m)** | **$V_{Bx}$ kip (kN)** | **$M_{By}$ ft-kip (kN-m)** |
| | 158.2-198.0 (704-881) | 12,630-15,730 (17,120-21,300) | 310-389 (1379-1730) | 51,100-64,000 (69,300-86,800) |
| **EOG50** | **$V_{Mx}$ kip (kN)** | **$M_{My}$ ft-kip (kN-m)** | **$V_{Bx}$ kip (kN)** | **$M_{By}$ ft-kip (kN-m)** |
| | 27.4-34.3 (121.9-152.6) | 2180-2720 (2960-3690) | 53.8-67.6 (239-301) | 8860-11,090 (12,010-15,040) |

### 2.2.2 Geometry

The six exterior columns of the tower provide a majority of its load resistance. Each column contains five post-tensioning ducts in which two are terminated at 110 ft (33.5 m), another two at 220 ft (67.0 m), and the last terminated at the tower top. The termination of strands was used to provide varying amounts of resistance to the tower along its height. At the base of the tower, where moment demand is the greatest, the maximum number of strands is used. The termination of two of the four outer ducts, shown in Figure 2.3, at 110 ft (33.5 m) and 220 ft (67.0 m) correspond to the further reduction in moment demand at each elevation. The center duct is left to extend the entire height of the tower, to provide additional resistance in the top 100 ft (30.5 m). In order to reduce the cost of the tower, the individual columns along with the overall tower diameter are tapered along the height. Table 2.6 summarizes both the dimensions and general properties of the UHPC Lattice tower.

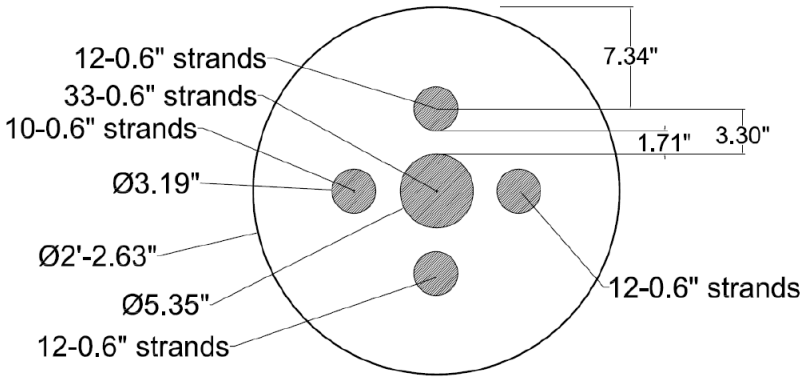


**Figure 2.3: Tendon Layout of the UHPC Lattice Tower (Lewin and Sritharan, 2010)**

**Table 2.6: Dimensions and Properties of UHPC Lattice Tower (Lewin and Sritharan, 2010)**

| | |
|---|---|
| Compressive Strength, ksi (MPa) | 26 (179.3) |
| Post-tensioning Effective Stress, ksi (MPa) | 180 (1241) |
| Outer Diameter, $D$, at Base, in. (m) | 354 (8.99) |
| Column Diameter, $d_{col}$, at Base, in. (mm) | 26.625 (676) |
| Number of 0.6-in. diameter strands, 0-110 ft (0-33.5 m) | 486 |
| Outer Diameter, $D$, at 110 ft (33.5 m), in. (m) | 294 (7.47) |
| Column Diameter, $d_{col}$, at 110 ft (33.5 m), in. (mm) | 24.625 (625) |
| Number of 0.6-in. diameters strands, 110-220 ft (33.5-67.1 m) | 342 |
| Outer Diameter, $D$, at 220 ft (67.1 m) , in. (m) | 246 (6.25) |
| Column Diameter, $d_{col}$, at 220 ft (67.1 m), in. (mm) | 19.75 (502) |
| Number of 0.6-in. diameter strands, 220-322ft (67.1-98.2 m) | 198 |
| Outer Diameter, $D$, at 322 ft (98.2 m), in. (m) | 120 (3.05) |
| Column Diameter, $d_{col}$, at 322ft (98.2 m), in. (m) | 14.875 (378) |
| UHPC Volume, Columns Only, $yd^3$ ($m^3$) | 173 (132.4) |
| Tower Weight, kip (kN) | 1120 (4980) |
| Fundamental Tower Natural Frequency, Hz | 0.495 |

## 2.3 Wind Models

The assumptions used in deriving the tower load magnitudes were obtained from a document released by Germanischer Lloyd (GL) in 2010 titled "Guideline for the Certification of Wind Turbines." GL is a German based company founded in 1867 that provides assurance of technical compliance for the wind energy sector. The certification document touches on nearly every aspect of a wind turbine system and is available for free through GL's website. Many of the guidelines provided within this document are direct references from other sources. The wind load assumptions for example originated from IEC 61400-1, which was also used by (Lewin et al., 2010). The (GL, 2010) guideline will be referenced from this point forward because it focuses strictly on the design of wind turbines and the requirements needing to be met to achieve certification. Although the loads were obtained directly from the NREL report, a general overview of the wind models used in the creation of individual load cases has been included.

The external loading conditions on the tower are divided into normal and extreme wind conditions. Normal conditions consist of long term loading and general operating conditions

that are predicted to occur frequently. The design load cases that include normal external conditions are assigned a recurrence interval of 1 year. Extreme conditions refer to those expected to occur on a rare occasion, but at potentially critical design loads. These are defined as having 1 or 50 year recurrence intervals depending on the wind condition.

In order to account for site specific wind conditions, wind turbine classes are defined in Table 2.7. Classes are each defined by three parameters: the average wind speed, extreme fifty year gust, and turbulence levels. Class IA, for example, represents the highest wind speed with 18% turbulence levels. Wind turbine class "S" is used when the manufacturer is able to determine the appropriate wind conditions at the turbine site and provide documentation on the models used. The design lifetime for wind turbine towers should be at least 20 years.

**Table 2.7: Parameters for Wind Turbine Classes as per GL (2010)**

| Wind turbine class | I | II | III | S |
|---|---|---|---|---|
| – $V_{ref}$ [m/s] | 50 | 42.5 | 37.5 | Values to be specified by the manufacturer |
| – $V_{ave}$ [m/s] | 10 | 8.5 | 7.5 | |
| – A $I_{15}$ (-) | 0.18 | 0.18 | 0.18 | |
| – $a$ (-) | 2 | 2 | 2 | |
| – B $I_{15}$ (-) | 0.16 | 0.16 | 0.16 | |
| – $a$ (-) | 3 | 3 | 3 | |

$V_{ref}$ = Reference wind speed: fundamental parameter of the extreme wind speed

$V_{ave}$ = Annual average wind speed at hub height

A = Category for higher turbulence intensity

B = Category for lower turbulence intensity

### 2.3.1 Normal Wind Conditions

Two separate models are used to define normal wind conditions. The normal wind profile model (NWP) is used to describe the distribution of wind speed along the height of the tower. In this case, the power law is used as shown in Equation 2-1. The power law exponent is assumed to be 0.2.

$$V(z) = V_{hub}(z/z_{hub})^{a} \quad \textbf{2-1}$$

where:

V(z) = wind speed at the height z [m/s];

z = height above ground [m];

$z_{hub}$ = hub height above ground [m]; and

α = power law exponent = 0.2.

Effects of turbulence are also taken into consideration under the normal wind conditions through the normal turbulence model (NTM). The GL guideline specifies a period of approximately ten minutes be used to account for the effects turbulence has on tower frequencies. These frequencies are determined at hub heights. For effects of turbulence on the tower, one can assume it changes based on the wind speed distribution described in the (NWP) model. In order to perform adequate load calculations in cases of fatigue, one must vary the initial wind speed to account for the full spectrum of turbulent wind fields.

### 2.3.2 Extreme Wind Conditions

In order to capture the effects of extreme wind conditions on the tower, a number of different wind models are used that have the potential of occurring during the life of the tower. The models used for the design loads cases are shown in Table 2.8.

**Table 2.8: Extreme Wind Conditions as per GL (2010)**

| Wind Condition | Abbreviation |
|---|---|
| Extreme wind speed model | EWM |
| Extreme operating Gust | EOG |
| Extreme direction change | EDC |
| Extreme coherent gust | ECG |
| Extreme coherent gust with direction change | ECD |
| Extreme Wind Shear | EWS |

The extreme wind speed model (EWM) can be used to describe both steady and turbulent wind conditions at one and fifty year recurrence intervals. Much like the (NWP) model, the power law is used to determine wind speed distribution along the tower height. The fifty year extreme wind speed can be determined using Equation (2-2). Both the added factor of 1.4 as well as the reduced exponent contributes to the increased magnitude along the tower height. The relationship between the one year, and fifty year recurrence intervals is shown in Equation (2-3). Although wind speed distribution along the tower height remains unchanged at both recurrence intervals, the velocity is reduced, making it less critical.

$$V_{e50}(z) = 1.4V_{ref}(z/z_{hub})^{0.11} \quad \textbf{(2-2)}$$

$$V_{e1}(z) = 0.8V_{e50}(z) \quad \textbf{(2-3)}$$

where $V_{eN}(Z)$ = The expected extreme wind speed (averaged over 3 seconds) with recurrence periods one and fifty years; and

$V_{ref}$= reference wind speed according to Table 2.7.

To account for the turbulent extreme model, the same wind speed distribution is used. The magnitudes of the wind speed, however, are reduced. The resulting wind speeds values of Equations (2-4) and (2-5) are averaged over a ten minute interval to once again account for the effects of turbulence on frequencies.

$$V_{50}(z) = V_{ref}(z/z_{hub})^{0.11} \quad \textbf{(2-4)}$$

$$V_1(z) = 0.8V_{ref}(z/z_{hub})^{0.11} \quad \textbf{(2-5)}$$

where $V_N(Z)$ = the expected extreme wind speed (averaged over 10 minutes), with a recurrence interval of one and fifty years.

The extreme operating gust (EOG) is determined based on the standard deviation of the wind velocity at hub height as well as the size and shape of the structure. The procedures for determining both of these values can be found in (GL, 2010). The (EOG) is determined based on recurrence intervals of both one and fifty years.

$$V_{gust,N} = \beta\sigma_1 B \quad \textbf{(2-6)}$$

where $\sigma_1$ = standard deviation of the wind speed;

$\beta$ = 4.8 for N=1;

$\beta$ = 6.4 for N=50; and

B = size reduction factor.

Rapid changes in wind direction can have significantly adverse effects on the wind turbine. To account for this, the extreme direction change (EDC) model is used. Equations (2-7) and (2-8) are used to quantify the value of the direction change in terms of degrees. The direction change occurs over a period of six seconds after which, it remains constant. Furthermore, the wind speed used is derived from the (NWP) model. The direction change is determined for recurrence intervals of both one and fifty years.

$$\theta_{eN} = \pm\beta\ arctan\left(\frac{\sigma_1}{V_{hub}}B\right) \quad \textbf{(2-7)}$$

$$\theta_N(t) = \begin{cases} 0 & for\ t < 0 \\ 0.5\ \theta_{eN}\left(1 - cos(\pi t/T)\right) & for\ 0 \le t \le T \\ \theta_{eN} & for\ t > T \end{cases} \quad \textbf{(2-8)}$$

where $\theta_{eN}$ = extreme direction change magnitude, with a recurrence period of N years, limited to the range of $\pm$ 180°; and

$\theta_N(t)$ = extreme direction change for a recurrence period of N years over time, t.

The extreme coherent gust (ECG) is used to describe a sustained change in wind speed, with a cosine-shaped curve. At the end of the interval over which the change occurs, wind speed remains constant. For the standard wind turbine classes, this gust has a magnitude of 15 m/s. The velocity change acts over a period of 10 seconds. The relationship between elevation and time with respect to wind speed can be seen in Equation (2-9).

$$\theta_N(t) = \begin{cases} V(z) & for\ t < 0 \\ V(z) + 0.5\, V_{cg}\left(1 - cos(\pi t/T)\right) & for\ 0 \le t \le T \\ V(z) + V_{cg} & for\ t > T \end{cases} \quad \textbf{(2-9)}$$

Much like the (EDC) model, direction change is also taken into account for the extreme coherent gust. The procedure is similar to that used to determine the direction change of the normal wind speed profile. For further information regarding the extreme coherent gust with direction change (ECD) model refer to (GL, 2010). The final wind model is used to determine the magnitude of wind shear on the turbine blades. The extreme wind shear (EWS) model includes equations for determining both vertical and horizontal transient shear values. These are also made available in GL (2010).

### 2.3.3 Limit States

For conventional civil design, there are generally two strength limit states that are used in the design of structures. The first is often referred to as the serviceability limit state. The serviceability limit state is satisfied if the structure can perform as it was intended, without compromising structural integrity or causing occupant discomfort. A number of limitations can control the serviceability of a structure including stresses, deflections, vibrations, etc. It is assumed that the designer has a good understanding of the load magnitudes at the serviceability state and therefor, no load factors are included. In order to satisfy the ultimate limit state, the structure must be able to withstand the peak design load without the possibility of collapse. Limitations are often related to the bending, shear, and tensile or compressive stresses for each structural component. Ultimate loads are generally more unpredictable and therefore various load factors are assigned based on the type of load

considered. Many of the design manuals such as ACI and AISC provide designers with a number of factored load combinations.

The design of wind turbines as per GL (2010) incorporates many of the same procedures used for civil structures. The serviceability state is determined based on a number of possible limitations that occur under normal operating circumstances. Possible limitations include deformations, vibration amplitudes, accelerations, and material stresses. The governing serviceability loads are determined by removing the load factors corresponding to the governing ultimate load case.

### 2.3.4 Load Cases

In order to determine the ultimate limit state, a minimum set of load cases have been created by GL (2010). Table 2.10 details the minimum load cases that must be considered in the design of a wind turbine, in which the load cases are subdivided into a number of design situations that have a reasonable probability of occurring over the life of the turbine. Each case uses a specific combination of erection, maintenance, and operational modes or design situations with external conditions. The type of analysis that must be performed for each load case can be found in the "Type of Analysis" column. Each load case has a corresponding load factor that can be defined as being part of the normal and extreme conditions, abnormal conditions, or transportation and erection (Table 2.9). Normal conditions are expected to occur frequently within the life of the turbine, while abnormal conditions occur on rare occasion, usually caused by severe malfunctions of the turbine. Any loads acting favorably on the wind tower should be reduced by applying a load factor of 0.9. The governing load case for the ultimate limit state is the one that creates the most adverse conditions on the wind turbine.

An operational limit state is also defined for the design of the wind turbine. The operational limit state accounts for only those load cases that involve normal wind conditions without any additional adverse effects. They are determined based on the requirement of a fatigue analysis, which suggests long term load variation due to turbine operation or parked conditions. Only two load cases fit within the category defining the operational limit state, which are 1.1 and 6.4. It is important to note that a load factor is still included in each of the load cases.

**Table 2.9: Partial Safety Factors for Loads as per GL (2010)**

| Source of loading | Unfavourable loads | | | Favourable loads |
|---|---|---|---|---|
| | Type of design situation (see Tables 4.3.1 and 4.3.2) | | | All design situations |
| | N Normal and extreme | A Abnormal | T Transport and erection | |
| Aerodynamic | 1.35 | 1.1 | 1.5 | 0.9 |
| Operational | 1.35 | 1.1 | 1.5 | 0.9 |
| Gravity | 1.1/1.35* | 1.1 | 1.25 | 0.9 |
| Other inertial forces | 1.25 | 1.1 | 1.3 | 0.9 |
| Heat influence | 1.35 | – | – | – |
| * in the event of the masses not being determined by weighing. | | | | |

**Table 2.10: Load Cases for Wind Turbine Tower Design as per GL (2010)**

| Design situation | DLC | Wind conditions[1] | Other conditions | Type of analysis | Partial safety factors |
|---|---|---|---|---|---|
| 1. Power production | 1.1 | NTM $V_{in} \leq V_{hub} \leq V_{out}$ | | F / U | * / N |
| | 1.2 | omitted | | | |
| | 1.3 | ECD $V_{in} \leq V_{hub} \leq V_r$ | | U | N |
| | 1.4 | NWP $V_{in} \leq V_{hub} \leq V_{out}$ | Grid loss | F / U | * / N |
| | 1.5 | $EOG_1$ $V_{in} \leq V_{hub} \leq V_{out}$ | Grid loss | U | N |
| | 1.6 | $EOG_{50}$ $V_{in} \leq V_{hub} \leq V_{out}$ | | U | N |
| | 1.7 | EWS $V_{in} \leq V_{hub} \leq V_{out}$ | | U | N |
| | 1.8 | NWP $V_{in} \leq V_{hub} \leq V_{out}$ | Ice formation | F / U | * / N |
| 2. Power production plus occurrence of fault | 2.1 | NWP $V_{in} \leq V_{hub} \leq V_{out}$ | Fault in the control system | F / U | * / N |
| | 2.2 | NWP $V_{in} \leq V_{hub} \leq V_{out}$ | Fault in the safety system or preceding internal electrical fault | F / U | * / A |
| 3. Start-up | 3.1 | NWP $V_{in} \leq V_{hub} \leq V_{out}$ | | F / U | * / N |
| | 3.2 | $EOG_1$ $V_{in} \leq V_{hub} \leq V_{out}$ | | U | N |
| 4. Normal shut-down | 4.1 | NWP $V_{in} \leq V_{hub} \leq V_{out}$ | | F / U | * / N |
| | 4.2 | $EOG_1$ $V_{in} \leq V_{hub} \leq V_{out}$ | | U | N |
| 5. Emergency shut-down | 5.1 | NWP $V_{in} \leq V_{hub} \leq V_{out}$ | | U | N |
| 6. Parked (standstill or idling) | 6.1 | EWM Recurrence period 50 years | | U | N |
| | 6.2 | EWM Recurrence period 50 years | Grid loss | U | A |
| | 6.3 | EWM Recurrence period 1 year | Extreme oblique inflow | U | N |
| | 6.4 | NTM $V_{hub} < V_{in}$ *and* $V_{out} < V_{hub} < 0.8\ V_{ref}$ | | F / U | * / N |
| 7. Parked plus fault conditions | 7.1 | EWM Recurrence period 1 year | | U | A |
| 8. Transport, erection, maintenance and repair | 8.1 | $EOG_1$ $V_{hub} = V_T$ or NWP $V_{hub} = max\ (EOG_1$ *based on* $V_T)$ | To be specified by the manufacturer | U | T |
| | 8.2 | EWM Recurrence period 1 year | Locked state | U | A |

* Partial safety factor for fatigue strength (see Section 4.3.5.2.2)
[1] If no cut-out wind speed $V_{out}$ is defined, $V_{ref}$ shall be used.

F = Fatigue analysis required

U = Ultimate load analysis required

## 2.4 Characteristics and Utilization of UHPC

### 2.4.1 Overview

A material is often classified as an Ultra-High Performance Concrete (UHPC), when it meets the following conditions: compressive stress greater than 21.7 ksi (150 MPa), internal fiber reinforcement to ensure nonbrittle behavior, and high binder content with special aggregates (Federal Highway Administration, 2006). Each of these properties gives it a unique advantage over both normal and high strength concrete. Although a material can be defined as UHPC at lower compressive strengths, it can easily reach compressive limits as high as 32 ksi (220 MPa). At this level, UHPC becomes competitive with steel in terms of weight/strength ratio making it much more competitive at a high cost.

### 2.4.2 Material Composition

According to polystructural theory, the overall properties of a material are a function of both the macro-level (cement and aggregate) and micro-level (modified cement paste and admixture) properties (Vande Voort et al., 2008). UHPC achieves much of its strength from highly compact, low porosity matrix. A concept known as "space packing" is used to determine the appropriate particle size distribution (Vande Voort et al., 2008). The result is a wide distribution in granular class size that gives UHPC a much more densified matrix than conventional concrete. This improved matrix also improves its corrosion resistance making it an ideal candidate for extreme environments. Table 2.11 and Table 2.12 show the typical material composition of UHPC. It is important to note the lack of coarse aggregates in the mix. UHPC can be described as a densified system with ultra-fine particles (DSP), meaning the use of coarse aggregates has been completely eliminated from the mix design (Vande Voort et al., 2008). With the elimination of coarse aggregates, UHPC exhibits improved flow characteristics allowing for reduced bar spacing in steel reinforced structures. Refer to Lewin and Sritharan (2010) for a detailed description of each of the material components listed.

**Table 2.11: Range of UHPC Mix Components (Vande Voort et al., 2008)**

| Component | Typical Range of Weight (Mass) per ft3 (m3) |
|---|---|
| Sand | 31 - 87 lb (490 - 1390 kg) |
| Cement | 38 - 67 lb (610 - 1080 kg) |
| Silica Fume | 3.1 - 21 lb (50 - 334 kg) |
| Crushed Quartz | 0 - 26 lb (0 - 410 kg) |
| Fibers | 2.5 - 15.5 lb (40 - 250 kg) |
| Superplasticizer* | 0.6 - 4.5lb (9 - 71 kg) |
| Water | 7.9 - 16.3 lb (126 - 261 kg) |

*Superplasticizer is expressed as the weight of the solid fraction; the liquid fraction is included in the water weight

**Table 2.12: Typical UHPC Mix Components (Cheyrezy and Behloul, 2001)**

| Component | Weight per Cubic Foot (Meter) | Mass Ratio/Cement | Volume Fraction |
|---|---|---|---|
| Sand | 61.9 lb (991 kg) | 1.43 | 38.8% |
| Cement | 42.3 lb (693 kg) | 1 | 22.7% |
| Silica Fume | 14.0 lb (225 kg) | 0.325 | 10.6% |
| Crushed Quartz/ Fly Ash | 13.0 lb (208 kg) | 0.3 | 8.1% |
| Fibers | 9.4 lb (151 kg) | 0.218 | 2.0% |
| Superplasticizer* | 0.90 lb (14.4 kg) | 0.021 | 1.4% |
| Water | 9.9 lb (159 kg) | 0.229 | 16.5% |

*Superplasticizer is expressed as the weight of the solid fraction; the liquid fraction is included in the water weight

### 2.4.3 Strength Characteristics

Although UHPC has existed for a number of years, it is only within the last decade that its use in structural design has begun to take hold. Even with the increased use of UHPC, there has yet to be a unified compilation of UHPC properties. The following, highlights some of the more general properties of UHPC compiled from a number of different sources.

*Compression*

The high compressive strength of UHPC is achieved through a number of sources. The largest contributor to the increased strength is the increased matrix density (Vande Voort et al., 2008). This allows the stress to be more evenly distributed through the specimen. The addition of steel fibers and use of steam treatments also has an effect on the compressive

strength of UHPC. The fibers main contribution to compressive strength of UHPC is in the form of confinement. A number of tests completed by the FHWA show that UHPC fails in a very brittle and explosive manner when fibers are not present. Although the material can reach compressive strengths of 31 ksi (214 MPa) when fibers are not present, there would essentially no warning if a member were to be overloaded. In this case, the application of UHPC in structural design would be extremely limited.

For the purposes of this report, the stress-strain behavior proposed by Gowripalan and Gilbert (2000) has been adopted. Figure 2.4 shows the idealized tri-linear stress-strain compressive behavior of the UHPC. In this model, linear-elastic behavior occurs until 85% of $f'_c$ is reached. Following the linear elastic behavior, perfectly plastic behavior is exhibited until a strain of 0.004 is reached. From this point a linear decrease in stress occurs between strains of 0.004 and 0.007. The strains used to define the transition between the slopes of the stress strain curve are very similar to those defining normal strength unconfined concrete curves developed by Mander.

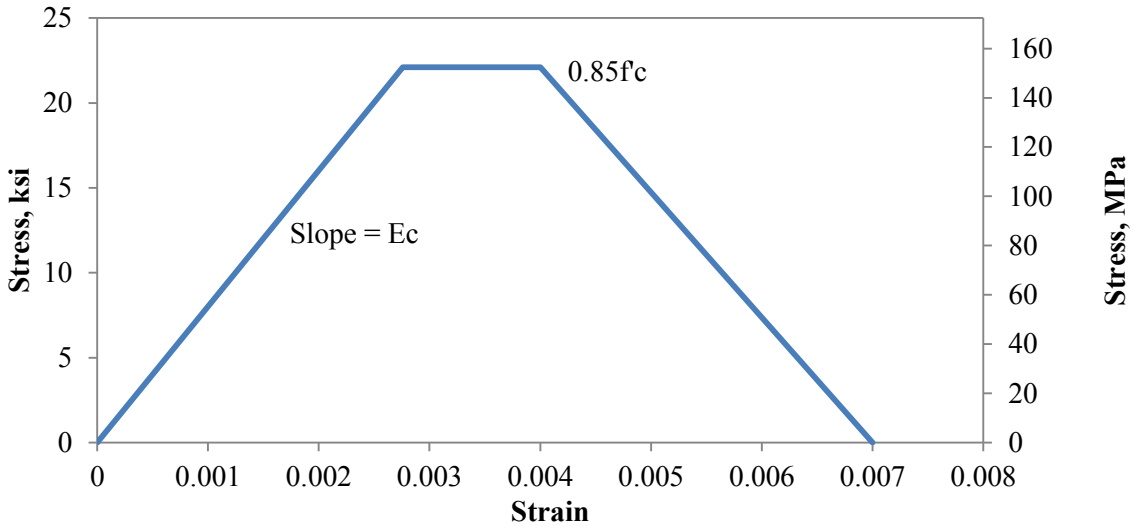


**Figure 2.4: Stress Strain Behavior of UHPC (Gowripalan and Gilbert, 2000)**

From a number of equations that attempted to describe the elastic modulus of UHPC, Vander Voort determined that Equation (2-10), originally proposed by Graybeal (2006) provided values similar to those achieved during testing.

$$E = 50{,}000\sqrt{f'_c\ (psi)} \qquad \textbf{(2-10)}$$

*Tension*

The tensile behavior can be divided into three distinct categories, as shown in Figure 2.5. As load is applied to a specimen, it first undergoes linear-elastic behavior in which no cracking occurs. After cracking has initiated strain hardening of the steel fibers begins to take place. The strain hardening helps in the dispersion of cracks along a member as well as provides some additional strength gain. After strain hardening has occurred, crack localization ultimately leads to a loss in tensile capacity.

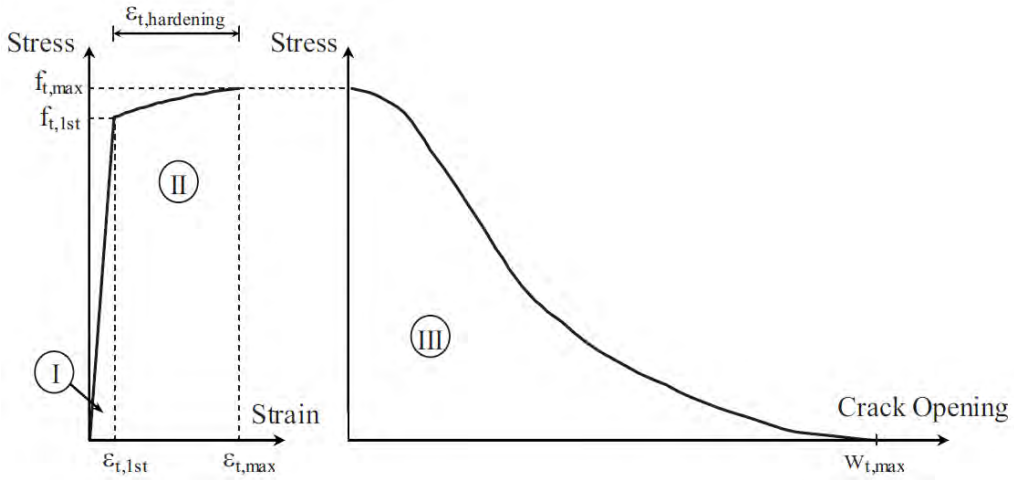


**Figure 2.5: Tensile Regions of UHPC (Graybeal, 2008)**

For the purposes of this report, the tensile stress-strain behavior developed by (Bristow and Sritharan, 2011) will be used. The behavior is illustrated in Figure 2.6. The equations used to define this behavior are shown directly below. Each equation has a set of strain limits that define each portion of the curve.

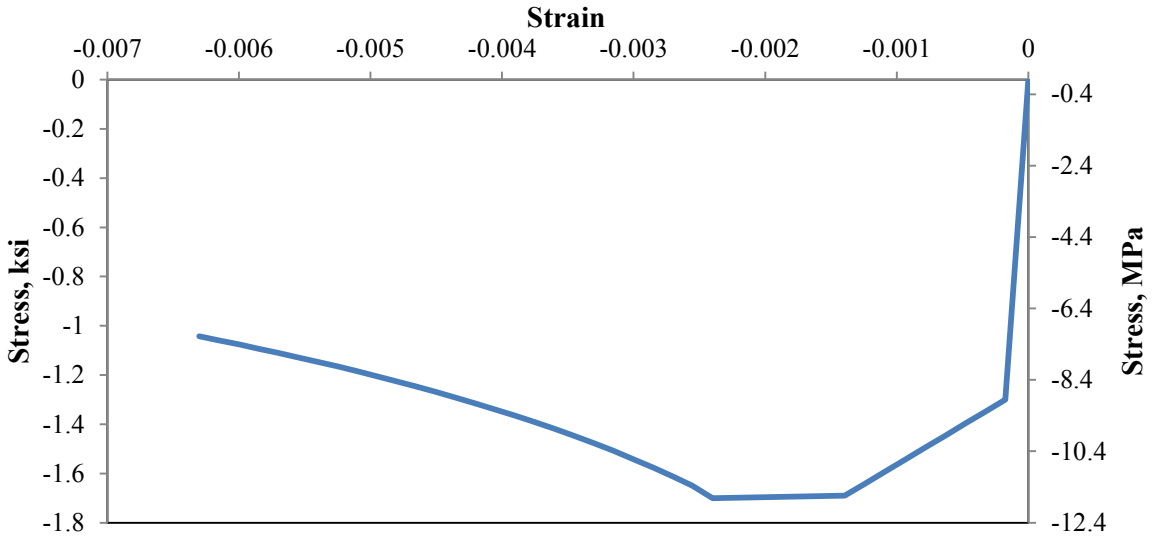


**Figure 2.6: Tensile Stress-Strain Behavior of UHPC (Lewin and Sritharan, 2010)**

$$f_t = E_c\varepsilon \qquad for\ \varepsilon \le f'_{te}E_c \tag{2-11}$$

$$f_t = f'_{te} + \frac{(f'_{teMAX} - f'_{te})(\varepsilon - f'_{te}/E_c)}{0.00125} \qquad for\ f'_{te}E_c < \varepsilon < 0.0014 \tag{2-12}$$

$$f_t = f'_{teMAX} \qquad for\ 0.0014 < \varepsilon < 0.0024 \tag{2-13}$$

$$f_t = f'_{teMAX} - 0.672\ln\varepsilon \qquad \varepsilon > 0.0024\ until\ f_t = 0 \tag{2-14}$$

where $f_t$ = tensile stress;

$E_c$ = the Elastic Modulus, recommended as 8000 ksi (55,000 MPa);

$\varepsilon$ = tensile strain;

$f_{te=}$ elastic tensile strength, recommended as 1.3 ksi (9.0 MPa); and

$f_{t,MAX}$ = maximum tensile strength, recommended as 1.7 ksi (11.7 MPa).

If cured using heat treatment, shrinkage of UHPC can be nearly eliminated. This greatly reduces the risk of cracking making, nearly impervious to environmental conditions. In the case of prestressing or post-tensioning, reduced shrinkage also allows engineers to better

predict the long term losses that occur as a result. Figure 2.7 illustrates the behavior of both steam treated and untreated UHPC.

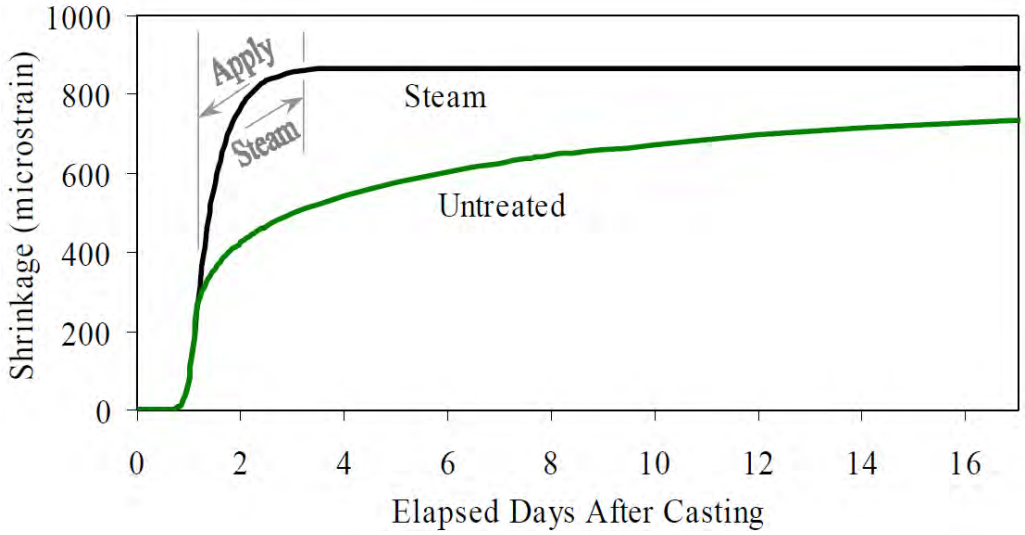


**Figure 2.7: UHPC Shrinkage Behavior over Time With and Without Steam Curing (Federal Highway Administration, 2006)**

### 2.4.4 Recent Applications

UHPC has experienced increased public exposure over the last couple of years through research and field applications. As the material properties and potential benefits are better understood, more designers are incorporating it into their designs. The projects shown below are some of the more recent applications of UHPC. Many of these projects are still associated with university research activities; however, an increasing number of private firms are becoming involved through various partnerships. Additional projects relating to UHPC can be found in Lewin and Sritharan (2010).

*UHPC Bridge Piles*

The push for increased service life in bridges, as well as reduced maintenance costs, has brought about the redesign of bridge piles using UHPC. They provide superior corrosion and deterioration protection that doesn't exist in steel and normal strength concrete piles. The use of precast, prestressed, UHPC piles also alleviates some of the problems associated with local buckling of steel piles and drivability issues with conventional concrete piles. Although UHPC requires a high upfront cost, reduction in both the section sizes and long-term

maintenance costs make it a more competitive solution. A recent research study performed at Iowa State University tested the behavior of the piles in a lab environment as well as in the field (Garder, 2012). Figure 2.8 shows one of the piles driven for field testing at a bridge construction site in Iowa.


**Figure 2.8: UHPC Bridge Pile (Garder, 2012)**

*Little Cedar Creek Bridge*

In 2008, researchers began development of a precast UHPC waffle deck design that would allow on site construction times and material requirements to be dramatically reduced. A series of laboratory and field tests were performed and published in Aaleti et al. (2011). Since the completion of the study, the waffle deck has been used in the construction of the Little Cedar Creek Bridge in Wapello County, Iowa (Figure 2.9). The system utilized UHPC not only in the UHPC waffle slabs, but also in the construction joints used to connect the panels on site (Figure 2.10).The bridge was the first-of-its kind and has proven to be very successful (Moore, 2012).

**Figure 2.9: Underside of UHPC Waffle Deck Bridge (Moore, 2012)**

**Figure 2.10: Construction Joints on Little Cedar Creek Bridge (Moore, 2012)**

## 2.5 Connections between Precast Concrete Members

Precast concrete has a number of advantages over the traditional cast-in-place alternative. Quality control is greatly improved with the use of a skilled workforce and temperature controlled environment. Construction times can also be reduced by eliminating much of the

on-site formwork. Utilizing precast concrete does, however, have challenges associated with it. One of these challenges deal with the structural connection between precast sections. Many times the connections are required to meet or exceed the capacities of the precast sections being connected. Connections are often distinguished as either wet or dry connections. For example, a wet connection is made by cast-in-place concrete between the precast concrete elements; a dry connection consists of steel embedded plates, angles or other steel elements that are either welded or bolted together through the use of a single steel plate (Hofheins et al., 2002). Although numerous connections have been used in past precast concrete designs, this section focuses on those considered to be applicable to the proposed wind turbine tower design.

### 2.5.1 Welded Connections

Welded connections are some of the most common types of connections in the precast industry. They often consist of embedded steel plates in the two precast sections being joined together. When erected, the embedded plates of both sections are placed within close proximity to one another as to allow for a single steel plate to be welded to both sections. The embedded plates are large enough to allow for small deviations in precast section dimensions. The number of connections required depends on the magnitude of the load being transferred between these sections. Figure 2.11 illustrates the use of welded connections in a precast building.


**Figure 2.11: Welded Plate Connections in a Precast Wall Application (Crisafulli and Restrepo, 2003)**

A number of reports have been published on the use of welded connections for precast structures subject to dynamic loads. The goal of the research often consisted of determining the most suitable connection for seismic regions. Each report used a different set of connection plates for testing, many of which were unique. Although each had a slightly different design, many fell into two general categories. The first of these categories is the perforated plate. This included notched, drilled, and slotted plates. Examples of slotted and drilled connections are shown in Figure 2.12. Because of their large initial elastic stiffness, this connection plate is well suited for strong coupling of shear wall panels (Schultz et al., 1994). In other words, the use of this connection allows the precast segments to emulate the behavior of a monolithic structure (Schultz et al., 1994). The second category of welded connections is the flat bar. Figure 2.13 gives examples of two different shapes of flat bars. Results from cyclic load tests on flat bar connections suggest they have a higher and more reliable capacity to dissipate energy than then the perforated plates (Schultz et al., 1994). In high seismic regions this is a very attractive feature.

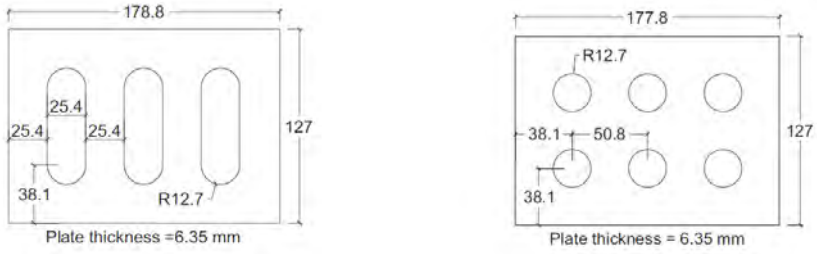


**Figure 2.12: Slotted/Drilled Plates for Welded Connections (Henry et al., 2010)**

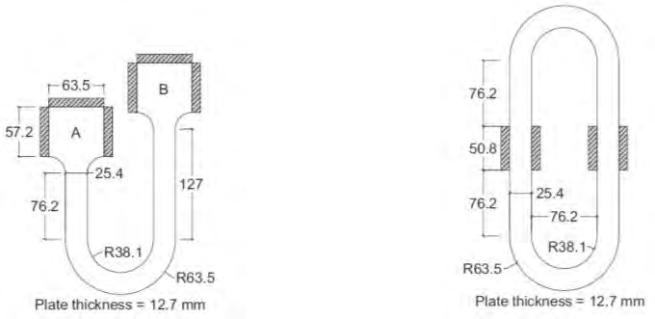


**Figure 2.13: Flat Bar Configurations for Welded Connections (Henry et al., 2010)**

Although welded connections can frequently be designed with significant load carrying capacity, they often perform poorly in structures subject to high-cycle fatigue. Fatigue failure can occur at stress levels well below the service capacity of a member. This is possible when defects are present in the material or weld. Over time, these defects develop into cracks that begin to propagate at a rate dependent on the frequency and magnitude of stress reversals (Hansen, 1996). When a material is welded, the number of defects increases dramatically, reducing the life of the structure (Lassen and Naman, 2006). The relatively short fatigue life of a welded detail is explained by three primary factors: the severe notch effect due to the attachment and weld filler metal, the presence of non-metallic intrusions of micro-flaws along the fusion line, and the presence of large tensile residual stresses (Lassen and Naman, 2006). Each type of weld experiences different levels of severity within these three factors. A butt weld, for example, has a much longer fatigue life then a T-joint because it dramatically reduces problems associated with the notch effect.

Many regulations exist that use a variety of methods to determine the fatigue life of welded joints. One of the more popular methods is presented in the Eurocode 3 (British Standards Institution, 2005). This method presents fourteen parallel curves that all have an inverse slope of 3. For constant amplitude fatigue loading (CAFL), a cut-off limit is assigned at $5x10^6$ cycles. If the stress range falls below the CAFL, fatigue life is infinite. For variable stress ranges, a cutoff limit is assigned at $1x10^8$cycles. Additionally, the slope of the curve changes to m=5 between the two cut-off limits. The S-N curve for each of the different classification groups is illustrated in Figure 2.14 where “S” represents cyclic stress and “N” represents the cycles to failure. A large number of different structural details are presented in Hobbacher (1996) along with their corresponding classification numbers. Some of these details have been presented in Table 2.13 to show the types of details assigned to the different FAT-classes (fatigue classes).

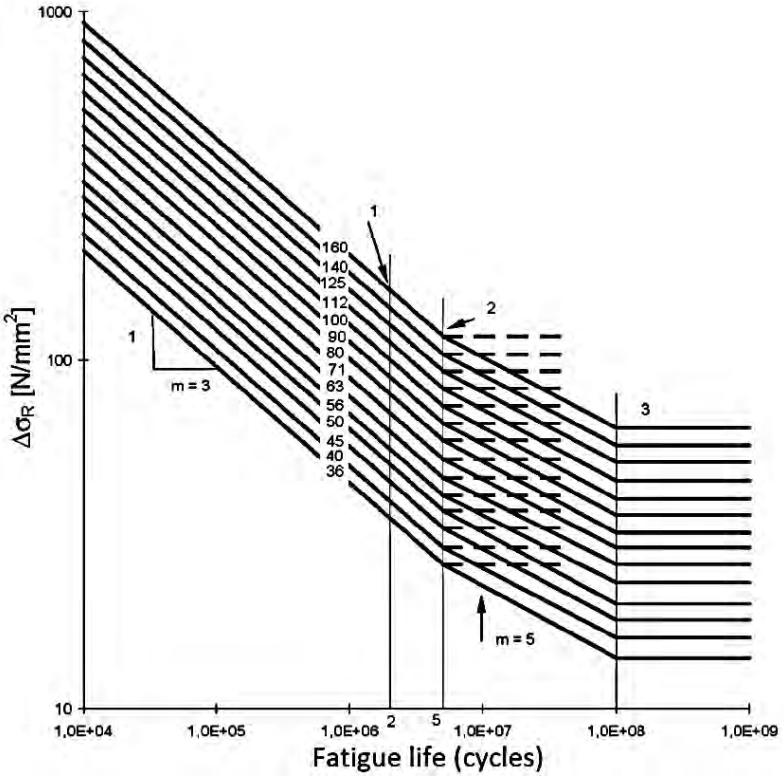


1 Detail Category, $\Delta\sigma_c$

2 Constant Amplitude Fatigue Limit, $\Delta\sigma_D$

3 Cut-off Limit, $\Delta\sigma_L$

**Figure 2.14: S-N Curve of Welded Joints as per Eurocode 3 (British Standards Institution, 2005)**

**Table 2.13: Fatigue Class of Various Steel Components (Hobbacher, 1996)**

| Description | FAT |
|---|---|
| Unwelded parts of a component<br>1) Plates and Flats<br>2) Rolled Sections<br>3) Seamless hollow sections | 160 |
| Transverse loaded butt weld (Full-Penetration) | 125 |
| Three Plate Connection | 71 |
| Longitudinal butt or fillet weld | 36-71 |

According to GL (2010), the endurance limit reached at $1x10^8$ cycles for the S-N curves shown in Figure 2.14 is not permissible in the design of wind turbine towers. Instead, the slope used prior to the endurance limit shall be continued until it intersects the horizontal

axis. With the twenty year service life of a wind turbine tower approaching $1x10^9$ cycles, it is clear that the welds on the lower spectrum of the fatigue class will have very little to no stress reversal capacity remaining. For this reason, the capacity of the weld is often governed by fatigue rather than strength limitations. The use of welded connections on structures subject to high-cycle fatigue such as wind turbine towers is not prohibited; however, their design should be carefully completed.

### 2.5.2 Bolted Connections

Bolted connections between precast concrete segments are also used quite frequently around the precast industry. Although not as popular as the welded connection, they provide a number of advantages other types of connections cannot. As owners continue the pressure engineers to develop new methods to reduce the on-site construction time, bolted connections are often considered. They provide a positive connection between two precast components immediately, without tying up crane time (NPCA, 2011). In addition to reducing erection times, the fatigue life of bolted connections is also an attractive feature.

There are two methods in which a bolt can be used to resist shear in a connection. The bearing-type connection is most commonly used when fatigue is not a major design consideration (Bickford, 2008). In this case, shear transfer between the two connected components takes place through the area of the bolt. The second type of connection is the slip-critical connection. Because shear transfer takes place through the area of the bolt and friction developed between the joined surfaces, this type of connection is useful in joints subject to high-cycle fatigue.

GL (2010) requires the use of IEC (2005) for the fatigue analysis of bolts. Like the fatigue analysis used for welds, classification numbers are assigned to different types of connections. These numbers are used to define the appropriate S-N curve to be used. Bearing-type and slip-critical connections are assigned different classification numbers to reflect the differences in fatigue capacity. For a bearing type connection, a classification number of 100 is assigned and the stress due to load reversal is based on the shank area of the bolt. Slip-critical connections are designed with a classification number of 112, but the stress due to load reversal is based on the gross surface area between the connected parts. The use

of a gross area for slip-critical connections is to account for friction resistance between the connected parts.

For bolts subjected to direct tensile stress, the S-N curve shown in Figure 2.14 is once again applicable. Bolts subjected to shear stress fatigue must be designed using Figure 2.16. The endurance limit is not applicable as per GL (2010) and the slope prior to $1x10^8$ cycles must be used.

Bolted connections provide a suitable solution to many of the challenges associated with precast connections. The frequent use of bolts between current steel tower segments and the foundation suggest they have performed well in past applications (e.g. see Figure 2.15). When transitioning to precast concrete designs, however, bolted connections require a number of embedded plates and increased tolerances from the precaster. This can lead to an increase in tower costs, thus making it a less attractive solution.

**Figure 2.15: Use of Bolted Connections in Current Tower Designs (Gundersen Envision, 2013; NIB Torque, 2013)**

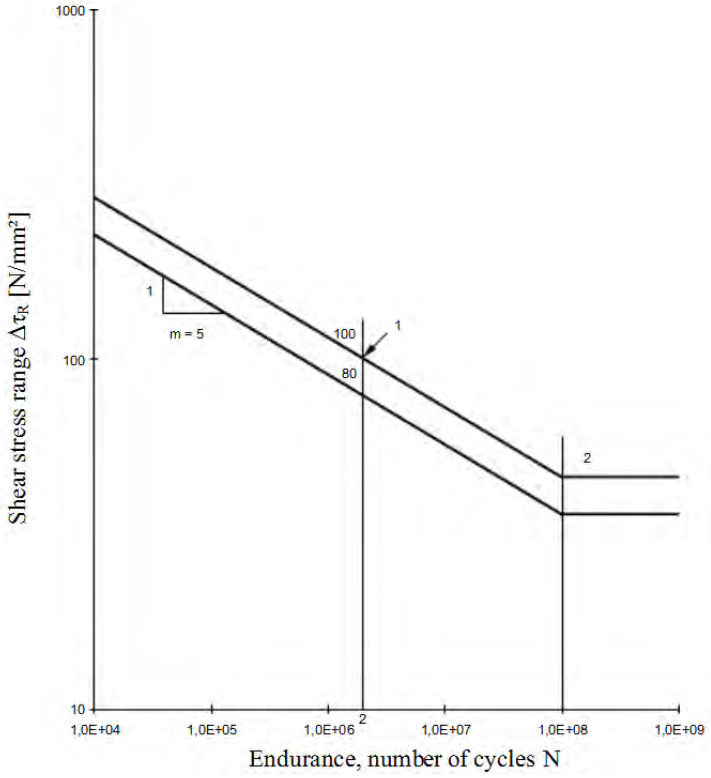


**Figure 2.16: Fatigue Strength Curves for Various Shear Stress Ranges (IEC, 2005)**

### 2.5.3 UHPC Wet Joint

The use of UHPC as a joint material is a concept that has been around for a number of years. Some of the earliest applications, dating back to 1995, were used as a connection between slab elements in buildings (Federal Highway Administration, 2010). Within the past five years interest in UHPC as an in situ joint material has accelerated as a result of the need for establishing reliable connections in the field as part of bridge construction. A number of reports have been published describing the strength and fatigue performance of UHPC joints through various tests (e.g. see Federal Highway Administration, 2010; Hartwell, 2011).

One of the most attractive features that UHPC has over many of the other grout solutions is the reduction in development lengths for mild-steel reinforcement. Tests were performed by the New York State Department of Transportation Materials Bureau to investigate the required development lengths for different sized deformed reinforcing bars. The tests involved casting bars into 15.74-in. (39.97 cm) diameter UHPC cylinders (Figure 2.17). The results of the test can be seen in Table 2.14.

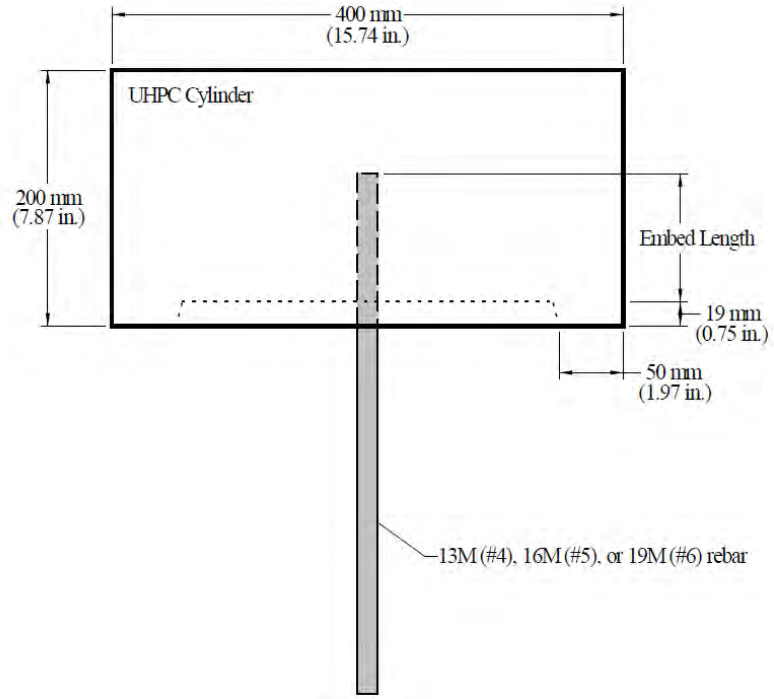


**Figure 2.17: NYSDOT Reinforcement Pullout Test Configuration (Federal Highway Administration, 2010)**

**Table 2.14: Results of NYSDOT UHPC Rebar Pullout Tests (Federal Highway Administration, 2010)**

| Bar Type | Bar Size | Embedment Length in. (cm) | UHPC Age (days) | Peak Bar Stress ksi (MPa) | Mode of Failure |
|---|---|---|---|---|---|
| Black | #4 | 2.9 (7.4) | 7 | 101.1 (697) | Rebar Fracture |
| Black | #5 | 3.9 (9.9) | 7 | 104.8 (723) | Rebar Fracture |
| Black | #6 | 4.9 (12.4) | 7 | 105.0 (724) | Rebar Fracture |
| Epoxy-Coated | #4 | 2.9 (7.4) | 7 | 102.0 (703) | Rebar Fracture |
| Epoxy-Coated | #5 | 3.9 (9.9) | 7 | 107.7 (743) | Rebar Fracture |
| Epoxy-Coated | #6 | 4.9 (12.4) | 7 | 105.9 (730) | Rebar Fracture |
| Epoxy-Coated | #4 | 2.9 (7.4) | 28 | 100.4 (692) | Rebar Fracture |
| Epoxy-Coated | #5 | 3.9 (9.9) | 28 | 107.3 (740) | Rebar Fracture |
| Epoxy-Coated | #6 | 4.9(12.4) | 28 | 106.0 (731) | Rebar Fracture |

Each of the tests resulted in rebar fracture, which shows the embedment lengths used were adequate. This represents a significant reduction in the length of straight bars needed to develop their full fracture capacity in the concrete. For #4 grade 60 bars in normal strength 4.0 ksi (28 MPa) concrete, the reduction in development length can be up to 16-in. (46 cm) when using the ACI 318 (2008) recommendations. For epoxy coated bars the reduction in development length increases to nearly 26-in. (66 cm). Even with the use of standard hooks, the volume required in joints using typical grouts will be significantly higher for this reason. The increase in joint volume means an increase in on-site labor and construction times.

A similar study was completed by Fehling et al. (2011) that suggested the use of 6 $d_b$ as a required development length. In this case the bars just reached yield capacity before some form of concrete breakout took place. Unlike the study completed by the NYSDOT, which used large cylinders to embed the bars, Fehling et al. (2011) tested various concrete coverage depths that ranged from 1 to 2.5 $d_b$, where $d_b$ is the diameter of the deformed bar. The three primary modes of concrete failure that took place were cone failure, v-type splitting, and splitting (Figure 2.18). The results from each of the tests have been compiled in Figure 2.19 to show the relationship between embedment length, concrete cover, and failure mode. As a result of both the Federal Highway Administration (2010) and Fehling et al. (2011) reports having similar outcomes, the use of 6 $d_b$ for a required development length was considered acceptable for design purposes.

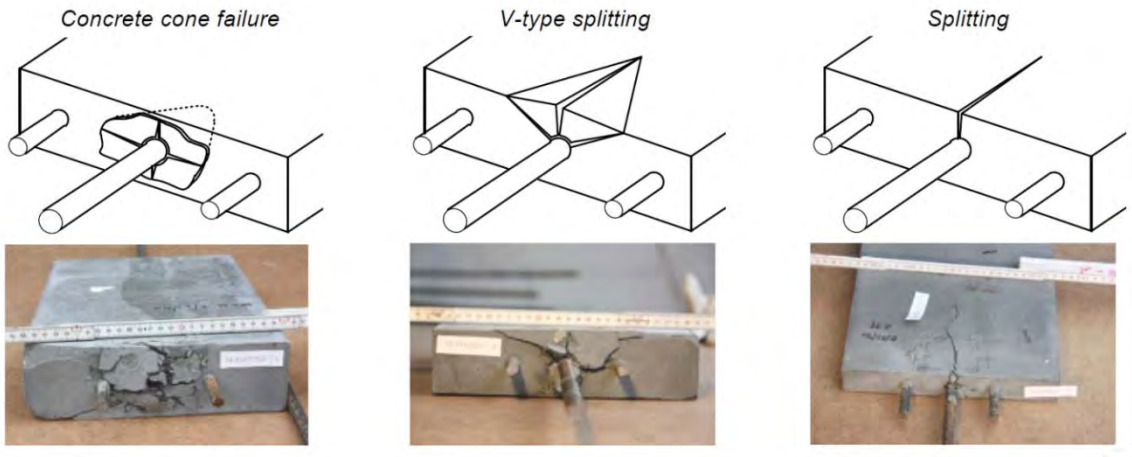


**Figure 2.18: Concrete Failure Modes of UHPC Pullout Test (Fehling et al., 2011)**

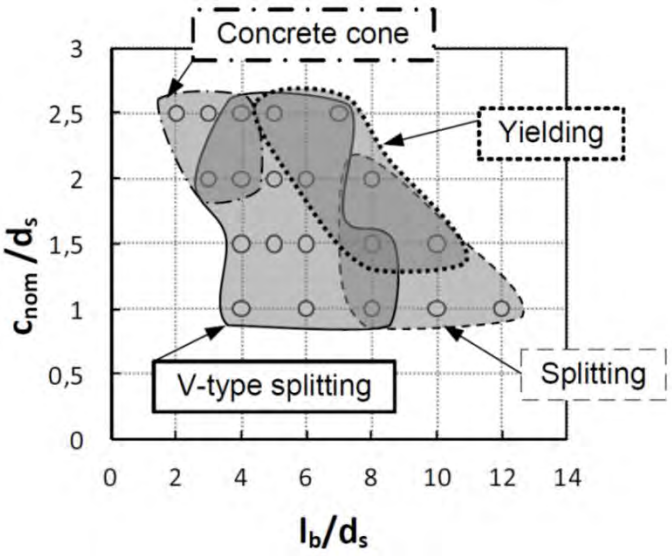


$c_{nom}$ = Depth of concrete cover

$d_s$ = Diameter of steel bar

$l_b$ = Embedment length of bar

**Figure 2.19: Failure Modes of UHPC Pullout Tests (Fehling et al., 2011)**

With the reduction in joint volume, clear cover, and spacing between bars, the formation of any potential voids in the joint can significantly reduce its capacity. The presence of large voids can be detrimental to the performance of the joint, especially if a large void forms along the short embedment lengths of the reinforcement. In order to address this issue, a constructability test of UHPC joints was conducted by Hartwell (2011) that examined the flow characteristics and consolidation. The test specimen shown in Figure 2.20 was used to perform the constructability test. The specimen represented a portion of a precast bridge joint designed with the same bar size and spacing that was to be used for a bridge in the field.

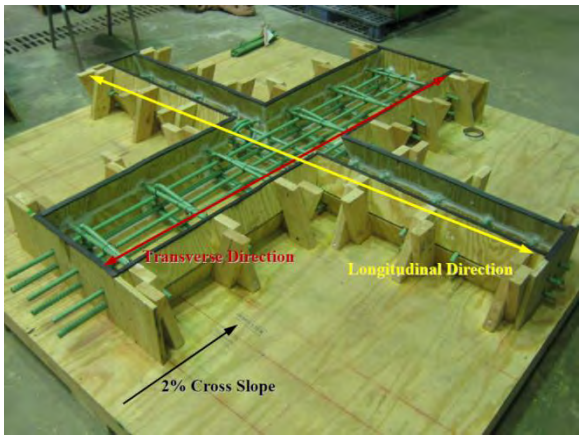


**Figure 2.20: UHPC Joint Constructability Test Specimen (Hartwell, 2011)**

As a result of this test, two key observations were reported. The first was that ambient temperature has a significant effect on the flow characteristic of UHPC. When batched at an ambient temperature of 65˚F, the UHPC reached approximately 85˚F at discharge. At this temperature adequate flow characteristics were obtained. When the ambient temperature reached 75.5˚F however, acceptable flow characteristics were not achieved and the batch needed to be discarded (Hartwell, 2011). The second observation made from this test was that the UHPC showed good consolidation around the steel reinforcement (Hartwell, 2011). Numerous sections of the specimen were examined after adequate curing was allowed to take place. Figure 2.21 illustrates good consolidation and lack of voids around the joint reinforcement.

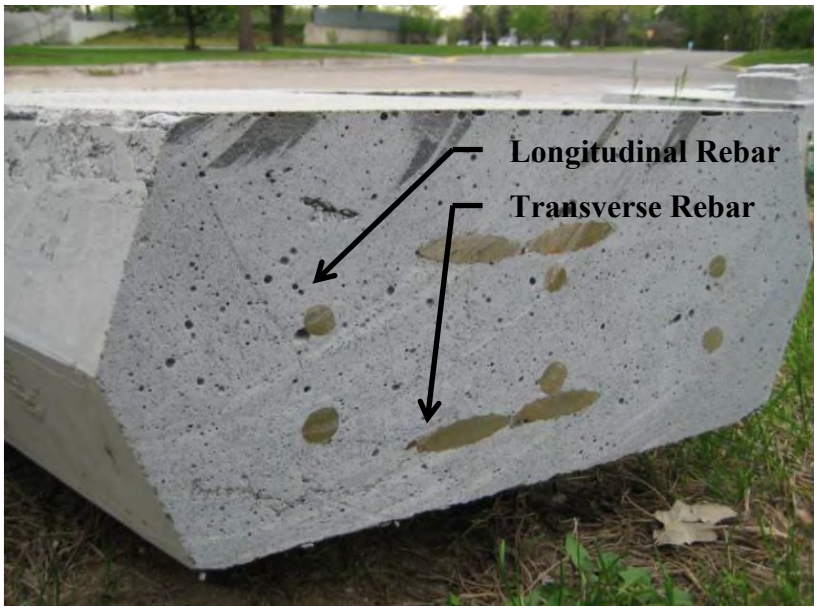


**Figure 2.21: Section of Transverse Joint from Constructability Test (Hartwell, 2011)**

A report released by the Federal Highway Administration (2010) presented the results of a series of strength and fatigue tests on joints using different bar configurations. Figure 2.22 shows the bar configurations used for three different specimens. The first configuration used #5, headed black reinforcement with 3.5-in. (8.9 cm) lap length. The second used hairpin epoxy-coated bars with 3.9-in. (9.9 cm) lap lengths. The bottom configuration of Figure 2.22 used galvanized straight bars with 5.9-in. (15.0 cm) lap lengths (Federal Highway Administration, 2010). The cyclic loading pattern of Figure 2.23 consisted of a number of

peak loads over the duration of approximately seven million cycles. The 16 kip (71.2 kN) load was selected because it was anticipated to generate the first tensile cracks in the panels. The 21.3 kip (94.7 kN) load was 1.33 times the first cracking load and was selected in order to achieve cracking in the panels. The static loading of the panels was done in a stair-step fashion with temporary holds at 5 kip (22.2 kN) intervals (Federal Highway Administration, 2010). After cracking was initiated along the bottom side of the panel, a displacement based loading procedure was used.

The results of the cyclic load test shown in Figure 2.24 were obtained from the top specimen of Figure 2.22. As expected some minor cracking was observed along the bottom of the panel after a period of 2 million cycles. This cracking became more apparent immediately after the 21.3 kips (94.7 kN) load was applied, which stabilized in the precast panels throughout the remaining cycles. Some additional cracking did continue to develop throughout the test. No interface cracking was observed throughout the entire test (Federal Highway Administration, 2010). It is important to note that the bar details were not engaged during cyclic loading because of good interface bonding.

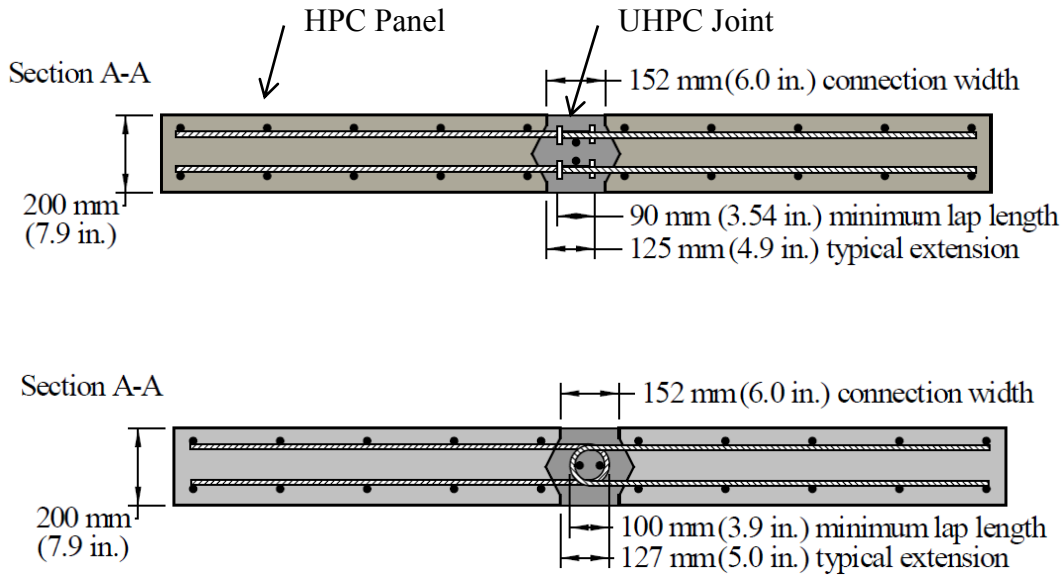

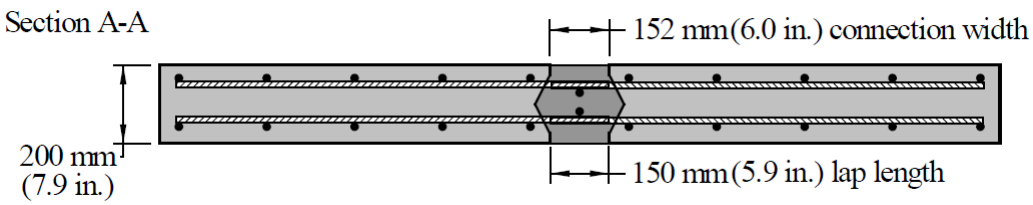


**Figure 2.22: UHPC Joint Layouts Tested for Strength and Fatigue (Federal Highway Administration, 2010)**

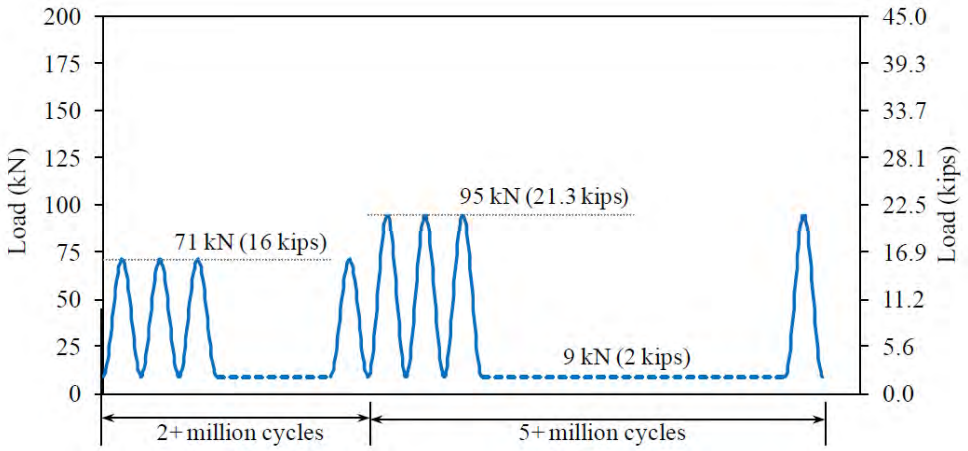


**Figure 2.23: Cyclic Loading Program for UHPC Joints (Federal Highway Administration, 2010)**

The results of the static load test are shown in Figure 2.25. Just before failure occurred, localized strain was observed in both the UPHC connection and precast panels. The strain localization resulted in the pullout of UHPC fibers across the critical midspan as well as yielding of the bottom mat of reinforcement. The cyclic and static load results of the panels utilizing the two other details were not included because the results were very similar to those shown. The similarity in results shows the adequacy of each of the three bar details. In the conclusion of the report, it was stated that "The structural behavior of the transverse connection tested herein emulated or surpassed the behaviors that would be anticipated from a monolithic concrete bridge deck." The results of these tests show the use of UHPC wet joints in a concrete wind tower application could potentially provide the required capacity to allow the tower to act as a monolithic structure.

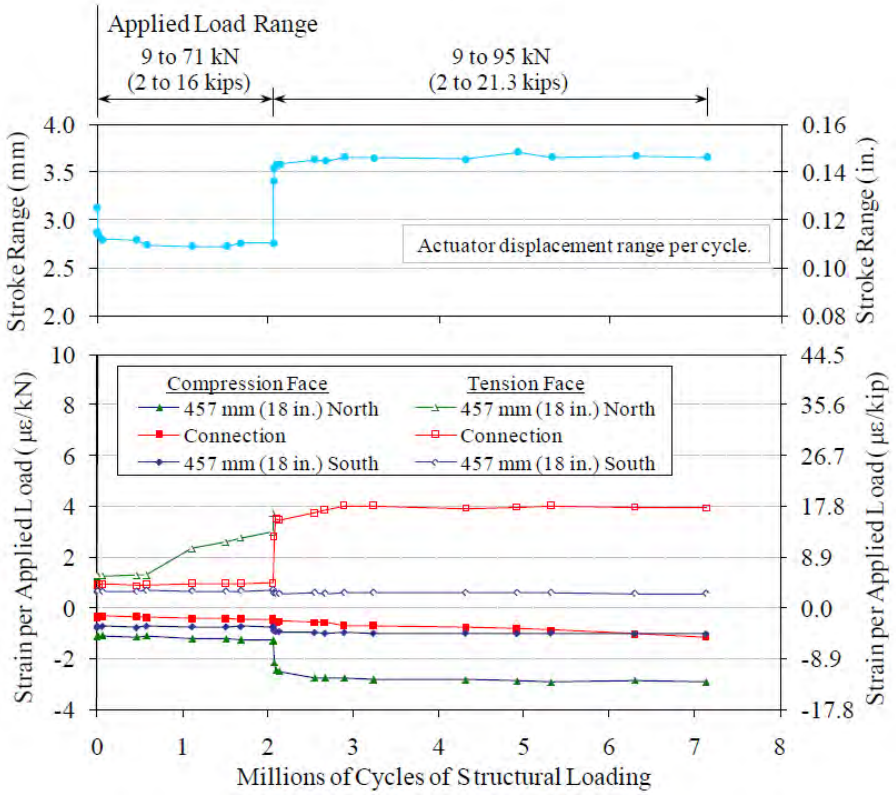


**Figure 2.24: Results of Cyclic Load Test on UHPC Joint (Federal Highway Administration, 2010)**

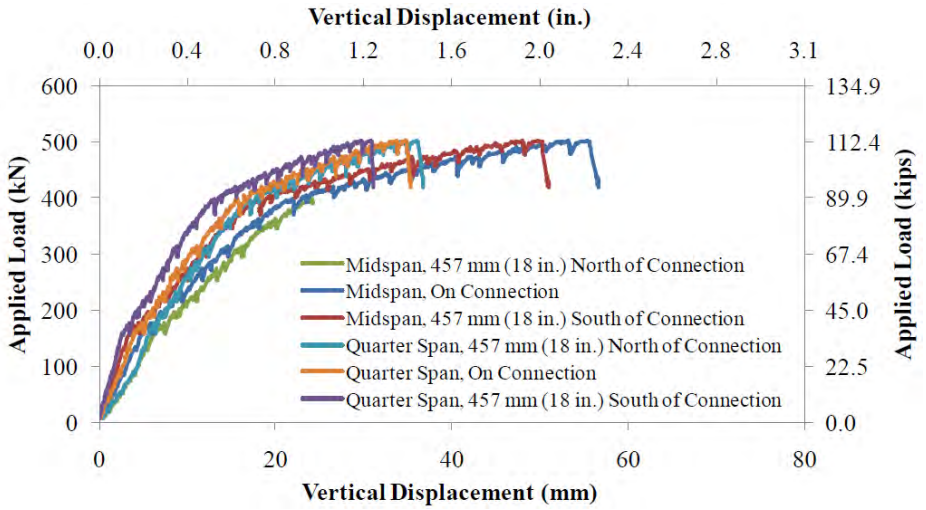


**Figure 2.25: Static Load Test Results for UHPC Joint (Federal Highway Administration, 2010)**

### 2.5.4 Post-Tensioned Connections

The use of post-tensioning as a precast connection has long been considered for a number of structural applications. Some of which include precast bridge decks, shear wall panels, beam-to-column connections, and column-to-slab connections (e.g. see Figure 2.26). These typed of joints are often less costly than alternative designs such as in situ connections which require more labor and time to construct. Depending on the type of elements being connected, other forms of connection such as dowel bars may be used in conjunction with the post-tensioning to improve the capacity joint. In addition, the use of post-tensioning often improves the performance of the connected region by generating a residual compressive stress throughout the connection. This can greatly reduce the maintenance costs by eliminating cracks from forming during extreme loading events.

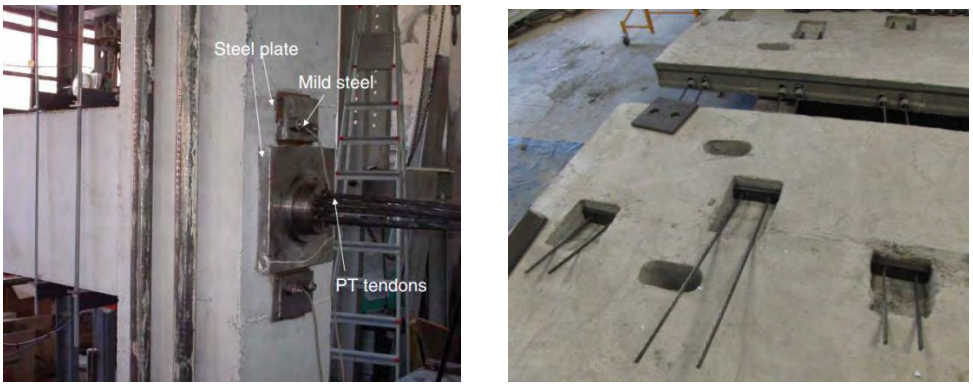


**Figure 2.26: Beam-to-Column and Transverse Bridge Deck Post-Tensioned Connections (Ozden and Ertas, 2007; Wells, 2012)**

A post-tensioned connection relies on different forms of load resistance to meet the required capacity of the joint. When considering a joint in which post-tensioning is the only form of connection, shear capacity is dependent on static friction between the components. This means the capacity is proportional to the level of stress developed normal to the interface. The coefficient of friction, which describes the resistance of the interface to slip, also has a significant effect on the shear resistance. Joints with rough surfaces or those that use wet concrete or grout generally have higher coefficients of friction. A certain level of slip is often used to define the ultimate limit state of a structure. The axial and moment capacities of a post-tensioned joint are also dependent on the level of stress normal to the interface. Higher stress levels require greater axial and bending forces to cause separation at the joint.

# CHAPTER 3. DEVELOPMENT OF A SEGMENTAL CONCRETE WIND TOWER

## 3.1 Introduction

The purpose of this chapter is to present the process used to complete the design of the 328 ft (100 m) tall segmental precast concrete tower. New load data has been presented that shows a variation between that used in Lewin and Sritharan (2010) and this report. A significant portion of this chapter is dedicated to describing the three towers developed using different combinations of high strength materials in the next phase of the tower proposed by Lewin and Sritharan (2010). The tower dimensions and properties are presented for each case, along with their own unique precast connection design. These connections are used to create a composite section between the precast components such that the entire tower will act as a single unit.

## 3.2 Loading Criteria

In order to provide a more comprehensive design for the 328 ft (100 m) tall UHPC Lattice Tower concept, additional load data needed to be obtained for the tower top loads. This includes a number of load combinations required by IEC 61400-1 as well as values associated with the operational and extreme limit states of the tower. Since the completion of the Lewin and Sritharan (2010) report, a partnership with Clipper Windpower, a U.S. based wind turbine manufacturer, was formed. Clipper was involved in the verification of the selected tower loads. These loads were targeted to satisfy Clipper's 2.5 MW Liberty turbine operating at 328 ft (100 m). They also provided input into the tower design with a focus on commercial applicability.

Clipper contributed to all of the necessary loads used to conduct a full evaluation of the tower for the study presented here. They included operation, extreme, and damage equivalent loads. Due to the proprietary nature of these loads, this report does not provide any loads obtained directly from Clipper. However, to provide some insight into the magnitude of the loads used for the tower design, loads obtained from the NREL report and used by Lewin and Sritharan (2010) were modified to suit a 2.5 MW turbine. Loads for the given EWM50 and

EOG50 wind models of GL (2010), were determined and approved by Clipper for their 2.5 MW turbine.

As mentioned previously, loads for 1.5, 3.6 and 5 MW turbines were provided in the NREL report used by Lewin and Sritharan (2010) (LaNier, 2005). In order to approximate loads for a 2.5 MW turbine, the best-fit line generated by Lewin and Sritharan (2010) was used. The results of both the static and damage equivalent loads can be seen in Table 3.1 and Table 3.2. The tower weight was estimated to be 420 kip (1870 kN). Refer to GL (2010) for a complete listing of all load cases used in this study.

**Table 3.1: Turbine Top Loads at Operational Estimated for a 2.5 MW Wind Turbine**

| | | | | | |
|---|---|---|---|---|---|
| **EWM50** | $V_{Tx}$ kip (kN) | $V_{Ty}$ kip (kN) | $M_{Tx}$ kip-ft (kN-m) | $M_{Ty}$ kip-ft (kN-m) | $M_z$ kip-ft (kN-m) |
| | 127.5 (567) | 169.1 (752) | 6218 (8430) | 3033 (4112) | 3315 (4495) |
| **EOG50** | $V_{Tx}$ kip (kN) | $V_{Ty}$ kip (kN) | $M_{Tx}$ kip-ft (kN-m) | $M_{Ty}$ kip-ft (kN-m) | $M_z$ kip-ft (kN-m) |
| | 209 (930) | 12.0 (54.7) | 1955 (2650) | 2882 (3908) | 451 (611) |

**Table 3.2: Estimated Damage Equivalent Loads at Tower Top for a 2.5 MW Turbine**

| | |
|---|---|
| $\Delta V_{Tx,fat}$, kip (kN) | 22.2 (98.7) |
| $\Delta M_{Ty,fat}$, ft-kip (kN-m) | 915 (4070.8) |

### 3.3 Tower Design Options

Through the evolution of the original UHPC Lattice Tower design, a number of different constraints were recognized that affected the total cost, construction, and dimensions of the tower. In order to address each constraint with the most economical solution, three separate tower designs, using the same basic concept, were developed. From one of these three designs, the operators and manufacturers would need to determine which option best suits each situation based on costs and site conditions. Each of the three towers uses a different combination of HSC and UHPC that changes both the member sizes and overall tower dimensions. The first of the three concepts uses HSC columns and UHPC panels and will be referred to as the HCUP tower from here onward, where "H" refers to HSC, "C" to columns, "U" to UHPC, and "P" to panels. A similar naming convention was used for the second tower that utilizes HSC Columns and HSC Panels, which will be referred to as the HCHP

tower. The last concept consists of UHPC Columns and UHPC Panels and will be referred to as the UCUP tower.

In addition to changes made to the type of material used in the tower, the bracing elements were also modified. Panel sections were used in place of diagonal cross-braces to allow the tower to be completely enclosed, adding additional protection to the internal components. Connections between the panels and columns were designed for each tower based on the required load demand. This section provides an overview of the design of each tower, including section geometry, tower capacity, and connection development.

### 3.3.1 HCUP Tower

This concept for the turbine tower was developed to reduce the overall cost. Although UHPC sections require significantly less material than HSC sections, the costs associated with UHPC often make it a less economical option when based solely on required material and unit cost. A drawback of this design is the increased weight of the tower. UHPC and HSC have very similar unit weights, which leads to increased tower weight when progressing towards larger sections. This has the potential to increase the foundation cost if poor soil conditions exist. If the foundation costs associated with the increased weight exceed those between the UHPC and HSC materials, one may elect to use one of the other concepts discussed later. The number of truckloads required to deliver the precast material on site was found to be approximately 60% higher when considering HSC columns. In a case where two or more columns could be transported simultaneously with UHPC columns, HSC sections would be limited to one based a twenty metric ton weight limitation.

The dimensions and some of the general properties of the 328 ft (100 m) tall HCUP tower are provided in Table 3.3. The column and tower diameters, as well as the number of post-tensioning strands required, were based on the moment capacity at the operational limit state, which governed the design of the tower. The capacity of the tower was considered satisfactory when none of the columns experienced complete decompression under operational loads. This is clearly illustrated in the section describing the procedure used to determine operational moment capacity. The clearance between the tower and tip of the blade was also limited by specifying a maximum circumscribed tower diameter of 165.3 ft (4.2 m)

at 170.6 ft (52 m) below the hub height. This was done to prevent the blade from striking the tower in the case of an extreme load event.

The fundamental natural frequency of the tower was found using the complete finite element model described in Chapter 5. In order to prevent resonance of the tower at the 1P and 3P excitations, it was required that the frequency falls between 0.30 Hz and 0.38 Hz. The 1P excitation represents the first excitation frequency of the rotor, while the 3P is used to describe the blade passing frequency of a turbine with three blades. This allowable frequency range is dependent on the type and size of the turbine used. Refer to Lewin and Sritharan (2010) for the working range of various turbine sizes. The fundamental frequency was also determined using Rayleigh's method to verify the results of the model. For the HCUP tower, the difference between the two methods was only 6.6%. Though not included in the report, the fundamental frequency calculation using Rayleigh's method is presented in Appendix A.

**Table 3.3: Dimensions and Properties for HCUP Tower**

| | |
|---|---|
| HSC Column Compressive Strength, ksi (MPa) | 13 (89.63) |
| UHPC Panel Compressive Strength, ksi (MPa) | 26 (179.3) |
| Vertical Post-Tensioning Effective Stress, ksi (MPa) | 180 (1241) |
| Outer Diameter, D, at Base, in. (m) | 228 (5.79) |
| Maximum Column Diameter, $d_{col}$, at base, in. (mm) | 36 (914) |
| Number of 0.6-in. Diameter Strands, 0-110 ft (0-33.5 m) | 402 |
| Outer Diameter, D, at 110 ft, in. (m) | 156 (3.96) |
| Maximum Column Diameter, $d_{col}$, at 110 ft, in. (mm) | 36 (914) |
| Number of 0.6-in. Diameter Strands, 110-220 ft (0-33.5 m) | 366 |
| Maximum Diameter 170.6 ft (52m) Below Hub Height, in. (m) | 164.2 (4.17) |
| Outer Diameter, D, at 220 ft, in. (m) | 132 (3.35) |
| Maximum Column Diameter, $d_{col}$, at 220 ft, in. (mm) | 29 (737) |
| Number of 0.6-in. Diameter Strands, 220-319.5 ft (0-33.5 m) | 198 |
| Outer Diameter, D, at 319.5 ft, in. (m) | 112.6 (2.86) |
| Maximum Column Diameter, $d_{col}$, at 319.5 ft, in. (mm) | 21 (533) |
| HSC Column Volume, $yd^3$ ($m^3$) | 304.6 (232.9) |
| UHPC Panel Volume, $yd^3$ ($m^3$) | 73.6 (56.3) |
| Tower Weight, kip (kN) | 1620 (7206) |
| Fundamental Tower Natural Frequency, Hz | 0.320 |
| Maximum Tower Top Drift at Extreme Limit State, % | 1.35 |

Each of the six columns of the tower each consists of five post-tensioning ducts. Figure 3.1 shows a typical column cross-section at the base of the tower. Two of the outside ducts contain 3, 0.6-in. (1.52 cm) strands that are to be terminated at 110 ft (33.5 m), while the other two containing 14, 0.6-in. (1.52 cm) strands will be terminated at 220 ft (67 m). The center duct containing 33 0.6-in. (1.52 cm) strands extends from the foundation to the top of the tower. The complete tower cross-section at the cut-off locations can be seen in Figure 3.2 through Figure 3.5. The ducts shown in these cross-sections represent the duct layout directly above the given elevation or, immediately after duct termination.

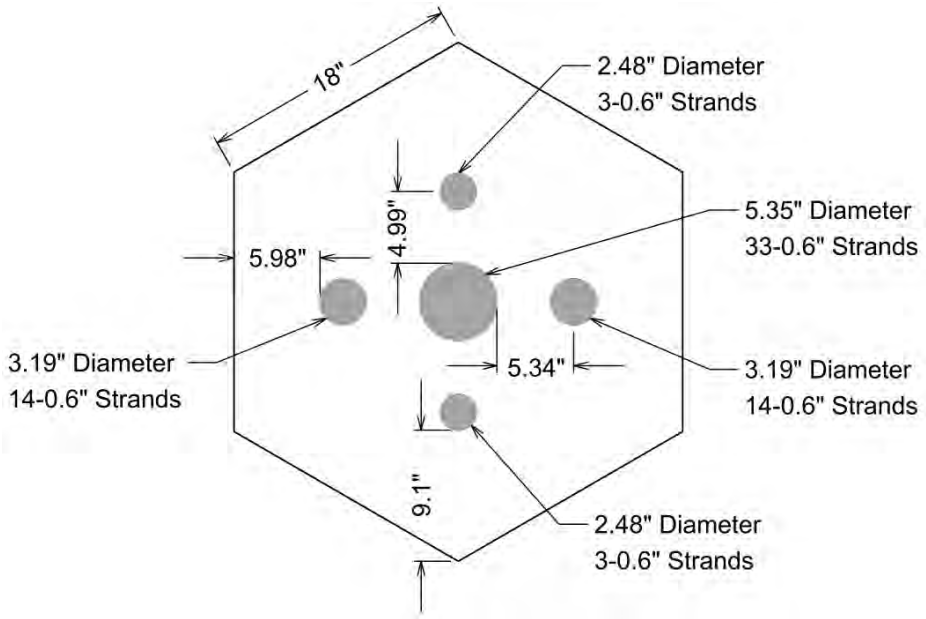


**Figure 3.1: HSC Column Cross-Section at the Base of the Tower**

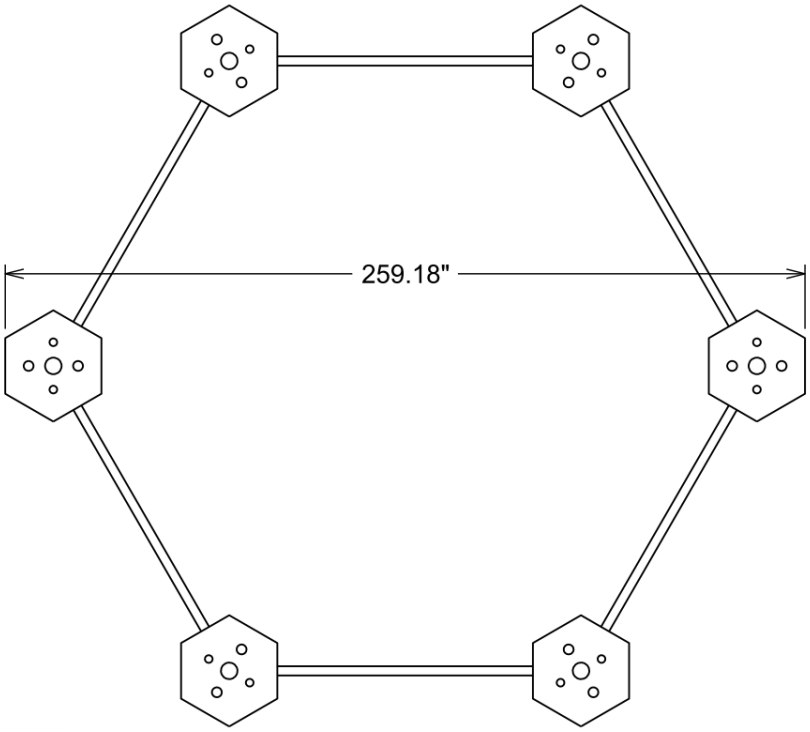


**Figure 3.2: HCUP Tower Cross-Section at the Base**

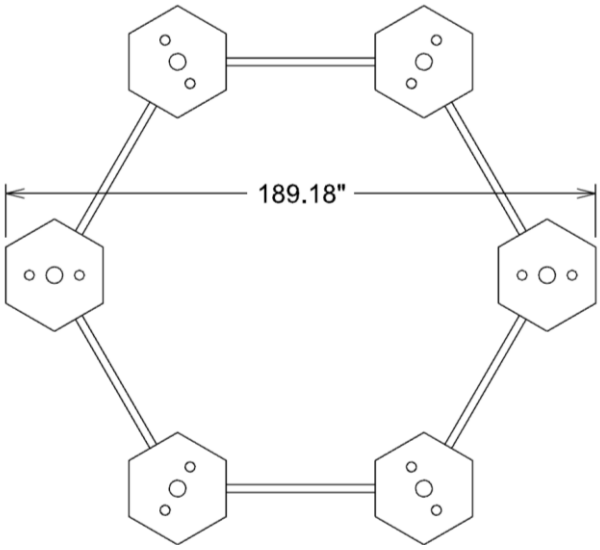


**Figure 3.3: HCUP Tower Cross-Section at 110 ft (33.5 m)**

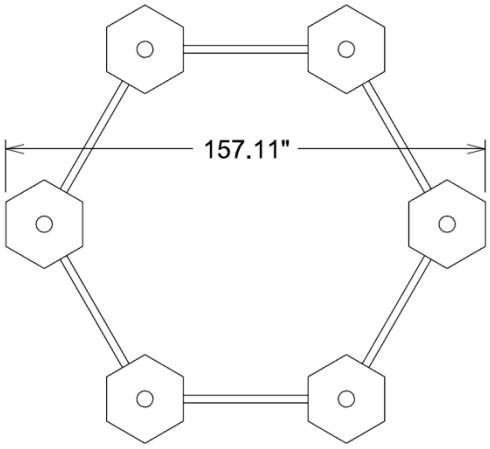


**Figure 3.4: HCUP Tower Cross-Section at 220 ft (67 m)**

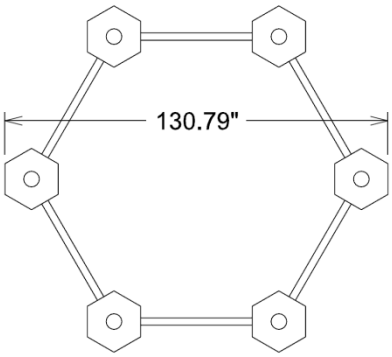


**Figure 3.5: HCUP Tower Cross-Section at 319.5 ft (97.4 m)**

Two potential construction sequences have been proposed for assembly of the tower on site. Both affect the individual components of the tower in different ways. The first "Cell Assembly" sequence, illustrated in Figure 3.6 consists of assembling sections or cells of the tower at a height dependent on the precast lengths. This would likely range from 25 ft (7.6 m) to 55 ft (16.8 m). During this stage, the columns and panels would be connected using one of the proposed connections discussed later in the chapter. Once connected, these segments would form the perimeter of the tower. After all segments of the tower are erected at ground level, each would be stacked accordingly with post-tensioning applied at the appropriate height to secure the tower to the foundation. Post-tensioning within the columns will take place as segments reach the cut-off elevations of 110 ft (33.5 m), 220 ft (67.0 m), and 320 ft (97.5 m). With the column/panel interface connections in place, the panels will be subjected to axial compression when the vertical post-tensioning is completed. This has a positive effect on the panels, as their capacity prior to cracking is increased, but negatively effects the

connections that must transfer the load between the columns and panels. This ultimately reduces their capacity to support loads on the tower.

The second "Column and Panel Assembly" sequence shown in Figure 3.6 consists of erecting each of the six columns independently to the elevation of one of the three post-tensioning cut-off elevations. After post-tensioning is completed, the panels are placed between the erected columns and fastened in place using one of the three proposed connections. With post-tensioning taking place prior to panel placement, the effects on the each component is different from the first construction sequence. The benefits of having compressed panel sections are lost; however, the capacity of the interface connections is improved with the removal of residual demand.

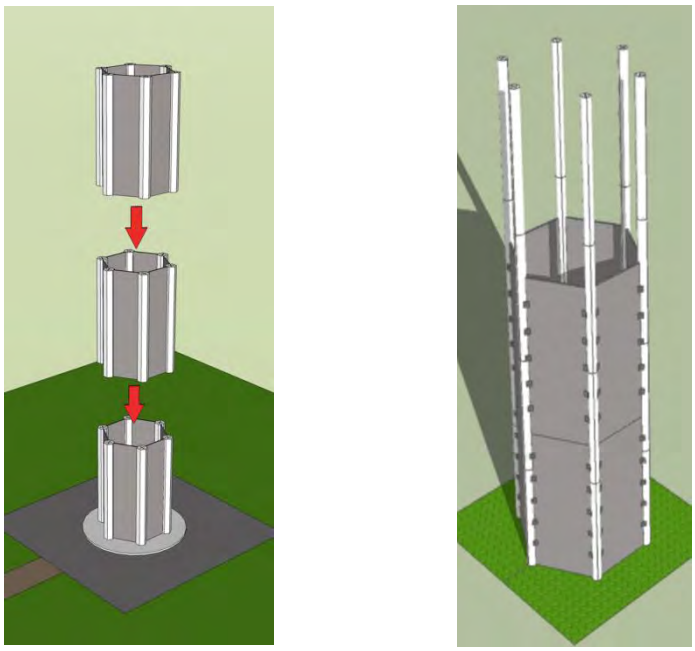

(a) Cell Assembly (b) Column and Panel Assembly

**Figure 3.6: Potential Construction Assembly Methods**

The following sections outline the design procedure used to verify the capacity of the tower at operational, extreme, and fatigue limit states. The equations used along with the resulting capacities are presented. Detailed design calculations are presented in Appendix A, B, and C.

*Operational Moment Capacity*

The operational moment capacity of the tower was determined under the assumption that the critical section of the tower should experience linear stress distribution about its centroid when subject to the maximum flexural demand. Equation (3-1) was used to determine the allowable moment resistance of the tower. The equation limits the moment capacity to that which causes decompression in any of the six columns at any loading orientation. In addition to the zero-tension limitation on the decompression side of the tower, Equation (3-2) limits the extreme compression fiber to a stress 53% of f'$_c$ as recommended in ACI 318 (2008). This value represents the average between the two extreme fiber compression limitations for prestressed members set by ACI 318 (2008). The first limitation is established for members subject to sustained loads, while the other includes the effects of transient loads. An average value was chosen conservatively because the loads imposed on the turbine are dynamically amplified and presented as equivalent static loads.

$$M_a = \left(\frac{F+P}{A_{trans}}\right)\left(\frac{I_{trans}}{c_{tension}}\right) \quad \textbf{(3-1)}$$

$$\left(\frac{F+P}{A_{trans}}\right) + \left(\frac{M_r c_{compression}}{I_{trans}}\right) \leq 0.53 f_c' \quad \textbf{(3-2)}$$

where $F$= prestressing force on the section;

$P$= operational axial load;

$A_{trans}$= transformed section area;

$I_{trans}$= transformed section moment of inertia;

$c_{tension} = c_{compression}$= distance from the neutral axis to the extreme compression or tension fiber; and

$f_c'$= 28-day concrete compressive strength.

The additional moment of inertia provided by the panels was not included when determining the operational moment capacity of the tower. This was done because of the discontinuity in the panels along the height of the tower. The discontinuity is a result of precast panel segments, limited to 55 ft (16.8 m) in length, being left unattached once fully

erected. At these particular cross-sections, the six columns will provide all of the moment capacity. For those sections that include the panels, the operational moment capacity is conservative.

With the geometry of the tower being hexagonal, the section modulus varies based on the axis about which the bending moment is applied. The most critical loading condition is that which causes bending about the 30˚ axis. The orientation of the tower bending axis, $\theta_B$, at any elevation can be determined using Equation (3-3**)**. This value varies as the shear forces acting on the top of the tower increase their respective moments at lower elevations. The load profiles correspond to a circular steel tower section which has the same moment capacity regardless of the axis about which they were applied.

$$\theta_B = \tan^{-1}\left(\frac{M_x}{M_y}\right) \quad \textbf{(3-3)}$$

where $M_x$ = moment about the x-axis, caused by across-wind loading; and

$M_y$ = moment about the y-axis, caused by along-wind loading.

In order to verify the operational moment capacity in the HCUP tower, the load orientation was considered at both zero and thirty degrees. This accounted for both critical loading orientations. Figure 3.7 shows the operational moment capacity of the tower along the height. The abrupt changes in moment capacity are a result of the termination of vertical post-tensioning at these locations. The extreme fiber compressive stress corresponding to the operational moment capacity is shown in Figure 3.8. For the 13.0 ksi (89.6 MPa) HSC columns used, the limiting compressive stress at operational was 6.89 ksi (47.5 MPa). The abrupt changes in compression are also the result of the termination of vertical post-tensioning.

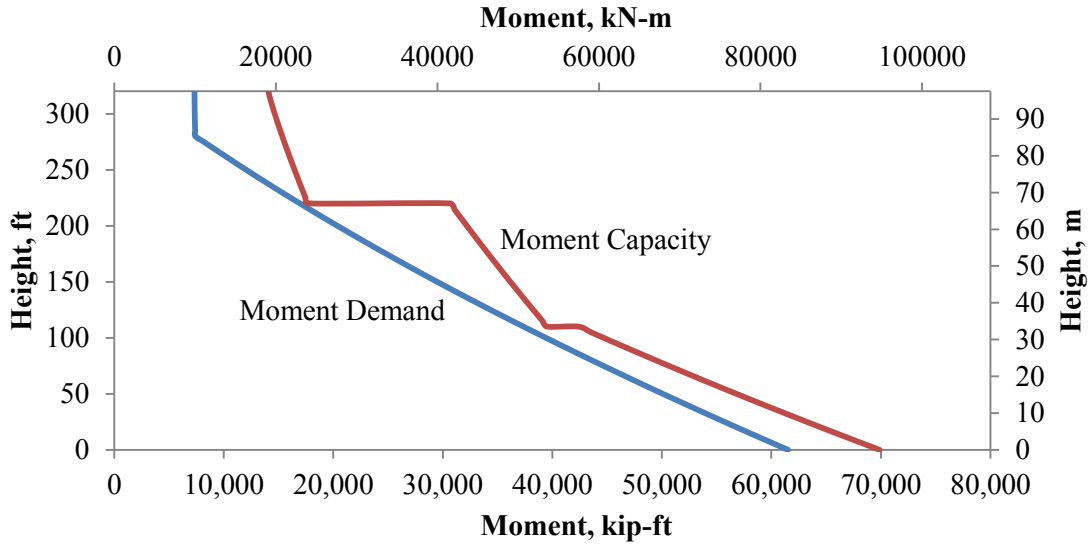


**Figure 3.7: Operational Moment Capacity vs. Demand of HSC Column, HCUP-BC**

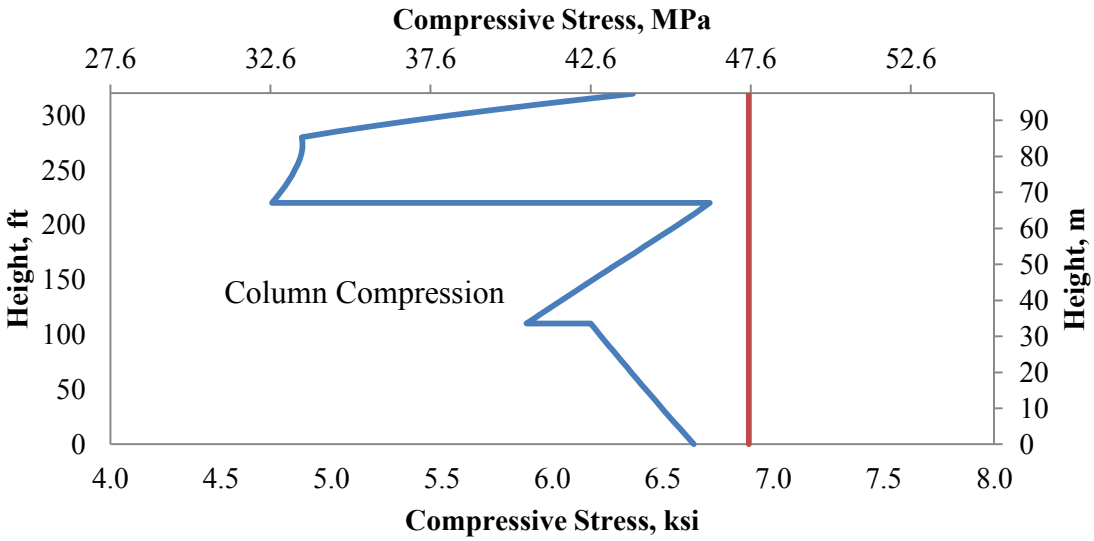


**Figure 3.8: HCUP-BC Extreme Compression Fiber Stress at Operational**

*Ultimate Moment Capacity*

The ultimate moment capacity of the tower was determined using bonded vertical post-tensioning tendons in the columns. This allowed for the use of strain compatibility between the concrete columns and tendons. Unlike steel reinforcement, the stress-strain curve of a post-tensioning strand does not possess a yield plateau in which stress remains constant over

a period of increasing strains. For this reason, an iterative process was developed to achieve force equilibrium in the tower. The ultimate capacity of the tower was determined for both zero and thirty-degree loading conditions. For the zero-degree loading condition, the columns were separated into three distinct groups that were used for the purposes of calculating the ultimate moment capacity. Figure 3.9 illustrates the position of each group with respect to the direction of loading on the tower.

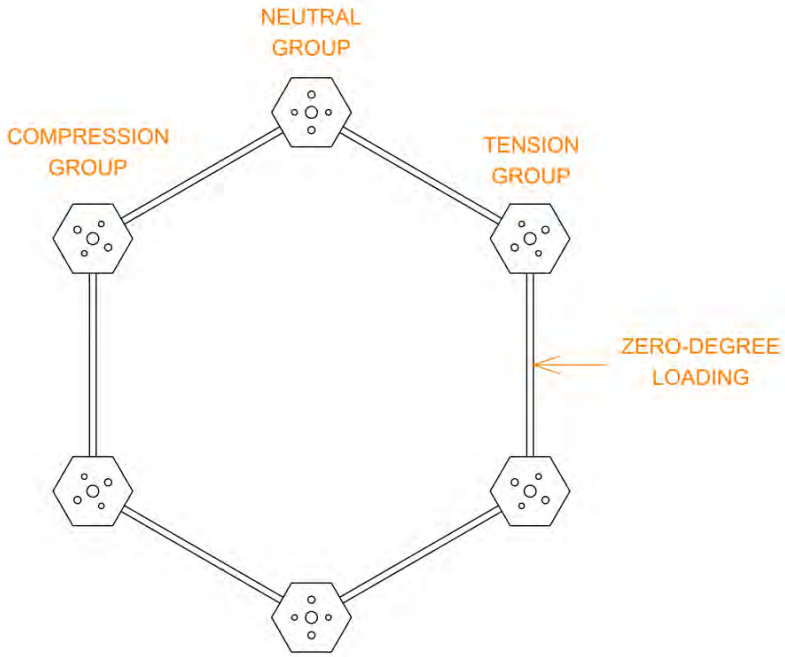


**Figure 3.9: Ultimate Moment Capacity Column Groups and Loading Direction**

The following steps outline the procedure used to determine the ultimate moment capacity of the tower at various elevations. The procedure was used for the zero-degree loading condition. A slightly modified approach, which accounted for a change in geometry, was used for the thirty-degree loading condition. Refer to the appendix for detailed calculations.

1. Determine the initial strain in the tendons after jacking

$$\varepsilon_{pe} = \frac{f_{pe}}{E_{steel}} \quad \textbf{(3-4)}$$

where $f_{pe}$= effective post-tensioning stress; and

$E_{steel}$= elastic modulus of steel.

2. Calculate the strain required to decompress the columns

$$\varepsilon_d = \frac{\sigma_{column}}{E_{HSC}} \quad \textbf{(3-5)}$$

where $\sigma_{column}$= compressive stress in column as a result of prestress; and

$E_{HSC}$= elastic modulus of high-strength concrete.

3. Solve for the initial depth of the equivalent rectangular stress block, a, assuming each tendon experiences 90 percent of the ultimate tendon stress.

$$0.85 * f_{HSC} * EQ_A + 0.85 * f_{UHPC} * EQ_B = N * 0.9 * f_{pu} * A_s \quad \textbf{(3-6)}$$

where $f_{HSC}$= 28-day compressive stress of high-strength concrete (ksi);

$EQ_A$ = equation describing the relationship between column area with respect to the depth of the tower section;

$f_{UHPC}$ = 28-day compressive stress of UHPC (ksi);

$EQ_B$ = equation describing the relationship between panel area with respect to the depth of the tower section;

$N$ = total number of strands in the tower;

$f_{pu}$ = ultimate stress of the post-tensioning strand (ksi); and

$A_s$ = Area of post-tensioning strand (in$^2$).

Equations $EQ_A$ and $EQ_B$ both contain the equivalent rectangular stress block depth, a. These equations are derived from plots in which the total column or panel area is defined at various depths along the section.

4. Calculate the neutral-axis depth of the section

$$c = \frac{a}{\beta_1} \quad \textbf{(3-7)}$$

where $a$= depth of the equivalent rectangular stress block (in); and

$\beta_1$= factor relating depth of equivalent rectangular stress block to neutral axis depth. Equal to 0.65 for f'$_c$ > 8 ksi.

5. Determine the strain in the neutral and tension tendon groups using a linear strain distribution. This can be derived knowing the neutral axis depth, and ultimate compressive strain of the concrete.

$$\varepsilon_M = \varepsilon_{cu} - \frac{\varepsilon_{cu}}{c} * \frac{\left(\frac{D_s}{2} * \sqrt{3} + D_c\right)}{2} \quad \textbf{(3-8)}$$

$$\varepsilon_T = \varepsilon_{cu} - \frac{\varepsilon_{cu}}{c} * \left(\frac{D_s}{2} * \sqrt{3} + \frac{D_c}{2}\right) \quad \textbf{(3-9)}$$

where $\varepsilon_M$= strain in neutral column group for zero-degree loading orientation;

$\varepsilon_T$= strain in tension column group for zero-degree loading orientation;

$\varepsilon_{cu}$= ultimate compressive strain in the concrete = 0.003 in/in;

$D_s$= diameter of the tower section from center to center of columns; and

$D_c$= outside diameter of a column (in.).

6. Calculate the total strain in each tendon using the results of steps 1, 2, and 5.

$$\varepsilon_{psT} = \varepsilon_{pe} + \varepsilon_d + \varepsilon_T \quad \textbf{(3-10)}$$

$$\varepsilon_{psM} = \varepsilon_{pe} + \varepsilon_d + \varepsilon_M \quad \textbf{(3-11)}$$

$$\varepsilon_{psC} = \varepsilon_{pe} - \varepsilon_{cu} \quad \textbf{(3-12)}$$

where $\varepsilon_{psT}$= total strain in tension column group tendons;

$\varepsilon_{psM}$= total strain in neutral column group tendons; and

$\varepsilon_{psC}$= total strain in compression column group tendons.

7. Using the two equations describing the stress-strain behavior of the post-tensioning strands from the PCI (2004), determine the stress in each tendon. Equation (3-13) gives an example of how to calculate the stress for the neutral column group. The same procedure is used for the tension and compression groups.

$$f_{psM} = \begin{cases} 28500\ ksi * \varepsilon_{psM}\ if\ \varepsilon_{psM} \leq 0.0086 \\ 270\ ksi - \dfrac{0.04\ ksi}{\varepsilon_{psM} - 0.007}\ if\ \varepsilon_{psM} > 0.0086 \end{cases} \quad \textbf{(3-13)}$$

8. Using the results of Equation (3-13), replace the original value of $0.9*f_{pu}$ that was estimated for all strand stresses with the three different stress values. Steps three through seven, which are used to derive the stress in each tendon group, were repeated until the results of step seven are sufficiently close to the stress values used in step three. It is important to note that the tendon stress in the compressive column group should not change through the iteration process because the column concrete strain in this group will control the capacity at 0.003 in/in.

9. Determine the distance between the centroid of the area within the compressive stress block and the tension and neutral tendon groups.

$$jd_T = \frac{D_s}{2} * \sqrt{3} + \frac{D_c}{2} - \bar{y} \quad \textbf{(3-14)}$$

$$jd_M = \frac{\frac{D_s}{2} * \sqrt{3}}{2} + \frac{D_c}{2} - \bar{y} \quad \textbf{(3-15)}$$

where $\bar{y}$ = centroid of the area within the equivalent rectangular stress block

10. Calculate the initial ultimate moment capacity of the section

$$M_{ni} = \left(2 * N_c * A_s * f_{psT}\right) * jd_T + \left(2 * N_c * A_s * f_{psM}\right) * jd_M \quad \textbf{(3-16)}$$

where $N_c$= number of strands in a single column

In order to account for the P-Delta effects experienced by the tower, the additional moment created by the P-Delta effects was subtracted from the ultimate moment capacity of the tower determined in step 10. Equation (3-17) was used to determine the additional moment created by P-delta effects at the base of the tower.

$$M_{p-\Delta} = P_u \Delta_{top} + \int_0^h \Delta(z)\, W(z) dz \quad \textbf{(3-17)}$$

where $P_u$ = total factored-level dead load created by the head mass;

$\Delta_{top}$ = total lateral displacement at the tower top;

$\Delta(z)$ = total lateral displacement at locations of distributed tower weight;

$W(z)$ = distributed tower weight; and

$h$ = tower height.

The variable $\Delta(z)$ is used to describe the lateral displacement of the tower along the height. It was determined using Equation (3-18).

$$\Delta(z) = \begin{cases} \int_0^{z_1} \frac{M(z)(z_1 - z)}{E_{HSC} I_{column}(z) + E_{UHPC} I_{panel}(Z)} dz & if\ h_1 < z \leq h_2 \\ \int_0^{z_1} \frac{M(z)(z_1 - z)}{E_{HSC} I_{column}(z) + E_{UHPC} I_{panel}(Z)} dz & if\ h_2 < z \leq h \\ \int_0^{z_1} \frac{M(z)(z_1 - z)}{E_{HSC} I_{column}(z) + E_{UHPC} I_{panel}(Z)} dz & if\ h_2 < z \leq h \end{cases} \quad \textbf{(3-18)}$$

where $M(z)$ = ultimate moment capacity from step 10 at elevation z;

$z_1$ = height along the tower at which deflection is calculated;

$I_{column}(z)$ = second moment of area of columns at elevation z; and

$I_{panel}(z)$ = second moment of area of panels at elevation z.

The final moment capacity of the tower, which includes a strength reduction factor, ϕ, as per ACI 318 (2008), is determined using Equation (3-19).

$$\phi M_n = M_{ni} - M_{p-\Delta} \quad \textbf{(3-19)}$$

where ϕ = 0.9

The most critical sections of the tower with respect to column stresses occur at post-tensioning cut-off locations. For this reason, the ultimate moment capacity was determined using the above steps at these locations as well as at the base of the tower. At the 110 ft (33.5 m) and 220 ft (67.0 m) elevations, moment capacity was determined directly above and below the post-tensioning cut-off sections to capture the change in capacity due to strand termination. Figure 3.10 illustrates the comparison between the ultimate moment capacity of the section and the extreme moment demand. As previously mentioned, the ultimate capacity of the tower section was limited by 0.003 in/in concrete strain in the extreme compression fiber as specified by ACI 318 (2008). The maximum tendon strain in the tower at the ultimate limit state can be found at the base of the tower at a value of 0.02092 in/in. According to PCI (2004), this is well below the approximate rupture strain that occurs between 0.05 and 0.07 in/in.

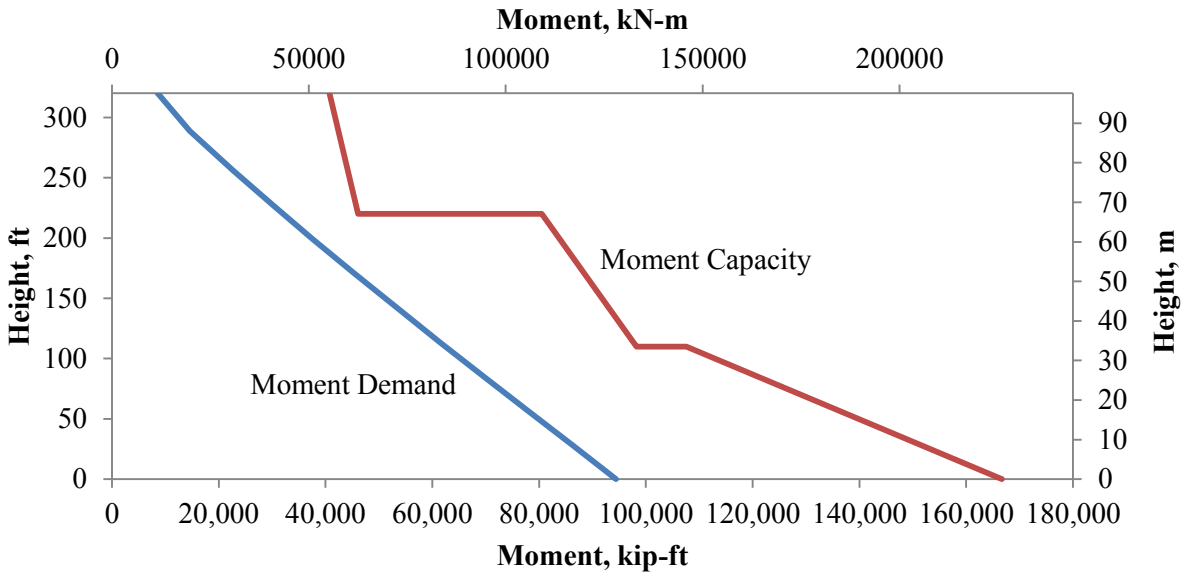


**Figure 3.10: Ultimate Moment Capacity of the HCUP Tower**

*Shear Capacity*

The shear demand on the tower and its influence was determined by calculating the maximum principal stresses. Equation (3-20) was used to determine this stress and compare it with the tensile strength of the concrete to examine the potential for cracking. The tensile resistance was limited by one-half its capacity to ensure cracking would not develop.

$$\sqrt{\left(\frac{f_{pc}}{2}\right)^2 + (\tau)^2} - \frac{f_{pc}}{2} \leq 0.5 f_{ct} \qquad \textbf{(3-20)}$$

where $f_{pc}$ = axial stress at the centroid due to prestressing;

$f_{ct}$ = tensile capacity of concrete as per Eq. (3-21); and

$\tau$ = total shear stress, Eq. (3-22).

The tensile strength of the concrete was found using an equation from CEB-FIP (1990). This equation was chosen over those provided in ACI 318 (2008) because it has no specified maximum strength limitation. Equation (3-21) expresses this equation in terms of ksi. The tensile capacity of the 13.0 ksi (89.6 MPa) concrete used in the columns was found to be 876 psi (6.04 MPa).

$$f_{ct} = f_{ctko,m}\left(\frac{f_{ck}}{f_{cko}}\right)^{2/3} \quad \textbf{(3-21)}$$

where $f_{ctko,m}$ = 0.203 ksi;

$f_{ck}$ = compressive strength of concrete; and

$f_{cko}$ = 1.450 ksi.

The maximum shear demand on the tower at the operational and extreme limit states results from a combination of horizontal and torsional loads. On one side of the tower, both loads are additive, while on the other side, the loads are contradicting one another. For the purpose of determining the maximum shear demand, the side of the tower experiencing additive forces was considered. The resulting shear stress is determined from Equation (3-22). Unlike the operational moment capacity of the tower, the panels were considered as part of the tower cross-section when determining the shear demand. Cracks caused by flexure typically form horizontally in the direction perpendicular to the axis of the tower, whereas shear cracks often develop diagonally over a given height. For this reason, the discretization of the panels will not adversely affect the shear capacity of the tower, and therefor can be included when determining capacity.

$$\tau = \tau_{torque} + \tau_{shear} \quad \textbf{(3-22)}$$

$$\tau_{torque} = \frac{T_{op}}{J} r \quad \textbf{(3-23)}$$

$$\tau_{shear} = \frac{V_{op} Q}{It} \quad \textbf{(3-24)}$$

where $\tau_{torque}$ = torsional shear stress (ksi);

$\tau_{shear}$ = shear stress caused by horizontal load components (ksi);

$T_{op}$ = maximum torque at operational (in.*kip);

$J$ = polar moment of inertia (in$^4$);

$r$ = centerline radius of the tower (in.);

$V_{op}$ = shear force from torsional load combination at operational (kip);

$Q$ = first moment of inertia (in$^3$);

$I$ = second moment of inertia (in$^4$); and

$t$ = thickness of section (in.).

The tower experiences the largest principal tensile stress near the top. At this location, the torque, which remains relatively constant along the height, generates larger shear stresses. The increase in torsional shear stress is caused by the reduction in tower diameter. At the base of the tower the maximum principal tensile stress was found to be 17 psi (117KPa) at operational and 31 psi (214 KPa) at the extreme. At the top of the tower, the maximum principal tensile stress reaches 98 psi (680 KPa) and 155 psi (1070 KPa) at operational and extreme. These values fall well below the limiting tensile stress of 438 psi (3.02 MPa).

*Fatigue*

In order to determine the fatigue life of the tower, the concrete and prestressing steel were each analyzed separately. As per (GL, 2010), the CEB-FIP Model Code was used to determine fatigue life. Due to the high number of cycles, which exceed $1x10^8$, verification by means of damage equivalent loads was used. The equation used to determine the fatigue life of the prestressing steel was:

$$\gamma_{Sd} max\Delta\sigma_{Ss} \leq \Delta\sigma_{Rsk}(n)/\gamma_{s,fat} \quad \textbf{(3-25)}$$

where $max\Delta\sigma_{Ss}$ = maximum fatigue stress range for steel;

$n$ = predicted number of fatigue cycles over the lifetime;

$\Delta\sigma_{Rsk}(n)$ = stress range relevant to $n$ cycles obtained from a characteristic fatigue function;

$\gamma_{Sd} = 1.1$, and is a fatigue load factor; and

$\gamma_{s,fat} = 1.15$, and is a fatigue material safety factor for steel.

The maximum fatigue stress range was determined for a 2.5 MW turbine. As mentioned, damage equivalent loads were used by first by utilizing the rainflow-counting algorithm. This process is used to reduce a spectrum of varying stress amplitudes into a simple set of stress reversals. By doing this, an equivalent static load, $R_{eq}$, can be found and applied to the structure to determine the magnitude of the stress reversals in each structural component. Equation (3-26) is used to determine the equivalent static load using Miner's rule. The slope of the S-N curve varied depending upon the type of material being used. For the concrete tower being analyzed, a slope of m=5 was used to determine the equivalent static load, $R_{eq}$. In collaboration with Clipper, the equivalent static loads at various heights and in all six

degrees-of-freedom were determined. Using this information, the extreme fiber stresses were determined for both spectrums of the load reversal. The difference between these two stresses represented the fatigue stress range.

$$R_{eq} = \left[\frac{\sum(n_i * {R_i}^m)}{N}\right]^{\left(\frac{1}{m}\right)} \quad \textbf{(3-26)}$$

where $n_i$= number of cycles occurring at a particular stress range, $R_i$

$R_i$= stress range (a larger number of stress ranges, i, provides more accurate results);

$m$= slope of S-N curve; and

$N$= total number of cycles over 20 year service life = 9.46 x $10^8$.

The allowable number of fatigue cycles at a given stress range can be determined using the appropriate S-N curve as illustrated in Figure 3.11. The parameters used for the prestressing steel are presented in Table 3.4.

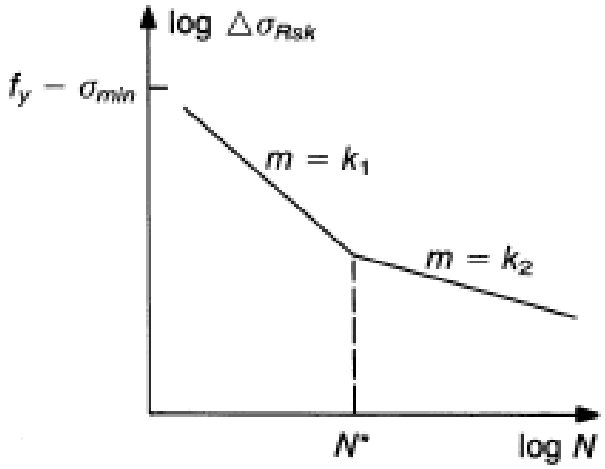


**Figure 3.11: An Example S-N Curve (CEB-FIP, 2010)**

**Table 3.4: Parameters of S-N Curves for Prestressing Steel (CEB-FIP, 2010)**

| | N* | Stress Exponent | | $\Delta\sigma_{Rsk}$ (MPa) | | $\Delta\sigma_{Rsk}$ (ksi) | |
|---|---|---|---|---|---|---|---|
| | | $k_1$ | $k_2$ | At N* cycles | At $10^8$ cycles | At N* cycles | At $10^8$ cycles |
| ***Pretensioning*** | | | | | | | |
| Straight Steels | $10^6$ | 5 | 9 | 160 | 95 | 23.21 | 13.78 |
| ***Post-tensioning*** | | | | | | | |
| Curved Tendons | $10^6$ | 3 | 7 | 120 | 65 | 17.40 | 9.43 |
| Straight Tendons | $10^6$ | 5 | 9 | 160 | 95 | 23.21 | 13.78 |
| Mechanical Connectors | $10^6$ | 3 | 5 | 80 | 30 | 11.60 | 4.35 |

In order to determine, $\Delta\sigma_{Rsk}(n)$, the second portion of the S-N curve was used because the number of fatigue cycles experienced by the tower exceeded $10^6$. The following two equations are used to derive this value based on the log-log S-N curve and parameters from the above tables.

$$\log[\Delta\sigma(n)_{Rsk}] = \log[\Delta\sigma(\mathrm{N}^*)_{\mathrm{Rsk}}] - \frac{1}{k_2}\log\left(\frac{n}{\mathrm{N}^*}\right) \quad \textbf{(3-27)}$$

$$\Delta\sigma_{Rsk}(n) = 10^{\log[\Delta\sigma(n)_{Rsk}]} \quad \textbf{(3-28)}$$

A value of $\Delta\sigma(N^*)_{Rsk}$= 23.21 ksi (160.0 MPa) was used for the prestressing steel. After considering the fatigue material safety factor, the allowable stress range was 7.23 ksi (49.85 MPa). This far exceeds the expected maximum stress range of 1.86 ksi (89.6 MPa), which occurs at the base of the tower.

The fatigue life of the concrete was determined by considering only the compression fatigue condition of the tower. Because the tower is heavily prestressed and was designed not to decompress in any of the columns at operational loads, it was not necessary to determine the fatigue life of concrete in tension. Different equations are used for a tension analysis and can be found in (CEB-FIP, 2010). In order for concrete in compression to meet the required fatigue life;

$$n \leq N \quad \textbf{(3-29)}$$

where $n$ = required number of cycles (lifetime) = 9.46 x $10^8$; and

$N$ = allowable number of load cycles.

The maximum and minimum stress values, $S_{cd,min}$and $S_{cd,max}$, needed to be determined in order to obtain the allowable number of load cycles. Equations (3-30) to (3-38) were used to determine these values as well as the allowable number of cycles.

$$logN_1 = \left(12 + 16S_{cd,min} + 8S_{cd,min}^2\right)\left(1 - S_{cd,max}\right) \quad \textbf{(3-30)}$$

$$logN_2 = 0.2logN_1(logN_1 - 1) \quad \textbf{(3-31)}$$

$$logN_3 = logN_2(0.3 - \frac{3}{8}S_{Sd,min})/\Delta S_{cd} \quad \textbf{(3-32)}$$

If $logN_1 \leq 6$, then $logN = logN_1$ **(3-33)**

If $logN_1 > 6$ and $\Delta S_{cd} \geq 0.3 - \frac{3}{8}S_{Sd,min}$, then $logN = logN_2$ **(3-34)**

If $logN_1 > 6$ and $\Delta S_{cd} < 0.3 - \frac{3}{8}S_{Sd,min}$, then $logN = logN_3$ **(3-35)**

Where

$$S_{cd,max} = \gamma_{Sd}\sigma_{c,max}\eta_c/f_{cd,fat} \quad \textbf{(3-36)}$$

$$S_{cd,min} = \gamma_{Sd}\sigma_{c,min}\eta_c/f_{cd,fat} \quad \textbf{(3-37)}$$

$$\Delta S_{cd} = S_{cd,max} - S_{cd,min} \quad \textbf{(3-38)}$$

$\sigma_{c,max}$ = maximum compressive stress; and

$\sigma_{c,min}$ = minimum compressive stress.

According to (CEB-FIP, 2010) the value of $S_{cd,min}$ exceeds 0.8, it is valid to use 0.8 in the above equations. The factor $\eta_c$, is used to determine the stress variation in a cracked section due to an applied moment. For the purposes of this analysis, it was found that the moment applied to the columns was minimal. Therefore, the factor was given a value of one, which represents a uniform stress distribution throughout the column section. A reference fatigue strength, $f_{cd,fat}$, is used to represent the maximum allowable stress level at one cycle. As the strength of the concrete increases, the reference fatigue strength increases at a progressively slower rate to account for increased fatigue sensitivity in higher strength concretes.

$$f_{cd,fat} = 0.85\beta_{cc}(t)\left[f_{ck}\left(1 - \frac{f_{ck}}{25f_{ck0}}\right)\right]/\gamma_c \quad \textbf{(3-39)}$$

where $\gamma_c = \gamma_{c.fat} = 1.5$;

$f_{ck0}$ =1.450 ksi (10 MPa); and

$f_{ck}$= approximate 28-day concrete strength, ksi (MPa).

$\beta_{cc}(t)$ is a variable used to represent the age of the concrete at first loading. For this analysis 28 days was used.

$$\beta_{cc}(t) = e^{s\left[1-\left(\frac{28}{t}\right)^{1/2}\right]} \quad \textbf{(3-40)}$$

where $s = 0.2$ for rapidly aging concretes; and

$t$ = age of concrete (days).

Using Equation (3-39), the reference fatigue strength for the 13.0 ksi (89.6 MPa) columns was found to be 5.03 ksi (34.6 MPa). Using this value, the concrete does not meet the required twenty year fatigue life. The results were unexpected given the history and superior performance of concrete in high-fatigue applications. The reason for the relatively short tower fatigue life was the sustained axial stress within the columns. The sustained load from the post-tensioning and turbine generate column stresses anywhere between 2.5 and 4.6 ksi (17.2 and 31.7 MPa), depending on the elevation. This leaves very little room for additional stresses generated by load reversals. The CEB-FIP Model code is specifically designed for concrete strengths ranging from 2 to 11.5 ksi (13.8 to 79.2 MPa). Although a maximum concrete strength to be used in the equations is not provided by the code, it is appropriate to assume that at higher strengths, a significant amount of error may exist. Very little research has been completed dealing with high-cycle fatigue of high strength concrete. Additionally the effects of the high sustained compressive stresses experienced by the tower may alter the reference fatigue strength set by (CEB-FIP, 1990). Given the need for further testing in this area, it was determined that the fatigue life would not be used as a governing limit state. In order for the concrete to achieve a 20 year service life using the equations of (CEB-FIP, 1990), the fatigue reference strength would need to increase by 1.94 ksi (13.4 MPa) or 38.5%. This is believed to be within the margin of error of the code equations when using a 13.0 ksi (89.6 MPa) concrete.

*Bolted Connection Design*

The connection developed for a HCUP tower was a bolted connection. A bolted connection was designed for two primary purposes. The first was to reduce on-site construction time, thereby potentially reducing the overall tower costs. The second was to provide a connection with a fatigue life equal to or greater than the 20 year service life of the tower. The required capacity of the connection was determined based on results from the finite element analysis of the complete tower model. The connection not only needed to provide adequate strength, but also adequate ductility during an extreme load event. The proposed connection can be seen in Figure 3.12.

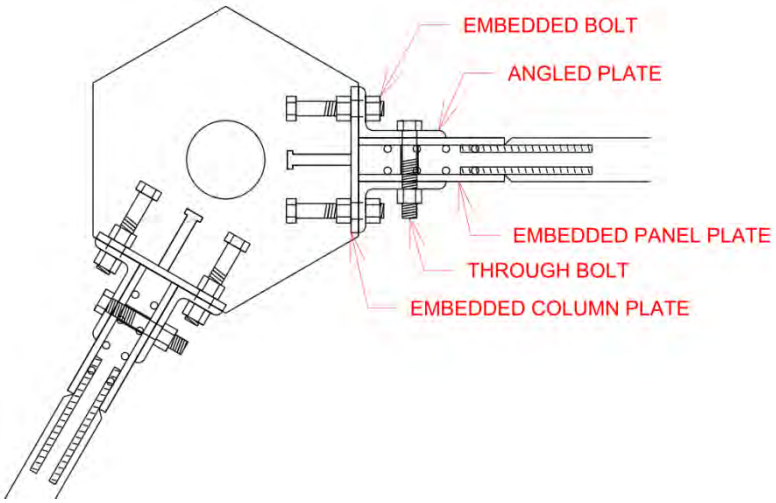


**Figure 3.12: Bolted Connection Detail Used for HCUP Tower**

The connection at each location consists of three primary components; an embedded column plate, a pair of embedded panel plates, and angled connection plates. The embedded column plate relies on welded shear studs and embedded bolts to provide the needed capacity. Because of the small thicknesses of the panels, the embedded panel plate used welded reinforcement to distribute the loads more evenly into the panel. Both of the embedded plates are designed to remain elastic during the plasticization of the angled plate. The angled plate was designed to undergo significant inelastic behavior in the case of an extreme loading event, protecting the embedded plate components of the connection. This would not only reduce the total energy absorption, but also simplify the inspection and replacement process keeping maintenance costs low.

The tolerances associated with bolted connections in steel structures are often very small. For precast concrete structures, bolted connections with standard hole sizes may potentially lead to construction challenges, as the tolerances required of precasters is often greater than the tolerance of the bolt holes. For this reason, oversized holes were created in the embedded panel plates. The connection between the embedded panel plates and angled plates was design as a slip-critical connection. AISC specifies the use of slip-critical connections with oversized holes. For this type of connection it is necessary to use high strength bolts to allow for pretensioning. A325 bolts were used in both the bearing connection between the angled plate and column as well as the slip-critical connection between the panel and angled plate. A bearing connection refers to an interface in which the connected components rely on the bolt area to provide shear resistance rather than friction generated by pretensioned bolts.

The load capacities of the A325 bolts protruding from the columns were designed using Equation (3-41), which is used for bearing type connections. Equation (3-42) was used for the slip-critical connection between the panel and angled plate. Not all equations used to verify the capacity of the connection are shown. These equations can be found in AISC (2005).

$$\phi R_n = \phi F_n A_b \tag{3-41}$$

where $R_n$ = design tension or shear strength;

$\phi$ = 0.75;

$F_n$ = nominal tensile or shear stress as specified in Table J3.2 of AISC; and

$A_b$ = nominal unthreaded body area of bolt.

$$\phi R_n = \phi \mu D_u h_{sc} T_b N_s \tag{3-42}$$

Where $\phi$ = 1.0 for serviceability limit state;

$\mu$ = mean slip coefficient;

$D_u$ = 1.13;

$h_{sc}$ = hole factor equal to 0.85 for oversized holes;

$T_b$ = minimum fastener tension; and

$N_s$ = number of slip planes.

Using the finite element analysis program, ANSYS, the capacity of the angled plate was determined for the condition of pure shear at the column/panel interface. Using nonlinear elements, a force-displacement curve was generated for the angled plate. Figure 3.13 shows the details of the plate as well as the three-dimensional non-linear model used in the analysis. A process of trial and error was used to determine size of plate needed to achieve the desired strength and ductility. The first step was to estimate a plate size and derive its force-displacement response. This was then applied to the connections used in the complete tower model generated in SAP2000. A nonlinear analysis was run in SAP2000 using the most detrimental load combinations for both the operational and extreme limit states. The most critical connection on the tower was then located and its resultant force determined. For the operational limit state, it was considered undesirable to have any of the angled plates on the tower exhibit nonlinear behavior. For the extreme limit state, a small degree of nonlinear behavior was acceptable. The final size and yield strength of the plate was determined by adjusting these properties in the ANSYS model and applying them back to the tower model in SAP2000.

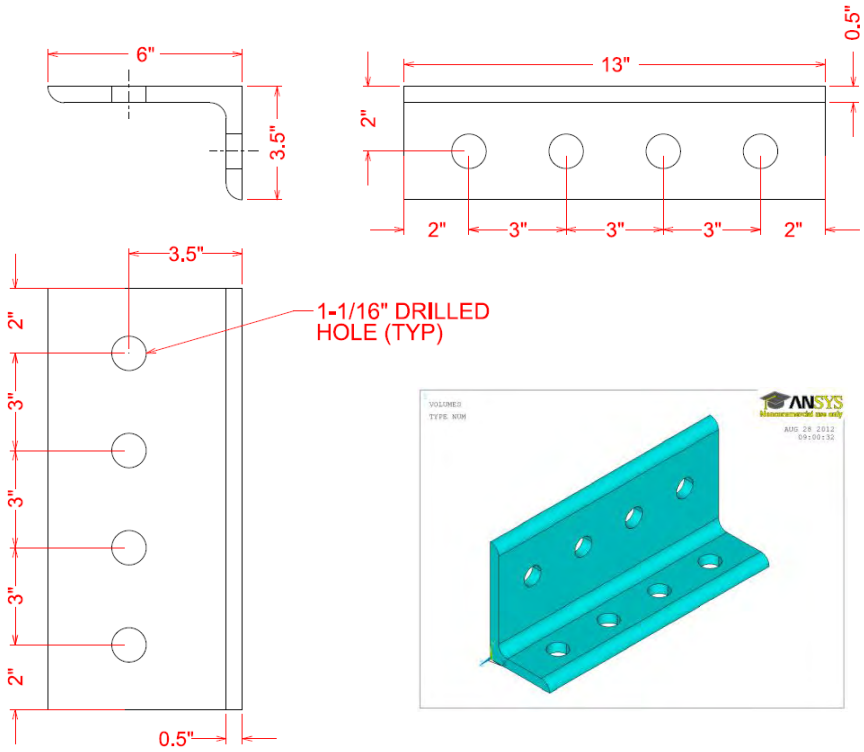


**Figure 3.13: Bolted Connection Angled Plate Designed for a HCUP Tower**

The force-displacement behavior of two plates can be seen in Figure 3.14. The curve was generated using two plates, which represented a single connection between the columns and panels. Each connection consisted of a plate on the front and back side of the panel. The predicted response of the most extreme tower connection, at both the operational and extreme limit states, was identified on the force-displacement curve. Each plate was expected to experience some degree of nonlinear behavior at the operational limit state. When observing the model, the region of the plate exceeding the estimated yield strength was found to be concentrated at the ninety degree bend. The stress level in this region only slightly exceeded the yield capacity. In addition, the demand on the critical connection, which is found at the tower top, is significantly higher than the other connections on the tower. For these reasons, the connection was deemed satisfactory if designed for the operational limit state.

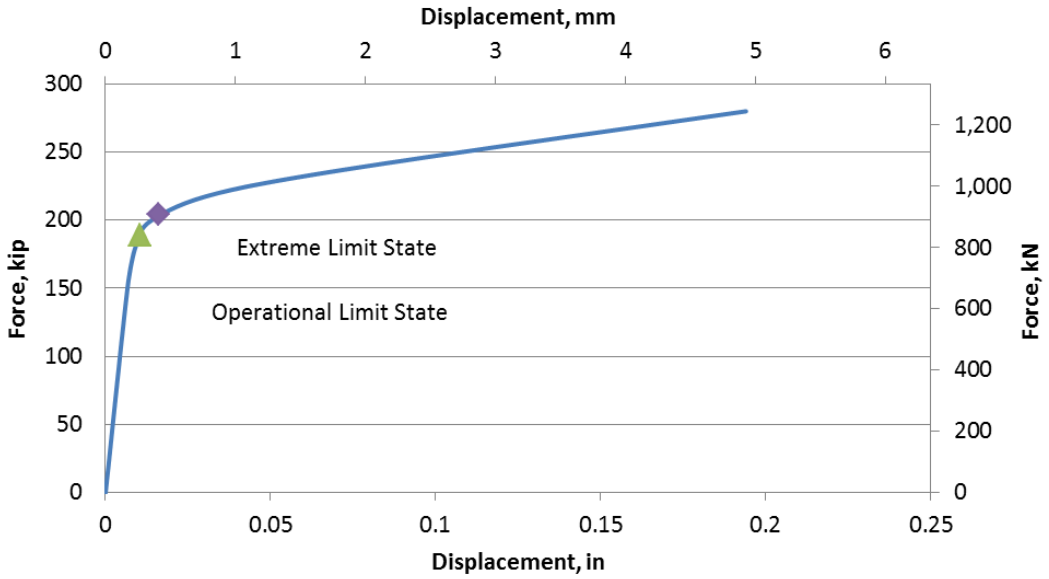


**Figure 3.14: Force-Displacement Response of Bolted Connection**

As previously mentioned, the embedded column plate was designed to remain elastic throughout the inelastic behavior of the angled plate. PCI (2004) was used to determine the capacity of the embedded plate and attached shear studs. Tension and shear breakout strengths as well as individual stud pullout strengths were each determined using the given equations. Equations (3-43) through (3-45) from PCI (2004) were used to determine the tensile breakout strength of the concrete.

$$\phi N_{cb} = \phi C_{bs}(d_{e1} + X + d_{e2})(Y + 3h_{ef})(\Psi_{ed,N})C_{crb} \quad \textbf{(3-43)}$$

$$C_{bs} = 3.33\lambda\sqrt{\frac{f'_c}{h_{ef}}} \quad \textbf{(3-44)}$$

$$\Psi_{ed,N} = 0.7 + 0.3\left(\frac{d_{e,min}}{1.5h_{ef}}\right) \leq 1.0 \quad \textbf{(3-45)}$$

where $\phi = 0.75$ with confinement reinforcement;

$C_{crb} = 1.0$ for uncracked concrete;

$h_{ef}$ = effective embedment depth of headed stud (in.);

$d_{e1}$ = minimum distance from center of outer stud to edge 1 of column;

$d_{e2}$ = minimum distance from center of outer stud to edge 2 of column;

$d_{e,min}$ = least of $d_{e1}$ and $d_{e2}$;

$X$ = horizontal distance between studs in group; and

$Y$ = vertical distance between studs in group.

The shear breakout strength of the embedded plate within the column is critical for the bolted connection as much of the load transfer between the columns and panels is in the form of shear. Equations (3-46) through (3-48) from PCI (2004) were used to determine the shear breakout capacity of the embedded column plate.

$$\phi V_{c1} = \phi V_{col}(C_{X1})(C_{Y1})(C_{ev1})(C_{vcr}) \quad \textbf{(3-46)}$$

$$V_{col} = 87\lambda\sqrt{f'_c}(d_{e1})^{1.33}(d_o)^{.75} \quad \textbf{(3-47)}$$

$$C_{Y1} = \frac{(n_y Y)^{.25}}{0.6 d_{e1}} + 0.15 \leq n_y \quad \textbf{(3-48)}$$

Where $V_{c1}$ = nominal shear strength of group;

$\phi = 0.75$ with confinement steel;

$C_{X1}$ = number of X-row stud lines;

$C_{ev1}$ = eccentricity factor;

$d_o$ = stud diameter; and

$n_y$ = number of Y-row stud lines.

$$\phi N_{ph} = \phi 11.2 A_{brg} f'_c C_{crp} \quad \textbf{(3-49)}$$

Where $\phi = 0.70$;

$A_{brg}$ = bearing area of the stud head in tension; and

$C_{crp} = 1.0$ for uncracked concrete.

The final details of the designed plate can be seen in Figure 3.15. Embedded hex bolts replaced eight of the shear studs in the group in order to attach the angled plate to the embedded column plate. The bearing area of the bolt head was similar to that of the ¾-in. (1.91 cm) shear studs and was therefore considered an acceptable replacement. The bolt ends protruding from the embedded plate are to provide a connection to the angled plate.

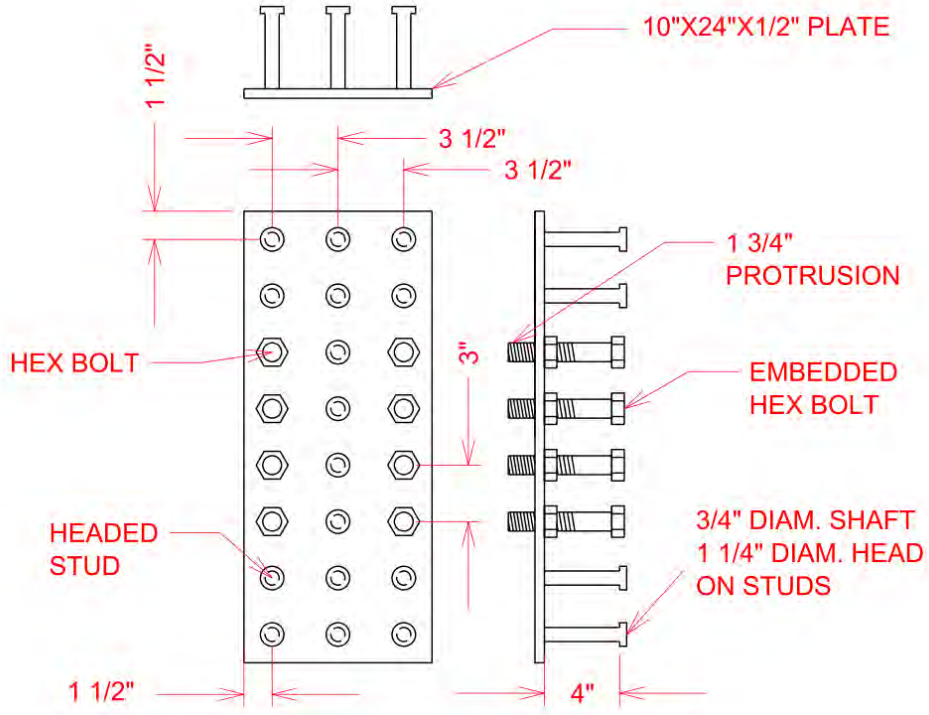


**Figure 3.15: HCUP Embedded Column Plate Detail**

Much like the embedded column plate, the embedded panel plate was also designed to remain elastic during the extreme loading condition of the tower. The number and size of the welded reinforcing bars on the plate can be seen in Figure 3.16. The bars were designed to support 100% of the load demand on the plate. As discussed in Chapter 2, the development length of #4 steel reinforcement in UHPC is only 3-in. (7.6 cm). The excess length of reinforcement shown on the plate was used to reinforce the panel in the connection region.

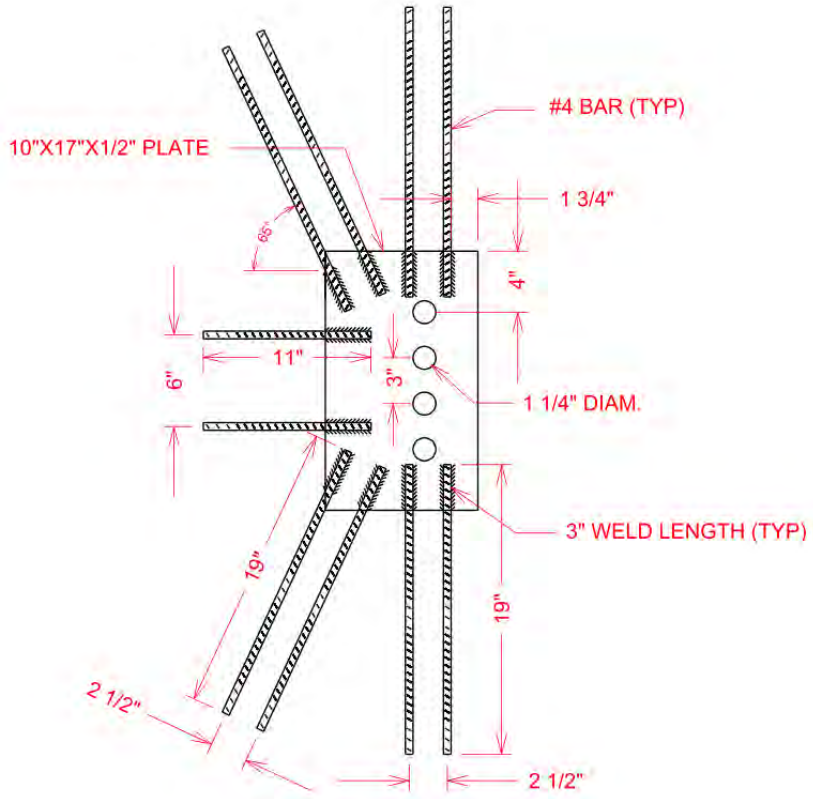


**Figure 3.16: Embedded Panel Plate Detail**

### 3.3.2 HCHP Tower

In many ways, the HCHP tower is very similar to the HCUP tower. The diameter of the tower and columns along the height are nearly identical. The variation between the two comes from the type of panels being used. Unlike the other two concepts, this design was not driven by the need to reduce costs or tower weight, but by the type of connection that would be used at the interface of the columns and panels. In order to allow for the use of a UHPC wet joint, described later in the section, the thickness of the panel needed to be increased. Given the requirements of a larger thickness, it was possible to use a reinforced HSC mix rather than UHPC. The use of HSC in the panels rather than UHPC, does provide some cost reduction; however, UHPC is still used in the interface joint. This, along with the need for additional reinforcement in the panels, makes the added cost benefit of HSC panels relatively small. The general properties and dimensions of the tower at various elevations are presented in Table 3.5.

Due to the increased rigidity of the interface connection and thicker panels used in this tower design, the fundamental tower natural frequency was found to be higher than that of the HCUP tower. A comparison of both the computer model and Rayleigh's method resulted in a difference of 12%, with Rayleigh's method having the higher frequency. It is believed the variation is a result of the assumed displacement function used in the Rayleigh's method.

**Table 3.5: Dimensions and Properties of a HCHP Tower**

| | |
|---|---|
| Column Compressive Strength, ksi (MPa) | 13 (89.63) |
| Panel Compressive Strength, ksi (MPa) | 13 (179.3) |
| Post-Tensioning Effective Stress, ksi (MPa) | 180 (1241) |
| Outer Diameter, D, at Base, in. (m) | 228 (5.79) |
| Maximum Column Diameter, $d_{col}$, at base, in. (mm) | 36 (914) |
| Number of 0.6-in. Diameter Strands, 0-110 ft (0-33.5 m) | 402 |
| Outer Diameter, D, at 110 ft, in. (m) | 156 (3.96) |
| Maximum Column Diameter, $d_{col}$, at 110 ft, in. (mm) | 36 (914) |
| Number of 0.6-in. Diameter Strands, 110-220 ft (0-33.5 m) | 366 |
| Maximum Diameter 170.6 ft (52m) Below Hub Height, in. (m) | 164.2 (4.17) |
| Outer Diameter, D, at 220 ft, in. (m) | 132 (3.35) |
| Maximum Column Diameter, $d_{col}$, at 220 ft, in. (mm) | 29 (737) |
| Number of 0.6-in. Diameter Strands, 220-319.5 ft (0-33.5 m) | 198 |
| Outer Diameter, D, at 319.5 ft, in. (m) | 112.6 (2.86) |
| Maximum Column Diameter, $d_{col}$, at 319.5 ft, in. (mm) | 21 (533) |
| HSC Column Volume, $yd^3$ ($m^3$) | 304.6 (232.9) |
| HSC Panel Volume, $yd^3$ ($m^3$) | 147.1 (112.5) |
| Tower Weight, kip (kN) | 1907 (8481) |
| Fundamental Tower Natural Frequency, Hz | 0.340 |
| Maximum Tower Top Drift at Extreme Limit State, % | 0.99 |

The size of ducts used within the columns as well as the spacing between each can be seen in Figure 3.1. The tower cross section at the base of the HCHP tower has been illustrated in Figure 3.17. The only variation between base cross-section of the HCUP and HCHP tower is the increased panel thickness. The outside diameter of the tower at 110 ft (33.5 m), 220 ft (67.0 m), and the tower top, is the same as the HCUP concept shown in Figure 3.3 through Figure 3.5.

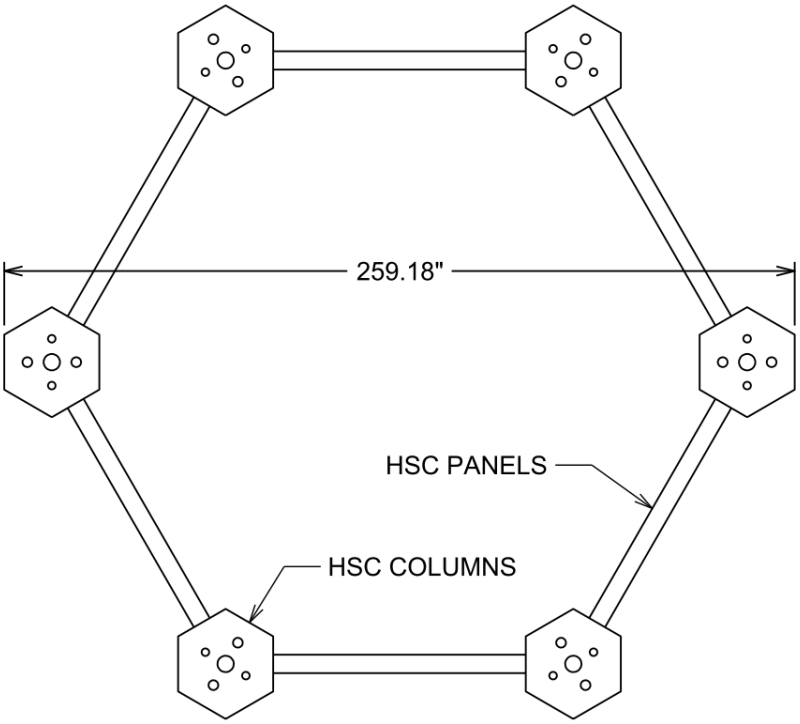


**Figure 3.17: Cross-Section at Base of HCHP Tower**

Many of the equations used to determine the capacity of each of the three towers are the same. For this reason, only equations that vary from those used in the previous tower will be provided. All those not shown, have been discussed previously.

*Operational Moment Capacity*

The locations governing the design at the operational moment capacity can be found just above the 110 ft (33.5 m) and 220 ft (67.0 m) elevations. Here, moment demand is the same for a section containing all five post-tensioning tendons and the section containing three tendons. As tendons are terminated the moment capacity of the tower at the given elevations was reduced as seen in Figure 3.18.

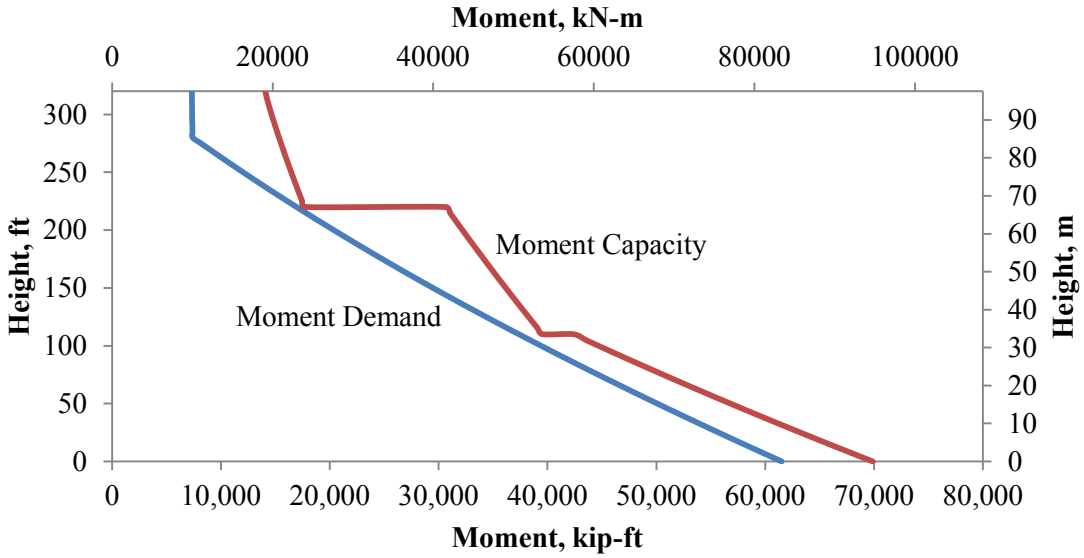


**Figure 3.18: Operational Moment Capacity of the HCHP Tower**

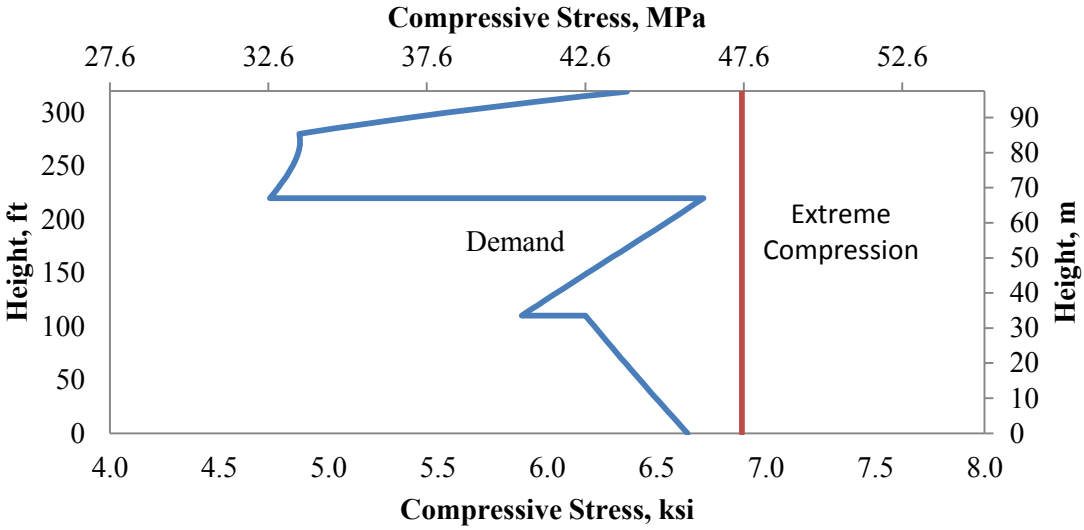


**Figure 3.19: Extreme Compression Fiber Stress at Operational Moment Capacity of HCHP Tower**

*Ultimate Moment Capacity*

Some modifications were made to the equations used to determine the ultimate moment capacity of the HCUP tower. These changes were related both the materials used for each component and their change in geometry. The increase in panel thickness from three to six

inches as well as the change from UHPC panels to HSC panels needed to be considered. The resulting ultimate moment capacity and moment demand curves are shown in Figure 3.20. A concrete compression strain of 0.003 in/in once again governed the capacity of the tower. Maximum post-tensioning tendon strain occurs at the base of the tower at a value of 0.021 in/in.

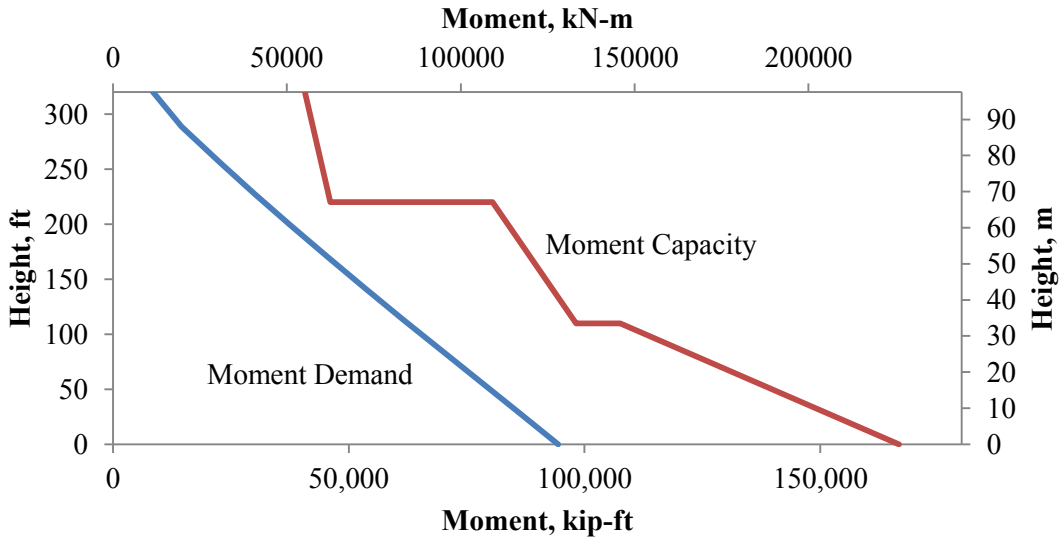


**Figure 3.20: Ultimate Moment Capacity of the HCHP Tower**

*Shear Capacity*

The shear capacity was determined using the procedure outlined in the HCUP concept for determining the maximum principal tensile stresses resulting from the combination of torsional and horizontal loads. With the section properties that result from an increased panel thickness, the maximum principal tensile stresses at the different limit states were reduced. At the base of the tower, the stress within the panel was limited to 10 psi (69 KPa) at operational and 12 psi (83 KPa) at extreme. The most critical location for principal tensile stresses in the tower was at the top. Even at the most critical location however, the stress was limited to 60.0 ksi (414 MPa) at operational and 89.0 ksi (614 MPa) at extreme. Both of these values fell well below the tensile capacity of the concrete; therefor, shear cracks were not expected to develop.

*Fatigue*

Refer to section 3.3.1 describing the HCUP tower for the procedures used to determine the fatigue life of the HCHP tower.

*UHPC Wet Joint Connection*

With the increased thickness of the high-strength concrete panel, the use of a wet joint connection at the column/panel interface becomes a more feasible option. The wet-joint developed for the HCHP tower can be seen in Figure 3.21. The use of UHPC as joint filler was chosen based on the allowable reduction in development lengths for the reinforcement. By providing a pocket in both the column and panel, adequate development lengths can be achieved for the bar size required to resist the shear and tensile forces at the interface. With the absence of large aggregate in UHPC, the material has much greater flow characteristic than lower strength concretes. This allows it to flow freely through the tight bar spacing of the connection. Over the past few years, the UHPC wet joint concept has been gaining popularity in the precast bridge industry. Results of past tests, discussed in Chapter 2, show promising results related to both the joints strength and fatigue capacity.

One of the challenges associated with this type of connection is the vertical orientation of the joint. UHPC would need to be placed from the top of the section, which could be as high as twenty-five feet. Additional testing would need to be completed to verify adequate consolidation takes place along the entire height of the joint. Special consideration would also need to be given to the separation of fibers and concrete near the bottom of the joint. Shoring would be required to cast the joints on site, adding to the overall cost and erection time. With the rapid strength gain characteristics of UHPC however, formwork could potentially be removed the same day casting takes place. According to FHWA (2012) the one, three, and seven-day compressive strengths of UHPC are approximately 13.0 ksi (89.6 MPa), 17.5 (121 MPa), and 20.0 ksi (138 MPa).

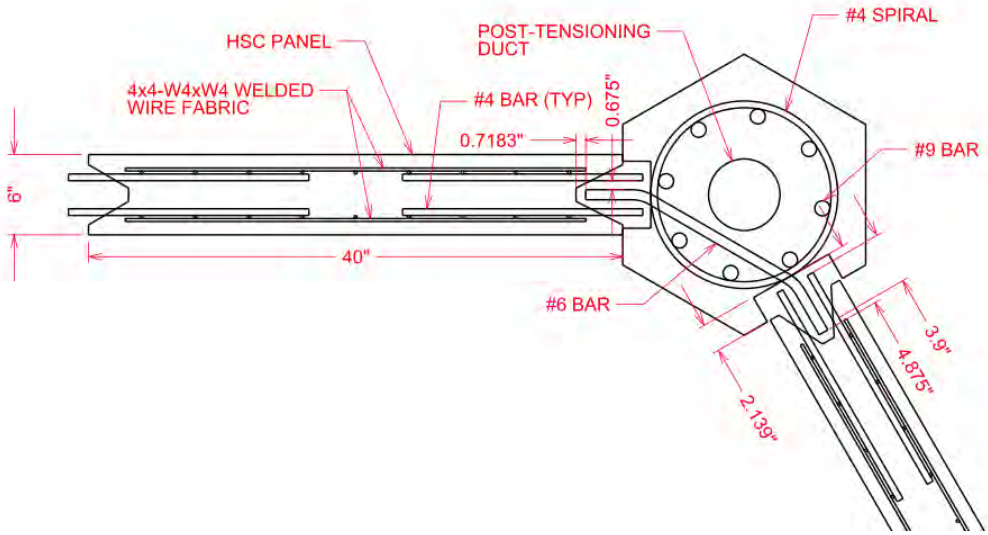


**Figure 3.21: UHPC Wet Joint Connection Details**

In order to provide additional tolerance in the spacing between columns, the two pockets within each column were designed at different widths. One side of the panel will rest outside of the pocket, providing an enclosed void for the UHPC. The other side will have the ability to slide into the column pocket an additional half of an inch. This is best illustrated in Figure 3.21.

The connection was designed based on provisions for shear-friction found in ACI 318 (2008). Equation (3-50) was used to determine the bar sizes required to resist shear at the interface. Using this equation, it was found that two #4 bars or one #6 bar would provide the capacity needed. In addition to determining the required development length for these bars in UHPC, the development lengths into the columns and panels were also found. Although not shown, the equations used to determine development lengths were found in ACI 318 (2008).

$$V_n = 0.8A_{vf}f_y + A_cK_1 \quad \textbf{(3-50)}$$

Where $A_{vf}$ = area of shear-friction reinforcement;

$A_c$ = area of concrete section resisting shear; and

$K_1$ = 400 psi for normal weight concrete.

### 3.3.3 UCUP Tower

The UCUP tower was designed to reduce the overall weight of the tower by taking advantage of the improved material properties of UHPC. The tower would be ideal for

project sites that have poor soil conditions, requiring a more intensive foundation design. The reduced tower weight would also lead to a reduction in the delivery costs of the precast concrete segments. The overall cost of the UCUP tower has a much greater potential to decrease over time when compared to the previous two concepts. The cost of UHPC makes up a large percentage of the total tower cost. If the demand for UHPC increases in the near future, the unit cost of the material may be reduced. Both the HCUP and HCHP towers utilize HSC, which is unlikely to see a significant change in unit cost in the near future. The benefit UHPC has over tradition concrete is not limited to the increased compressive and tensile strengths. The material also performs better in highly corrosive environments such as coastal regions. The UCUP tower dimensions and general properties are provided in Table 3.6. The overall tower diameter remained unchanged from the previous two models; however, the column diameters are significantly reduced.

With the reduction sections sizes, and subsequently tower weight, the fundamental tower natural frequency of this design falls slightly below the allowable frequency range for the 2.5 MW Liberty Turbine. Although the tower may not be acceptable for this turbine, it will likely meet the requirements of larger turbines. According to Lewin and Sritharan (2010) the working frequency range shifts to lower levels as the size of the turbine increases. This may ultimately prove to be a more attractive solution, as larger turbines are produced in the coming years.

**Table 3.6: Dimensions and Properties of UCUP Tower**

| | |
|---|---|
| Column Compressive Strength, ksi (MPa) | 26 (89.63) |
| Panel Compressive Strength, ksi (MPa) | 13 (179.3) |
| Post-Tensioning Effective Stress, ksi (MPa) | 180 (1241) |
| Outer Diameter, D, at Base, in. (m) | 228 (5.79) |
| Maximum Column Diameter, $d_{col}$, at base, in. (mm) | 25.5 (648) |
| Number of 0.6-in. Diameter Strands, 0-110 ft (0-33.5 m) | 390 |
| Outer Diameter, D, at 110 ft, in. (m) | 160 (4.06) |
| Maximum Column Diameter, $d_{col}$, at 110 ft, in. (mm) | 25.5 (648) |
| Number of 0.6-in. Diameter Strands, 110-220 ft (0-33.5 m) | 354 |
| Maximum Diameter 170.6 ft (52m) Below Hub Height, in. (m) | 162.5 (4.13) |
| Outer Diameter, D, at 220 ft, in. (m) | 134 (3.40) |
| Maximum Column Diameter, $d_{col}$, at 220 ft, in. (mm) | 20 (508) |

| | |
|---|---|
| Number of 0.6-in. Diameter Strands, 220-319.5 ft (0-33.5 m) | 210 |
| Outer Diameter, D, at 319.5 ft, in. (m) | 112.6 (2.86) |
| Maximum Column Diameter, $d_{col}$, at 319.5 ft, in. (mm) | 17 (431.8) |
| UHPC Column Volume, $yd^3$ ($m^3$) | 145.1 (110.9) |
| HSC Panel Volume, $yd^3$ ($m^3$) | 173.2 (132.4) |
| Tower Weight, kip (kN) | 1384 (6156) |
| Fundamental Tower Natural Frequency, Hz | 0.293 |
| Maximum Tower Top Drift at Extreme Limit State, % | 1.68 |

*Operational Moment Capacity*

The operational moment capacity was determined in the same manner as the HCUP and HCHP towers. Figure 3.22 shows the capacity and demand curves for the tower along its height. The allowable compressive stress in UHPC at the operational limit-state, was limited to the same factor as the HSC, at 0.53f'c. For a UHPC with 26.0 ksi (179 MPa) compressive strength, this results in a stress limit of 13.8 ksi (95.1 MPa).

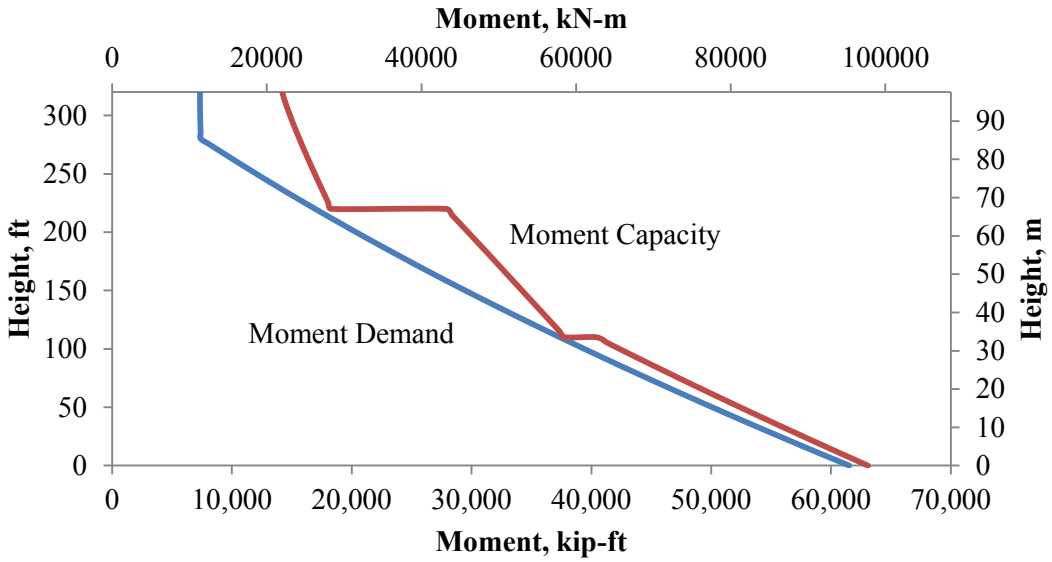


**Figure 3.22: Operational Moment Capacity of UCUP Tower**

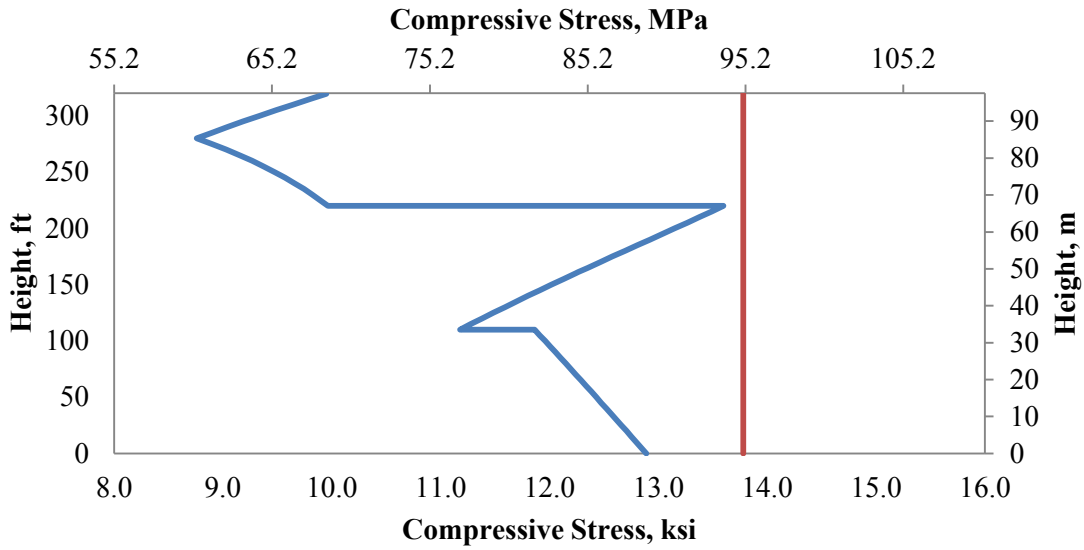


**Figure 3.23: Extreme Compression Fiber at Operational Loads**

*Ultimate Moment Capacity*

The steps used to determine the ultimate moment capacity of the UCUP tower are similar to those outlined in the HCUP tower. The only modification was to the properties of the columns which change from HSC to UHPC. This includes both the modulus of elasticity and compressive strength. The ultimate moment capacity and moment demand curves are shown in Figure 3.24. A compressive strain limitation of 0.004 in/in governed the ultimate moment capacity. This value represents the maximum strain at which the 28-day compressive strength is maintained. Like the previous towers, tendon yielding does take place at the ultimate capacity of the tower. The most critical location occurs at the base of the tower at a magnitude of 0.03683 in/in.

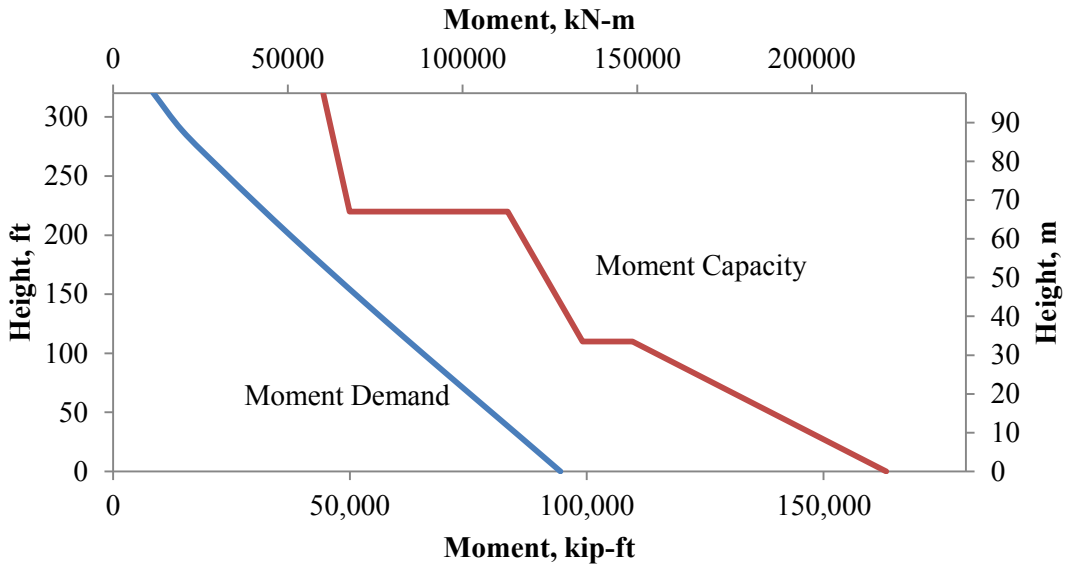


**Figure 3.24: Ultimate Moment Capacity of UCUP Tower at Extreme**

*Shear Capacity*

The procedures outlined in the HCUP concept description, were once again used to determine the shear capacity of the UCUP tower. The lowest value of principal tensile stress can be found at the base of the tower at a magnitude of 16 psi (110 KPa) at operational and 28 psi (190 KPa) at extreme. The tower top is the location of the greatest principal tensile stress of 168 psi (1160 KPa) at the extreme limit state. At operational, the tower is subjected tensile stress of 106 psi (730 KPa).

*Fatigue*

The concrete fatigue capacity of the tower was determined based on the guidelines provided by the Japan Society of Civil Engineers (JGC No. 9). If the magnitude of stress reversals was less than fatigue strength, $f_{rd}$, the section was deemed acceptable.

$$f_{rd} = 0.85 f_d \left(1 - \frac{\sigma_p}{f_d}\right)\left(1 - \frac{\log(N)}{17}\right) \quad \textbf{(3-51)}$$

Where $f_{rd}$ = design fatigue strength of UHPC in compression only;

$\sigma_p$ = permanent stress that the section is subject to;

$f_d$ = design compressive strength, taken as the 28-day strength of concrete (f'$_c$), divided by a safety factor of 1.3; and

$N$ = number of load cycles.

*Horizontally Post-Tensioned Connection*

The horizontally post-tensioned system was designed for both the UCUP tower as well as the HCUP tower. The connection relies on friction between the columns and panels to resist the large shear forces experienced at the interface. By running post-tensioning through the columns and panels perpendicular to the column/panel interface, the capacity of the interface to resist shear is greatly improved.

ACI 318 (2008) was used to determine the additional resistance horizontal post-tensioning would provide at the interface. Section 11.6.7 states that permanent net compression across a shear plane may be permitted to be taken as being additive to the resistance provided by reinforcement as shown in Equation (3-52). Because no shear reinforcement will be used across the interface, the nominal shear strength of the connection can be determined by multiplying the normal force and coefficient of friction.

$$\phi V_n = \phi\left(A_{vf} f_y + N\right)\mu \quad \textbf{(3-52)}$$

Where $V_n$ = Nominal shear strength;

$\phi$ = strength reduction factor = 0.75;

$A_{vf}$ = Area of shear friction reinforcement;

$f_y$ = specified yield strength of reinforcement;

$N$ = Normal force acting through shear plane; and

$\mu$ = coefficient of friction.

ACI 318 (2008) provides values for friction coefficients that vary depending on the placement of the two sections being analyzed. For concrete placed monolithically, a friction coefficient of 1.4 is to be used. For concrete placed against hardened concrete with an intentionally roughened surface the coefficient drops to 1.0. When placing two hardened concrete segments without intentionally roughened surfaces the coefficient drops even further to a value of 0.6. In order to reduce the required number of strands across the

interface, various options were considered to increase the friction coefficient from 0.6. It was determined that by reducing the width of the panel enough to allow for the placement of grout between the columns and panels, a friction coefficient of 1.0 would be acceptable. In addition, the grout would allow for greater tolerance during the construction of the different segments and act to seal the interface joints. This would improve the protection of internal components from the environment.

There are a number of ways in which the horizontal duct could be placed in the column. Figure 3.25 shows one of these options. In order to reduce the difficulty of running the strands around the circumference of the tower, it is suggested that two tendons be used at each location. Each tendon would cover half of the towers circumference and terminate on one of the three outside faces of the column.

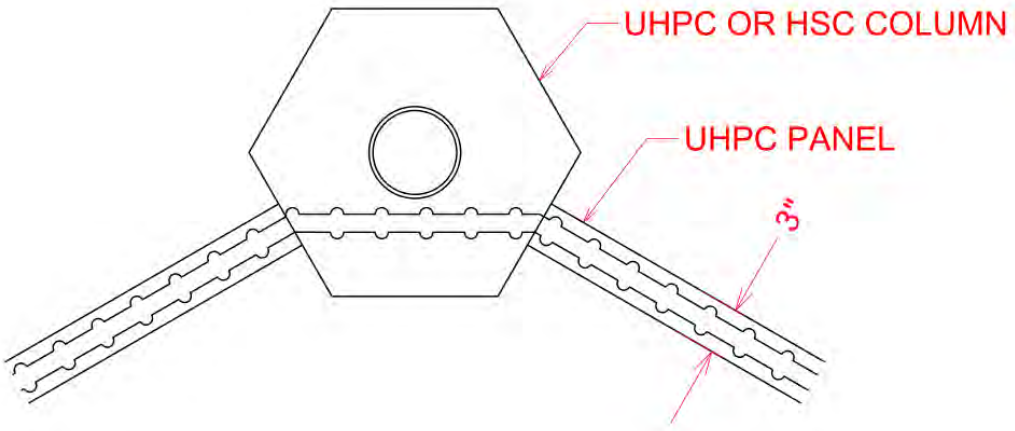


**Figure 3.25: Horizontally Post-Tensioned Connection Detail**

### 3.4 Conceptual Design for Yaw Bearing Connection and Foundation

Given the unique design of the proposed towers, traditional means of attaching each to the foundation and yaw bearing are not suitable. Some modifications need to be made that would allow manufacturers to utilize the towers without making changes to other components. Although a detailed design of both the yaw bearing connection and foundation was not covered in this project's scope, a conceptual design has been completed for each.

The yaw bearing is located at the bottom of the nacelle. It allows the entire head mass to rotate 360˚ to utilize wind from every direction. The only component separating the yaw

bearing from the tower is a brake plate used to prevent this rotation. Steel towers often provide a flange at the top, in which the yaw bearing can be bolted around their perimeter. In the case of the precast concrete towers, this is not feasible. Figure 3.26 illustrates the proposed replacement. Because the column post-tensioning anchors sit directly on top of the columns, the brake plate is not able to rest directly on the tower. Instead, risers are used to allow it to sit above the anchorages. The risers are attached to a steel ring beam, which is placed between the columns and anchorages to secure it in place. The yaw bearing is then attached directly to the brake plate. The only modification to the current design of the brake plate and yaw bearing would be a reduction in the number of bolts used around the perimeter.

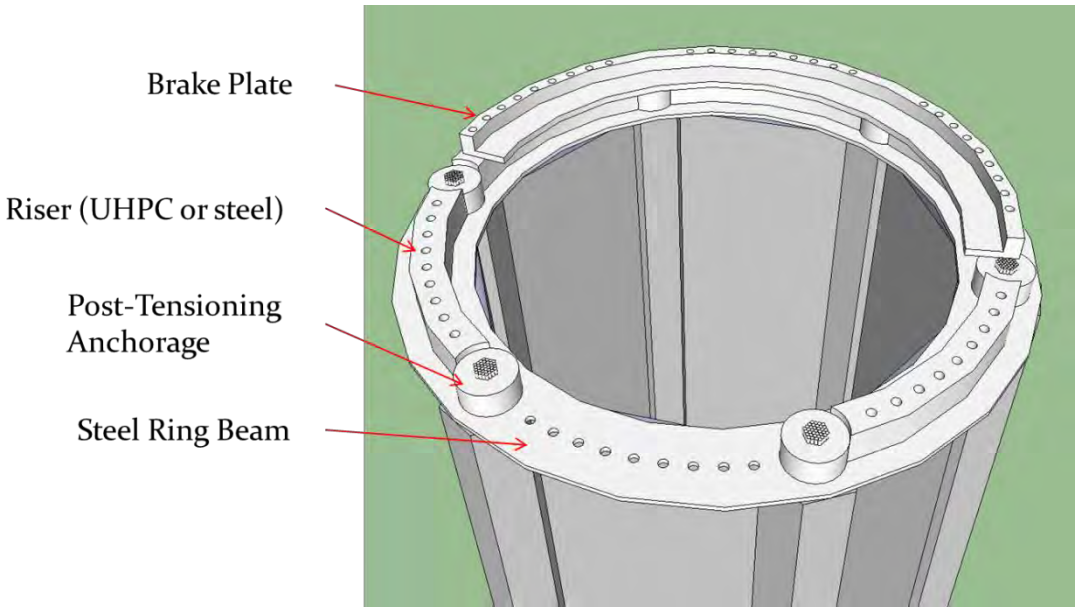


**Figure 3.26: Proposed Yaw Bearing Connection at Tower Top**

In order to stress the vertical post-tensioning tendons running through each column, jacking needs to take place at eigher the top or bottom of the tower. With the size of jack required, and difficulties associated with working at 328 ft (100 m), it was desireable to tension the tendons at the bottom of the tower. In order to do so, an access compartment would need to be constructed underneath the foundation. The conceptual details, shown in Figure 3.27, illustrate how access directly beneath each column would be made possible. Outside of the added compartment, the foundation would utilize a standard spread footing.

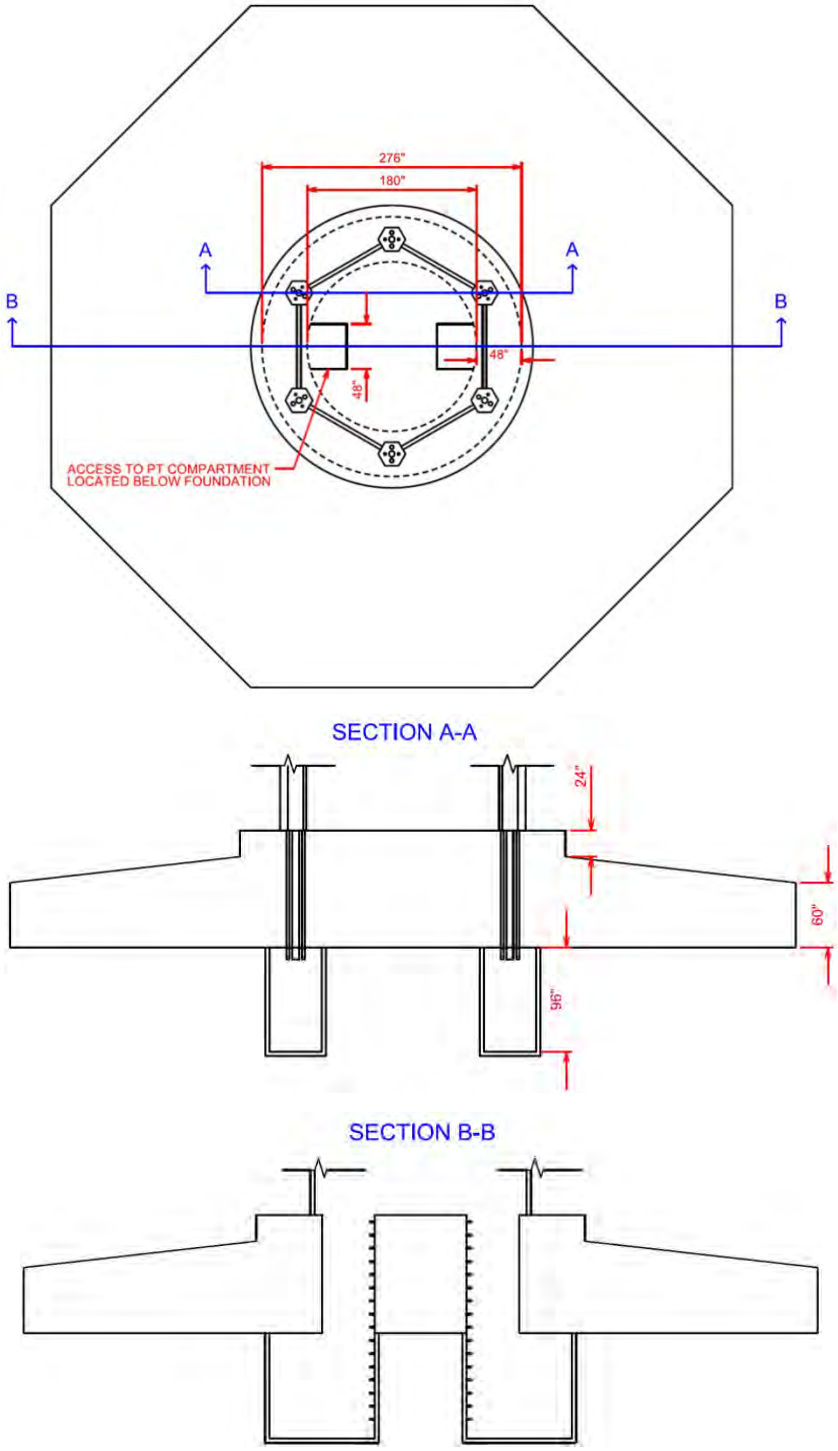


**Figure 3.27: Proposed Foundation Layout with Access Compartment**

# CHAPTER 4. LABORATORY TESTING OF WIND TURBINE TOWER COMPONENTS

In order to verify the design of the tower at both the operational and extreme limit states, a series of lab tests were conducted. Specimens from two of the three tower designs were constructed and subject to in-plane loading conditions. All three of the proposed connections were tested using one of the two tower designs. The construction of each precast component as well as the assembly of each test unit is discussed in detail. The results of each of the three tests are also presented.

## 4.1 Loading Criteria

### 4.1.1 Identifying Critical Tower Sections

Understanding the behavior of the individual tower components is critical when determining the overall capacity of the tower. In order to do so, a complete finite element model of the tower, which is discussed in detail in Chapter 5, was created. Using the finite element model, results of each of the six load cases were reviewed to identify the most critical regions of the tower. The focus of the experimental testing was to not only verify the capacity at different limit states, but to also understand the process in which load is distributed throughout the panel. For this reason, it was important to test a section of the tower experiencing the highest panel and connection stresses. Using the finite element model the locations of the largest principal compression, principal tension, and connection forces were identified.

The largest principal tensile stress in the panels occurred in the top twenty-five feet of the tower as a result of the torsion load case. This is illustrated on the left of Figure 4.1. The torsional load combination is unique as it does not generate large forces at the bottom of the tower due to increased moment, as many of the other load cases do. The high panel stresses found near the top of the tower can be contributed to the tapered tower diameter. From the base of the tower to the top, the diameter is reduced by nearly a half. Larger shear stresses in both the columns and panels must develop to resist the torque generated by the head mass.

Because the magnitude of the torque does not vary significantly along the height, stress is reduced at lower elevations.

The largest principle compressive stress occurs at approximately 150 ft (45.7 m) in elevation as a result of the X-directional shear load case. This is illustrated on the right of Figure 4.1. The large shear force generated by the head mass at the top of the tower results in increased moment demand at lower elevations. The construction sequence of the tower significantly affects the residual stresses within both the panels and connections. The model utilized a construction sequence in which the column/panel interface connections were in place prior to vertical post-tensioning of the columns. This type of construction sequence is illustrated in Figure 3.6. As a result, both the columns and panels are permanently compressed. When subjected to the X-directional shear load case, the moments and resulting panel stresses at the bottom of the tower are not great enough to overcome this initial compressive stress. This prevents cracking of the panels in large portion of the tower.

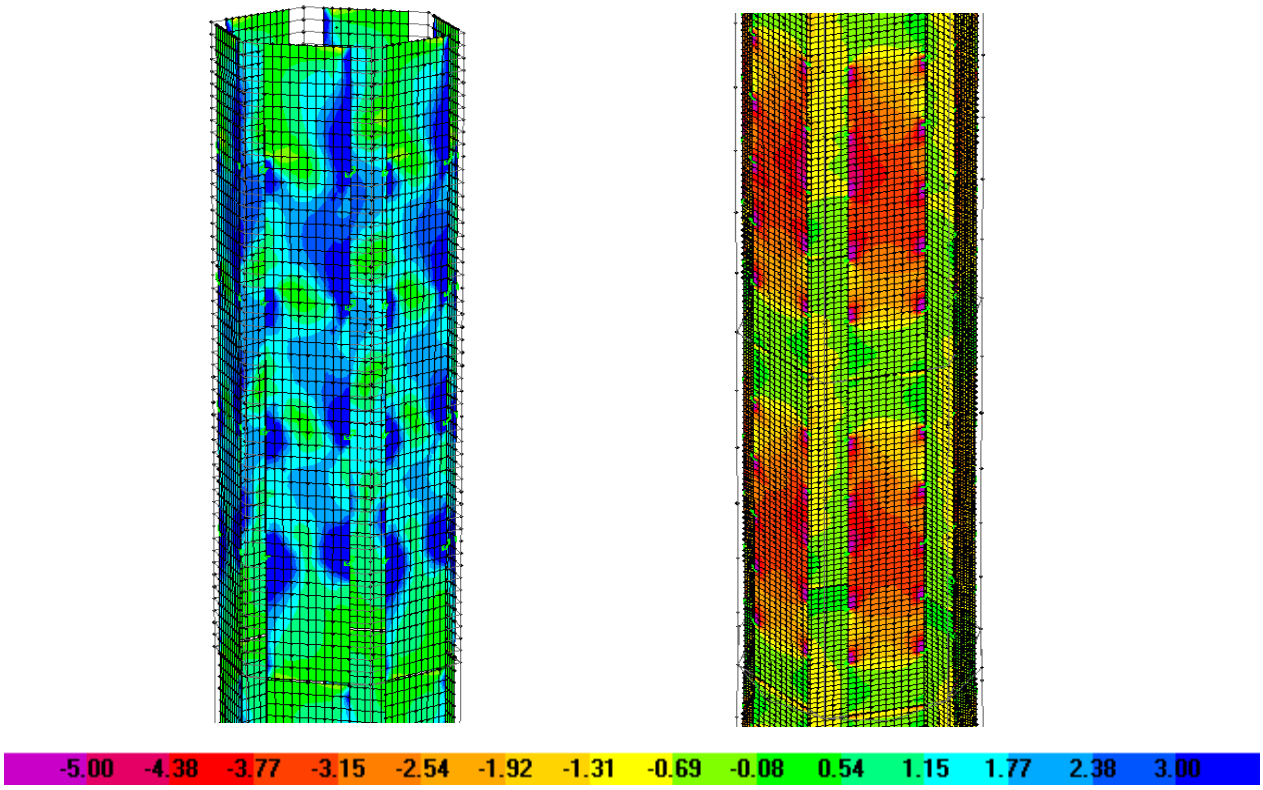


**Figure 4.1: Location of Maximum Compressive and Tensile Principal Stresses**

Results from all six load cases show the correlation between the panel stresses and connection loads. The torsional load case, which resulted in the maximum principal tensile stress, also resulted in the maximum demand on the connections. As expected this occurred in the top row of connections, where higher shear capacity is required to resist the torsional load.

### 4.1.2 Development of an In-Plane test Specimen

A number of considerations were made when exploring how to replicate the loading conditions of a fully erected tower in a laboratory setting. First, and foremost, was the size of the components that could be tested using existing frames and equipment. The largest load frame would allow for a maximum test specimen height of approximately fifteen feet. This included the height of the foundation block through which the tower components would be anchored to the floor. The actuator needed to have the capacity to test the components up to the extreme limit state and beyond if necessary. Often, scaled specimens are used in a lab environment to test items of large magnitude such as the wind turbine tower. In this case however, scaling was not desirable because of the thin UHPC panel sections being considered for the complete tower. Any further reduction in thickness would make fabrication and transportation of the panels very difficult. These limitations, along with a few less critical ones, ultimately defined what was to be tested.

Using results of the finite element model, it was determined that the top section of the tower would be best suited for lab testing. The panels and connections in this region experienced a higher demand than anywhere else on the tower. Although the maximum principal compressive stress does not occur in this location, large compressive stresses similar in magnitude the principal tensile stresses are developed. This compressive stress is similar in magnitude to that found at the 150 ft (45.7 m) elevation when subjected to the X-directional shear load case.

Given the limitations mentioned above, it was not feasible to construct a test unit that included all six exterior columns and panels. By observing the results of the finite element model when subjected to the torsional load case, it can be seen that each of the six panels near the top of the tower exhibit similar stress distribution (Figure 4.1). The demand on the connections was also found to be consistent around the tower perimeter. For these reasons, it

was determined that a single panel, two column setup could be used to represent all six sides of the tower. Load would be applied in a way that would generate stresses similar to what was found in the complete tower model.

The most suitable orientation of the load, with respect to the test specimen, was found to be along the plane of the panel. The reason for this is best illustrated in Figure 4.2, in which the reaction at the top of each column at the operational and extreme limit state is presented. These reaction forces were determined from the torsional load case and used as the basis for the in-plane test loads. It is important to note that the design of the tower calls for the yaw bearing to be fastened to the tops of the columns though vertical post-tensioning. The yaw bearing acts as the transition piece between the turbine, where a majority of the load is generated, and the tower. No connection is to be made between the yaw bearing and panels. For this reason, the summation of the reactions shown, are equivalent to the tower top loads applied to the model.

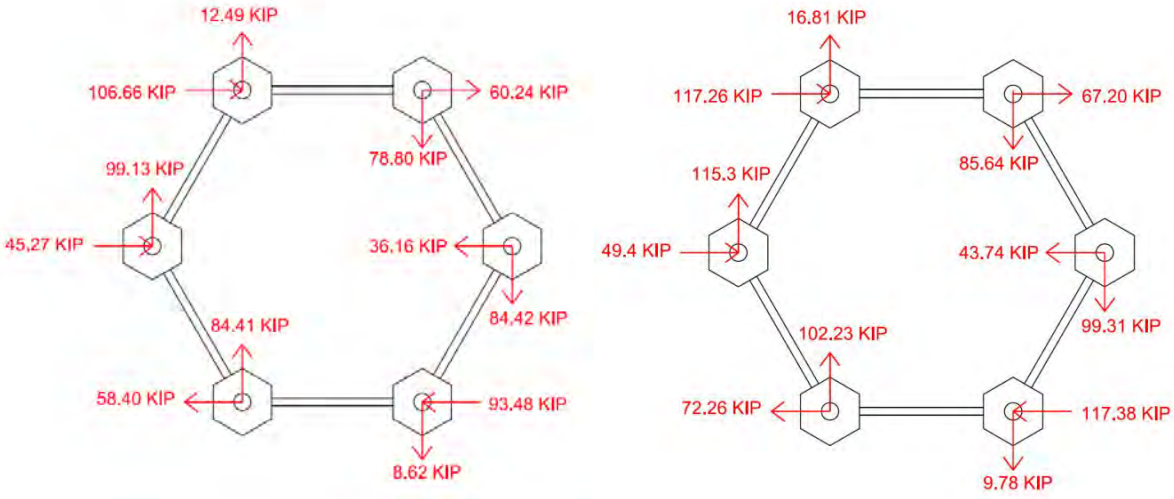


**Figure 4.2: Operational and Extreme Reactions at the Tower Top**

### 4.1.3 Comparison of Test Specimen and Completed Tower Models

The test load corresponding to the extreme limit state was taken from the bottom left column on the right side of Figure 4.2. By rotating the axis of the resultants 30 degrees counterclockwise, the in-plane reaction force of the bottom left panel can be obtained. This reaction force was equal to 124.7 kip (554.7 kN). The same procedure was used to determine the required operational load for the test specimen. The maximum in-plane operational load was found to be 102.3 kip (455.1 kN). When comparing the torque differential of the

operational and extreme load cases in the complete tower model with the same differential in the resultant in-plane forces used for testing, it can be seen that the percent increase is nearly identical. Table 4.1 shows the variation to be only 0.4%. This further verifies that the loads used during testing are equivalent to those applied to the complete tower.

**Table 4.1: Load Variation between Complete Tower Model and Test Unit**

| | Load Case | | |
|---|---|---|---|
| | **MZ Operational** | **MZ Extreme** | **% Difference** |
| **Test Load, kip (kN)** | 102.3 (455.0) | 124.7 (554.7) | 21.86 |
| **Tower Torque, ft*kip (kN*m)** | -4770 (6467) | -5831 (7906) | 22.26 |
| | | **Variation=** | **0.398** |

It was determined early on in the development of the test specimens that it would be difficult to use the number of vertical post-tensioning strands called for in the complete tower design. The challenges associated with obtaining the required jacking equipment for an experimental test limited the number of strands used. The number of strands per column was chosen based on the required moment capacity at the tower top. The elevations with the lowest reserve capacity occur at the post-tensioning cut-off locations at 110 ft (33.5 m) and 220 ft (67.0 m) (Figure 4.3). Other locations of the tower have a significant amount of reserve capacity because the strands are only terminated at the three designated locations. This is the case for the top of the tower as well. By targeting a moment capacity at this location that only slightly exceeded the demand, the number of strands was reduced to 16 per column. This reduction was significant enough to allow for laboratory testing. The reduction in moment capacity over the height of the tower as a result of the decrease in strands from 33 to 16 can be seen in Figure 4.4.

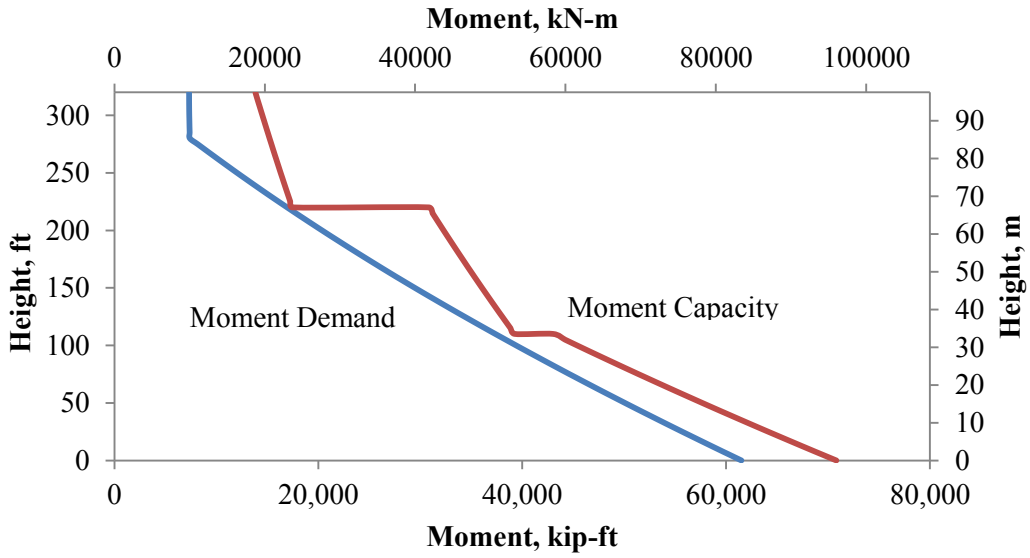


**Figure 4.3: Operational Moment Capacity vs. Demand for Complete Strand Layout**

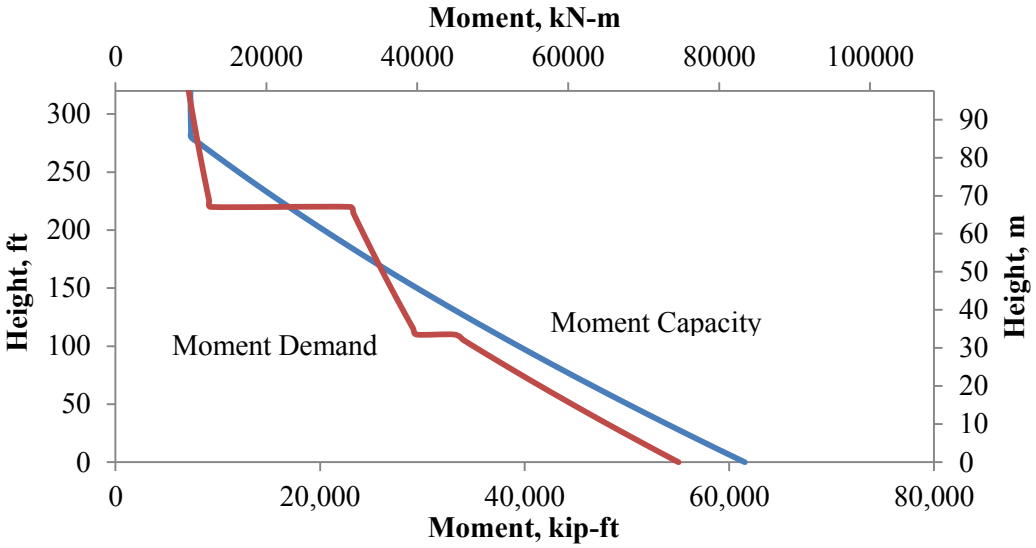


**Figure 4.4: Operational Moment Capacity vs. Demand for Reduced Strand Layout**

## 4.2 Development of Experimental Test Units

Three separate in-plane tests were completed using the bolted, horizontally post-tensioned (HPT), and UHPC wet joint connection details described in Chapter 3. From here onward, the name of each test specimen will correspond to the tower type and connection used. The bolted connection test will consist of HSC columns and UHPC panels; it will be referred to as HCUP-BC. The horizontally post-tensioned specimen uses the same materials

for each component and will be referred to as HCUP-HPT. The final test unit which replaces the UHPC panel with HSC will be referred to as HCHP-UHPC.

Each test consists of a foundation block, tower specimen, and top beam. The foundation block provided a means through which to secure the test specimen to the laboratory strong floor. It also contained one of the two strand anchorages required to post-tension each tendon. The top beam represented the yaw bearing located at the top of the complete tower. Its primary purpose is to provide equal load distribution to each of the columns; however, it is also the location of the second post-tensioning anchorage. The position of each of these three components can be seen in Figure 4.5. All dimensions shown are representative of each of the three specimens. The only variation between the three specimens is the interface connection, panel thickness, and panel material.

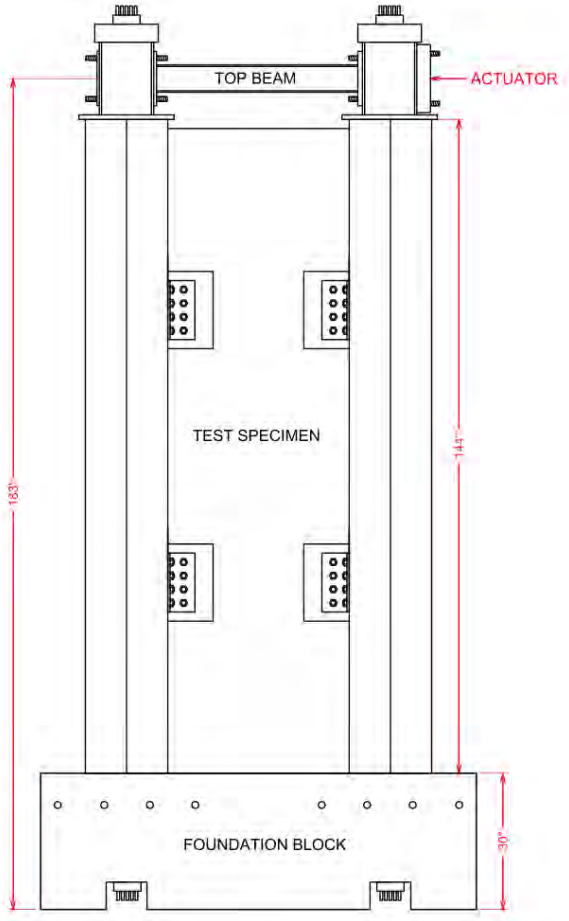


**Figure 4.5: General In-Plane Test Setup**

All three tests utilized two HSC columns with maximum outside diameters of twenty-one inches. The column diameter was not tapered in order to match the designs of the complete tower, due the insignificance of the taper over the shortened height. The position and number of post-tensioning strands within the columns was also identical for each test. Two ducts containing eight strands each were used within each column. Each of the vertical strands was jacked to an initial stress of $0.7f_{pu}$. For the 270 ksi (1860 MPa) low-relaxation strands being used, this resulted in an initial prestressing force of 656 kip (2920 kN) per column. The amount of longitudinal reinforcement used was based on a moment-curvature analysis of the column. The same longitudinal reinforcement ratio was used along the entire height. Initially the transverse reinforcement was designed based on the minimum requirement of ACI 318 (2008). Because two of the columns would be used for both the HCUP-BC and HCUP-HPT specimens, additional hoops were added to improve confinement of the post-tensioned column and prevent shear cracks from developing during testing. The use of the columns in multiple tests was possible given the limited amount of damage expected to occur.

The cross-sections of each of the three tests can be seen in Figure 4.6, Figure 4.7, and Figure 4.8. For the complete tower, a single duct running through the center of the column was designed for the upper 100 ft (30.5 m) of the tower. Unlike the proposed duct layout of Figure 3.1, which included one large single duct extending the height of the tower, the duct was split into two separate channels. This was done to accommodate the horizontal post-tensioning anchors and dowel bars of the UHPC wet joint columns. The separation of the center tendon does not affect the performance of the columns during testing because the two tendons remain in line with the bending axis of the column.

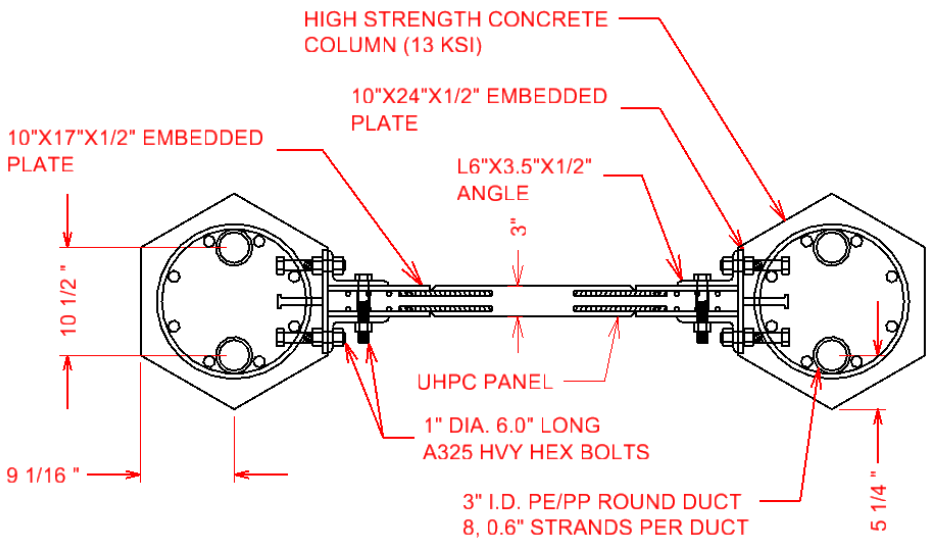


**Figure 4.6: HCUP-BC Test Cross-Section**

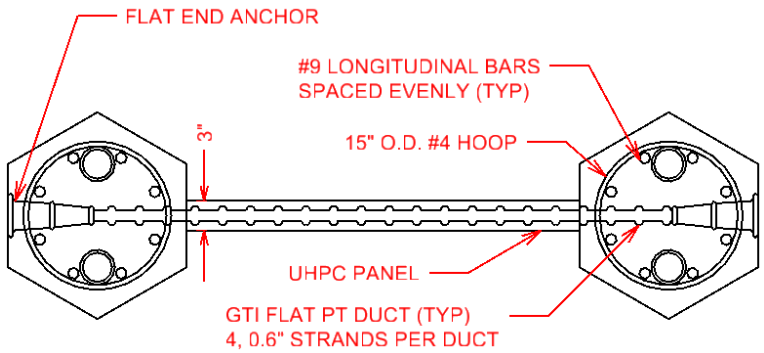


**Figure 4.7: HCUP-HPT Test Cross-Section**

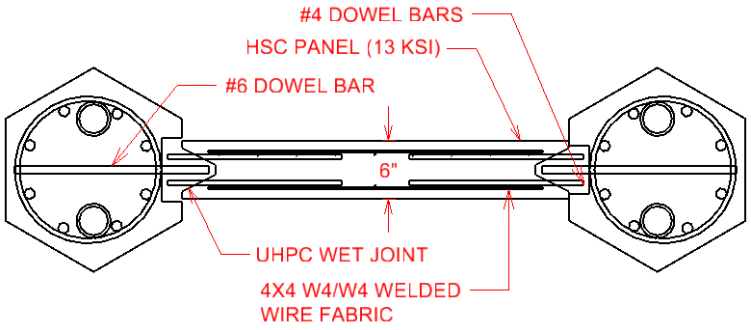


**Figure 4.8: HCHP-UHPC Test Cross-Section**

The elevations of the columns used for both the HCUP-BC and HCUP-HPT specimens are shown in Figure 4.9. They include both the embedded column plates used in the bolted connection and the HPT anchors. Additional confinement was included around the HPT anchorages to restrain any bursting stresses that may develop during tendon stressing and testing.

The panel details of both the bolted connection and HPT connection can be seen in Figure 4.10. Outside of the welded reinforcement attached to the embedded plates in the HCHP-BC specimen, no other form of reinforcement was required in the either UHPC panel. With the presence of fibers in the UHPC, it was determined that the tensile capacity of the panel would sufficiently meet the demand at both limit states. The column and panel details developed for the HCHP-UHPC specimen have also been presented in Figure 4.11 and Figure 4.12.

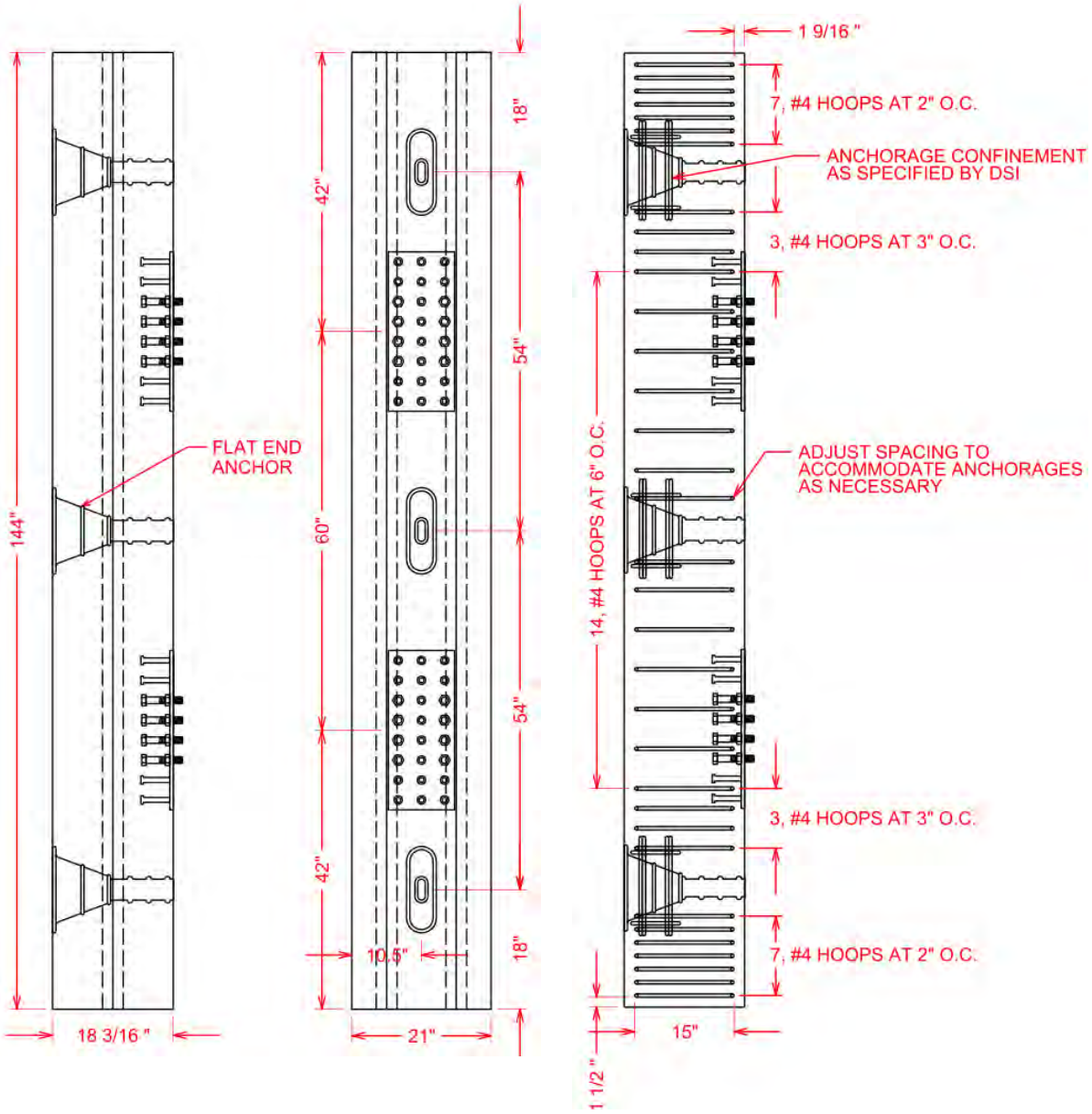


**Figure 4.9: General Dimensions and R/F Details for HCUP-BC/HCUP-HPT Columns**

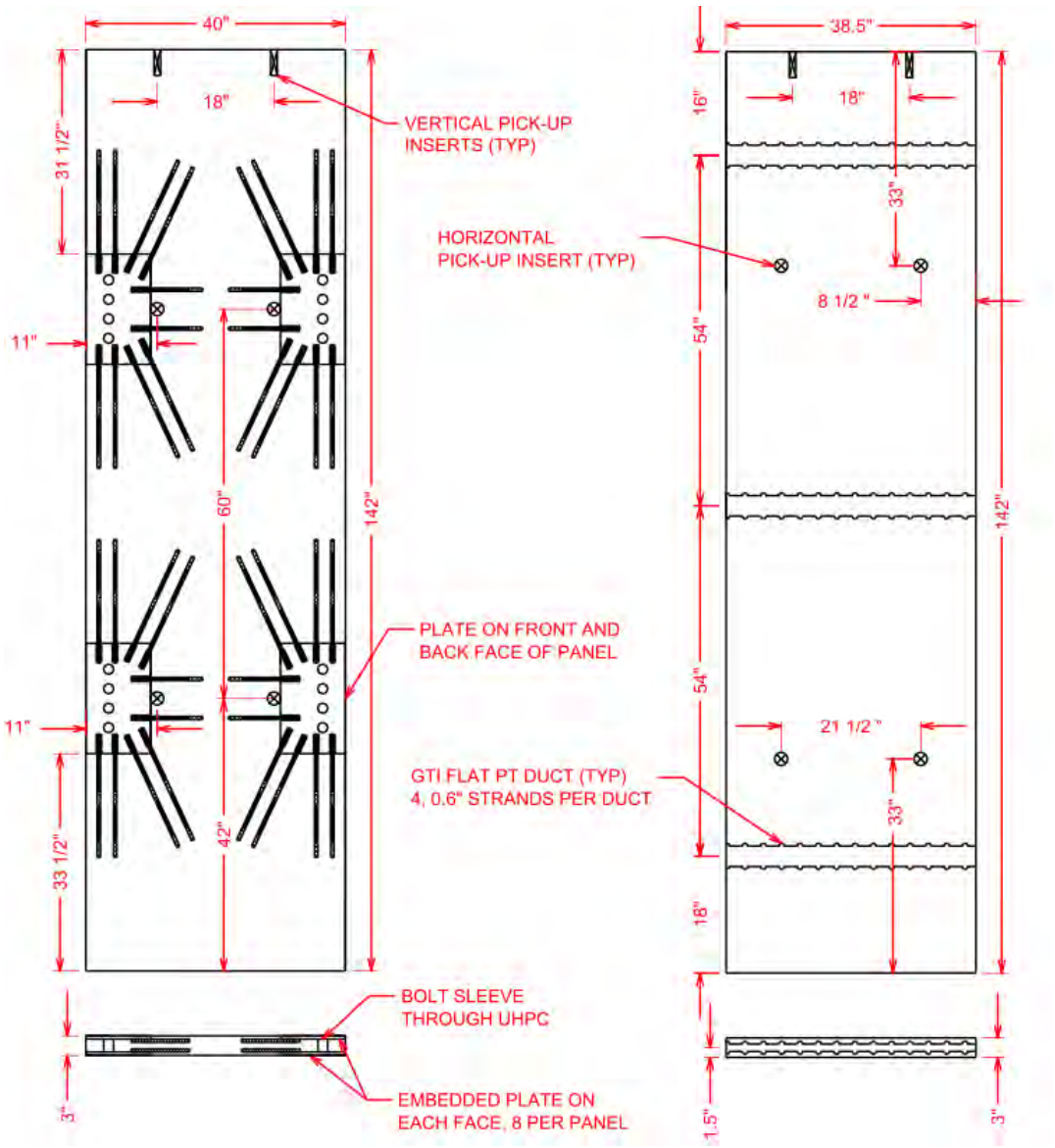


**Figure 4.10: HCUP-BC and HCUP-HPT Panel Elevations**

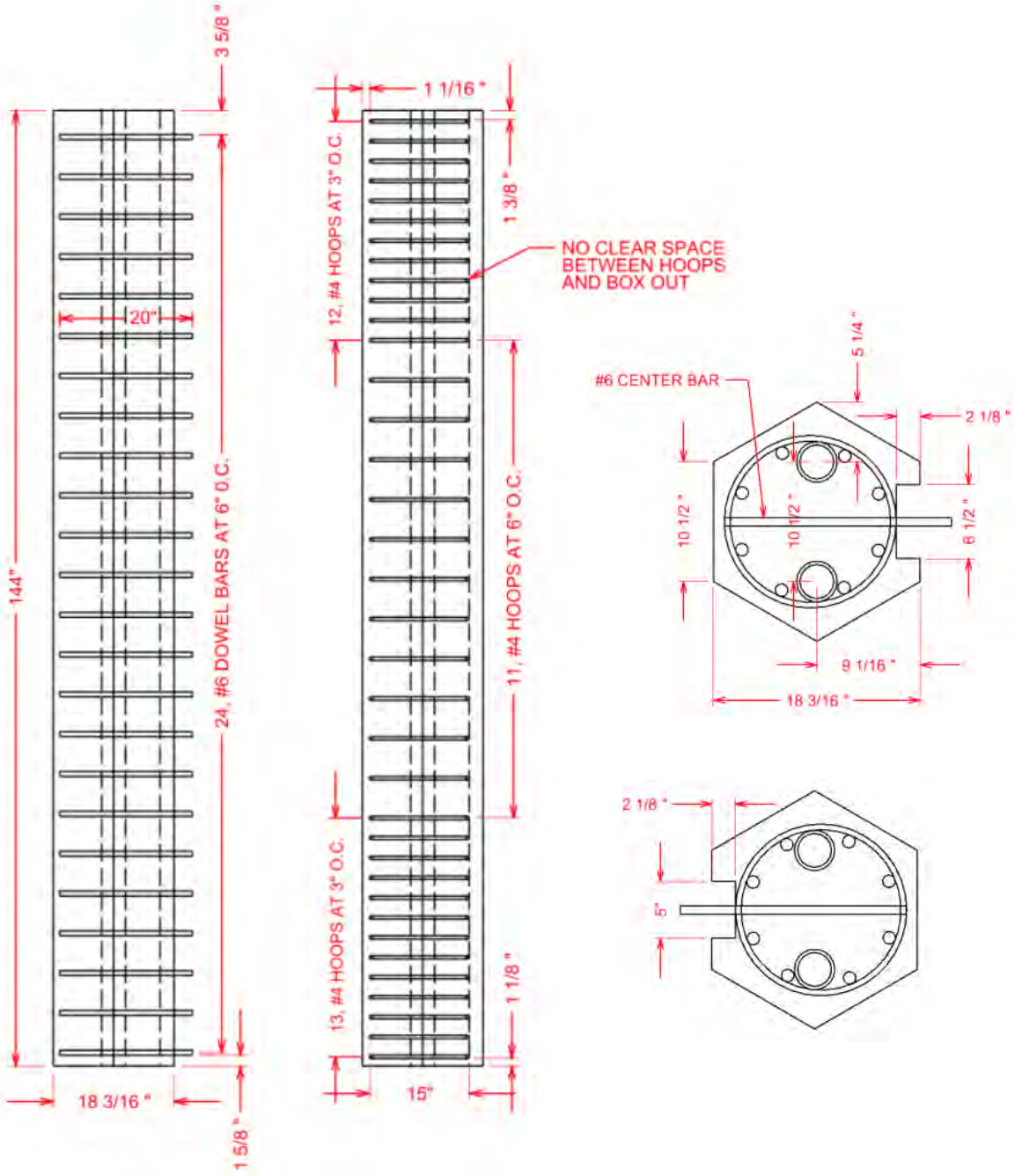


**Figure 4.11: HCHP-UHPC Column Details**

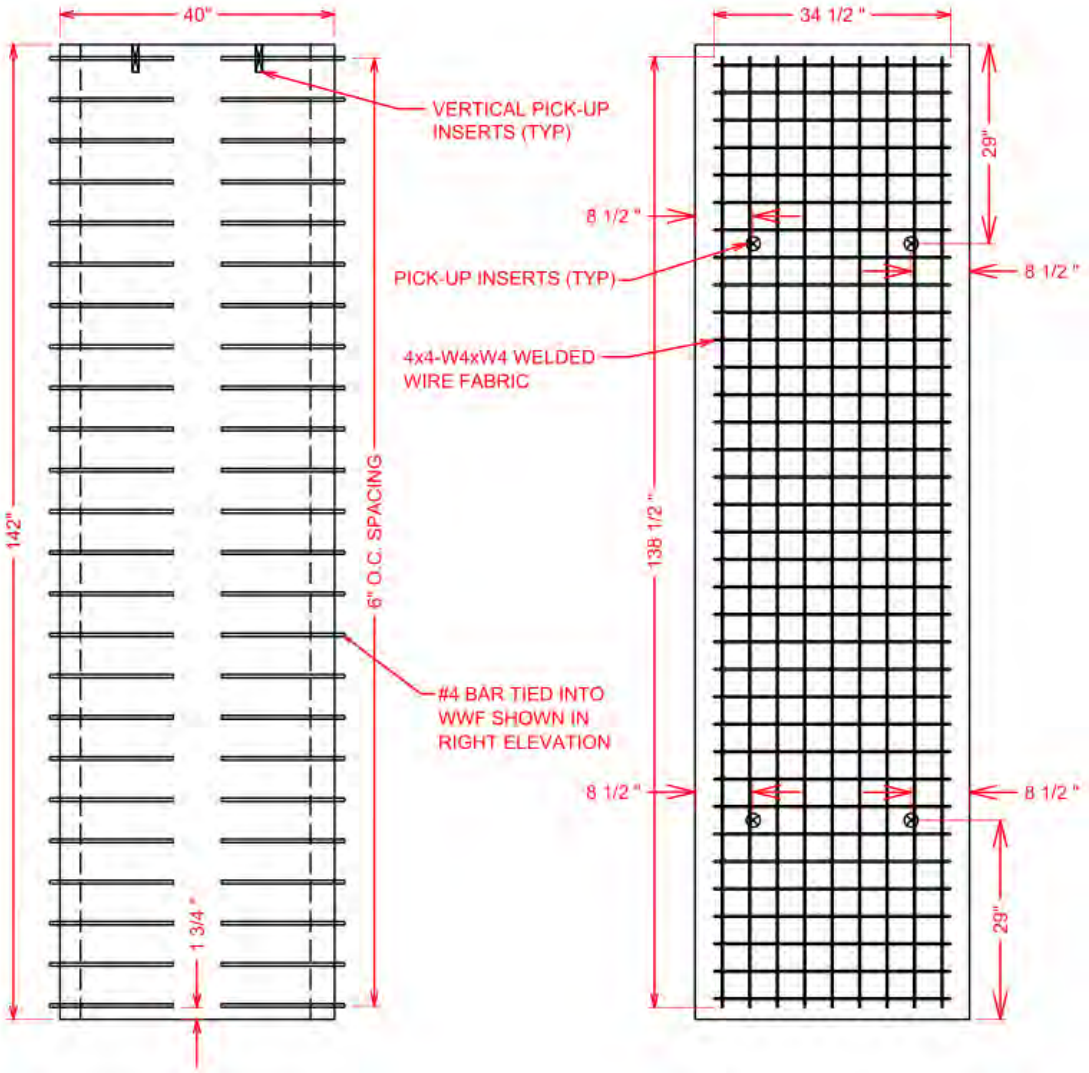


**Figure 4.12: HCHP-UHPC Panel Elevation**

## 4.3 Construction of Full-Scale Test Specimen

### 4.3.1 Precast Construction

Construction of the in-plane test components took place at Coreslab Structures, Inc. in Omaha, NE. Over a period of four days, four HSC columns, two UHPC panels, and one HSC panel were cast. The construction process began with the erection of the embedded plates for the HCUP-BC specimen. The cutting and drilling of the half-inch steel plates took place at a local fabrication shop, while the attachment of welded reinforcement and shear studs was done at Iowa State University. Some concern was raised about the integrity of the welded reinforcement on the embedded panel plate shown in Figure 4.13. Although the welding process did appear to diminish the cross-sectional area of the bar in the welded region, tests

conducted afterwards confirmed that the performance of the welded bar was nearly identical to that of an unwelded bar. The shear studs of the embedded column plate shown in Figure 4.14 and Figure 4.15 were attached using a stud welder. The bolts are held in place by tightened nuts on both sides of the plate. Upon casting of the columns, the nuts on the face opposite the shear studs were removed to allow for the placement of the angled plate.

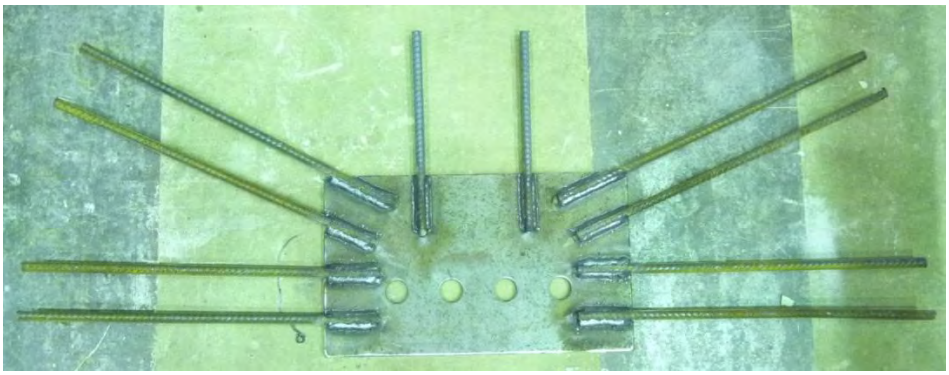

**Figure 4.13: Embedded Panel Plate for the Bolted Connection**

**Figure 4.14: Embedded Column Plate for the Bolted Connection**

**Figure 4.15: Embedded Column Plate for the Bolted Connection**

The formwork for both UHPC panels was erected on steel prestressing beds at Coreslab. This not only reduced construction time, but also provided a smooth surface on which cracks could be easily identified during testing. One of the major challenges of the bolted connection is the relatively low tolerance associated with the position of the plates. Originally the plates were placed out of tolerance requiring the foreman to make adjustments accordingly. This raises concerns as to whether this type of connection can consistently meet the required tolerances when constructing a complete tower. The bolted connection panel can be seen in Figure 4.16. The HCUP-HPT panel had the shortest erection time of any of the three panels (Figure 4.17). The only embedded components were the three flat ducts used for HPT. The cast specimens are shown in Figure 4.18. Because of the self-consolidating feature of UHPC, conventional means of consolidation were not required. This made casting a quick and easy process that required less manpower then casting of standard concrete. The specimens were immediately covered and heated to a temperature of 90˚F for approximately three days. In order to enhance the curing process, a treatment was also used on each UHPC panel. This consisted of heating the specimens to 195˚F for 48 hours in a steamed environment.

**Figure 4.16: Formwork for Bolted Connection Panel**

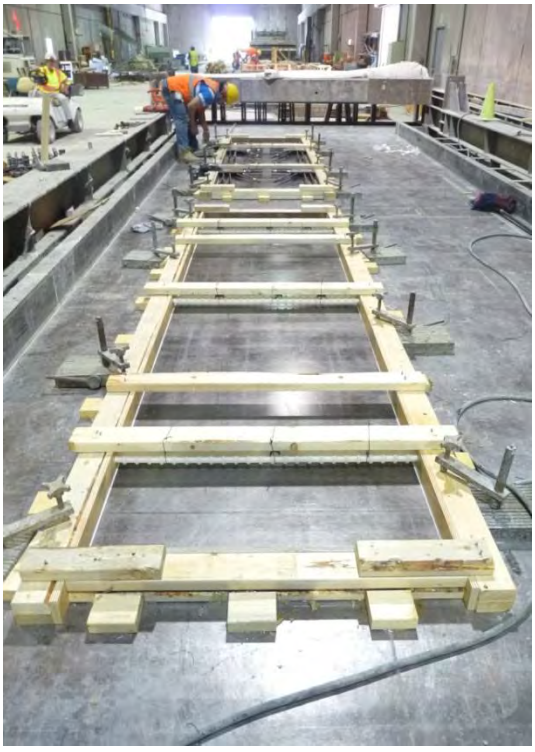

**Figure 4.17: Horizontally Post-Tensioned Panel Construction**

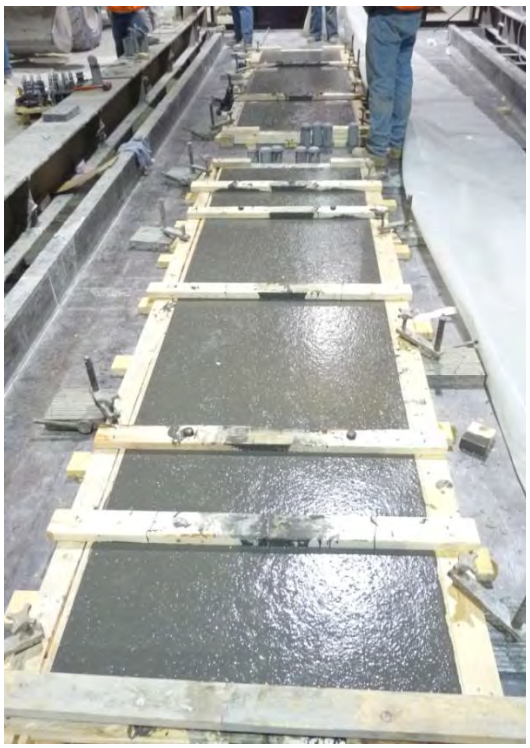

**Figure 4.18: UHPC Panels after Casting**

The HSC components consisted of four columns and a single panel. Custom formwork was created for the columns because of the nonstandard hexagonal shape. Two sets of formwork were built to allow four columns to be cast over two consecutive days. Although custom formwork was used for the test specimens, precast plants would likely fabricate reusable formwork to greatly reduce costs and construction times. Figure 4.19 shows the column formwork and steel reinforcement prior to casting. The process used to construct the HSC panel was similar to the UHPC panel construction. In order to create the void needed for the UHPC wet joint connection, Styrofoam was attached to the sides of the formwork as shown in Figure 4.20 and removed after curing. Standard practices were followed during the casting of both the HSC columns and panels. The concrete was vibrated to improve consolidation, and immediately covered with wet burlap and plastic. Unlike the UHPC panels, the HSC components were not subjected to any form of thermal treatment after casting. All seven test components were left disconnected and delivered via flatbed trailer to the Iowa State University structures lab.

**Figure 4.19: In-Plane Test Column Formwork**

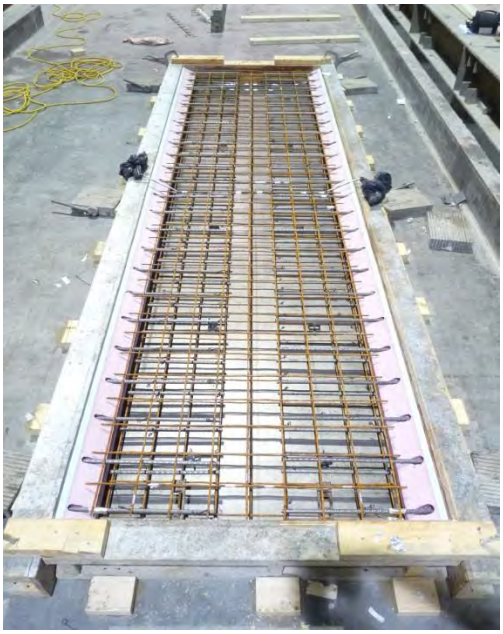

**Figure 4.20: In-Plane Test HSC Panel Formwork**

The foundation block, which would be used to anchor the test specimens to the laboratory strong floor, was constructed at Iowa State University. It was designed to remain uncracked during testing with the use of post-tensioned bars. This limited the effects deflections of the foundation block would have on those of the test specimen. Figure 4.21 and Figure 4.22 show the layout of the steel reinforcement and post-tensioning duct as well as the cast specimen. The horizontal ducts shown on the sides of the block are to accommodate a bar stressed to 100 kip (445 kN). The vertical ducts used to fasten the block to the strong floor, will each contain a bar stressed to 200 kip (890 kN). An impression of the columns and panel was made on the top of the block to allow for the creation of an epoxy pad underneath the columns. This was done to ensure uniform contact between the bottom of the columns and anchor block. Two channels running the width of the block and located directly underneath each column provided access to the vertical post-tensioning anchorages used in each column.

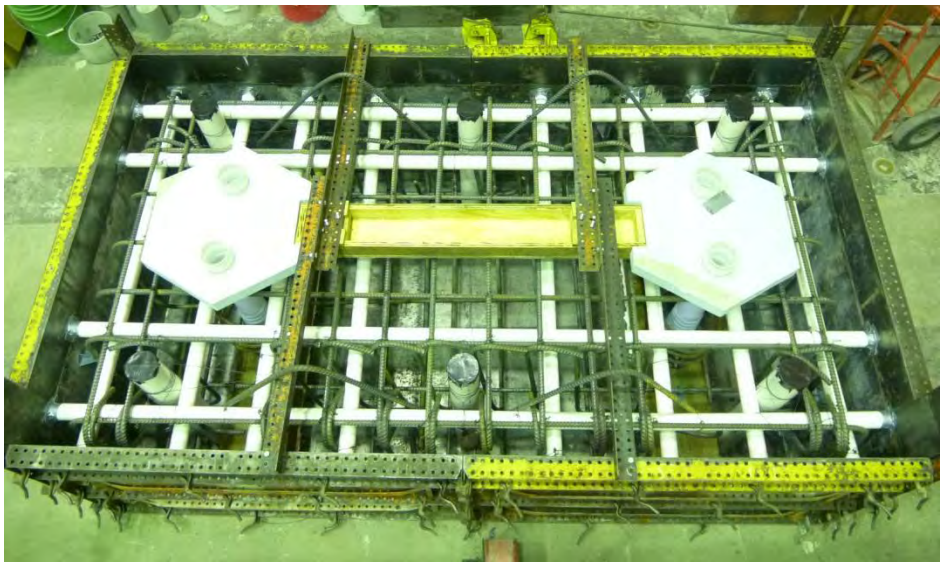

**Figure 4.21: Foundation Block Formwork**

**Figure 4.22: In-Plane Test Foundation Block**

### 4.3.2 Component Assembly

The procedures used to erect each of the test units have been included to provide a reference for future construction. Many of the techniques used in the lab were chosen based on their applicability to the complete tower construction on site. Overall cost and erection times were considered when determining what materials and methods would be used.

*HCUP-BC Specimen*

The HCUP-BC specimen was erected horizontally on the lab floor. The columns were set in the correct position forty inches apart, after which, the bottom angled plates were attached. The panel was then lifted into place, and lowered onto the angled plates. The top angles were then attached and bolted to both the columns and panel. All bolts were hand-tightened prior to setting the specimen in its upright position. As mentioned in Chapter 3, the bolts running through the panel were designed using a slip-critical connection between the angled and embedded plates. In order to ensure the proper pretension of 51 kip (227 kN) was applied to each bolt, Squirter Direct Tension Indicators (DTI) were used. They eliminate the need for hydraulic torque wrenches or load cells to verify the tension on the bolt. Instead, the correct tension is achieved when a designated amount of paint is ejected from pockets within the washer. This allowed for the use of a torque multiplier, which reduced the overall erection cost. Figure 4.23 illustrates the ejected material after proper tensioning has been reached. The

center washer, in this configuration, is the Squirter DTI. Using this process, the proper tension was applied to the panel bolts.

**Figure 4.23: Squirter Direct Tension Indicator**

Throughout the design and construction process, concerns were raised as to whether the tolerance required to utilize bolted connections would be insufficient in a precast application. For the specimen erected in the lab, this was not an issue; however, during the construction of a complete tower, tolerance issues would likely arise at some locations along the tower. For this reason, some modifications should be made to bolted connection, if used in the complete tower, to increase the allowable tolerance to those set forth by the Precast/Prestressed Concrete Institute. These values can be found in PCI (2004).

Once the specimen was fully erected, it was placed on top of the foundation block. Sika 31, Hi-Mod Gel was used at the interface between the foundation block and columns to ensure full contact. To prevent spalling of the cover concrete at the base of columns, the epoxy was only placed underneath the confined region of the columns. A Styrofoam ring was created to limit the epoxy to this region (Figure 4.24). Once the epoxy was placed within the ring, the test specimen was lowered onto the foundation block. In order to allow the specimen to be lifted off the foundation block after testing with minimal damage, a thin layer of adhesive plastic was placed on the bottom surface of the column. The prevented the epoxy

from bonding to the column, which in turn allowed the specimen to be removed after vertical post-tensioning was released.

**Figure 4.24: Placement of HCUP-BC Specimen on the Foundation Block**

Post-tensioning of the columns was completed using a multi-stage process in order to prevent the development of flexural cracks due to the eccentricity of the two tendons in each column. Three stages were to be used that required each tendon be stresses to 20%, 70%, and 100% of the total load. After completing the 20% load stage, the stresses were found to be significantly below the targeted values. This was a result of higher than expected seating losses after using the power seating feature on the hydraulic jack. An alternative stressing procedure was adopted. This procedure included one additional stage at 85% load. The final stress values on the tendon can be seen in Table 4.2. In total, the specimen was within 3% of the targeted prestress value of 1312 kip (5836 kN).

**Table 4.2: Final Column Post-tensioning Load for HCUP-BC and HCUP-HPT**

| Tendon | Load per Tendon kip (kN) | Load per Column kip (kN) |
|---|---|---|
| NE | 360.5 (1604) | 705.5 (3138) |
| SE | 345.0 (1535) | |
| NW | 335.7 (1493) | 646.1 (2874) |
| SW | 310.4 (1381) | |

*HCUP-HPT Specimen*

Assembly of the HCUP-HPT specimen took place in a slightly different manner then the other two specimens. Because it utilizes the same two columns as the HCUP-BC specimen, the bolted panel was removed after completion of the test and subsequently replaced with the HPT panel (Figure 4.25). This eliminated the need to replace and retension the vertical tendons in the columns.

In order to ensure uniform contact between the column and panel over the entire area of the interface, Sika 31, Hi-Mod Gel was used. The panel was cast at a width of 38.5-in. (97.8 cm), which provided a ¾-in. (1.91 cm) gap between the columns and panel. After the panel had been placed in the correct position between the columns, the gap was filled with epoxy (Figure 4.25). The high viscosity of the epoxy prevented it from slumping during placement. By observing the interface gap surrounding the flat post-tensioning ducts, it was determined that sufficient contact between the precast components was achieved.

**Figure 4.25: Placement of HCUP-HPT Panel and Interface Epoxy**

The horizontal post-tensioning was completed using a pair of 60 ton hydraulic jacks. Each 0.6-in. (1.52 cm) diameter strand was stressed to 165 ksi (1140 MPa). This resulted in a

total tendon force of 143 kip (636 kN). The outside two strands shown in Figure 4.25 were stressed simultaneously followed by the inside two strands. A test was completed prior to post-tensioning to approximate the seating loss in the horizontal tendons. By doing this, the final post-tensioning force was assumed to be within close proximity to the target load.

*HCHP-UHPC Specimen*

In order to simulate field conditions, the UHPC wet joint specimen was erected in the upright position. The columns were first set upright with a clearance of forty inches between their inside faces. The panel was then placed between the two columns, forming the voids that would later be filled with UHPC. As shown in Figure 4.8, the width of the void within each column is different. The column void with the reduced width was designed to allow the panel to come in direct contact with the outside face of the column. This created an enclosed void that reduced the amount of material needed to seal the joint. The larger column void was designed to allow the panel to slide into the column a short distance to insure the proper column spacing was achieved. A larger volume of material was required to completely seal this joint.

Sikadur 31, Hi-Mod Gel epoxy was used to seal the joints at all four corners of the panel along its height. Because of its high bond strength, it also prevented the columns from separating due to the internal pressure of wet UHPC during casting. The fast setting time of the material allowed for the placement of UHPC within 8 hours. Figure 4.26 shows the erected specimen prior to UHPC placement.

**Figure 4.26: UHPC Wet Joint Specimen Assembly**

The UHPC was mixed at Iowa State University using a portable mixer. Two batches were used to allow time for the UHPC to settle into the joints thereby eliminating undesirable voids. Self-consolidating concrete is often measured using the slump cone test. For UHPC, it is more widely accepted to use the ASTM C1437 test, which is used for hydraulic cement mortars. The difference is the dynamic aspect of the test that applies a certain number of blows to the flow plate. The dynamic flow tests for both batches resulted in flow diameters of 7.75-in. (19.7 cm). This value was significantly less than the recommended upper limit of 9.5-in. (24.1 cm). Although this increases the viscosity and can potentially lead to reduced flow rates in the joint, it also reduces the possibility of fiber segregation when placed.

Prior to placement, the walls and dowel bars within the joints were moistened to eliminate absorption from the UHPC. Eight inch high wooden boxes were placed directly above each joint to make casting easier and increase the head pressure at the top of the joint (Figure 4.26). During placement of the UHPC, volumes of each bucket were measured to

verify the correct amount of UHPC was used. Using this information, checks were made at various times during casting to ensure the level of UHPC matched predictions. This process was used to alleviate the development of large voids. Minimal rodding was also used for this reason. The strength of the UHPC joint material was 12.3 ksi (84.8 MPa) at the time of testing.

After removal of the HCUP-HPT specimen from the foundation block, it was found that the epoxy pad used at the base of the column was not damaged. It was determined that the same grout pad would be used to support the final HCHP-UHPC specimen. The same process used for placing the HCUP-BC specimen on the foundation block was used with some modifications. The adhesive plastic was not placed on the bottom of the column, which allowed a new ¼-in. (0.64 cm) lift to bond to the bottom of the columns. 1/8-in. (0.32 cm) grooves were also ground into the existing pad to improve shear resistance (Figure 4.27).

**Figure 4.27: Epoxy Pad Modification for HCHP-UHPC Specimen**

The multi-stage post-tensioning process used on the HCUP-BC specimen was once again used. With data from the previous test, seating losses were appropriately accounted for. The final post-tensioning load on each tendon is presented in Table 4.3. The load on each column is within 0.25% of the target load of 656.2 kip (2919 kN).

**Table 4.3: Final Column Post-Tensioning Load for the HCHP-UHPC Specimen**

| Tendon | Load per Tendon kip (kN) | Load per Column kip (kN) |
|---|---|---|
| NE | 339.8 (1512) | 663.7 (2952) |
| SE | 323.9 (1441) | |
| NW | 329.7 (1467) | 671.3 (2986) |
| SW | 341.6 (1520) | |

During the post-tensioning process, cracking in the panel was observed at the 70% load stage. The crack, shown in Figure 4.28 continued to extend throughout the remainder of the post-tensioning process. The crack extended down the center of the panel 30-in. (76.2 cm) at a maximum width of 0.025-in. (0.64 mm) at the top. The development of a crack in this location was a result of non-uniform compression of the specimen. In additional to crack development on the top of the panel, cracks were also observed at the bottom of the panel (Figure 4.28). The cracks had significantly smaller widths than the top crack, and only extended 8.0-in. (20.3 cm) upward. Chapter 5, detailing the analytical results of the in-plane test models, explains the development of large tensile stresses in this region.

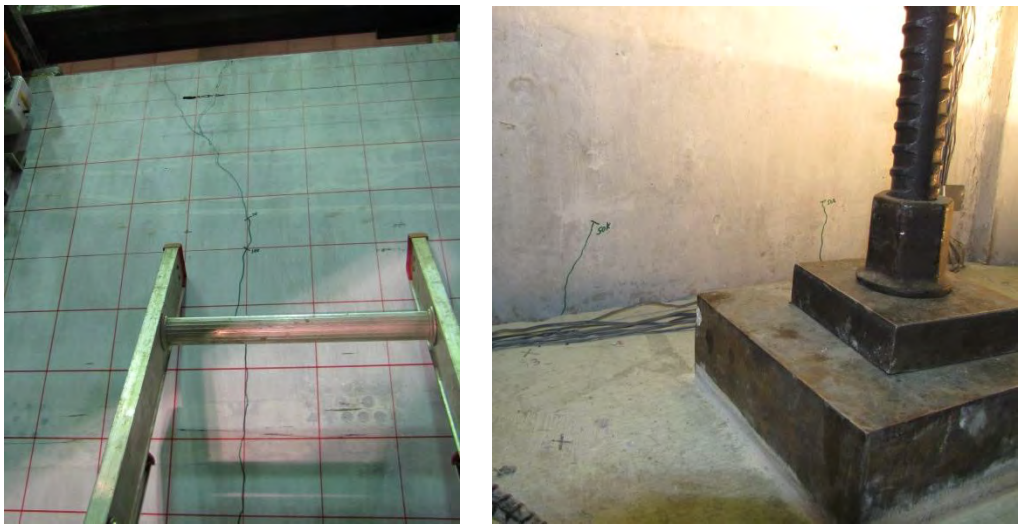

**Figure 4.28: HCHP-UHPC Panel Cracking During Post-Tensioning**

## 4.4 Experimental Results and Observations

The results and observations from each of the three in-plane tests units are presented below. The overall response of the specimen is examined first, followed by an in depth look into the performance of individual components such as the panel, columns, and connections. A comparison between the experimental and analytical results can be found in Chapter 5.

### 4.4.1 HCUP-BC Specimen

The HCUP-BC test configuration can be seen in Figure 4.29. Load was applied to the specimen via a hydraulic actuator tied directly to the HSS sections. These sections were part of the rigid top beam used to distribute load between the columns. They were also used to support the vertical post-tensioning anchors. The tower, shown to the right of the specimen, supported a series of string pots used to measure the deflected shape of the specimen along its height. The tower was tied directly to strong floor to eliminate the effect load frame displacements on the recorded data. Additional instrumentation including strain gauges, DCDT's, and an optical tracker were used to fully understand the behavior of the specimen.


**Figure 4.29: HCUP-BC Test Configuration**

The HCUP-BC test was subjected to a maximum load of 150 kip (667 kN). At the operational load of 102.3 kip (455 kN), the columns remained uncracked along their height, while the connections showed no signs of inelastic behavior. Minimal cracking was detected in the regions of the panel surrounding the embedded connection plates. At the extreme load of 124.6 kip (553 kN), many of the same observations were made. The columns remained uncracked, while crack distribution and extension took place in the panel. Though not visibly apparent, some inelastic behavior was believed to have occurred in the connections based on the overall response of the specimen. At the maximum load level, the panel was the only component showing visible signs of damage. The cyclic hysteretic response of the HCUP-BC specimen is presented in Figure 4.30.

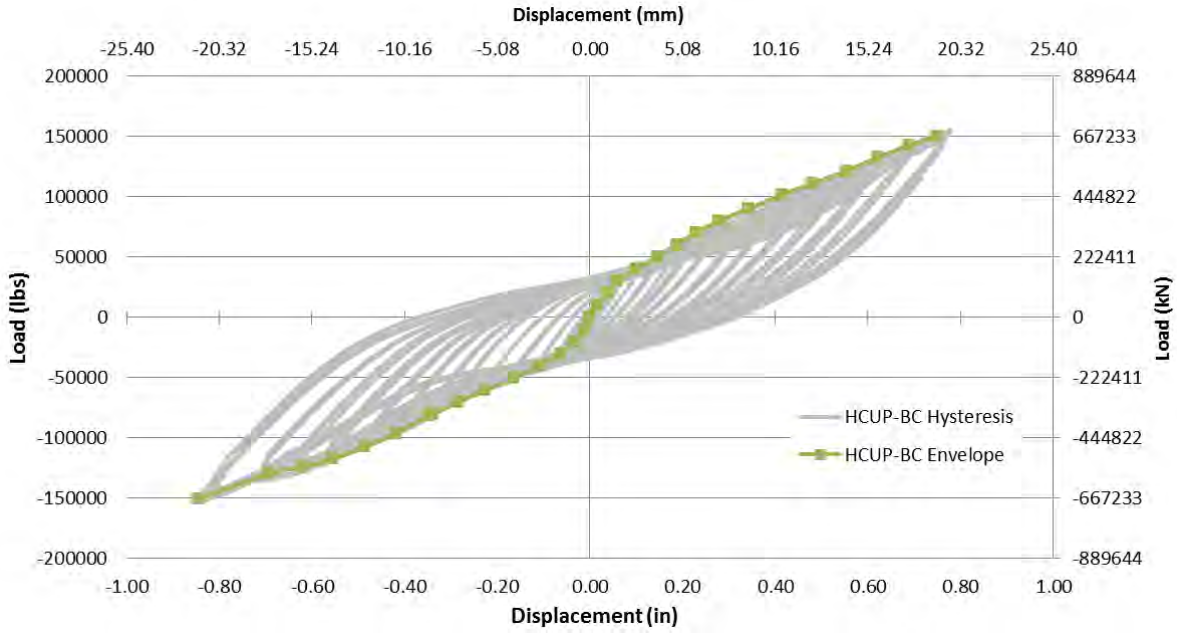


**Figure 4.30: HCUP-BC Cyclic Hysteretic Response**

The high-degree of energy dissipation is believed to be a direct result of both inelastic plate behavior and Coulomb damping. The damping takes place in the slip-critical portion of the connection assembly. As the specimen was subjected to cyclic loading, kinetic friction opposes the direction of motion. Further analysis of the connections confirms the source of energy dissipation by plotting the hysteretic behavior of the connection displacement. This was done using the optical tracker data points placed on the surface of the connection. The horizontal displacement between the two bolt groups, shown in Figure 4.31, represents the separation and closure of the column/panel interface gap at the location of the connection. At

approximately 80 kip (360 kN), significant energy dissipation within the connection initiates. This corresponds to the development of higher energy dissipation in the total hysteretic response of the HCUP-BC specimen. Loops in the horizontal connection response only develop when subjected to tension. During the push, or positive, portion of the load cycle, the entire plate surface in contact with the column supports the load, thereby reducing the demand on the connection.

The vertical displacements between the bolt groups are also shown in Figure 4.32. Although this component of displacement does not contribute as much to energy dissipation, it does confirm the source of noise generated by the specimen during loading. The noise was noticeable at approximately ±40 kip (178 kN). The vertical displacement response shows significant slip within a relatively small load interval at or around the 40 kip (178 kN) load level. The initial vertical displacement response of the connection follows a consistent path during the early stages of loading, up the operational limit state. As load increases from this level, energy dissipation increases. The highlighted cycle in Figure 4.32 illustrates this behavior at the extreme load level.

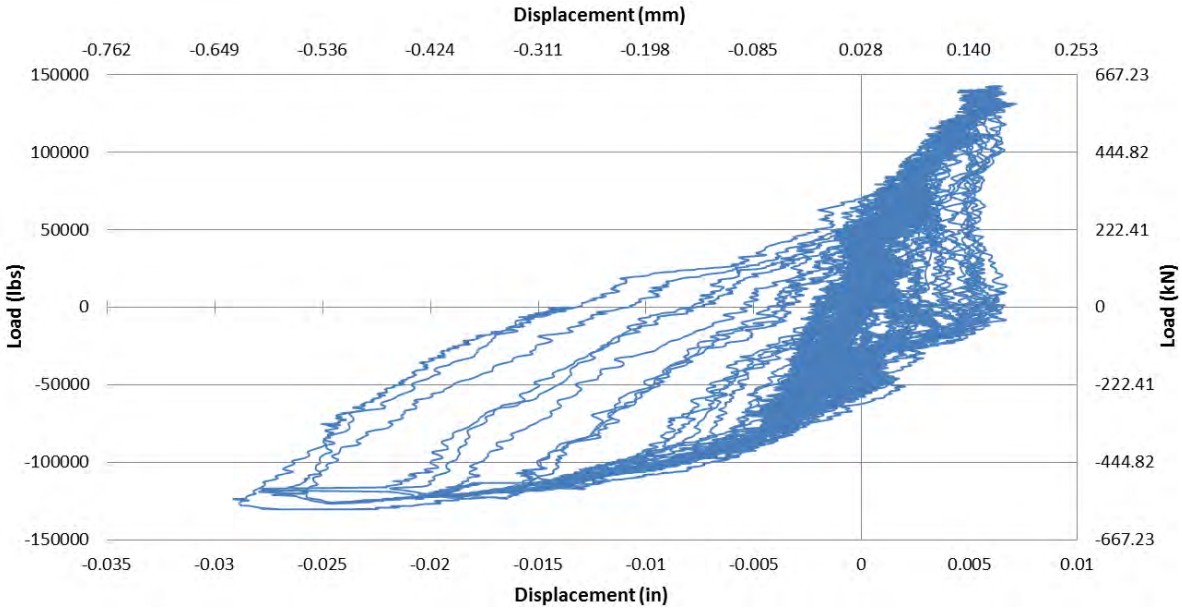


**Figure 4.31: Horizontal HCUP-BC Plate Displacement**

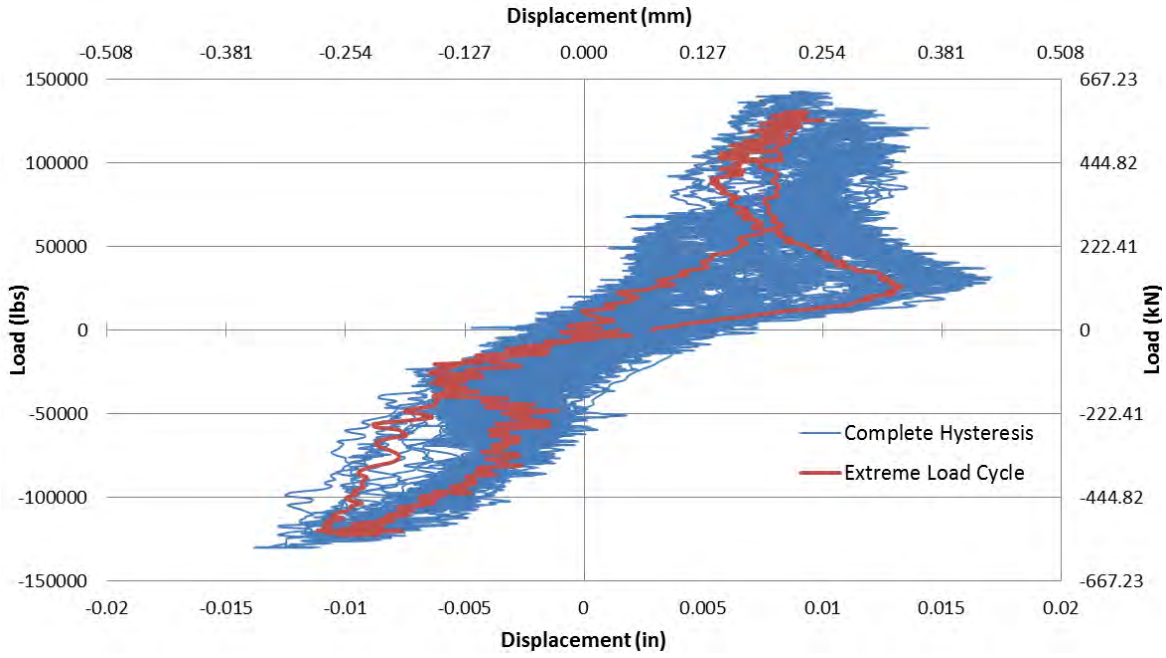


**Figure 4.32: Vertical HCUP-BC Plate Displacement**

By observing the horizontal connection displacement response, some inelastic behavior is suggested. A series of strain gauge rosettes were used on four of the eight connections at the top and bottom of the angled plate. They were placed on the inside surface of the plate near the 90˚ bend. Using the three strain components of the rosettes, principal stresses were determined. The time-history response of the bottom left connection at both the top and bottom of the angled plate can be seen in Figure 4.33. It can be seen that the plate stresses remained slightly below the solid orange line representing yield at 36.0 ksi (248 MPa). This does not correspond with the horizontal plate displacement response, which clearly suggests inelastic behavior exists. The variation is likely caused the by the placement of the strain gauges on the plate. When the angled plate is subjected to horizontal tension, represented by the separation of the column panel interface, the maximum tensile stresses develop on the back face of the plate in contact with the column. This region of the plate was not instrumented due to inaccessibility of the back side, and limited space for the rosettes on the front side. Therefore, it is believed that yielding in the angled plate initiated at approximately the operational load level on the side in contact with the column.

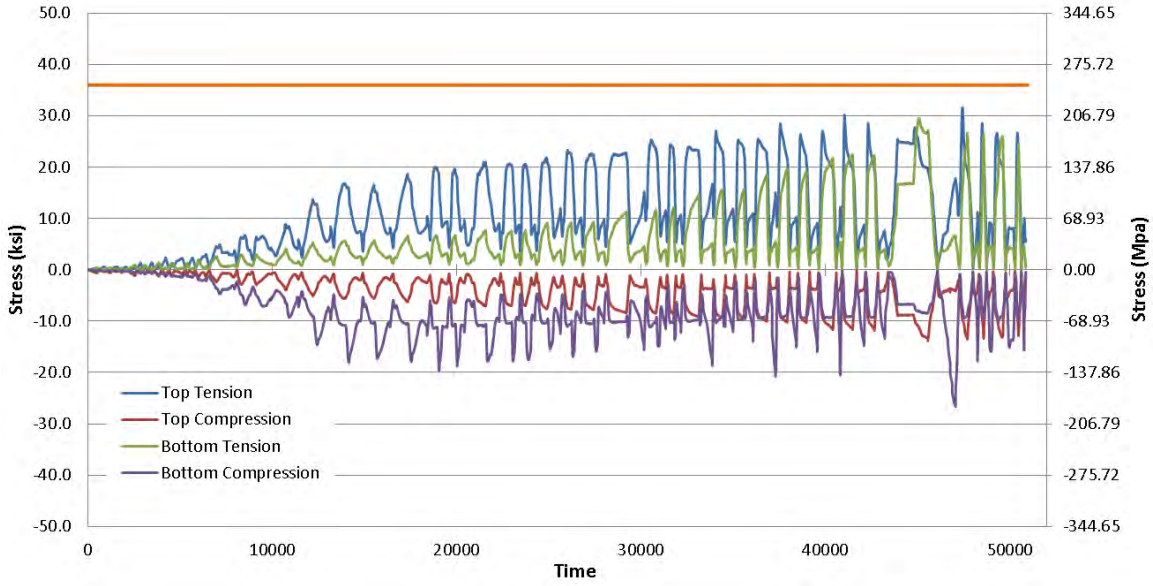


**Figure 4.33: Principal Tension/Compression in HCUP-BC Angled Plates**

The performance of the panel was found to be satisfactory at both operational and extreme limit states. The crack pattern on the back side of the panel at the operational and extreme load levels is shown in Figure 4.34. As expected, the crack angle corresponded to the direction of compression and tension force flow between the connections. The even distribution of cracks surrounding the bolted connections was expected with the use of UHPC components. After cracking takes place, the fibers within the UHPC become fully engaged, thereby improving the capacity of the section. This leads to broader crack distribution in the surrounding regions. Although the number of cracks increases, their widths are significantly smaller than those found in conventional concrete. The crack widths at operational were found to be less than one-hundredth of an inch. At the maximum load level of 150 kip (667 kN), the maximum crack width was observed at sixteen-hundredths of an inch.

After assembly of the HCUP-BC specimen, gaps were observed at different elevations of the interface gap. This was not considered critical, as the designed load capacity did not rely on the contact between the components, but rather the bolted connections. Both sides of the panel, near the top, were in direct contact with the column. During testing, crushing was observed in these regions (Figure 4.35). As crushing took place, the gap at lower elevations began to close, increasing the bearing area between the columns and panel. The damage was

localized in the top two inches of the panel and is believed to have little effect on the total response.


**Figure 4.34: HCUP-BC Operational and Extreme Panel Cracking**

**Figure 4.35: Localized Crushing at Top of HCUP-BC Panel**

No column damage was observed during the entirety of the HCUP-BC test. This included areas surrounding the embedded column plates used in the bolted connections. Both the axial load and moments on each column were recorded using the optical tracking system. Six LED tracking points were used to capture the displacements at three separate depths of the column. This configuration, which was used for all three tests, can be seen in Figure 4.36. By observing the relative vertical displacements between each of the three sets, column moment and axial loads were determined. The three sets of data points also provide a means through

which to examine curvature. When analyzing the data produced during testing, a significant amount of scatter was present. The tracker has the capability of measuring changes in position down to ten-thousandths of an inch; however, when requiring the degree of precision needed to capture small stress variations in concrete, vibrations in the specimen or near the camera can create the type of scatter observed. It is believed that these vibrations, and the distance the camera needed to be placed from the specimen to capture all of the LEDs, are the source of the scatter.

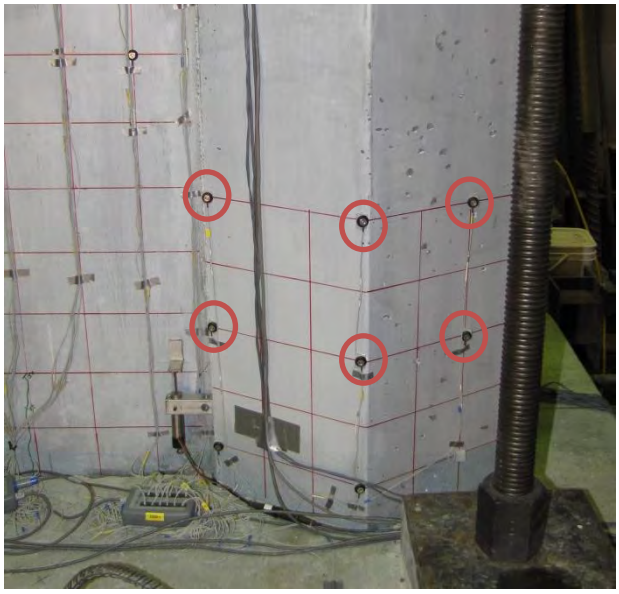

**Figure 4.36: Column Optical Tracker LED Point Layout**

In spite of the presence of scatter in the optical tracker data, the general trend of this scatter was similar to what was predicted in the analytical models. For this reason, trendlines are used to present the data. The bending moments for both the right and left columns are illustrated in Figure 4.37. At the maximum load level, the change in the extreme fiber stress in either column was found to be approximately 2.60 ksi (17.9 MPa). Without the presence of vertical post-tensioning, a significant level of cracking would have developed in the columns. The post-tensioning provides each column with 2.41 ksi (16.6 MPa) of axial compression, thereby allowing the extreme tension fiber to remain in an uncracked state. The change in axial compression or tension on the column is presented in Figure 4.38. In both the bending moment and axial load plots, some of the trendlines appear shifted from their expected zero

load level. For this reason, the data must be used in general terms and not relied upon for accurate measurements at specific load levels.

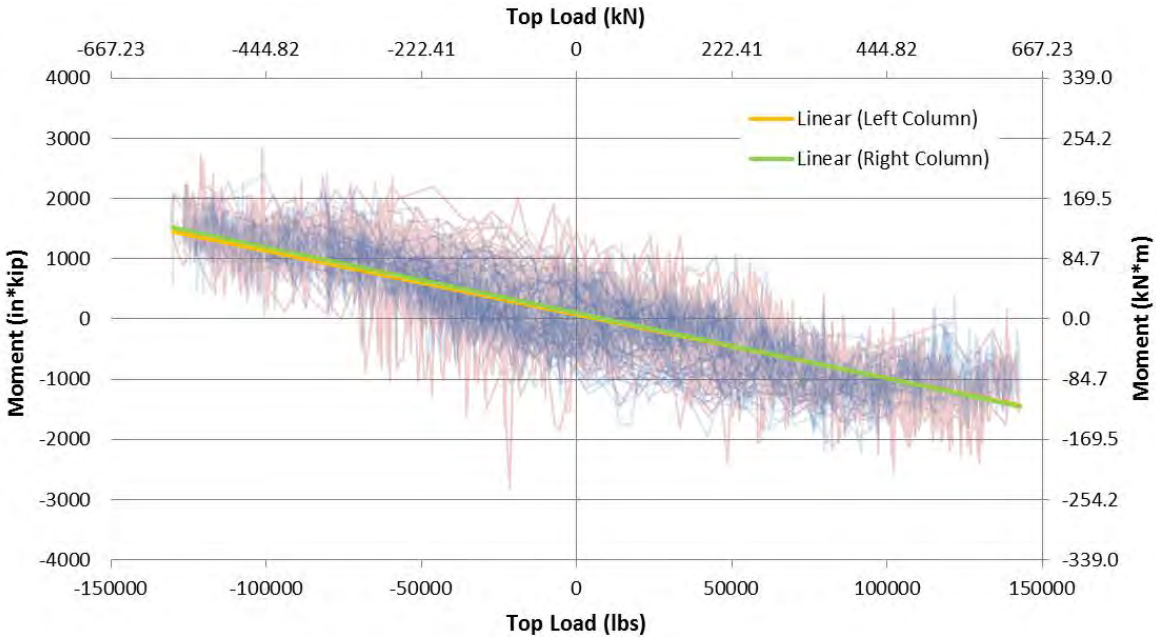


**Figure 4.37: HCUP-BC Column Bending**

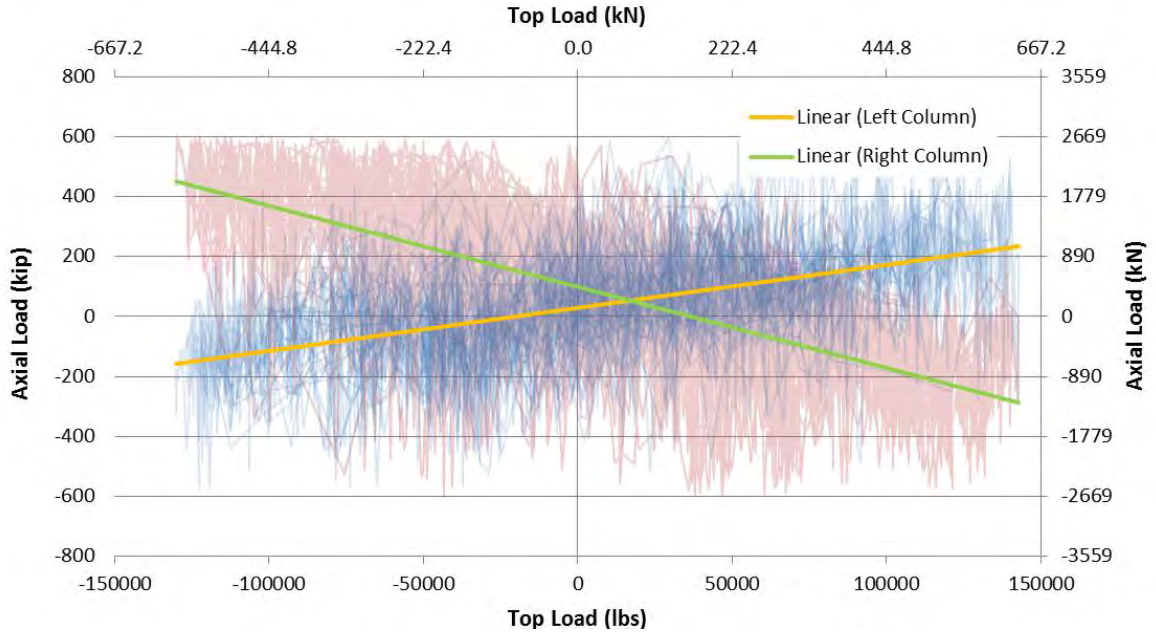


**Figure 4.38: HCUP-BC Column Axial Load**

At approximately the ±140 k cycles, instrumentation at the base of the column began detecting significant changes in horizontal displacement (Figure 4.39). The cause of the

movement was found to be a result of slip of the entire specimen on the epoxy pads used to create uniform contact between the columns and foundation block. It is believed that the adhesive plastic, used at the base of the columns for the purposes of removing the specimen, significantly reduced the friction between it and the foundation block. To verify this, plastic adhesive was not included on the HCHP-UHPC specimen. The presence of slip did not appear to affect the overall response of the test specimen, but does highlight the importance of using roughened surfaces when relying on friction to resist shear between components in the complete tower.

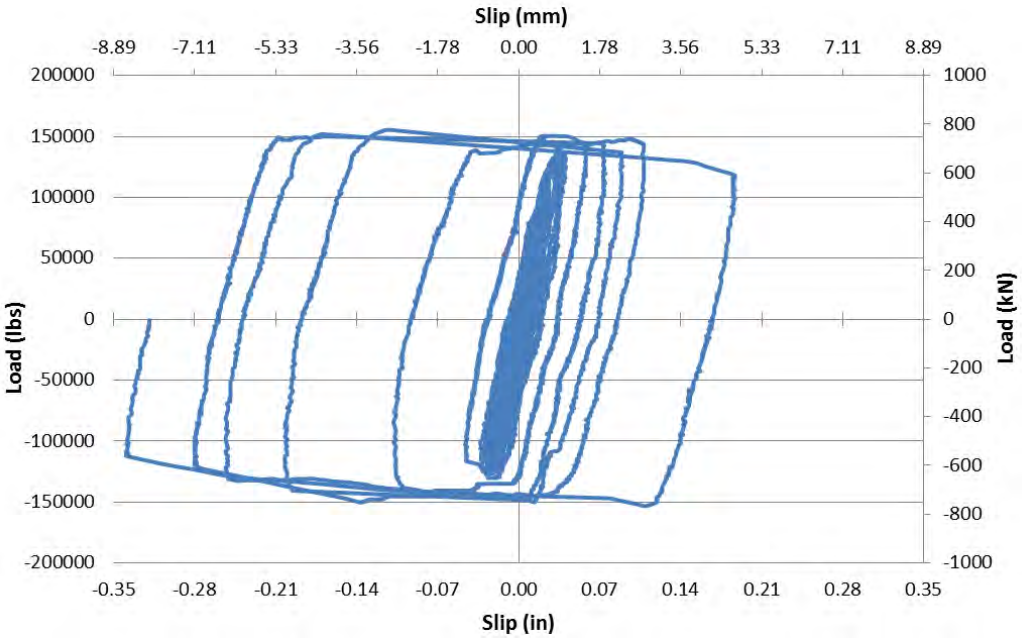


**Figure 4.39: HCUP-BC Specimen Slip on Foundation Block**

The displacement profile of the HCUP-BC specimen at the positive and negative peaks of the load cycles can be seen in Figure 4.40. The deflected shape was measured from the outside face of the right column. During positive loading, the deflected shape at the maximum load level shows a linear profile. The drift at both the operational and extreme limit states was measured at 0.26% and 0.35% respectively over the twelve foot height of the specimen. In the negative direction, the column shows a higher degree of curvature along its height. The recorded drift values were found to be 0.28% at operational and 0.39% at extreme. The variation in drift during positive and negative load application is believed to have been caused by the variation of load distribution to each column. During the positive

load sequences, the panel acts to transfer much of the load between columns, whereas the top beam is more effective during the negative loads.

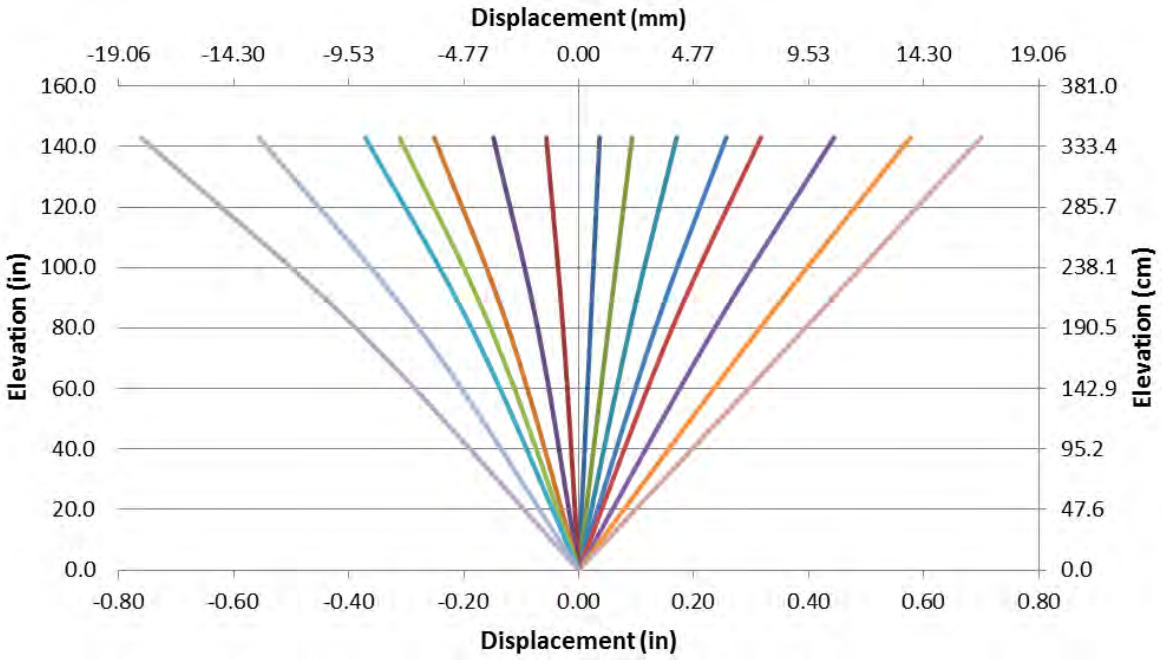


**Figure 4.40: HCUP-BC Specimen Bending Profile at Peak Loads**

### 4.4.2 HCUP-HPT Specimen

The layout of the HCUP-HPT test was nearly identical to that of the HCUP-BC test shown in Figure 4.29. The instrumentation layout was also similar with the exception of a few additional DCDT's at the column/panel interface to measure slip, and a more distributed LED layout. The specimen was tested to a maximum load level of 150 kip (667 kN). Throughout the entirety of the test, including the operational, extreme, and maximum load levels, there were no visible signs of damage in any component of the specimen. The interface between the columns and panel did not appear to slip outside of a localized region, suggesting the horizontal post-tensioning adequately increased its capacity. The overall linear behavior of the specimen is well illustrated by the cyclic hysteretic response presented in Figure 4.41.

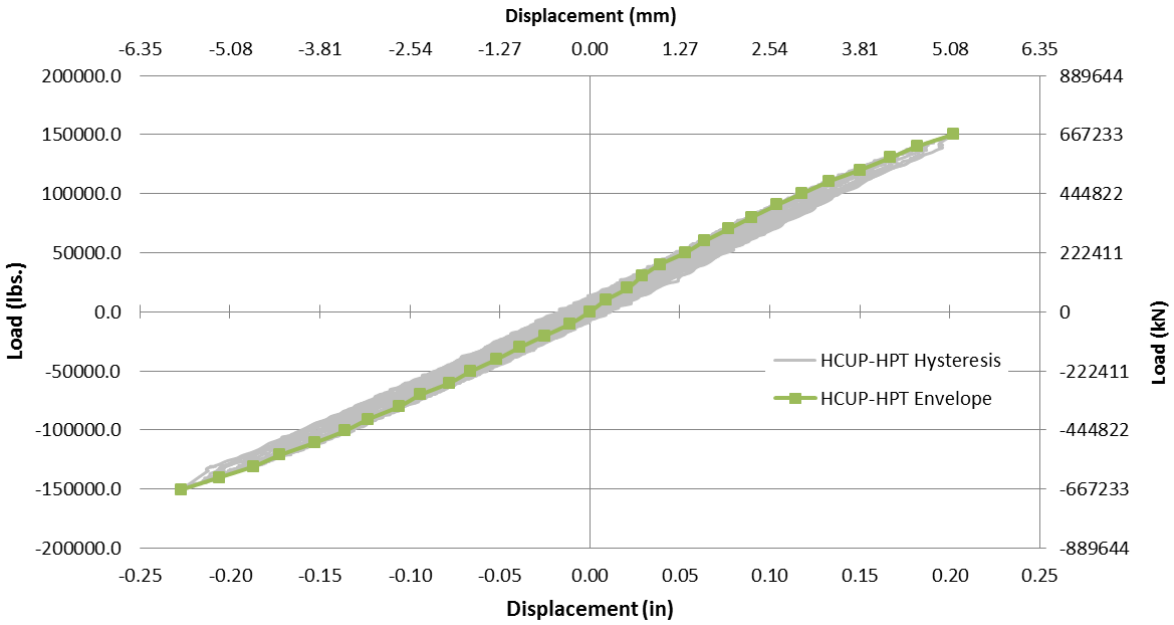


**Figure 4.41: HCUP-HPT Cyclic Hysteretic Response**

Using a series of DCDT's, slip was measured at the top, center, and bottom of both interfaces. The top left portion of the interface experienced significantly higher slip than what was recorded at the other five locations. At the operational load level, separation between the epoxy used to ensure uniform contact at the interface and the column was observed (Figure 4.42). Separation occurred due to unequal load distribution between the top of the columns during the negative portions of the loading cycle. When pulling at approximately the operational load level, the left column, connected directly to the actuator, experienced a shear demand of 58.7 kip (261 kN). The right column, connected to the actuator through the top beam, experienced 41.9 kip (186 kN) of shear. Assuming the system acts as a monolithic section, the shear reaction at the base of the columns will be equal. In order to evenly distribute the loads at the top of the columns when pulled, horizontal tensile stresses develop in the top portion of the panel. The tensile stress required to distribute this load, exceeded the bond strength of the HSC columns and epoxy, thereby separating the interface down to the uppermost horizontally post-tensioned tendon location. A maximum slip of 0.012-in. (0.30 mm) was recorded at the peak load level of 150 kip (667 kN) in the upper left region of the interface. During the positive load, slip was limited to 0.002-in. (0.05 mm), which was consistent with the other interface measurements.

The failure mechanism of the HCUP-HPT specimen was designed for slip along the entire interface. ACI 318 (2008) provides various friction coefficients for determining the shear capacity between two concrete components. A friction coefficient of 1.0 was used for the interface design. This corresponds to an interface in which fresh concrete is cast against hardened concrete. Given the use of an epoxy between the components, it was believed this coefficient would most accurately represent the capacity of the interface.

Slip was expected at the extreme limit state given the amount of horizontal post-tensioning that was applied. This was not the case, however, as no signs of slip were observed at the extreme or maximum load levels outside of the localized region at the top of the specimen. When ignoring the strength reduction factor of 0.75 used in the design of the interface, the capacity increases to a level capable of supporting a horizontal top load of 165 kip (734 kN). This, in combination with the improved bond strength of the epoxy to concrete, is believed to have prevented interface slip at and above the extreme load level. Even with the improved capacity of the interface, the ultimate capacity of the specimen is still governed by slip between the components.

Based on the observed performance of the HCUP-HPT specimen, the amount of horizontal post-tensioning can be reduced. By reducing the strands to 0.5-in. (1.27 cm) in diameter, while maintaining the spacing used in the test, interface slip is expected to occur at the extreme load level. The reduction in strand diameter would not only reduce the material costs, but also improve the flexibility of the strands. This would make placing them around the perimeter of the tower an easier and less time consuming process.

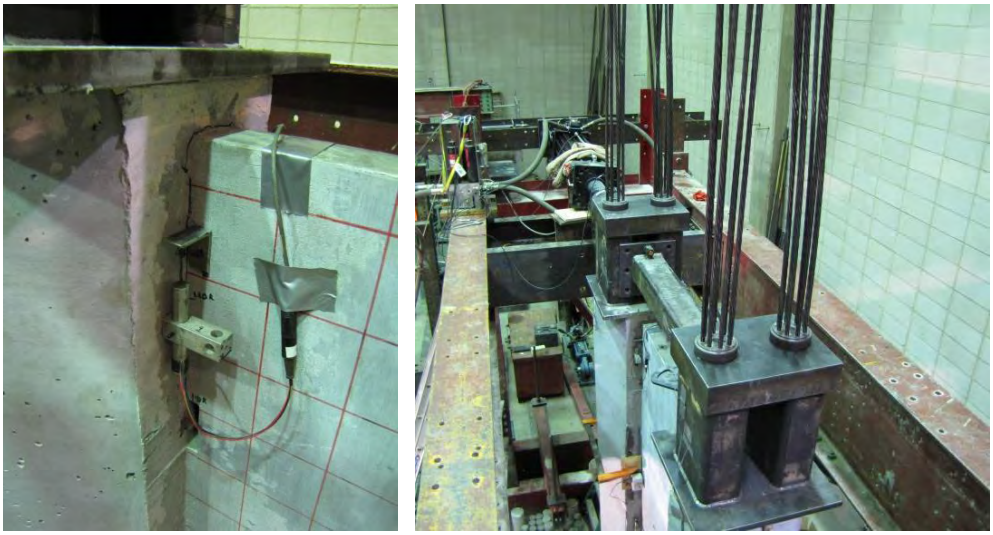

**Figure 4.42: HCUP-HPT Interface Separation**

Figure 4.43 illustrates the condition of the HCUP-HPT specimen at the operational and extreme load levels. As mentioned, no visible signs of damage were observed during the entirety of the test with the exception of localized interface separation.

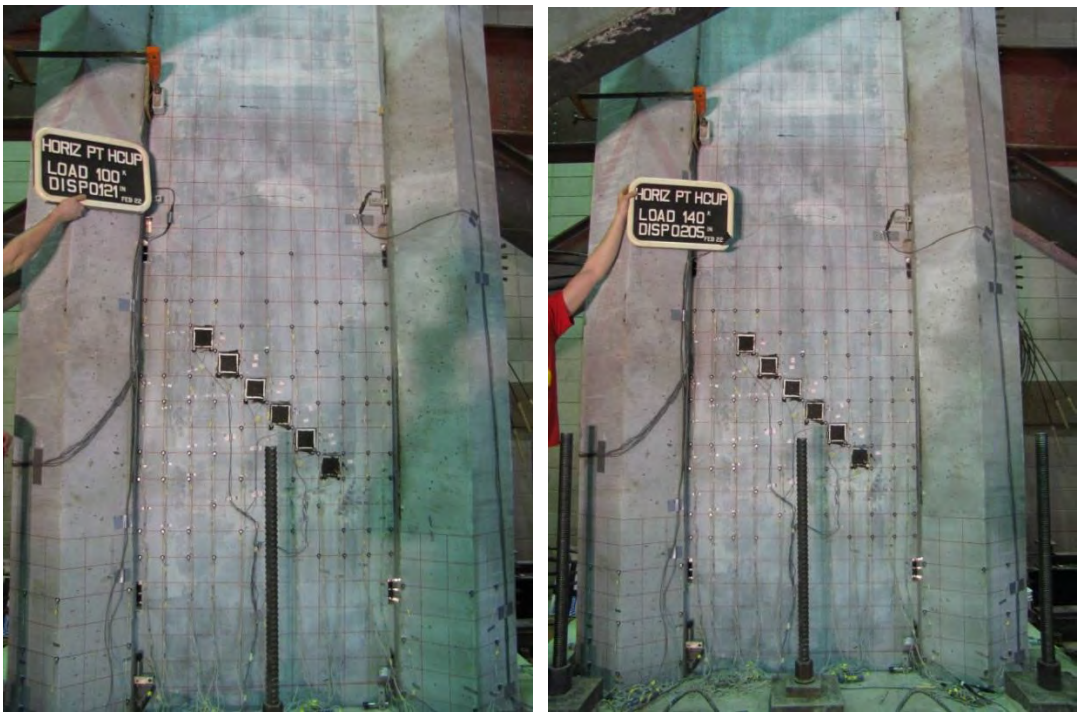


**Figure 4.43: HCUP-HPT Performance at Operational and Extreme**

The changes in the axial load level and bending moment of both columns is presented in Figure 4.44 and Figure 4.45. When compared to the HCUP-BC specimen, it can be seen that the magnitude of the bending moment is significantly lower in the HCUP-HPT specimen. This can be contributed to the interface connection used. The bolted connection only secures the columns to the panel in four distinct locations. The interface above, below, and between, is not prevented from slip or separation allowing each component to act independently. In the case of the HPT connection, slip and separation are prevented by the HPT tendons and the subsequent static friction generated. The result is a more monolithic response at each elevation, limiting the magnitude of bending moments in each column. As expected, the axial load response of the test unit was similar to that of the HCUP-BC test.

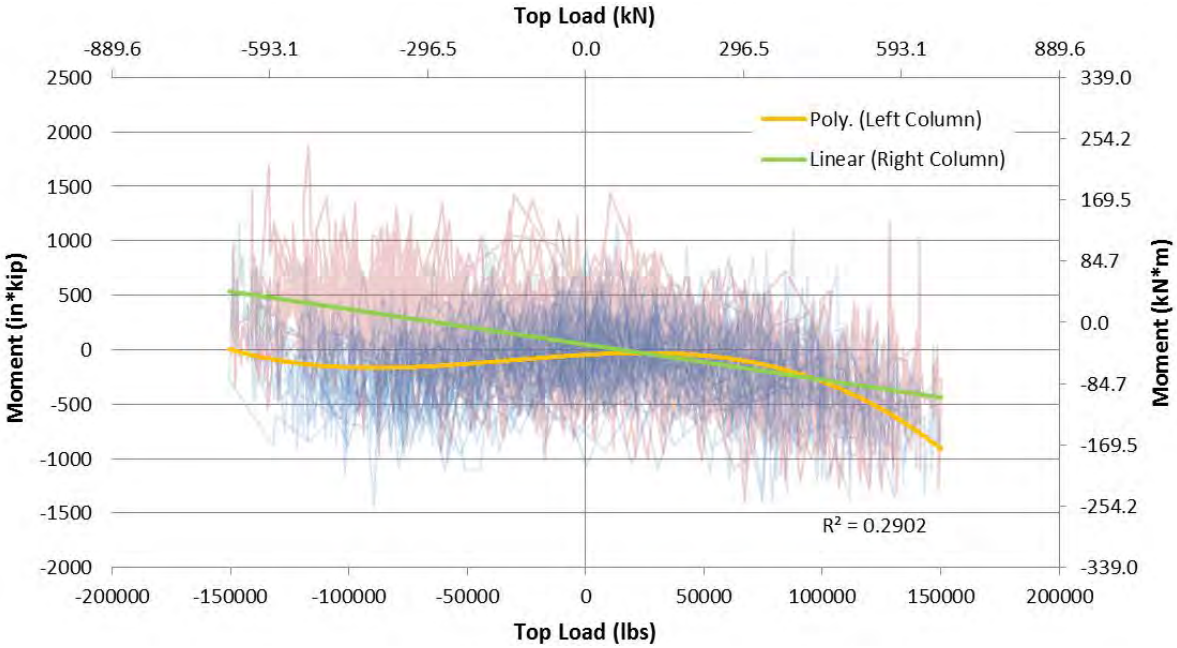


**Figure 4.44: HCUP-HPT Column Bending**

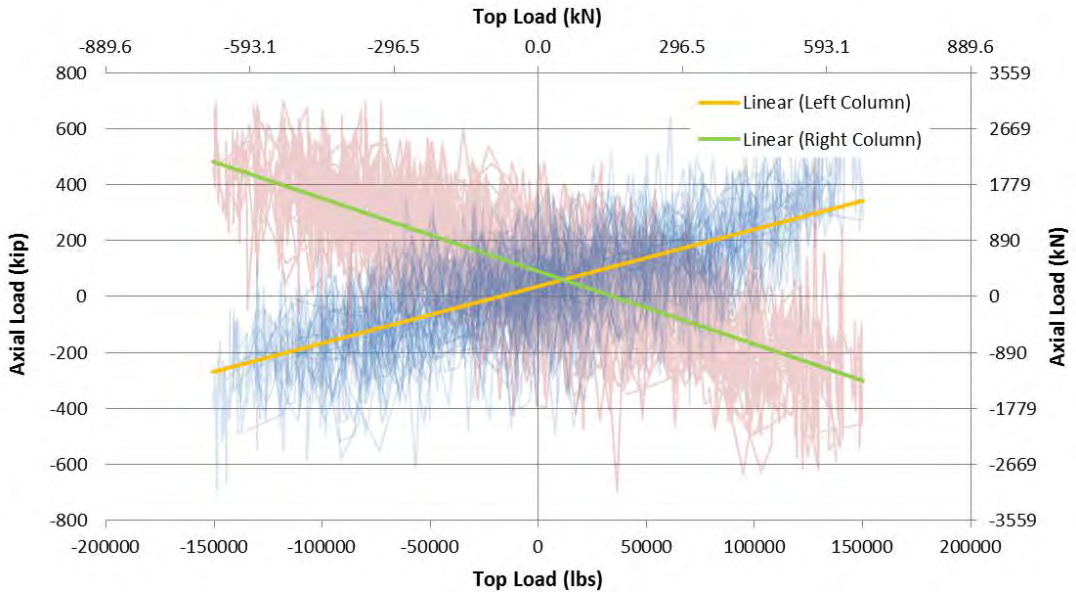


**Figure 4.45: HCUP-HPT Column Axial Load**

The displacement profile of the test unit along it height is illustrated in Figure 4.46. The response in both the positive and negative directions is very similar. The curvature of the profile suggests the two columns and panel are acting as a single monolithic unit. The recorded drift in the positive loading direction was 0.075% at operational and 0.110% at extreme. In the negative loading direction drift values for the operational and extreme were 0.085% and 0.105% respectively.

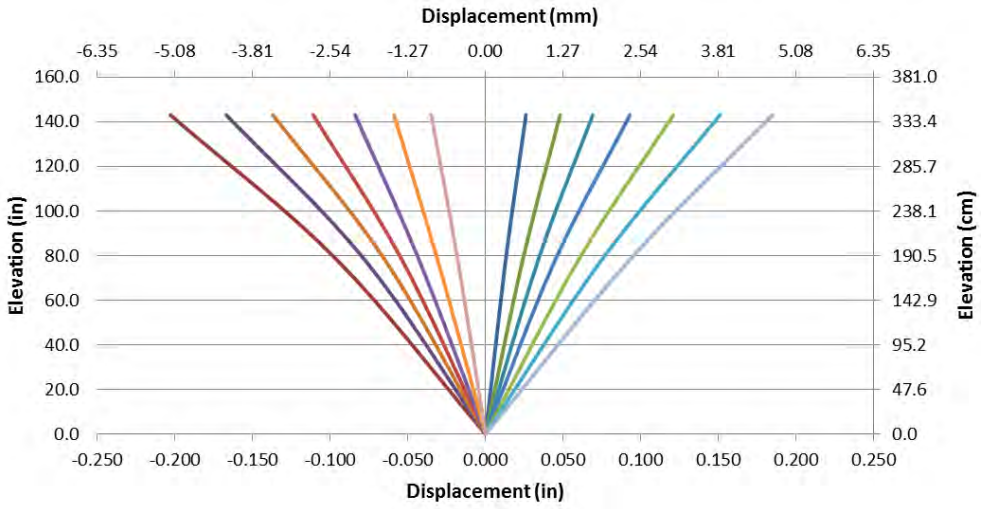


**Figure 4.46: HCUP-HPT Specimen Bending Profile at Peak Loads**

### 4.4.3 HCHP-UHPC Specimen

The HCHP-UHPC specimen, consisting of two HSC columns and a six inch thick HSC panel, was loaded to a maximum value of 170 kip (756 kN) in the positive direction and 163 kip (725 kN) in the negative direction. The capacity of the actuator limited the load magnitude in the negative direction. A higher maximum load level was applied to this specimen because it was the last of the three test units. The foundation block, which was designed to withstand 150 kip (667 kN) on the test unit, was not needed for any further testing.

The overall stiffness of the specimen was very comparable to the HCUP-HPT specimen. In addition to the cracking observed after post tensioning, discussed in the construction section of this chapter, further cracks developed at the operational and extreme load levels. The effect of cracking on the cyclic hysteretic response of the specimen can be seen in Figure 4.47. The stiffness in the negative loading direction was found to be approximately 20% less than what was found in the positive loading direction.

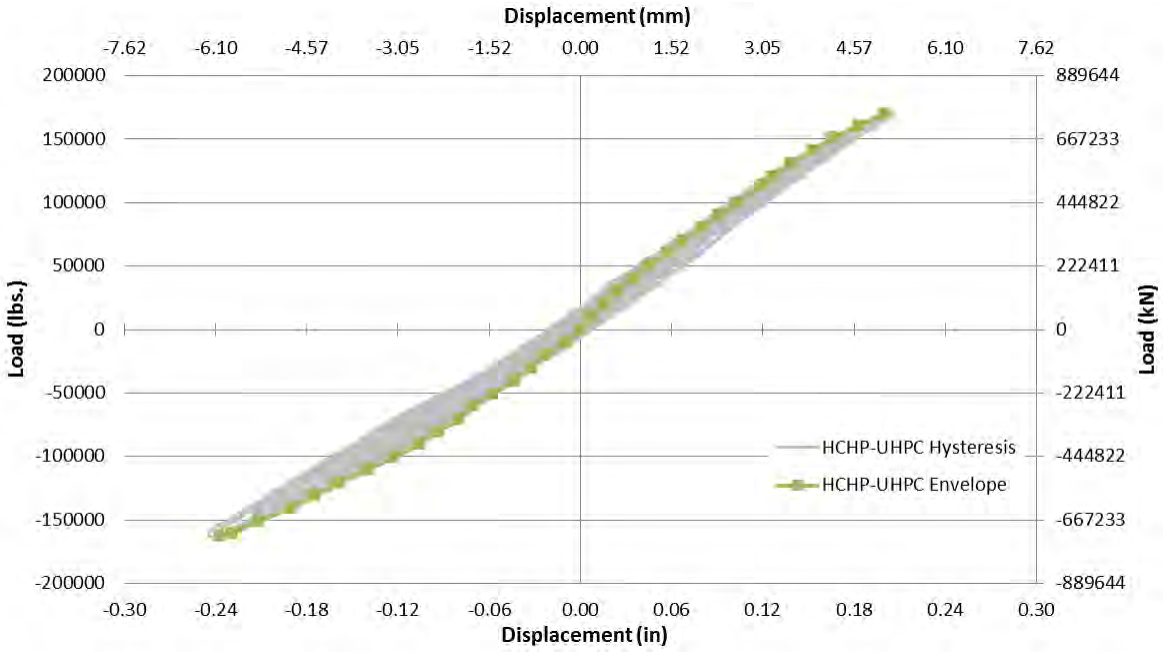


**Figure 4.47: Cyclic Hysteretic Response of the HCHP-UHPC Specimen**

Crack development within the panel is believed to be a result of stresses generated by the horizontal in-plane loading in combination with the permanent tensile stresses created during vertical post-tensioning of the columns. At the operational load level, minimal crack

extension was observed on the primary crack created during post-tensioning. Near the top of the panel, a shift in crack directionality above the operational load limit suggested the diagonal force transfer from the horizontal top load was becoming more critical. As the extreme load level was reached, the effect of the in-plane loading was prevalent by the by observing further crack extensions. Figure 4.48 illustrates the shift in the direction of the cracks from operation to the extreme load level.

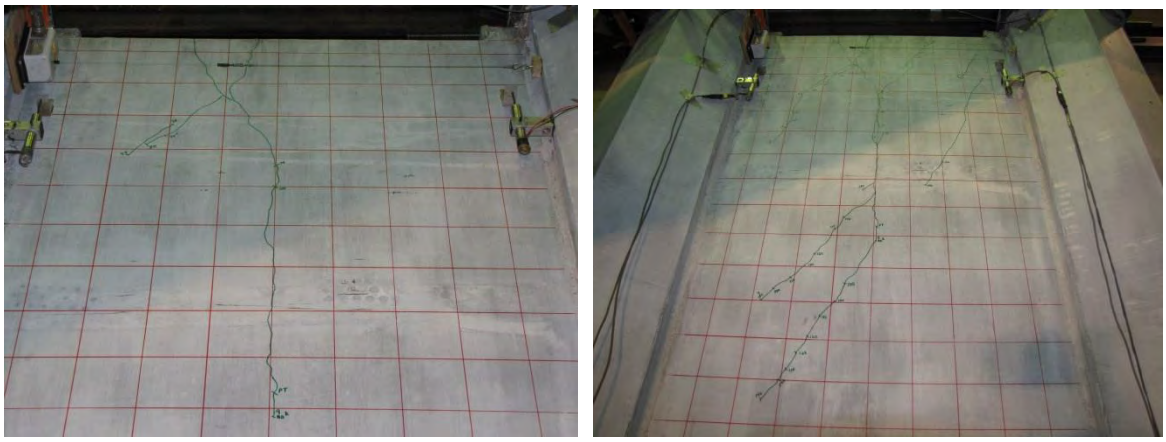

**Figure 4.48: HCHP-UHPC Panel Performance at Operational and Extreme Loads**

**Figure 4.49: HCHP-UHPC Panel Performance at Maximum Load Level**

The performance of the UHPC wet joint was found to be excellent at the operational, extreme, and maximum load levels. The cracks observed in the panel terminated when reaching the edges of the panel partially composed of UHPC (Figure 4.49). Strain gauges

were placed on both the column and panel dowel bars protruding into the joint to better understand the demand at different elevations. The panel dowel bar gauges were located in the HPC panel within one inch of the UHPC wet joint. The largest strain values were recorded at the top and bottom of the specimen. The response of the bottom dowel bar remained linear throughout the test with little variation from its initial response. The two top right dowel bars, however, showed deviation from their initial response shown in Figure 4.50. The deviation was not a result of inelastic behavior, rather, the development of a crack in the panel near the interface. The crack is not believed to have penetrated into the UHPC wet joint, thereby diminishing its performance. The remaining dowel bars in the column and center portions of the panel saw small strain variations suggesting no damage to the wet joint.

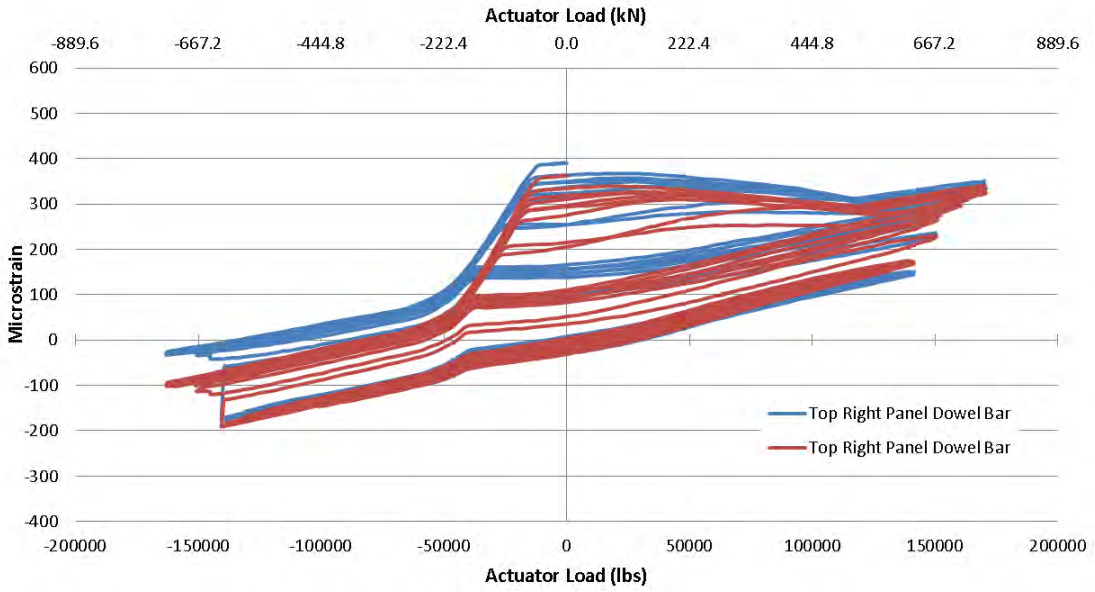


**Figure 4.50: HCHP-UHPC Top Panel Dowel Bar Response**

As expected, the trendlines generated for the moment demand in the columns as a function of horizontal top loading, were very similar to those of the HCUP-HPT specimen (Figure 4.51). Both specimens utilized connections restraining the entire length of the column/panel interface. This, in turn, improved the performance of each individual component by relying on the monolithic section properties of the combined section.

The axial load variation shown in Figure 4.52 is consistent with the expected results at the bottom of the columns based on the theoretical moment demand. In this plot, as well as

some of those previously generated from the optical tracker data, there appears to be a shift from the expected demand when the top load is zero. In this case, both columns are showing approximately 50 kip (222 kN) of compression. This shift is not as much a function of the trendline generated through the scatter, as it is the original position of each LED prior to loading. Even before testing had begun, the readings from each LED were showing signs of scatter. When the change in position is determined by subtracting the sensors original position from subsequent positions recorded during testing, the overall response becomes heavily dependent on which original position is selected. For the graphs shown, an average of approximately 200 readings at the zero load level was used as the reference point.

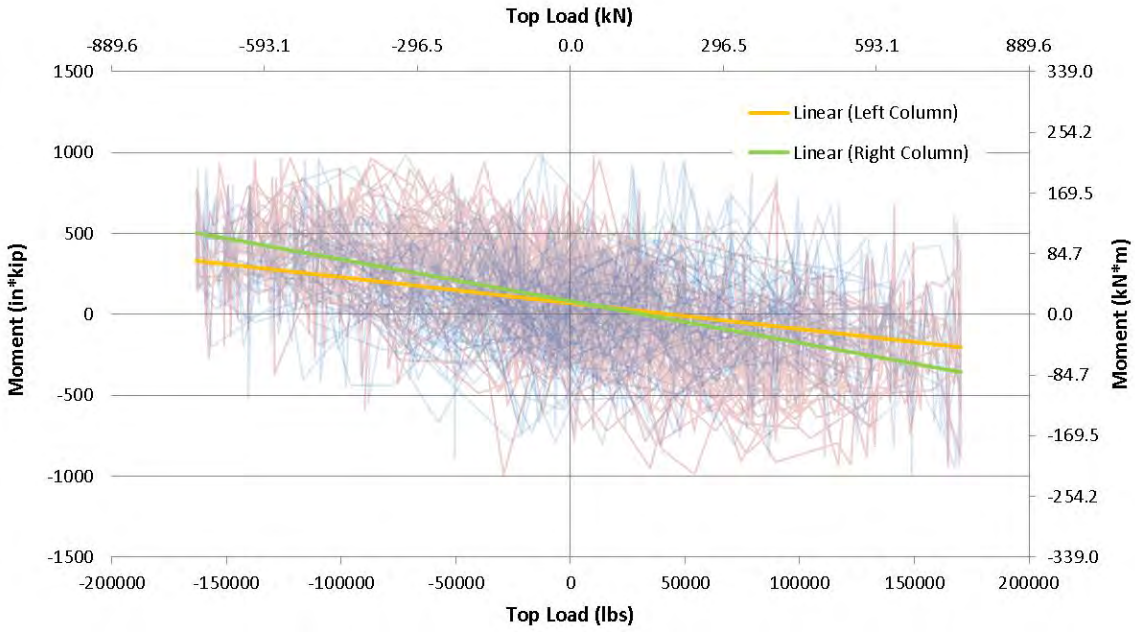


**Figure 4.51: HCHP-UHPC Column Bending**

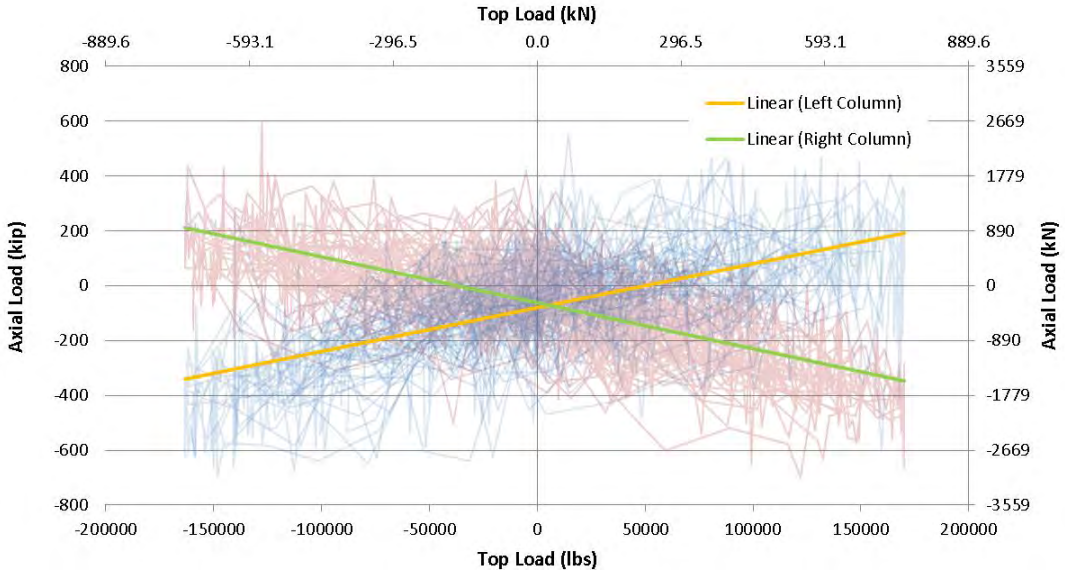


**Figure 4.52: HCHP-UHPC Column Axial Load**

The bending profile of the HCHP-UHPC specimen was slightly higher in the negative loading direction than it was in the positive direction. The discrepancy is likely the results of cracks widening during negative loading and closing during positive loading. The recorded drift values at the operation and extreme load levels in the positive direction were 0.065% and 0.082% respectively. When subjected to negative loading drift values were 0.072% at operational and 0.097% at extreme.

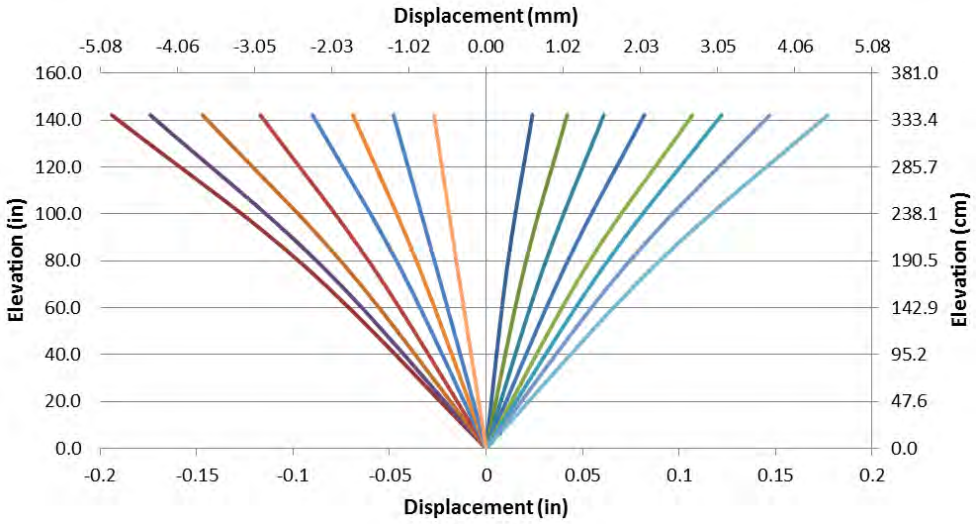


**Figure 4.53: HCHP-UHPC Specimen Bending profile at Peak Loads**

Due to the severity and premature development of cracking in the top and bottom portions of the panel during post-tensioning, modifications to the design were made. Figure 4.54 shows the proposed elevation and cross-sectional view of the HCHP-UHPC panel. The #4 dowel bars were originally designed to meet the estimated demand at the interface. These bars were terminated at the required development length into the panel. The higher than expected horizontal tensile stresses generated during post-tensioning require additional reinforcement in the top and bottom regions. The continuation of the dowel bars from one side to the other provides a significant increase in capacity over the W4 welded wire fabric used in the original design. Although additional horizontal reinforcement is not required in the center portions of the panel, the continuation of the panel dowel bars was used at each location. The relatively small increase in steel cost is believed to be offset by reduced labor costs associated with cutting and placing shorter bars. Even with the continuation of dowel bars across the panel, the top and bottom layer of steel still did not provide sufficient capacity for post-tensioning stresses. An additional #4 bar was bundled with the top and bottom set of dowel bars to meet this demand.

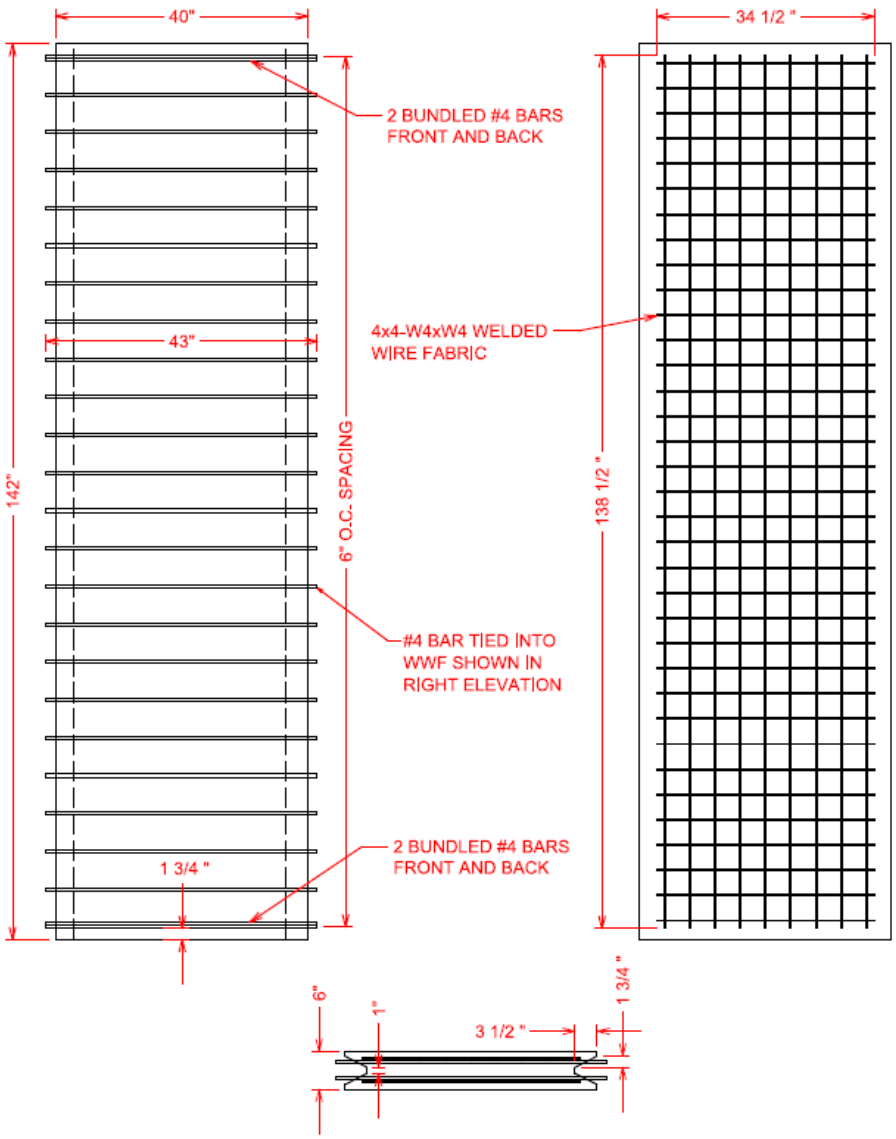


**Figure 4.54: HCHP-UHPC Modified Panel Design**

# CHAPTER 5. MODELING OF THE TURBINE TOWERS AND TEST UNITS

The purpose of this chapter is to describe the development of analytical models for both the complete tower and individual test units. The complete tower model was originally created to better understand the performance of a fully erected tower. The results of this model also assisted in the development of the in-plane test units described in the previous chapter. Using the experimental results, the modeling techniques used in the in-plane test models would be either verified, or require modification to better predict the actual response. Any modification made to the test models would then be incorporated into the complete tower models to improve their reliability.

## 5.1 Complete Tower Model Design

A complete finite element model of the three towers was created to gain a better understanding of how the structures, as well as their individual components, would perform under certain loading conditions. The design of some of the individual components, such as the panels and connections, was based on these analytical results. In addition, some of the general tower properties such as natural frequency and deflection were also obtained.

The model was developed using the finite element analysis software, SAP2000 V.15. This program was chosen for some of the unique features it provides, such as an easy-to-use graphical user interface and a staged construction analysis tool. A centerline model was chosen over a solid model because of the complexities associated with the complete tower model. Because the model itself was often used to design some of the different segments of the tower, its design was constantly evolving. The centerline model made the transition between iterations, a much less time consuming process.

### 5.1.1 Material Properties

Material properties were defined for the HSC, UHPC, and steel post-tensioning tendons. All materials except for the reinforcement exhibited isotropic behavior. The reinforcement was given uniaxial directional symmetry. Both steel and concrete were assigned nonlinear material properties. The nonlinear material properties of UHPC, described in Chapter 2, were used, while the Mander stress-strain curve was used for HSC. Although time-dependent

features are available for both linear and nonlinear materials, they were not included in the analysis. Table 5.1 summarizes the properties used for each material.

**Table 5.1: Material Properties of Analytical Model**

| | Material | | |
|---|---|---|---|
| | **HSC** | **UHPC** | **PT Steel** |
| **$f'_c$ /$f_y$, ksi (MPa)** | 13 (89.6) | 26 (179) | 245 (1690) |
| **E, ksi (GPa)** | 6,500 (44.8) | 7,770 (53.6) | 28,500 (197) |
| **$\gamma$, lb/ft$^3$ (kg/m$^3$)** | 150 (2400) | 155 (2480) | 490 (7850) |

### 5.1.2 Elements

The model included a variety of elements that represented different components of the tower. Two node linear frame elements were used to model the tower columns. To model the taper of the columns along the height, multiple prismatic sections were created. Tendons were used for the post-tensioning running through each column. Although tendons are only defined by two end nodes, they can have an arbitrary curved or segmented shape, as required in the tower model. Link elements were used to model the connections between the columns and panels. The response of links in all six degrees-of-freedom can be assigned by the user. A multi-linear elastic response was used to replicate the response of the bolted connections, derived in ANSYS (Figure 3.14). Two-dimensional, quadrilateral shell elements were used to model the panels of the tower. Multiple layers were created to account for the areas of the panel composed of various levels of steel reinforcement.

### 5.1.3 Model Construction

The use of a centerline model simplified many of the challenges associated with three-dimensional elements. Various locations, however, did required added consideration. One such location was at the interface of the columns and panels. The line elements used to define the columns could not adequately represent their diameter. When considering the cross-section of the tower, the panel width is based on the distance between the faces of the columns parallel to one another. If the shell elements used in the model were connected directly to the frame elements, they would be wider than what was called for in the design. This additional width would increase the overall stiffness of the tower and provide artificial

results. To account for this, rigid constraints were assigned to joints along the frame and edge of the shell elements defining the panel. The constraints were only assigned at the elevations of the links, which represent the connection between the panels and columns. Two constraints were assigned to each column at the link elevations to maintain the gap between both panels. In addition to rigid constraints, zero-tension frame elements were used directly above and below each link. This prevented the panel from closing the gap representing the geometric boundary of the column. Shear, moment, and torsion, were also released in the boundary frame elements, limiting their response to axial compression. The boundary elements were also placed between each connection location. The layout, used for the HCUP model, is illustrated in Figure 5.1. The same layout, shown in the bottom 35 ft, was used along the entire height.

In order to model the connection between the columns and panels, two-joint links were used. This was done so that a number of different connection types could be used for the analysis of the tower. By obtaining the force-displacement response of each proposed connection and incorporating it into the model, the effect of each on the overall tower performance could be assessed. It also provided the load demand on each connection. The links were incorporated into the model by first adding an additional node in the exact locations of each of the nodes defining the vertical edges of the panels. At these locations, there was now a node defining the boundary of the shell elements, and a free node. A two node link was used to connect these two nodes. The duplicated node was then constrained to the columns as previously described. Using this configuration, all loads transferred from the columns to the panels could be quantified, and were dependent on the properties of the link stiffness. The connections were spaced at five foot intervals as shown in Figure 5.1.

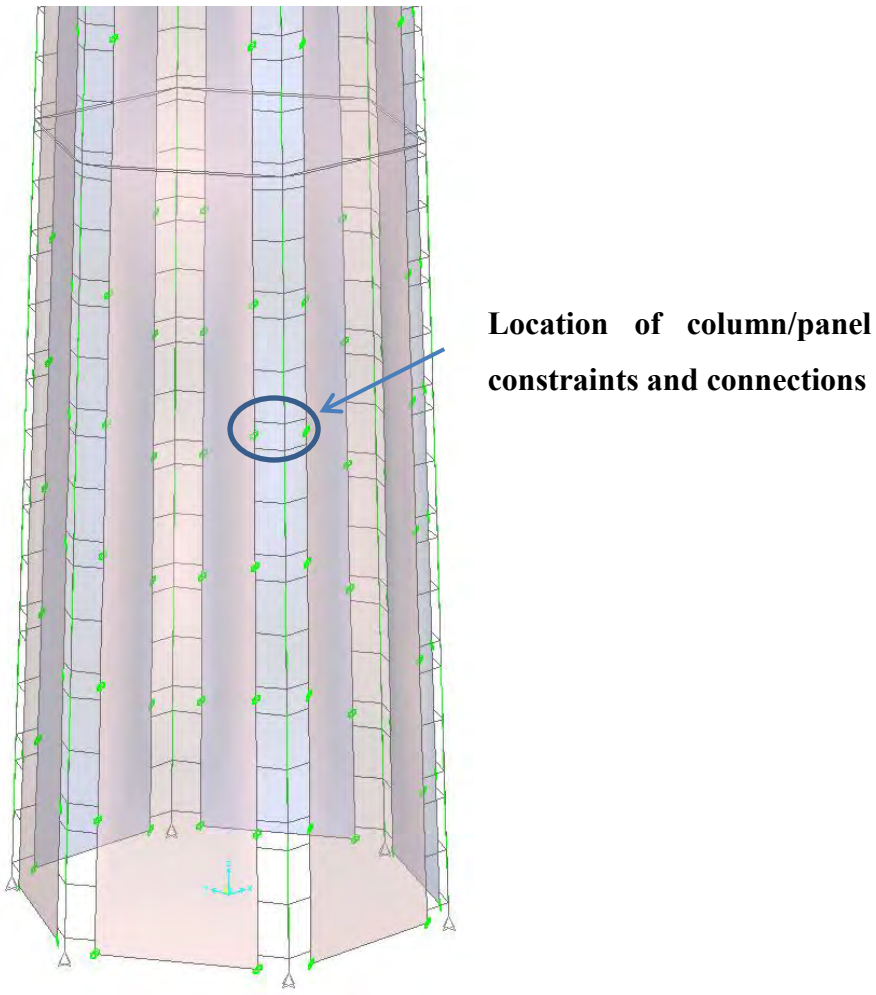


**Figure 5.1: General Layout of Tower Model**

Three tendons were assigned to each column, in order to represent the vertical post-tensioning. The tendons extended from 0-110 ft (0-33.5 m), 0-220 ft (0-67.0 m), and 0-320 ft (0-97.5 m) as specified by the design. The tendons were modeled as loads to allow for losses to be accounted for using an independent analysis. Even during an extreme load condition, the tendons were predicted to remain elastic.

The taper of the columns was accounted for through the use of multiple prismatic sections. A section length of five feet was determined to be adequate based on the degree of taper. The division of the columns into multiple segments also provided a convenient location to constrain the panels to the columns.

Pinned supports were used at the base of the columns. This best represented the tower, because the columns would only be connected to the foundation though the post-tensioning

strands. The base of the panels is not supported by the foundation. In order to model the yaw bearing at the top of the tower, a rigid constraint was assigned to the six nodes defining the tops of the columns. Although the yaw bearing would not provide a perfectly rigid connection between the columns in the tower, it is believed to be a reasonable assumption based on its dimensions.

### 5.1.4 Construction Sequencing

The sequence in which the tower would be erected has a significant effect on the loads acting on each tower component. Two different construction sequences were considered that could be used by the contractor. The first would require the erection of the columns to an elevation of 110 ft (33.5 m), after which they would be vertically post-tensioned. The panels would then be placed between the erected columns to complete the lower portion of the tower. The same process would be used to an elevation of 220 ft (67.0 m) and the tower top. The second conceivable erection sequence would call for the assembly of shorter segments whose height would be determined based on the length of the precast column segments. In this case, the columns and panels would be connected together forming hexagonal segments that would then be erected vertically and post-tensioned. The stage at which the tower is vertically post-tensioned is the reason for the variation of stress throughout the tower. In the first erection sequence the post-tensioning is applied to the columns prior to the connection of the panels. This prevents any of the post-tensioning loads from being transferred by the connections into the panels. This is not the case in the second erection sequence in which vertical post-tensioning is applied after the column panel connection has been established. Both construction sequences are illustrated in Figure 3.6.

SAP2000 has a unique feature that allows user to analyze a structure at different stages of construction. For the complete tower model, this was used to determine how the two difference erection sequences affected the overall stress distribution. The feature, known as staged construction, allows the user to add or subtract elements and/or load patterns from a structure during each stage of the analysis. The member forces that result from each stage's load patterns are included in the analysis of the subsequent stage. In the case of the wind tower, this allowed the columns to be erected and post-tensioned prior to the placement of the panels and connections.

## 5.2 Experimental Test Unit Models

Models of each of the three test units were created for the ultimate purpose of translating the empirical results to the complete tower model. A pre-experimental response of each specimen was found to assist in the development of each unit's loading criteria, as well as the placement of instrumentation in critical regions. Upon completion of testing, the empirical results were compared with those originally predicted by the model. Adjustments were then made to any discrepancies found between the analytical models and test units. These same adjustments were then applied to the complete tower model to improve the predicted response.

### 5.2.1 Model Development

Many of the same procedures used in the development of the complete tower model were used to generate the in-plane test models. Because the sizes of the test models were significantly smaller than the complete tower model, a more detailed analysis could be done. Some of the improvements included a finer panel mesh, as well as the inclusion of nonlinear behavior within the layered shells. Each of the three models created was unique in their overall response, and the response of their individual components.

The HCUP-BC specimen shown on the left of Figure 5.2 uses zero-length link elements with a user defined force-displacement response to model the connection. In order to improve the accuracy of the stress distribution in the panel due to the bolted connection, four links were used rather than a single link used in the complete tower model. The four links represented the four bolts connecting the angled plate to the panel. Each link was assigned 25% of the connection stiffness. The spacing of the compression only frame elements, used to model the geometric constrains of the perimeter of the column, was also reduced to the height of the shell elements to improve the accuracy.

The models created for both the HCUP-HPT and HCHP-UHPC specimens were identical in appearance and can be represented by elevation on the right side of Figure 5.2. Because both specimens relied on the entire interface to transfer load between the columns, links were assigned at four inch increments. The links were then assigned the appropriate force-displacement response for each of the two specimens. The top beam included in all three

models was used to represent the yaw bearing at the top of the tower. It provides load distribution to both columns and is also replicated in the experimental testing described in Chapter 4.

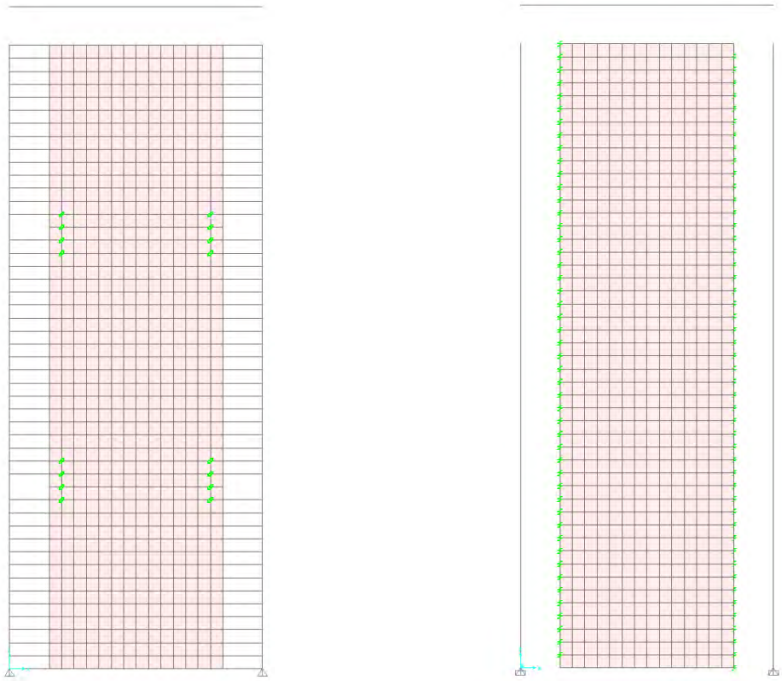

**Figure 5.2: In-plane Test Model Elevation Views**

Layered shell elements were used to model the presence of steel reinforcement within the panels. By observing the HCUP-BC panel details of Figure 4.10, it can be seen that some areas have added reinforcement from the embedded panel plate, while others remained unreinforced. Each shell element of Figure 5.2 was assigned the appropriated level of reinforcement based on this detail. The same was done for the HCHP-UHPC specimen. No additional reinforcement was provided in the HCUP-HPT specimen; therefore, the shell elements only comprised of a 3.0-in. (7.62 cm) thick UHPC layer. Each layer was capable of responding inelastically based on the material properties assigned to it.

To verify the in-plane test models accurately represented the corresponding section of the complete tower model, a comparison was made between the panel stress distribution and connection load demand. Figure 5.3 illustrates the differences between the principal compressive stresses that were predicted for the in-plane test and complete tower at the extreme load level. The stresses found in the complete tower model are a result of the

extreme torsional load case from which the in-plane loads were derived in Chapter 3. When comparing the two models, it was clear that the complete tower model showed higher compressive stresses than the in-plane model. This variation can be contributed to the effect of out-of-plane loading on the panels in the complete tower model. Although this force is relatively small compared to the in-plane loads, it has a more prominent effect due to weak-axis bending. Some stress variation can also be contributed to the reduced vertical post-tensioning used for the in-plane test. Because the panels are in place before vertical post tensioning takes place, the reduction in strands reduces the compressive stress between the connections prior to horizontal top load application.

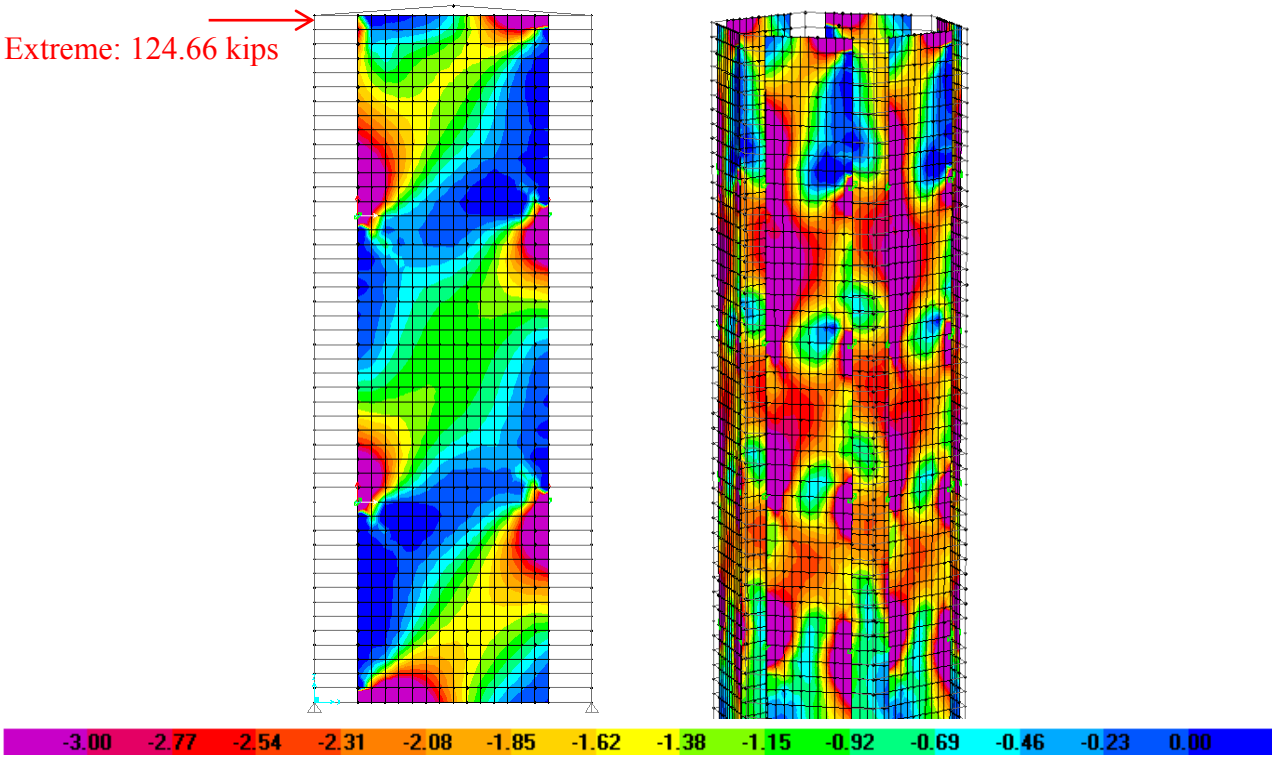


**Figure 5.3: Comparison of In-Plane Test and Complete Model Principal Compressive Stresses**

Figure 5.4 illustrates the differences between the principal tensile stresses predicted to take place in the in-plane test model and full-scale model. The differences are very similar to those found in the principal compressive stresses. This variation can also be contributed to the effects of out-of-plane bending and reduced post-tensioning.

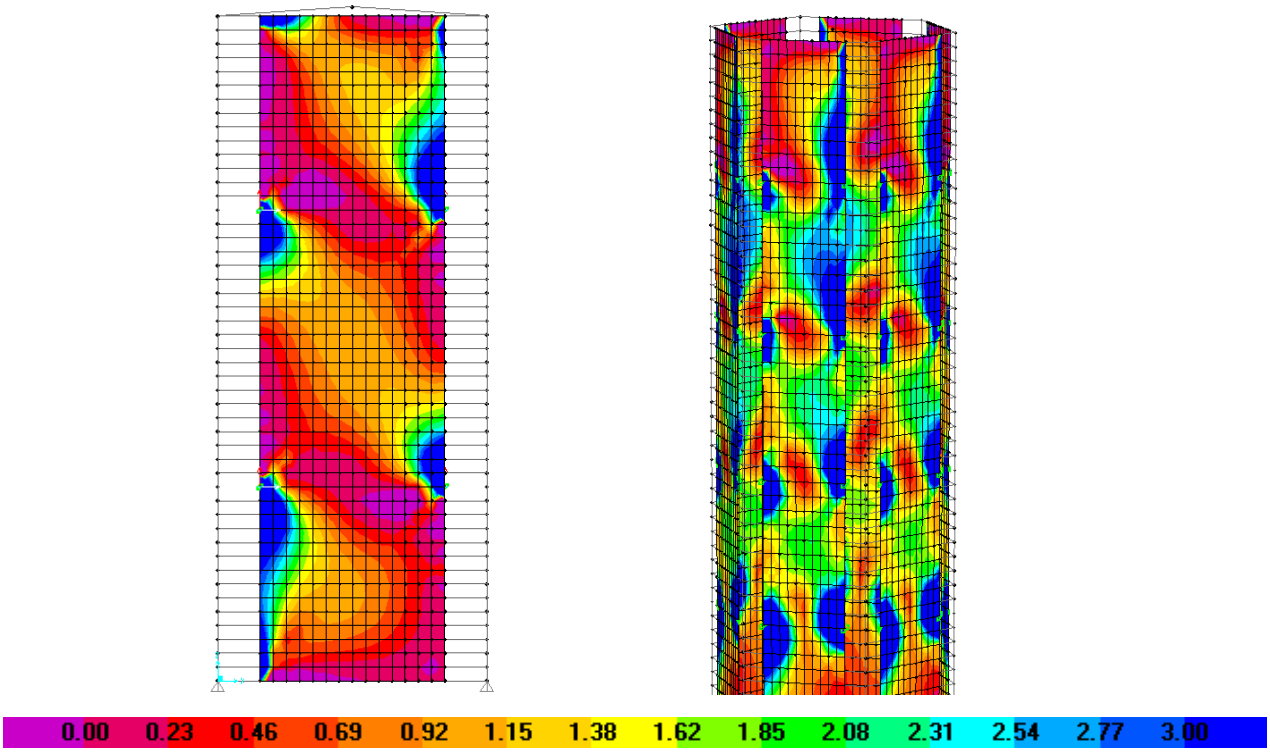


**Figure 5.4: Comparison of In-Plane Test and Complete Model Principal Tensile Stresses**

The vertical shear demand on the connections from both models was also compared. Table 5.2 provides the loads from each of the four connections and compares the summation of the forces on each side of the panel. The connection loads developed in the test unit are very comparable to those predicted to occur in the full-scale model. The comparisons made between the test unit and full-scale model show the adequacy of the test unit in representing a critical section of the complete tower model. By subjecting the in-plane test unit to both the operational and extreme loads, one can determine adequacy of the overall tower design.

**Table 5.2: Comparison of Complete and In-Plane Test Model Connection Loads at the Extreme Limit State**

| | Connection | Test Model Connection Load kip (kN) | Full-Scale Model Connection Load kip (kN) | % Difference |
|---|---|---|---|---|
| Left | 1 | 157.5 (700.8) | 150.7 (670.3) | 4.32% |
| | 2 | 162.8 (724.2) | 155.7 (692.6) | 4.36% |
| **Σ =** | | **320.3 (1424)** | **306.4 (1363)** | **4.34%** |
| Right | 3 | 161.5 (718.4) | 180.3 (802.0) | 10.43% |
| | 4 | 157.3 (699.7) | 166.7 (741.5) | 5.64% |
| **Σ =** | | **318.8 (1418)** | **347.0 (1544)** | **8.13%** |

### 5.2.2 Analytical Results and Comparisons

The following, describes the response of the analytical models for each of the three specimens. Using these models, stress distribution within the panels at the operational and extreme limit states, as well as axial and moment demand on the columns will be presented. Comparisons will then be made with the empirical response of each specimen to both understand the observed behavior of the experimental tests and verify the model designs.

*HCUP-BC Analysis*

The analytical response of the specimen was found to be heavily dependent on the characteristics of the bolted connections. At the operational limit state, the connections were expected to experience minor inelastic behavior as shown in Figure 3.14. The magnitude of this behavior increased as loads escalated to the extreme limit state and beyond. In addition to inelastic behavior in the connections, the panel was also predicted to crack diagonally between the connections. This behavior was found to be very consistent with that observed in the experimental tests. As a result, the overall force-displacement response of the analytical model represented the observed response very well. No changes to the in-plane test or complete tower models were required. Both the analytical and experimental force-displacement responses of the HCUP-BC specimen can be seen in Figure 5.5. The predicted behavior at the operational and extreme limit states is also included.

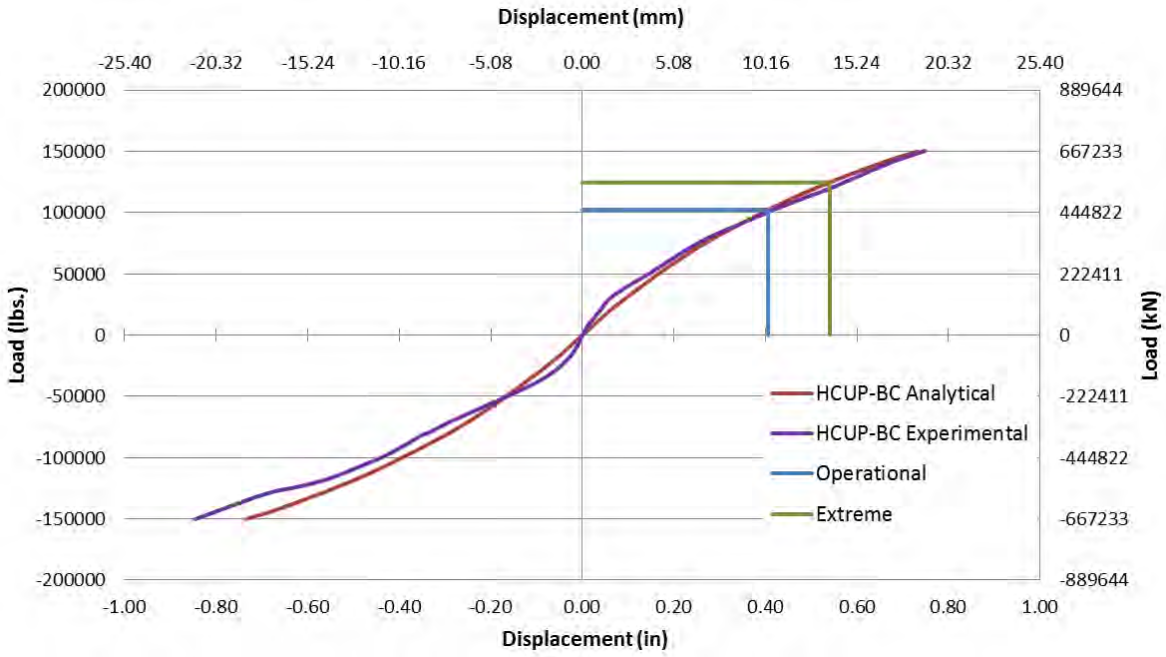


**Figure 5.5: HCUP-BC Force-Displacement Curve**

Post-tensioning for the HCUP-BC specimen took place after the column and panels were connected. This resulted in some of the column post-tensioning load being distributed to the panel between the bolted connections. Because the panel is not supported by the foundation at the base, the entirety of the vertical post-tensioning load is transferred into the foundation through the columns. By subjecting this region of the panel to compression prior to horizontal loading, principal tensile stresses are reduced, making for an improved section. The bolted connections, however, will experience a permanent load at a magnitude of approximately 60 kip (267 kN) per connection. This corresponds to 30% of the connection yield capacity. As seen in Figure 5.6, only the region of the panel between the top and bottom connections experiences axial compression due to the post-tensioning. Outside of these regions, little to no, stress develops.

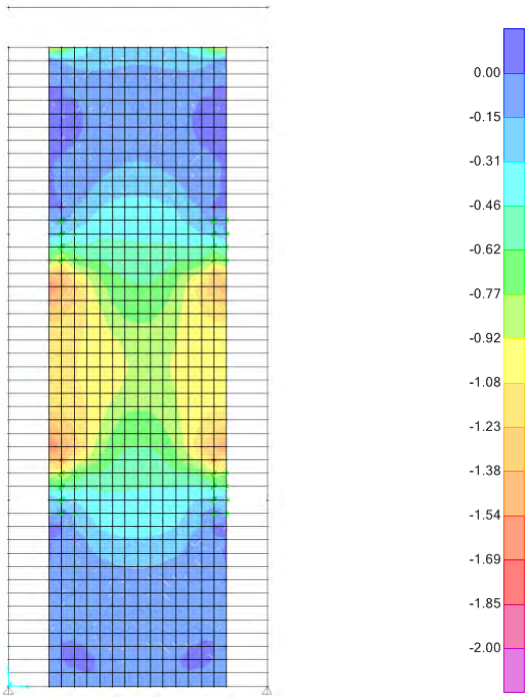


**Figure 5.6: HCUP-BC Analytical Stress Distribution after Post-Tensioning**

The principal tension stress distribution within the panel, as suggested by the analytical model, is illustrated in Figure 5.7. By observing the stress magnitudes at each limit state, it can be seen that microcracking was expected around the embedded panel plates. Some of the modeling techniques used lead to the development of high concentrated stress regions. These areas, which typically surround the nodes used for the connection links, are not believed to accurately represent the expected performance in these areas. Directly outside of these regions, however, stress distribution is believed to be accurate. As expected, compression and tension load paths develop within the four connections of the specimen. Additional paths also form outside of this connected region. Panel cracking, as a result of experimental testing, can be seen in Figure 4.34. By understanding the stress levels associated with cracking in UHPC, a general comparison between the experimental and the analytical models can be made. The magnitude at the operational, extreme, and maximum load levels in both appears to be very comparable within the connected region. Outside of these regions, the experimental tests did not show the high stress concentrations between the connections and top or bottom of the panel. This is again believed to be a function of load application on single nodes within the model. Some variation in stress distribution can also be contributed to the assumption that the entire interface between the column and panel was in contact prior to loading. This was

clearly not the case in the test unit, as concentrated regions of the panel experienced minor crushing (Figure 4.35).

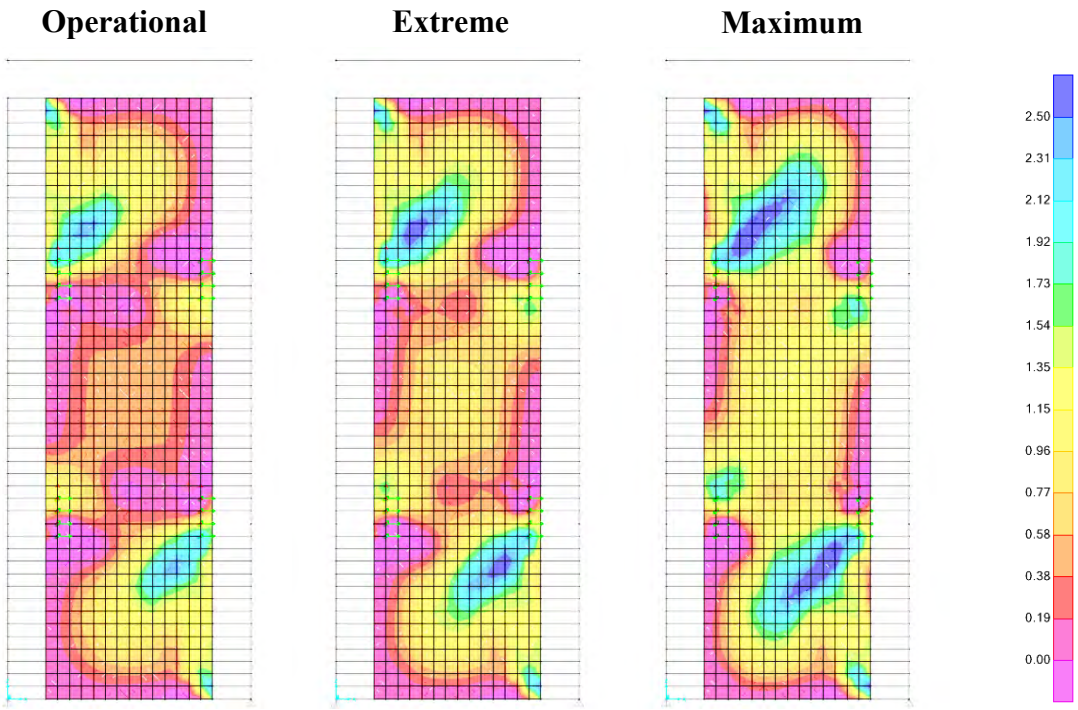


**Figure 5.7: HCUP-BC Analytical Stress Distribution at Various Limit States**

Given the load limitations associated with the anchor block and load frame used during experimental testing, the failure mechanism of the specimen was not clearly identifiable. A significant amount of damage, however, was observed throughout the panel. Yielding of the connection was also detected after a review of the collected data. Using the analytical model, the load at which failure of the specimen is expected to occur can be found.

One of the advantages of the bolted connection is that is can be easily replaced after an extreme loading event, which restores the capacity to its original state. For this reason, failure of the section was based on the damage within the panel. The criterion used to define failure in the panel was based on stress levels in the unreinforced sections of the panel, shown in Figure 4.10, reaching a tensile stress of 1.7 ksi. This represents the maximum tensile capacity of UHPC. Any further increase in strain will degrade the capacity of the section.

Using this criterion, failure was found to occur at approximately 170 kip in the center of the connected region. A check of the reinforced areas of the panel at this load level shows stress levels at or below 20 ksi in the steel reinforcement.

*HCUP-HPT Analysis*

The analytical and experimental response of the HCUP-HPT specimen is shown in Figure 5.8. During both the operation and extreme limit states, the specimen was expected to remain elastic. Unlike the HCUP-BC specimen, which relies on interface connections at discrete locations, the HCUP-HPT specimen distributes load by means of static friction developed along the entire interface. This, in combination with the reduced stress magnitudes, is believed to the source of increase stiffness. Some modifications to the model were required after comparisons made between the pre-experimental model and empirical results showed significant variation in the overall stiffness. These modifications included changing the restraints at the base of the column to account for the effects of post-tensioning stress, as well as increasing the stiffness of the interface connection elements. Both of these changes were justified using results and observations made during testing.

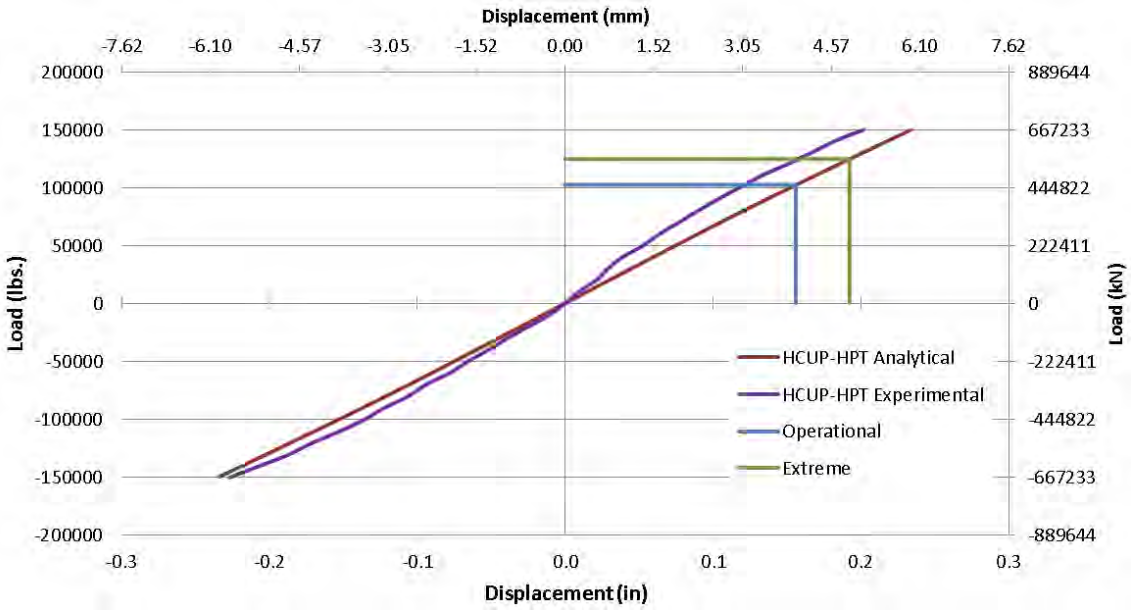


**Figure 5.8: HCUP-HPT Force-Displacement Curve**

The effects of the horizontal post-tensioning stress on the panel from the analytical model can be seen in Figure 5.9. The regions containing post-tensioning, experience little to no principal tension up to an ultimate load of 150 kip (667 kN); whereas, the areas in-between are subjected to higher stress levels. The absence of cracking in the experimental test suggests the entire panel remained below the 1.3 ksi (8.9 MPa) cracking stress of UHPC, which is consistent with the analytical results. The columns of the HCUP-HPT specimen were post-tensioned prior to the placement of the UHPC panel. This eliminated the residual compressive stress seen in the HCUP-BC specimen.

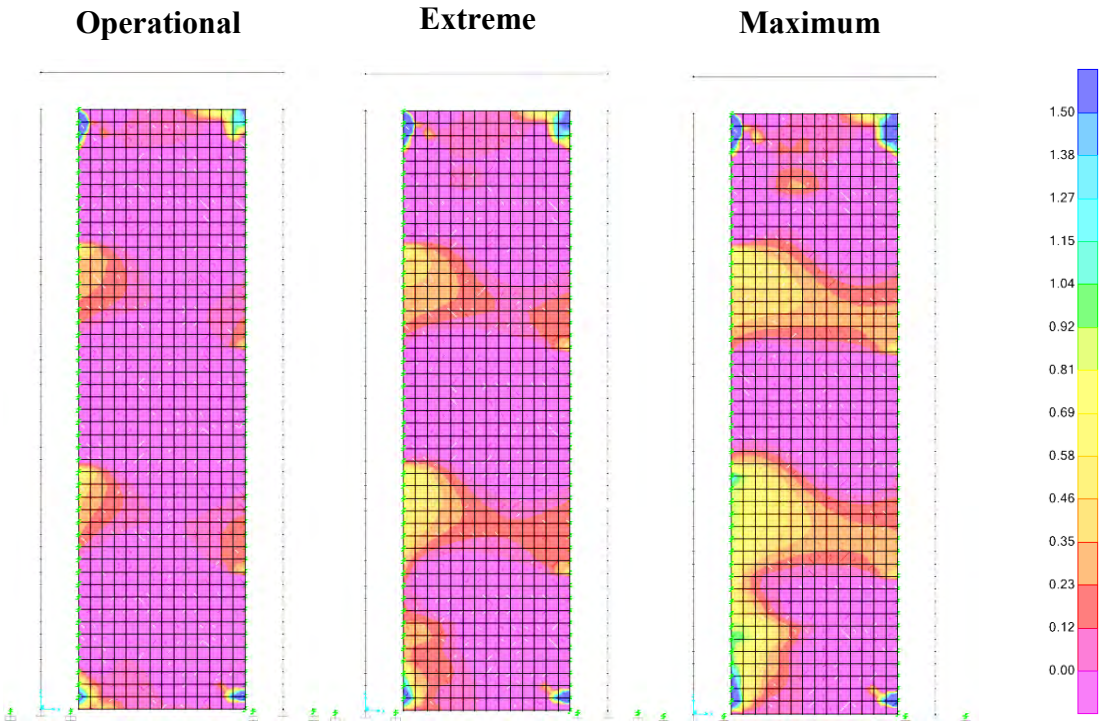


**Figure 5.9: HCUP-HPT Analytical Principal Tensile Stress**

The analytical response of the horizontal post-tensioning tendons was observed at each limit state. Only slight variations in the stress levels of the tendons were detected which corresponds to stress levels recorded during experimental testing. Using this information, it is appropriate to assume the capacity of the interface remains constant at all load levels.

*HCHP-UHPC Analysis*

The HCHP-UHPC specimen utilizes a six inch reinforced HSC panel in place of the three inch UHPC panel found in the other specimens. The thicker panel accommodates the UHPC wet joint used as the column/panel interface connection. A pre-experimental model was completed that suggested very similar behavior to that of the HCUP-HPT specimen in terms of overall response. This was expected given the similarities between the connections. The force-displacement response of both the experimental test and analytical model is presented in Figure 5.10. It can be seen that the stiffness predicted by the model was slightly lower than that of the experimental test. This, in part, can be contributed to uncertainty in the elastic modulus of the concrete. Current studies being conducted at Iowa State University suggest the elastic modulus of concrete is often underestimated by up to 25% when using the recommended equations of ACI 318 (2008). This has not been included in the model used for comparison purposes, due to insufficient evidence from the actual material used in the specimen.

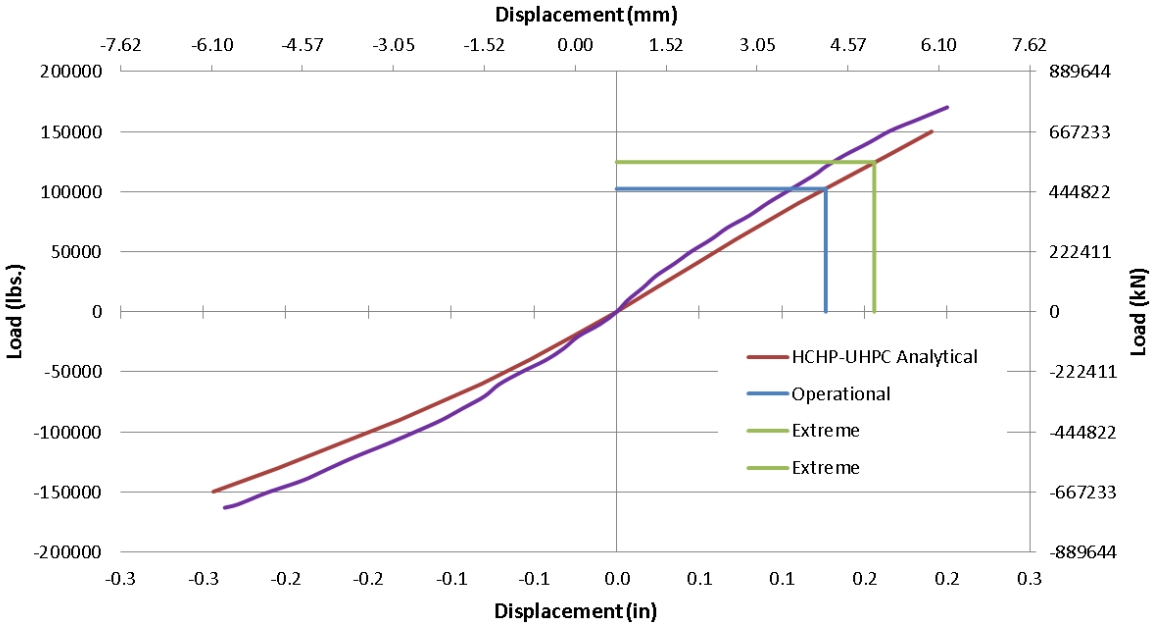


**Figure 5.10: HCHP-UHPC Analytical Force-Displacement**

The UHPC wet joint connection was placed prior to vertical post-tensioning. Much like that of the HCUP-BC specimen, this construction sequence leads to the development of residual stresses within the panel. The distribution of these stresses can be seen in Figure 5.11. Because post-tensioning is applied exclusively to the boundary elements, or columns,

the resulting vertical compressive stress across the top and bottom of the specimen is not uniform. The strut and tie model overlaying the panel in Figure 5.11 is used to show the effects of this process. The black compression struts form at approximately 35˚ from vertical. The red tension tie is required to stabilize the model at the top and bottom of the panel. The stress contour plot on the right illustrates the horizontal stress component that results from the compression of the columns. The total horizontal tension force within the top twelve inches of the panel was found to be approximately 46 kip (205 kN). The same is true for the bottom of the panel.

The development of high tensile stress in these regions was not fully understood prior to detailing and construction of the test unit. As a result, insufficient horizontal reinforcement was used. After revaluating the performance of the panel during post-tensioning, the stress levels detected in the model were consistent with those observed in the experimental test unit. A design modification, shown in Figure 4.54, was made to account for these higher tensile stresses.

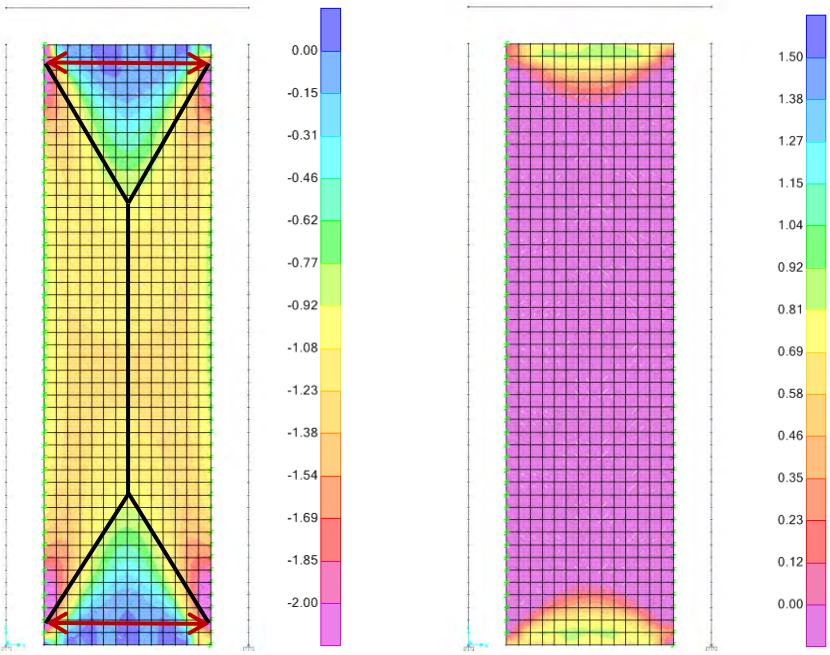


**Figure 5.11:HCHP-UHPC Post-Tensioning Stresses**

When considering the effects of the horizontal top load, the principal tensile stress distribution of Figure 5.12 suggests no cracking at the operational limit state. As load

progresses to the extreme limit state, cracks were expected to develop along the bottom section of the panel at the interface. The analytical model suggests crack widening and further distribution as load levels approach the maximum. The principal compressive stress within the panel is similar in magnitude to the principal tension stress, and therefor is not critical in regards to compression type failure.

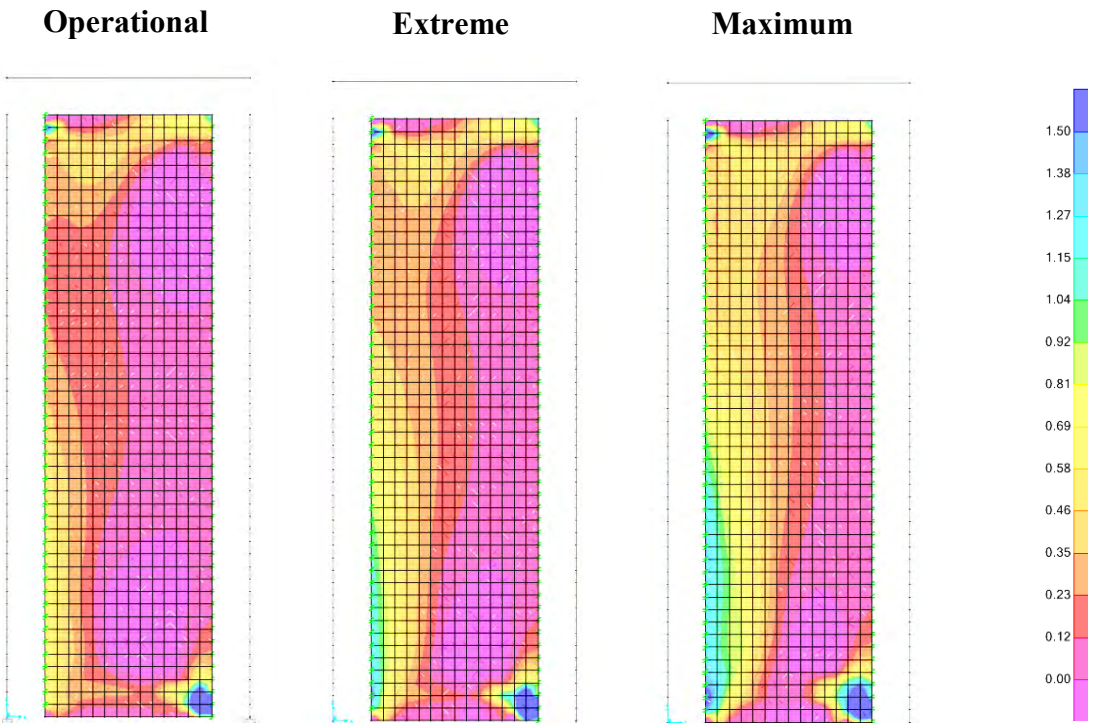


**Figure 5.12: HCHP-UHPC Analytical Principal Tensile Stress**

# CHAPTER 6. SUMMARY AND CONCLUSIONS

## 6.1 Summary of Research

The information presented in this report, is the second phase development of a high strength precast concrete solution to taller wind turbine towers. During the preliminary design stages, completed in phase one of the study, a number of alternatives including steel, conventional concrete shell, UHPC shell, and UHPC lattice designs were all considered possible solutions for reaching a 328 ft (100 m) hub height. After determining the UHPC lattice was most suitable, a detailed design was completed using load data made available through a number of published reports. At the conclusion of phase one of the study, a detailed design of a UHPC lattice towers was presented.

Chapter 1 of this report provided a brief history of wind energy and the need for technological improvements in order to meet future goals. The benefits of taller towers and the potential increase in energy production were discussed along with 328 ft (100 m) concrete tower designs currently used today. A description of the UHPC lattice tower design completed during phase one of the study, as well as the origin of wind loads used for design were presented in Chapter 2. The chapter also covered the material properties and current applications of UHPC. A number of precast concrete connections that are both common and newly developed in the industry were discussed for the purposes of finding the best solution for a precast concrete wind tower. Chapter 3 provided an in-depth look into the continued development of the UHPC lattice tower and the design of three separate towers utilizing different combinations of UHPC and HPC. Identification of critical tower sections and the development of three separate in-plane test specimens were presented in Chapter 4. The construction of each specimen, along with the results and observations from each test were included. Chapter 5 detailed the development of a complete finite element model, as well as models for each of the in-plane tests. A comparison between the analytical and experimental results was also included.

## 6.2 Conclusions

### 6.2.1 HCUP Tower

Based on the experimental and analytical results of this study, it was found that the HCUP tower would perform exceptionally well under the loads of a 2.5 MW turbine. The HSC columns showed little to no damage at both the operational and extreme limit states. The same can be said about the UHPC panels, which provide a number of attractive features over standard or high strength concrete panels. With the reduction in panel thickness, the overall weight and transportation costs of the tower are lowered. Additionally, UHPC requires less labor and is more resistant to corrosive environments. By utilizing HSC columns with larger cross-sectional areas, tower deflections at the operational and extreme limit states are also reduced.

The bolted connection was found to be the weakest of the three tested. Although it met the required load demand of the tower, it had the least favorable effect on the overall tower response in terms of drift and panel performance. Based on observations made during construction, the tight tolerances required for a bolted connection may also create problems during assembly. The horizontally post-tensioned connection demonstrated a much more desirable response. It improved the rigidity of the tower, and limited stress concentrations in the panel. Based on this information, use of this connection in the HCUP tower would be recommended prior to the bolted connection.

### 6.2.2 HCHP Tower with UHPC Wet Joint Connections

The HCHP tower performed well during experimental testing. Its response was very similar to that of the HCUP-HPT concept. With the use of a six inch reinforced high strength concrete panel, without the presence of prestressing steel, cracking at the extreme limit state is expected. This allows the steel reinforcement to be fully engaged at higher strain levels that are associated with the extreme load demand on the tower. The widths of these cracks remain small and largely unnoticed to the naked eye, while increasing the capacity of the section. Some consideration should be made, however, regarding the environment in which the tower is located. Highly corrosive environments could increase long term maintenance costs if cracks are prevalent.

As a result of experimental testing, the UHPC wet joint was found to perform exceptionally well at each limit state. Little to no damage was observed during testing of the critical tower section, verifying the use of the joint at all interface locations. In addition to creating a monolithic section at each elevation, the joint also provides better protection to the internal components of the tower by eliminating the possibility of column/panel separation at the interface. If an efficient method for casting a large number of UHPC wet joints at once can be developed for the construction of a complete tower, the benefits of the joint and HCHP tower in general may be outweigh those of the other two concepts.

### 6.2.3 UCUP Tower with Horizontally Post-Tensioned Connections

Although UHPC columns were not tested experimentally, the results of the HCUP-HPT and analytical models could be used to accurately predict the response of the UCUP tower with horizontally post-tensioned connections. The results show excellent performance in the panels at and above the extreme limit state will little to no cracking taking place. Similar performance is expected of the UHPC columns given the improved material properties. With the reduction in the cross-sectional area of the tower, tower deflections were higher than those found in a HCUP tower utilizing the same connection. The decreased stiffness also reduces the fundamental natural frequency of the tower, which falls slightly below the requirements of a 2.5 MW turbine. The use of this tower may be most beneficial in coming years when larger turbines require lower tower frequencies and minimal tower weight. Additionally, the costs associated with UHPC may be reduced as the market becomes more competitive with increased usage.

## 6.3 Future Research

In order to fully understand the behavior of the precast connections and panels, out-of-plane load testing should be completed. The tests conducted in this study verify the predicted performance of the columns, panels, and connections when subjected to in-plane loading. By examining this type of behavior, the capacity of the connected elements can be verified at the operational and extreme limit states.

In order to verify the effects of wind loading on the tower, an aerodynamic analysis should be completed. The loads used for the design of the tower accurately represented the full spectrum of loads expected for a 2.5 MW Liberty turbine manufactured by Clipper Windpower. The loads applied to the tower, however, were equivalent to those acting on a 328 ft (100 m) steel tower. The presence of the hexagonal shape with different orientations can greatly affect the aerodynamic properties of the tower leading to unexpected loading conditions. Through the development of an aerodynamic model and/or experimental wind tunnel testing, much of the uncertainty associated with this type of loading can be eliminated.

Much of this study has been dedicated to the design and testing of the tower assuming certain conditions at the base and top. In order to make the tower commercially available, a detailed foundation design must be completed. The foundation will be unlike many of those used for other types of towers given the need to access the vertical post-tensioning at the base or underneath the foundation. The transition between the tower top and yaw bearing used to support the nacelle must also be designed for the tower. This section of the tower is critical as a majority of the loads acting on the tower are generated in the head mass.

## REFERENCES


Aaleti, S., S. Sritharan, T. Wipf, & D. Bierwagen. (2011). *Structural Behavior of Waffle Bridge Deck Panels and Connections of Precast Ultra-High-Performance Concrete*. Transportation Research Record: Journal of the Transportation Research Board 2251: 82-92.

ACI Committee 318. (2008). *Building Code Requirements for Structural Concrete (ACI-318) and Commentary*. Farmington Hills: American Concrete Institute.

American Institute of Steel Construction (AISC), Inc. (2005). Specification for Structural Steel Building. Chicago: American Institute of Steel Construction, Inc.

Bickford, J. H. (2008). *Introduction to the Design and Behavior of Bolted Joints: Non-Gasketed Joints*. 4th ed. Boca Raton: Taylor & Francis. Print.

Bristow, B., & Sritharan, S. (To be submitted). *Uniaxial and Cyclic Behavior of Ultra-High Performance Concrete*. ACI Materials Journal .

British Standards Institution. (2005). *Eurocode 3: Design of steel structures*. London: BSI.

Cheyrezy, M., & Behloul, M. (2001). *Creep and Shrinkage of Ultra-High Performance Concrete. Creep, Shrinkage and Durability Mechanisms of Concrete and other Quasi-Brittle Materials* - Proceedings of the Sixth International Conference CONCREEP-^@MIT, (pp. 527-538). Cambridge.

Crisafulli, F. J., & Restrepo, J. I. (2003). *Ductile Steel Connections for Seismic Resistant Precast Buildings*. Journal of Earthquake Engineering 7.4: 541-53.

EG-BLOG. (2010) *Why Only Large and Small Wind Turbines and Nothing in Between?* Web log post. 16 Aug. 2010. Web. 24 Apr. 2013.

Federal Highway Administration. (2006). *Material Property Characterization of Ultra-High Performance Concrete*. Publication no. FHWA-HRT-06-103.

Federal Highway Administration. (2010). *Behavior of Field-Cast Ultra-High Performance Concrete Bridge Deck Connection under Cyclic and Static Structural Loading*. Publication no. FHWA-HRT-11-023.

Federal Highway Administration. (2012). *Compression Response of Rapid-Strengthening Ultra-High Performance Concrete Formulation*. Publication no. FHWA-HRT-12-064.

Fehling, E., Lorenz, P., & Leutbecher, T. (2011). *Experimental Investigations on Anchorage of Rebars in UHPC*. University of Kassel, Germany.

Garder, J. (2012). *Use of UHPC Piles in Integral Abutment Bridges*. Thesis. Iowa State University.

Germanischer Lloyd. (2010). *Guideline for the Certification of Wind Turbines*. Hamburg, Germany.

Gowripalan, N., & Gilbert, R. I. (2000). *Design Guidelines for RPC Prestressed Concrete Beams*. Sydney: VSL Pty Ltd.

Graybeal, B. A. (2008) *Flexural Behavior of an Ultrahigh-Performance Concrete I-Girder*. Journal of Bridge Engineering 13.6 (2008): 602-10.

Graybeal, B. A. (2009, January/February). *UHPC Making Strides*. Retrieved November 27, 2012, from U.S. Department of Transportation: Public Roads: http://www.tfhrc.gov/pubrds/09janfeb/03.htm

Grupo Inneo. (2008). Assembly Process. Retrieved November 27, 2012, from Precast Concrete Wind Towers: http://www.inneo.es/index.php/en/installation-process.html

Gundersen Envision. (2013). *Bolt Pattern Critical to Turbine Structural Integrity*. 13 Mar. 2103. <http://gundersenenvision.wordpress.com/>.

Hansen, T. C. (1996). *Fatigue in Welded Connections*. Thesis. Institut for Baerende Konstruktioner Og Materialer.

Hartwell, D. R. (2011). *Laboratory Testing of Ultra High Performance Concrete Deck Joints for Use in Accelerated Bridge Construction*. Thesis. Iowa State University.

Henry, R. S., Aaleti, S., Sritharan, S., & Ingham, J. M. (2010). *Concept and Finite Element Modeling of New Steel Shear Connectors for Self-Centering Wall Systems*. Journal of Engineering Mechanics: 220-29.

Hobbacher, A. (1996). *Fatigue Design of Welded Joints and Components: Recommendations of IIW Joint Working Group XIII-XV*. Cambridge, England: Abington in Association with "The Welding Institute". Print.

Hofheins, C. L., Reaveley, L. D., & Pantelides, C. P. (2002). *Behavior of Welded Plate Connections in Precast Concrete Panels under Simulated Seismic Loads*. PCI Journal 47.4: 122-33.

International Electrotechnical Commission (IEC). (2007). IEC 61400-1: *Wind Turbines - Part 1: Design Requirements*.

International Electrotechnical Commission (IEC). (2005). Eurocode 3. *Design of Steel Structures. Fatigue*. BS EN 1993-1-9:2005.

Karkos, T. (2010, August 19). *Wind-turbine sections squeeze through 1935 Rumford bridge*. River Valley Sun Journal, Retrieved March 16, 2013, from www.sunjournal .com

LaNier, M. P. (2005). *LWST Phase I Project Conceptual Design Study: Evaluation of Design and Construction Approaches for Economical Hybrid Steel/Concrete Wind Turbine Towers*. Golden: National Renewable Energy Laboratory.

Lassen, T., & Naman, R. (2006). *Fatigue Life Analyses of Welded Structures*. London: ISTE. Print.

Lewin, T., & Sritharan, S. (2010). *Design of 328-ft (100-m) Tall Wind Turbine Towers Using UHPC*. Thesis. Iowa State University

Moore, B. P. (2012). *Little Cedar Creek Bridge— Big Innovation*. ASPIRE Spring: 27.

NIB Torque. (2013) *WIND TURBINE BOLTING AND TORQUE TOOLS*. Web. 07 May 2013. <http://www.nibtorque.com/id57.html>.

NPCA. (2011). *Architectural Precast Concrete Wall Panels Connection Guide*. Publication. National Precast Concrete Association.

National Renewable Energy Laboratory (NREL). (2010) *New Wind Resource Maps and Wind Potential Estimates for the United States*. U.S. Department of Energy. Web. 24 Apr. 2013. <http://www.windpoweringamerica.gov/pdfs/wind_maps/us_contiguous_wind_potential_chart.pdf>.

Ozden, S., & Ertas, O. (2007). *Behavior of Unbonded, Post- Tensioned, Precast Concrete Connections with Different Percentages of Mild Steel Reinforcement*. PCI Journal March-April 2007: 32-44.

PCI Industry Handbook Committee. (2004). *PCI Design Handbook*. Chicago: Precast/Prestressed Concrete Institute.

Schultz, A. E., Tadros, M. K., Magana R. A., & Huo, X. M. (1994). *Precast Assemblies under Seismic Conditions.* Seismic Resistance of Vertical Joints in Precast Shear Walls. Proc. of FIP - XIIth International Congress, Washington. Vol. 1: 23-27.

Structural Engineering Institute (SEI). (2005). *Minimum Design Loads for Building and Other Structures*. Structural Engineering Institute of the American Society of Civil Engineers.

The Concrete Centre. (2005). *Concrete Wind Towers*. 2005. Web. 27 Nov. 2012. <http://www.ecocem.ie/downloads/Concrete_Windmills.pdf>.

U.S. Department of Energy (DOE). (2008, May). 20% Wind Power by 2030. Retrieved January 9, 2013 from 20percentwind.org

Vande Voort, T. L., Suleiman, M. T., & Sritharan, S. (2008). *Design and Performance Verification of UHPC Piles for Deep Foundations*. Ames: Center for Transportation Research and Education, Iowa State University

Wells, Z. B. (2012). *Performance of Post-Tensioned Curved-Strand Connections in Transverse Joints of Precast Bridge Decks*. Thesis. Utah State University. Print.

Zhang, H., David, J., McCalley, J., & Jackman, J. (2013). Proceedings of the ASME 2013 7th International Conference on Energy Sustainability & 11th Fuel Cell Science, Engineering and Technology Conference. *Cost-production Impact of Increasing Wind Turbine Tower Height*, Minneapolis, MN.

## APPENDIX A: HCUP-BC DESIGN CALCULATIONS

# HCUP-BC Tower Natural Frequency

$Height := 319.5ft$ — Tower height

$\gamma_{concrete} := 150\frac{lbf}{ft^3}$ — Unit weight of high strength concrete (HSC)

$P_{turbine} := 314.1kip$ — Weight of head mass

$E_{hsc} := 6449ksi$ — Elastic Modulus of HSC

$y(z) := \left(1 - \cos\left(\frac{\pi \cdot z}{2 \cdot Height}\right)\right)$ — Assumed displacement function of the tower

$y_1(z) := \frac{\pi}{2 \cdot Height} \cdot \sin\left(\frac{\pi \cdot z}{2 \cdot Height}\right)$ — First derivative of the displacement function

$y_2(z) := \frac{\pi^2}{4 \cdot Height^2} \cdot \cos\left(\frac{\pi \cdot z}{2 \cdot Height}\right)$ — Second derivative of the displacement functior

$h_1 := 110ft \qquad h_2 := 220ft$ — Height variables

$$A_{tower}(z) := \begin{cases} 5.5511 \cdot 10^{-17} \cdot z^2 - 4.0909 \cdot 10^{-2} \cdot z \cdot ft + 4.3422 \cdot 10^{1} ft^2 & \text{if } 0ft \le z < h_1 \\ 1.0960 \cdot 10^{-4} \cdot z^2 - 1.5486 \cdot 10^{-1} ft \cdot z + 5.5032 \cdot 10^{1} ft^2 & \text{if } h_1 \le z < h_2 \\ 1.7477 \cdot 10^{-4} \cdot z^2 - 2.0652 \cdot 10^{-1} ft \cdot z + 6.3910 \cdot 10^{1} ft^2 & \text{otherwise} \end{cases}$$

Note: The above equations describe the area of the tower. This includes both the column and panel area

$$I_{col}(z) := \begin{cases} -3.5527 \cdot 10^{-15} \cdot z^3 \cdot ft + 1.2300 \cdot 10^{-2} \cdot z^2 \cdot ft^2 - 8.568 \cdot z \cdot ft^3 + 1.5091 \cdot 10^{3} \cdot ft^4 & \text{if } 0 \le z < h_1 \\ -1.4027 \cdot 10^{-5} \cdot z^3 \cdot ft + 1.5621 \cdot 10^{-2} \cdot ft^2 \cdot z^2 - 7.666 ft^3 \cdot z + 1.3956 \cdot 10^{3} ft^4 & \text{if } h_1 \le z < h_2 \\ -1.7982 \cdot 10^{-5} \cdot z^3 \cdot ft + 1.9392 \cdot 10^{-2} ft^2 \cdot z^2 - 9.1434 ft^3 \cdot z + 1.5870 \cdot 10^{3} ft^4 & \text{otherwise} \end{cases}$$

Note: The above equations describe the moment of inertia of the colums as a function of height for the columns. The three equations presented below describe the moment of inertia as a funtion of height for the panels.

$$I_{pan}(z) := \begin{cases} -1.268\cdot10^{-5}\cdot z^3\cdot ft + 1.180\cdot10^{-2}\cdot z^2\cdot ft^2 - 3.640\cdot z\cdot ft^3 + 3.710\cdot10^{2}\cdot ft^4 & \text{if } 0 \le z < h_1 \\ -2.148\cdot10^{-7}\cdot z^3\cdot ft + 5.661\cdot10^{-4}\cdot ft^2\cdot z^2 - 4.96\cdot10^{-1}ft^3\cdot z + 1.444\cdot10^{2}ft^4 & \text{if } h_1 \le z < h_2 \\ -8.683\cdot10^{-8}\cdot z^3\cdot ft + 3.037\cdot10^{-4}ft^2\cdot z^2 - 3.367\cdot10^{-1}ft^3\cdot z + 1.208\cdot10^{2}ft^4 & \text{otherwise} \end{cases}$$

**Tower Frequency and Period Calculations**

$$M := \int_0^{Height} \left(\frac{\gamma_{concrete}}{g}\right)\cdot\left(A_{tower}(z)\right)\cdot\left(y(z)\right)^2 dz + \frac{P_{turbine}}{g}\cdot y(Height)^2$$ Mass variable

$$k := \int_0^{Height} E_{hsc}\cdot\left(I_{col}(z) + I_{pan}(z)\right)\cdot\left(y_2(z)\right)^2 dz$$ Stiffness variable

$$k = 7.561\cdot\frac{kip}{in}$$

$$\omega_{rad} := \sqrt{\frac{k}{M}} = 2.3\cdot\frac{1}{s}$$ Tower Frequency (rad/second)

$$\omega_{sec} := \frac{\omega_{rad}}{2\cdot\pi} = 0.366\cdot\frac{1}{s}$$ Tower Frequency (cycles/second)

$\lambda := 0.82$ Tower frequency reduction factor (See below Note)

$$\omega_{rrad} := \lambda\cdot\omega_{rad} = 1.886\cdot\frac{1}{s}$$ ReducedTower Frequency (rad/second)

$$\omega_{rsec} := \frac{\omega_{rrad}}{2\cdot\pi} = 0.30\cdot\frac{1}{s}$$ Reduced Tower Frequency (cycles/second)

Note: The above equations assume the tower is monolitic around its parimeter. When using bolted connections, this is not an appropriate assumption. For this reason, a reduction factor of 0.82 has been applied. This value was determined based on a pushover analysis of the HCUP tower in the finite element model using both bolted and rigid connections.

# Ultimate Moment Capacity of the HCUP-BC Tower
## 0-Degree Loading, Low Relaxation Bonded Tendons

### Geometric and Material Properties

| | |
|---|---|
| $f_{hsc} := 13ksi$ | Compressive strength of high strength concrete (HSC) |
| $E_{hsc} := 6499ksi$ | Elastic modulus of HSC |
| $f_{uhpc} := 26ksi$ | Compressive strength of UHPC |
| $E_{uhpc} := 7449.5ksi$ | Elastic modulus of UHPC |
| $\varepsilon_{cu} := .003\frac{in}{in}$ | HSC compressive strain limit |
| $\gamma_c := 150\frac{lbf}{ft^3}$ | Unit weight of HSC |
| $f_{pu} := 270ksi$ | Ultimate capacity of steel tendons |
| $E_s := 28500ksi$ | Elastic modulus of steel tendons |
| $f_{seo} := .6666 \cdot f_{pu} = 179.982 \cdot ksi$ | Applied tendon stress from post-tensioning |
| $\gamma_D := 1.2$ | Dead load factor |
| $A_{col} := 793.651in^2$ | Single column area at the base |
| $D_{base} := 228in$ | Tower diameter at the base |
| $D_{column} := 36in$ | Column diameter at the base |
| $P_{top} := 314.16kip$ | Dead load at the tower top |
| $A_{centerduct} := 22.48in^2$ | Area of the center duct in the columns |
| $A_{radial1duct} := 7.99in^2$ | Area of two of the radial ducts in the columns |
| $A_{radial2duct} := 4.83in^2$ | Area of remaining two radial ducts in the columns |
| $P_{width} := 82.82in$ | Width of the panel at the base of the tower |
| $P_{thickness} := 3in$ | Thickness of the panel |

$N_{Center} := 33$ Number of strands in the center duct

$N_{Radial1} := 14$ Number of strands in two of the radial ducts

$N_{Radial2} := 3$ Number of strands in the remaining two radial ducts

$A_{strand} := 0.217in^2$ Area of the steel strand

$N_{column} := N_{Center} + 2 \cdot (N_{Radial1} + N_{Radial2})$ Total number of strands in each column at the tower base

$A_{stot} := A_{strand} \cdot [N_{Center} + 2 \cdot (N_{Radial1} + N_{Radial2})] = 14.539 \cdot in^2$ Total tendon area per column

$f_{psTension} := 267.135ksi$ $f_{psMiddle} := 263.451ksi$ $f_{psCompression} := 94.482ksi$

Note: The three values listed above, are part of the iterative procedure used to determine the ultimate capacity. They represent the tendon stress in each column group also presented below.

$$\sigma_{ColumnC} := \frac{(N_{column} \cdot A_{strand} \cdot f_{psCompression})}{A_{col}} = 1.731 \cdot ksi$$

Column stress in the compression group

$$\sigma_{ColumnAB} := \frac{(N_{column} \cdot A_{strand} \cdot f_{sco})}{A_{col}} = 3.297 \cdot ksi$$

Column stress in the tension group

$$\varepsilon_d := \frac{\sigma_{ColumnAB}}{E_{hsc}} = 5.073 \times 10^{-4}$$

Decompression strain of the columns

$$y(x) := (0.85 \cdot f_{hsc}) \cdot (5.824 \cdot 10^{-3} x^3 - 1.177 \cdot x^2 + 7.856 \cdot 10^1 \cdot x - 1.438 \cdot 10^2) + .85 \cdot f_{uhpc} \cdot (6.4007 \cdot x + 85.2$$
$$- (f_{psCompression} + f_{psTension} + f_{psMiddle}) \cdot \frac{A_{strand}}{in^2} \cdot (2 \cdot N_{column})$$

Note: The above equation represents the equilibrium equation for the tower, which is used to determine the neutral axis at the base of the tower.

$p := root(y(x), x, -200, 200) = 24.513$

$a := p - 1in$ Depth of equivalent rectangular stress block

$a = 24.513 \cdot in$

$\beta_1 := .65$ Rectangular stress block distribution for HSC

$c_{AA} := \frac{a}{\beta_1} = 37.712 \cdot in$ Bending neutral axis depth at base of tower

$\varepsilon_{sM} := \left| \varepsilon_{cu} - \frac{\varepsilon_{cu}}{c} \cdot \frac{\left( \frac{D_{base}}{2} \cdot \sqrt{3} + D_{column} \right)}{2} \right| = 6.286 \times 10^{-3} \cdot \frac{in}{in}$ Strain caused by bending in center tendon group

$\varepsilon_{sT} := \left| \varepsilon_{cu} - \frac{\varepsilon_{cu}}{c} \cdot \left( \frac{D_{base}}{2} \cdot \sqrt{3} + \frac{D_{column}}{2} \right) \right| = 0.014 \cdot \frac{in}{in}$ Strain caused by bending in tension tendon group

Note: The previous two equations assume a linear strain distribution at the base of the tower. Neither tendon approaches the approximate rupture strain of 0.05 in/in.

$\varepsilon_{pe} := \frac{f_{sco}}{E_s} = 6.315 \times 10^{-3} \cdot \frac{in}{in}$

$\varepsilon_{psT} := \varepsilon_{pe} + \varepsilon_d + \varepsilon_{sT} = 0.02096 \cdot \frac{in}{in}$ Final strain of tension tendon at ultimate moment

$\varepsilon_{psM} := \varepsilon_{pe} + \varepsilon_d + \varepsilon_{sM} = 0.01311 \cdot \frac{in}{in}$ Final strain of center tendon at ultimate moment

$\varepsilon_{psC} := \varepsilon_{pe} - \varepsilon_{cu} = 3.31516 \times 10^{-3} \cdot \frac{in}{in}$ Final strain of compression tendon at ultimate moment

$f_{psT} := \begin{cases} 28500ksi \cdot \varepsilon_{psT} & \text{if } |\varepsilon_{psT}| \le 0.0086 \\ \left( 270ksi - \frac{.04ksi}{\varepsilon_{psT} - .007} \right) & \text{if } \varepsilon_{psT} > 0.0086 \end{cases} = 267.135 \cdot ksi$ Tension tendon stress

$f_{psM} := \begin{cases} 28500ksi \cdot \varepsilon_{psM} & \text{if } |\varepsilon_{psM}| \le 0.0086 \\ \left( 270ksi - \frac{.04ksi}{\varepsilon_{psM} - .007} \right) & \text{if } \varepsilon_{psM} > 0.0086 \end{cases} = 263.451 \cdot ksi$ Center tendon stress

$f_{psC} := \begin{cases} 28500ksi \cdot \varepsilon_{psC} & \text{if } \varepsilon_{psC} \le 0.0086 \\ \left( 270ksi - \frac{.04ksi}{\varepsilon_{psC} - .007} \right) & \text{if } \varepsilon_{psC} > 0.0086 \end{cases} = 94.482 \cdot ksi$ Compresion tendon stress

$$y_{bar} := \frac{\left[\frac{(3\cdot\sqrt{3})}{2}\cdot\left(\frac{D_{column}}{2}\right)^2 - \left(\frac{D_{column}}{2}\right)\cdot 2 + P_{thickness}\cdot P_{width}\cdot\left(\frac{D_{column}}{2}\right) + 2\left(a - D_{column}\cdot .75 - P\right.\right.}{\frac{(3\cdot\sqrt{3})}{2}\cdot\left(\frac{D_{column}}{2}\right)^2\cdot 2 + 2\cdot\left(a - D_{column}\cdot .75 - P_{thi}\right.}$$

Note: The above equation is used to determine the centroid of the concrete area in compression. This will in turn be used for finding the ultimate moment capacity. The equation exceeds the width limitation of the sheet, and therefore, is only patially displayed. The resulting value is 17.74 inches from the extreme compression fiber.

$$jd_T := \frac{D_{base}}{2}\cdot\sqrt{3} + \frac{D_{column}}{2} - y_{bar} = 197.551\cdot in$$ Length of moment arm to tension tendons

$$jd_M := \frac{\frac{D_{base}}{2}\cdot\sqrt{3}}{2} + \frac{D_{column}}{2} - y_{bar} = 98.824\cdot in$$ Length of moment arm to center tendons

$$T_T := 2\cdot N_{column}\cdot A_{strand}\cdot\left(f_{psT}\right) = 7.768\times 10^3\cdot kip$$ Tendon force in tension group

$$T_M := 2\cdot N_{column}\cdot A_{strand}\cdot\left(f_{psM}\right) = 7.661\times 10^3\cdot kip$$ Tendon force in center group

$$M_{initial} := \left(T_T\cdot jd_T + T_M\cdot jd_M\right) = 190965.086\cdot ft\cdot kip$$ Ultimate moment capacity

Note: The above capacity does not include P-Delta effects, which will reduce the total capacity. See below for further analysis.

## Subtract P-Delta Effect

### HCUP-BC Ultimate Moment Capacity at Base

$M_{Base} := 190965.09\text{ft}\cdot\text{kip}$ $M_{110} := 128057.57\text{ft}\cdot\text{kip}$ $M_{220} := 93428.72\text{ft}\cdot\text{kip}$ $M_{Top} := 45296.70\text{ft}\cdot\text{kip}$

Note: The above moment demand values at four seperate tower elevations were obtained from seperate spreadsheets. Each is included in this appendix below.

$Z_{bot} := 0\text{ft}$ $Z_{110} := 110\text{ft}$ $Z_{220} := 220\text{ft}$ $Z_{top} := 319.55\text{ft}$

$$M_{cst}(z) := \begin{cases} M_{Base} - \dfrac{(M_{Base} - M_{110})}{(Z_{110} - Z_{bot})}\cdot z & \text{if } 0\text{ft} \le z < 110\text{ft} \\ M_{110} - \dfrac{(M_{110} - M_{220})}{(Z_{220} - Z_{110})}\cdot(z - Z_{110}) & \text{if } 110\text{ft} \le z < 220\text{ft} \\ M_{220} - \dfrac{(M_{220} - M_{Top})}{(Z_{top} - Z_{220})}\cdot(z - Z_{220}) & \text{otherwise} \end{cases}$$

Note: The above set of equations is used to estimate the moment demand at any elevation, z, for the purposes of including P-delta effects in the ultimate moment capacity. Below, six seperate equations are shown that describe the moment of inertia of both the columns and panels.

$$I_{col}(z) := \begin{cases} -3.5527\cdot10^{-15}\cdot z^3\cdot\text{ft} + 1.230\cdot10^{-2}\cdot z^2\cdot\text{ft}^2 - 8.568\cdot z\cdot\text{ft}^3 + 1.509\cdot10^3\cdot\text{ft}^4 & \text{if } Z_{bot} \le z < Z_{110} \\ -1.4027\cdot10^{-5}\cdot z^3\cdot\text{ft} + 1.562\cdot10^{-2}\cdot\text{ft}^2\cdot z^2 - 7.666\text{ft}^3\cdot z + 1.3956\cdot10^3\text{ft}^4 & \text{if } Z_{110} \le z < Z_{220} \\ -1.7982\cdot10^{-5}\cdot z^3\cdot\text{ft} + 1.9392\cdot10^{-2}\text{ft}^2\cdot z^2 - 9.1434\text{ft}^3\cdot z + 1.5870\cdot10^3\text{ft}^4 & \text{otherwise} \end{cases}$$

$$I_{pan}(z) := \begin{cases} -1.268\cdot10^{-5}\cdot z^3\cdot\text{ft} + 1.180\cdot10^{-2}\cdot z^2\cdot\text{ft}^2 - 3.640\cdot z\cdot\text{ft}^3 + 3.710\cdot10^2\cdot\text{ft}^4 & \text{if } Z_{bot} \le z < Z_{110} \\ -2.15\cdot10^{-7}\cdot z^3\cdot\text{ft} + 5.66\cdot10^{-4}\cdot\text{ft}^2\cdot z^2 - 4.96\cdot10^{-1}\text{ft}^3\cdot z + 1.444\cdot10^2\text{ft}^4 & \text{if } Z_{110} \le z < Z_{220} \\ -8.683\cdot10^{-8}\cdot z^3\cdot\text{ft} + 3.037\cdot10^{-4}\text{ft}^2\cdot z^2 - 3.367\cdot10^{-1}\text{ft}^3\cdot z + 1.208\cdot10^2\text{ft}^4 & \text{otherwise} \end{cases}$$

$$\Delta_{flex}(z_1) := \int_0^{z_1} \frac{M_{cst}(z)\cdot(z_1 - z)}{(E_{hsc}\cdot I_{col}(z) + E_{uhpc}\cdot I_{pan}(z))}\,dz$$

Equation used to describe tower displacement as a function of height

$$Wt(z) := \begin{cases} \gamma_c \cdot \left(8.3267 \cdot 10^{-17} \cdot z^2 - 1.4211 \cdot 10^{-14} \cdot z \cdot ft + 3.3069 \cdot 10^{1} ft^2\right) & \text{if } 0ft \le z < Z_{110} \\ \gamma_c \cdot \left(1.0960 \cdot 10^{-4} \cdot z^2 - 1.4811 \cdot 10^{-1} ft \cdot z + 4.8437 \cdot 10^{1} ft^2\right) & \text{if } Z_{110} \le z < Z_{220} \\ \gamma_c \cdot \left(1.7477 \cdot 10^{-4} \cdot z^2 - 2.0304 \cdot 10^{-1} ft \cdot z + 5.8034 \cdot 10^{1} ft^2\right) & \text{otherwise} \end{cases}$$

Note: The above set of equations describe the weight of the columns as a function of height

$$M_{pd}(z_1, z_2) := \int_{z_2}^{z_1} \Delta_{flex}(z) \cdot Wt(z)\, dz$$

P-delta moment demand generated by column weight

$$H_{panel} := \begin{pmatrix} 15ft \\ 45ft \\ 75ft \\ 100ft \\ 130ft \\ 160ft \\ 185ft \\ 210ft \\ 240ft \\ 270ft \\ 305ft \\ 310ft \end{pmatrix} \quad Wt_{panel} := \begin{pmatrix} 43.83kip \\ 38.30kip \\ 27.70kip \\ 23.87kip \\ 30.11kip \\ 20.75kip \\ 20.11kip \\ 19.48kip \\ 26.51kip \\ 25.87kip \\ 21.35kip \\ 0kip \end{pmatrix}$$

Total panel weight discretized into ten foot elevation intervals

$$M_{pdpanel} := \sum_{i=0}^{11} \left(\Delta_{flex}\left(H_{panel_i}\right) \cdot Wt_{panel_i}\right) = 628.226 \cdot ft \cdot kip$$

P-delta moment generated by panels

$$M_{pdtop} := \left[\gamma_D \cdot \left(P_{top}\right)\right] \cdot \Delta_{flex}(319.55ft) = 3263.665 \cdot ft \cdot kip$$

P delta moments generated by head mass

$$M_n := M_{initial} - M_{pdtop} - M_{pd}(319.55ft, 0ft) - M_{pdpanel}$$

$$M_n = 184808.18 \cdot ft \cdot kip$$

Nominal moment capacity

$$\phi := 0.9$$

Resistance factor

$$M_u := \phi \cdot M_n = 166327.37 \cdot ft \cdot kip$$

Ultimate moment capacity at the base of the HCHP-HPC tower

## Ultimate Capacity at 110'

Note: The same procedures used to determine the ultimate moment capacity at the base of the tower including P-delta effects, is used for the remaining elevations. Because these are locations of post-tensioning tendon cut-offs, the moment capacity directly above and below the designated elevation has been determined.

$$M_{pd110}(z_1, z_2) := \int_{z_2}^{z_1} \Delta_{flex}(z_1) \cdot Wt(z)\, dz$$

$$M_{pdpanel110} := \sum_{i=3}^{11} \left[ \left( \Delta_{flex}\left(H_{panel_i}\right) - \Delta_{flex}(110ft) \right) \cdot Wt_{panel_i} \right] = 475.459 \cdot ft \cdot kip$$

$$M_{pdtop110} := \gamma_D \cdot P_{top} \cdot \left( \Delta_{flex}(319.55ft) - \Delta_{flex}(110ft) \right) = 2985.278 \cdot ft \cdot kip$$

$$M_{n110} := M_{est}(110ft) - M_{pdtop110} - M_{pd110}(319.55ft, 110ft) - M_{pdpanel110}$$

$$M_{n110} = 118642.43 \cdot ft \cdot kip$$

$M_{blw110} := \phi \cdot M_{n110} = 106778.19 \cdot ft \cdot kip$ Ultimate moment demand directly below 110'

$M_{abv110} = 117559.559 \cdot kip$ Ultimate moment demand above 110', not including P-delta effects. (From seperate sheet)

$$M_{above110} := M_{abv110} - M_{pdtop110} - M_{pd110}(319.55ft, 110ft) - M_{pdpanel110}$$

$M_{uabove110} := \phi \cdot M_{above110} = 97329.97 \cdot ft \cdot kip$ Ultimate moment demand directly above 110'

## Ultimate Capacity at 220'

$$M_{pd220}(z_1, z_2) := \int_{z_2}^{z_1} \Delta_{flex}(z_1) \cdot Wt(z)\, dz$$

$$M_{pdbrace220} := \sum_{i=7}^{11} \left[ \left( \Delta_{flex}\left(H_{panel_i}\right) - \Delta_{flex}(220ft) \right) \cdot Wt_{panel_i} \right] = 160.876 \cdot ft \cdot kip$$

$$M_{pdtop220} := \gamma_D \cdot P_{top} \cdot \left( \Delta_{flex}(319.55ft) - \Delta_{flex}(220ft) \right) = 1948.478 \cdot ft \cdot kip$$

$$M_{n220} := M_{est}(220ft) - M_{pdtop220} - M_{pd220}(319.55ft, 220ft)$$

$$M_{n220} = 89396.02 \cdot ft \cdot kip$$

$M_{u220} := \phi \cdot M_{n220} = 80456.42 \cdot ft \cdot kip$ Ultimate moment demand directly below 220'

$M_{abv220} := 54504.52ft \cdot kip$ Ultimate moment demand above 110', not including P-delta effects. (From seperate sheet)

$$M_{above220} := M_{abv220} - M_{pdtop220} - M_{pd220}(319.55ft, 220ft)$$

$M_{uabove220} := \phi \cdot M_{above220} = 45424.64 \cdot ft \cdot kip$ Ultimate moment demand directly above 110'

## Ultimate Capacity at Tower Top

$$M_{ntop} := M_{est}(319.55ft) = 45296.7 \cdot ft \cdot kip$$

$M_{utop} := \phi \cdot M_{ntop} = 40767.03 \cdot ft \cdot kip$ Ultimate moment demand at tower top

## APPENDIX B: HCHP-UHPC DESIGN CALCULATIONS

### HCHP-UHPC Tower Natural Frequency

$Height := 319.55ft$ Tower height

$\gamma_{concrete} := 150 \frac{lbf}{ft^3}$ Unit weight of high strength concrete (HSC)

$P_{turbine} := 314.16kip$ Weight of head mass

$E_{hsc} := 6449ksi$ Elastic Modulus of HSC

$y(z) := \left(1 - \cos\left(\frac{\pi \cdot z}{2 \cdot Height}\right)\right)$ Assumed displacement function of the tower

$y_1(z) := \frac{\pi}{2 \cdot Height} \cdot \sin\left(\frac{\pi \cdot z}{2 \cdot Height}\right)$ First derivative of the displacement function

$y_2(z) := \frac{\pi^2}{4 \cdot Height^2} \cdot \cos\left(\frac{\pi \cdot z}{2 \cdot Height}\right)$ Second derivative of the displacement function

$h_1 := 110ft \qquad h_2 := 220ft$ Height variables

$$A_{tower}(z) := \begin{cases} -2.775610^{-17} \cdot z^2 - 8.181810^{-2} \cdot z \cdot ft + 5.375510^{1} ft^2 & \text{if } 0ft \le z < h_1 \\ 1.096010^{-4} \cdot z^2 - 1.616110^{-1} ft \cdot z + 6.162810^{1} ft^2 & \text{if } h_1 \le z < h_2 \\ 1.747710^{-4} \cdot z^2 - 2.100010^{-1} ft \cdot z + 6.978610^{1} ft^2 & \text{otherwise} \end{cases}$$

Note: The above equations describe the area of the tower. This includes both the column and panel area

$$I_{col}(z) := \begin{pmatrix} 3.553110^{-15} \cdot z^3 \cdot ft + 1.2310^{-2} \cdot z^2 \cdot ft^2 - 8.568 z \cdot ft^3 + 1.50910^{3} \cdot ft^4 & \text{if } 0 \le z < h_1 \\ 1.402710^{-5} \cdot z^3 \cdot ft + 1.562210^{-2} \cdot ft^2 \cdot z^2 - 7.6662 ft^3 \cdot z + 1.395610^{3} ft^4 & \text{if } h_1 \le z < h_2 \\ 1.798210^{-5} \cdot z^3 \cdot ft + 1.939210^{-2} ft^2 \cdot z^2 - 9.1434 ft^3 \cdot z + 1.587010^{3} ft^4 & \text{otherwise} \end{pmatrix}$$

Note: The above equations describe the moment of inertia of the colums as a function of height for the columns. The three equations presented below describe the moment of inertia as a funtion of height for the panels.

$$I_{pan}(z) := \begin{cases} -2.536\cdot10^{-5}\cdot z^3\cdot ft + 2.360\cdot10^{-2}\cdot z^2\cdot ft^2 - 7.281\cdot z\cdot ft^3 + 7.421\cdot10^{2}\cdot ft^4 & \text{if } 0 \le z < h_1 \\ -4.296\cdot10^{-7}\cdot z^3\cdot ft + 1.132\cdot10^{-3}\cdot ft^2\cdot z^2 - 9.919\cdot10^{-1}\,ft^3\cdot z + 2.890\cdot10^{2}\,ft^4 & \text{if } h_1 \le z < h_2 \\ -1.737\cdot10^{-7}\cdot z^3\cdot ft + 6.074\cdot10^{-4}\,ft^2\cdot z^2 - 6.735\cdot10^{-1}\,ft^3\cdot z + 2.416\cdot10^{2}\,ft^4 & \text{otherwise} \end{cases}$$

**Tower Frequency and Period Calculations**

$$M := \int_0^{Height} \left(\frac{\gamma_{concrete}}{g}\right)\cdot\left(A_{tower}(z)\right)\cdot\left(y(z)\right)^2 dz + \frac{P_{turbine}}{g}\cdot y(Height)^2$$ Mass variable

$$k := \int_0^{Height} E_{hsc}\cdot\left(I_{col}(z) + I_{pan}(z)\right)\cdot\left(y_2(z)\right)^2 dz$$ Stiffness variable

$$k = 9.227\cdot\frac{kip}{in}$$

$\omega_{rad} := \sqrt{\frac{k}{M}} = 2.425\cdot\frac{1}{s}$ Tower Frequency (rad/second)

$\omega_{sec} := \frac{\omega_{rad}}{2\cdot\pi} = 0.386\cdot\frac{1}{s}$ Tower Frequency (cycles/second)

# Ultimate Moment Capacity of the HCHP-UHPC Tower
## 0-Degree Loading, Low Relaxation Bonded Tendons

### Geometric and Material Properties

| | |
|---|---|
| $f_{hsc} := 13ksi$ | Compressive strength of high strength concrete (HSC) |
| $E_{hsc} := 6499ksi$ | Elastic modulus of HSC |
| $\epsilon_{cu} := .003\frac{in}{in}$ | HSC compressive strain limit |
| $\gamma_c := 150\frac{lbf}{ft^3}$ | Unit weight of HSC |
| $f_{pu} := 270ksi$ | Ultimate capacity of steel tendons |
| $E_s := 28500ksi$ | Elastic modulus of steel tendons |
| $f_{seo} := .6666 \cdot f_{pu} = 179.982 \cdot ksi$ | Applied tendon stress from post-tensioning |
| $\gamma_D := 1.2$ | Dead load factor |
| $A_{col} := 793.651in^2$ | Single column area at the base |
| $D_{base} := 228in$ | Tower diameter at the base |
| $D_{column} := 36in$ | Column diameter at the base |
| $P_{top} := 314.16kip$ | Dead load at the tower top |
| $A_{centerduct} := 22.48in^2$ | Area of the center duct in the columns |
| $A_{radial1duct} := 7.99in^2$ | Area of two of the radial ducts in the columns |
| $A_{radial2duct} := 4.83in^2$ | Area of remaining two radial ducts in the columns |
| $P_{width} := 82.82in$ | Width of the panel at the base of the tower |
| $P_{thickness} := 6in$ | Thickness of the panel |
| $N_{Center} := 33$ | Number of strands in the center duct |
| $N_{Radial1} := 14$ | Number of strands in two of the radial ducts |

$N_{Radial2} := 3$ Number of strands in the remaining two radial ducts

$A_{strand} := 0.217in^2$ Area of the steel strand

$N_{column} := N_{Center} + 2 \cdot (N_{Radial1} + N_{Radial2})$ Total number of strands in each column at the tower base

$A_{stot} := A_{strand} \cdot [N_{Center} + 2 \cdot (N_{Radial1} + N_{Radial2})] = 14.539 \cdot in^2$ Total tendon area per column

$f_{psTension} := 267.135ksi$ $f_{psMiddle} := 263.451ksi$ $f_{psCompression} := 94.482ksi$

Note: The three values listed above, are part of the iterative procedure used to determine the ultimate capacity. They represent the tendon stress in each column group also presented below.

$$\sigma_{ColumnC} := \frac{(N_{column} \cdot A_{strand} \cdot f_{psCompression})}{A_{col}} = 1.731 \cdot ksi$$

Column stress in the compression group

$$\sigma_{ColumnAB} := \frac{(N_{column} \cdot A_{strand} \cdot f_{sco})}{A_{col}} = 3.297 \cdot ksi$$

Column stress in the tension group

$$\epsilon_d := \frac{\sigma_{ColumnAB}}{E_{hsc}} = 5.073 \times 10^{-4}$$

Decompression strain of the columns

$$y(x) := (0.85 \cdot f_{hsc}) \cdot (5.824 \cdot 10^{-3} x^3 - 1.177 \cdot x^2 + 7.856 \cdot 10^{1} \cdot x - 1.438 \cdot 10^{2}) + .85 \cdot f_{hsc} \cdot (12.801 \cdot x + 170.5$$
$$- (f_{psCompression} + f_{psTension} + f_{psMiddle}) \cdot \frac{A_{strand}}{in^2} \cdot (2 \cdot N_{column})$$

Note: The above equation represents the equilibrium equation for the tower, which is used to determine the neutral axis at the base of the tower.

$p := root(y(x), x, -200, 200) = 24.513$

$a := p \cdot 1in$ Depth of equivalent rectangular stress block

$a = 24.513 \cdot in$

$\beta_1 := .65$ Rectangular stress block distribution for HSC

$c := \frac{a}{\beta_1} = 37.712 \cdot in$ Bending neutral axis depth at base of tower

$$\varepsilon_{sM} := \left| \varepsilon_{cu} - \frac{\varepsilon_{cu}}{c} \cdot \frac{\left( \frac{D_{base}}{2} \cdot \sqrt{3} + D_{column} \right)}{2} \right| = 6.286 \times 10^{-3} \cdot \frac{in}{in}$$

Strain caused by bending in center tendon group

$$\varepsilon_{sT} := \left| \varepsilon_{cu} - \frac{\varepsilon_{cu}}{c} \cdot \left( \frac{D_{base}}{2} \cdot \sqrt{3} + \frac{D_{column}}{2} \right) \right| = 0.014 \cdot \frac{in}{in}$$

Strain caused by bending in tension tendon group

Note: The previous two equations assume a linear strain distribution at the base of the tower. Neither tendon approaches the approximate rupture strain of 0.05 in/in.

$$\varepsilon_{pe} := \frac{f_{sco}}{E_s} = 6.315 \times 10^{-3} \cdot \frac{in}{in}$$

$$\varepsilon_{psT} := \varepsilon_{pe} + \varepsilon_d + \varepsilon_{sT} = 0.02096 \cdot \frac{in}{in}$$

Final strain of tension tendon at ultimate moment

$$\varepsilon_{psM} := \varepsilon_{pe} + \varepsilon_d + \varepsilon_{sM} = 0.01311 \cdot \frac{in}{in}$$

Final strain of center tendon at ultimate moment

$$\varepsilon_{psC} := \varepsilon_{pe} - \varepsilon_{cu} = 3.31516 \times 10^{-3} \cdot \frac{in}{in}$$

Final strain of compression tendon at ultimate moment

$$f_{psT} := \begin{cases} 28500ksi \cdot \varepsilon_{psT} & \text{if } \left| \varepsilon_{psT} \right| \le 0.0086 \\ \left( 270ksi - \frac{.04ksi}{\varepsilon_{psT} - .007} \right) & \text{if } \varepsilon_{psT} > 0.0086 \end{cases} = 267.135 \cdot ksi$$

Tension tendon stress

$$f_{psM} := \begin{cases} 28500ksi \cdot \varepsilon_{psM} & \text{if } \left| \varepsilon_{psM} \right| \le 0.0086 \\ \left( 270ksi - \frac{.04ksi}{\varepsilon_{psM} - .007} \right) & \text{if } \varepsilon_{psM} > 0.0086 \end{cases} = 263.451 \cdot ksi$$

Center tendon stress

$$f_{psC} := \begin{cases} 28500ksi \cdot \varepsilon_{psC} & \text{if } \varepsilon_{psC} \le 0.0086 \\ \left( 270ksi - \frac{.04ksi}{\varepsilon_{psC} - .007} \right) & \text{if } \varepsilon_{psC} > 0.0086 \end{cases} = 94.482 \cdot ksi$$

Compresion tendon stress

$$y_{bar} := \frac{\left[ \frac{(3 \cdot \sqrt{3})}{2} \cdot \left( \frac{D_{column}}{2} \right)^2 \cdot \left( \frac{D_{column}}{2} \right) \cdot 2 + P_{thickness} \cdot P_{width} \cdot \left( \frac{D_{column}}{2} \right) + 2 \left( a - D_{column} \cdot .75 - I \right.}{\frac{(3 \cdot \sqrt{3})}{2} \cdot \left( \frac{D_{column}}{2} \right)^2 \cdot 2 + 2 \cdot \left( a - D_{column} \cdot .75 - P_{thi} \right.}$$

Note: The above equation is used to determine the centroid of the concrete area in compression. This will in turn be used for finding the ultimate moment capacity. The equation exceeds the width limitation of the sheet, and therefore, is only patially displayed. The resulting value is 17.74 inches from the extreme compression fiber.

$$jd_T := \frac{D_{base}}{2}\cdot\sqrt{3} + \frac{D_{column}}{2} - y_{bar} = 197.714\cdot in$$ Length of moment arm to tension tendons

$$jd_M := \frac{\frac{D_{base}}{2}\cdot\sqrt{3}}{2} + \frac{D_{column}}{2} - y_{bar} = 98.987\cdot in$$ Length of moment arm to center tendons

$$T_T := 2\cdot N_{column}\cdot A_{strand}\cdot\left(f_{psT}\right) = 7.768\times 10^{3}\cdot kip$$ Tendon force in tension group

$$T_M := 2\cdot N_{column}\cdot A_{strand}\cdot\left(f_{psM}\right) = 7.661\times 10^{3}\cdot kip$$ Tendon force in center group

$$M_{initial} := \left(T_T\cdot jd_T + T_M\cdot jd_M\right) = 191175.015\cdot ft\cdot kip$$ Ultimate moment capacity

Note: The above capacity does not include P-Delta effects, which will reduce the total capacity. See below for further analysis.

## Subtract P-Delta Effect

### HCHP-UHPC Ultimate Moment Capacity at Base

$M_{Base} := 191175.02\,ft\cdot kip \quad M_{110} := 128144.85\,ft\cdot kip \quad M_{220} := 92905.89\,ft\cdot kip \quad M_{Top} := 45258.16\,ft\cdot kip$

Note: The above moment demand values at four seperate tower elevations were obtained from seperate spreadsheets. Each is included in this appendix below.

$Z_{bot} := 0ft \qquad Z_{110} := 110ft \qquad Z_{220} := 220ft \qquad Z_{top} := 319.55ft$

$$M_{est}(z) := \begin{cases} M_{Base} - \dfrac{(M_{Base} - M_{110})}{(Z_{110} - Z_{bot})} \cdot z & \text{if } 0ft \le z < 110ft \\ M_{110} - \dfrac{(M_{110} - M_{220})}{(Z_{220} - Z_{110})} \cdot (z - Z_{110}) & \text{if } 110ft \le z < 220ft \\ M_{220} - \dfrac{(M_{220} - M_{Top})}{(Z_{top} - Z_{220})} \cdot (z - Z_{220}) & \text{otherwise} \end{cases}$$

Note: The above set of equations is used to estimate the moment demand at any elevation, z, for the purposes of including P-delta effects in the ultimate moment capacity. Below, six seperate equations are shown that describe the moment of inertia of both the columns and panels.

$$I_{col}(z) := \begin{pmatrix} -3.5527\cdot10^{-15}\cdot z^3\cdot ft + 1.230\cdot10^{-2}\cdot z^2\cdot ft^2 - 8.568\cdot z\cdot ft^3 + 1.509\cdot10^3\cdot ft^4 & \text{if } Z_{bot} \le z < Z_{110} \\ -1.4027\cdot10^{-5}\cdot z^3\cdot ft + 1.562\cdot10^{-2}\cdot ft^2\cdot z^2 - 7.666ft^3\cdot z + 1.3956\cdot10^3 ft^4 & \text{if } Z_{110} \le z < Z_{220} \\ -1.7982\cdot10^{-5}\cdot z^3\cdot ft + 1.9392\cdot10^{-2} ft^2\cdot z^2 - 9.1434ft^3\cdot z + 1.5870\cdot10^3 ft^4 & \text{otherwise} \end{pmatrix}$$

$$I_{pan}(z) := \begin{pmatrix} -2.536\cdot10^{-5}\cdot z^3\cdot ft + 2.360\cdot10^{-2}\cdot z^2\cdot ft^2 - 7.281\cdot z\cdot ft^3 + 7.421\cdot10^2\cdot ft^4 & \text{if } Z_{bot} \le z < Z_{110} \\ -4.296\cdot10^{-7}\cdot z^3\cdot ft + 1.13\cdot10^{-3}\cdot ft^2\cdot z^2 - 9.92\cdot10^{-1} ft^3\cdot z + 2.89\cdot10^2 ft^4 & \text{if } Z_{110} \le z < Z_{220} \\ -1.737\cdot10^{-7}\cdot z^3\cdot ft + 6.074\cdot10^{-4} ft^2\cdot z^2 - 6.735\cdot10^{-1} ft^3\cdot z + 2.416\cdot10^2 ft^4 & \text{otherwise} \end{pmatrix}$$

$$\Delta_{flcx}(z_1) := \int_0^{z_1} \frac{M_{est}(z)\cdot(z_1 - z)}{(E_{hsc}\cdot I_{col}(z) + E_{hsc}\cdot I_{pan}(z))}\,dz$$

Equation used to describe tower displacement as a function of height

$$Wt(z) := \begin{cases} \gamma_c \cdot \left(8.3267 \cdot 10^{-17} \cdot z^2 - 1.4211 \cdot 10^{-14} \cdot z \cdot ft + 3.3069 \cdot 10^{1} ft^2\right) & \text{if } 0ft \le z < Z_{110} \\ \gamma_c \cdot \left(1.0960 \cdot 10^{-4} \cdot z^2 - 1.4811 \cdot 10^{-1} ft \cdot z + 4.8437 \cdot 10^{1} ft^2\right) & \text{if } Z_{110} \le z < Z_{220} \\ \gamma_c \cdot \left(1.7477 \cdot 10^{-4} \cdot z^2 - 2.0304 \cdot 10^{-1} ft \cdot z + 5.8034 \cdot 10^{1} ft^2\right) & \text{otherwise} \end{cases}$$

Note: The above set of equations describe the weight of the columns as a function of height

$$M_{pd}(z_1, z_2) := \int_{z_2}^{z_1} \Delta_{flex}(z) \cdot Wt(z)\, dz$$

P-delta moment demand generated by column weight

$$H_{panel} := \begin{pmatrix} 15ft \\ 45ft \\ 75ft \\ 100ft \\ 130ft \\ 160ft \\ 185ft \\ 210ft \\ 240ft \\ 270ft \\ 305ft \\ 310ft \end{pmatrix} \qquad Wt_{panel} := \begin{pmatrix} 87.65kip \\ 76.61kip \\ 55.40kip \\ 47.73kip \\ 60.22kip \\ 41.49kip \\ 40.23kip \\ 38.96kip \\ 53.02kip \\ 51.74kip \\ 42.69kip \\ 0kip \end{pmatrix}$$

Total panel weight discretized into ten foot elevation intervals

$$M_{pdpanel} := \sum_{i=0}^{11} \left(\Delta_{flex}\left(H_{panel_i}\right) \cdot Wt_{panel_i}\right) = 1113.041 \cdot ft \cdot kip$$

P-delta moment generated by panels

$$M_{pdtop} := \left[\gamma_D \cdot \left(P_{top}\right)\right] \cdot \Delta_{flex}(319.55ft) = 2882.544 \cdot ft \cdot kip$$

P delta moments generated by head mass

$$M_n := M_{initial} - M_{pdtop} - M_{pd}(319.55ft, 0ft) - M_{pdpanel}$$

$$M_n = 185173.33 \cdot ft \cdot kip$$

Nominal moment capacity

$$\phi := 0.9$$

Resistance factor

$$M_u := \phi \cdot M_n = 166656 \cdot ft \cdot kip$$

Ultimate moment capacity at the base of the HCHP-HPC tower

## Ultimate Capacity at 110'

Note: The same procedures used to determine the ultimate moment capacity at the base of the tower including P-delta effects, is used for the remaining elevations. Because these are locations of post-tensioning tendon cut-offs, the moment capacity directly above and below the designated elevation has been determined.

$$M_{pd110}(z_1, z_2) := \int_{z_2}^{z_1} \Delta_{flex}(z_1) \cdot Wt(z)\, dz$$

$$M_{pdpanel110} := \sum_{i=3}^{11} \left[ \left( \Delta_{flex}\left(H_{panel_i}\right) - \Delta_{flex}(110ft) \right) \cdot Wt_{panel_i} \right] = 845.385 \cdot ft \cdot kip$$

$$M_{pdtop110} := \gamma_D \cdot P_{top} \cdot \left( \Delta_{flex}(319.55ft) - \Delta_{flex}(110ft) \right) = 2638.468 \cdot ft \cdot kip$$

$$M_{n110} := M_{est}(110ft) - M_{pdtop110} - M_{pd110}(319.55ft, 110ft) - M_{pdpanel110}$$

$$M_{n110} = 119401.93 \cdot ft \cdot kip$$

$M_{blw110} := \Phi \cdot M_{n110} = 107461.74 \cdot ft \cdot kip$ Ultimate moment demand directly below 110'

$M_{abv110} = 117747.3[illegible] \cdot kip$ Ultimate moment demand above 110', not including P-delta effects. (From seperate sheet)

$$M_{above110} := M_{abv110} - M_{pdtop110} - M_{pd110}(319.55ft, 110ft) - M_{pdpanel110}$$

$M_{uabove110} := \Phi \cdot M_{above110} = 98104 \cdot ft \cdot kip$ Ultimate moment demand directly above 110'

## Ultimate Capacity at 220'

$$M_{pd220}(z_1, z_2) := \int_{z_2}^{z_1} \Delta_{flex}(z_1) \cdot Wt(z)\, dz$$

$$M_{pdbrace220} := \sum_{i=7}^{11} \left[ \left( \Delta_{flex}\left(H_{panel_i}\right) - \Delta_{flex}(220ft) \right) \cdot Wt_{panel_i} \right] = 284.404 \cdot ft \cdot kip$$

$$M_{pdtop220} := \gamma_D \cdot P_{top} \cdot \left( \Delta_{flex}(319.55ft) - \Delta_{flex}(220ft) \right) = 1713.85 \cdot ft \cdot kip$$

$$M_{n220} := M_{cst}(220ft) - M_{pdtop220} - M_{pd220}(319.55ft, 220ft)$$

$$M_{n220} = 89351.21 \cdot ft \cdot kip$$

$M_{u220} := \phi \cdot M_{n220} = 80416.08 \cdot ft \cdot kip$ Ultimate moment demand directly below 220'

$M_{abv220} := 54682.63ft \cdot kip$ Ultimate moment demand above 110', not including P-delta effects. (From seperate sheet)

$$M_{above220} := M_{abv220} - M_{pdtop220} - M_{pd220}(319.55ft, 220ft)$$

$M_{uabove220} := \phi \cdot M_{above220} = 46015.17 \cdot ft \cdot kip$ Ultimate moment demand directly above 110'

## Ultimate Capacity at Tower Top

$$M_{ntop} := M_{cst}(319.55ft) = 45258.16 \cdot ft \cdot kip$$

$M_{utop} := \phi \cdot M_{ntop} = 40732.34 \cdot ft \cdot kip$ Ultimate moment demand at tower top

## APPENDIX C: UCUP-HPT DESIGN CALCULATIONS

# UCUP-HPT Tower Natural Frequency

$Height := 319.55ft$ — Tower height

$\gamma_{concrete} := 155\frac{lbf}{ft^3}$ — Unit weight of high strength concrete (HSC)

$P_{turbine} := 314.1kip$ — Weight of head mass

$E_{hsc} := 7449.5ksi$ — Elastic Modulus of HSC

$y(z) := \left(1 - \cos\left(\frac{\pi \cdot z}{2 \cdot Height}\right)\right)$ — Assumed displacement function of the tower

$y_1(z) := \frac{\pi}{2 \cdot Height} \cdot \sin\left(\frac{\pi \cdot z}{2 \cdot Height}\right)$ — First derivative of the displacement function

$y_2(z) := \frac{\pi^2}{4 \cdot Height^2} \cdot \cos\left(\frac{\pi \cdot z}{2 \cdot Height}\right)$ — Second derivative of the displacement function

$h_1 := 110ft \qquad h_2 := 220ft$ — Height variables

$$A_{tower}(z) := \begin{cases} -2.775610^{-17} \cdot z^2 - 3.863610^{-2} \cdot z \cdot ft + 2.708210^{1} ft^2 & \text{if } 0ft \le z < h_1 \\ 6.765810^{-5} \cdot z^2 - 9.325610^{-2} ft \cdot z + 3.267410^{1} ft^2 & \text{if } h_1 \le z < h_2 \\ 2.457810^{-5} \cdot z^2 - 5.361010^{-2} ft \cdot z + 2.670310^{1} ft^2 & \text{otherwise} \end{cases}$$

Note: The above equations describe the area of the tower. This includes both the column and panel area

$$I_{col}(z) := \left( \begin{cases} 8.881810^{-16} \cdot z^3 \cdot ft + 5.172510^{-3} \cdot z^2 \cdot ft^2 - 3.8155z \cdot ft^3 + 7.075510^{2} \cdot ft^4 & \text{if } 0 \le z < h_1 \\ -9.384410^{-6} \cdot z^3 \cdot ft + 9.760010^{-3} \cdot ft^2 \cdot z^2 - 4.4406ft^3 \cdot z + 7.418210^{2} ft^4 & \text{if } h_1 \le z < h_2 \\ -3.433910^{-6} \cdot z^3 \cdot ft + 4.410310^{-3} ft^2 \cdot z^2 - 2.4963ft^3 \cdot z + 5.257410^{2} ft^4 & \text{otherwise} \end{cases} \right)$$

Note: The above equations describe the moment of inertia of the colums as a function of height for the columns. The three equations presented below describe the moment of inertia as a funtion of height for the panels.

$$I_{pan}(z) := \begin{cases} -1.068 \cdot 10^{-5} \cdot z^3 \cdot ft + 1.090 \cdot 10^{-2} \cdot z^2 \cdot ft^2 - 3.700 \cdot z \cdot ft^3 + 4.17 \cdot 10^2 \cdot ft^4 & \text{if } 0 \le z < h_1 \\ -3.556 \cdot 10^{-7} \cdot z^3 \cdot ft + 8.768 \cdot 10^{-4} \cdot ft^2 \cdot z^2 - 7.2 \cdot 10^{-1} ft^3 \cdot z + 1.967 \cdot 10^2 ft^4 & \text{if } h_1 \le z < h_2 \\ -3.256 \cdot 10^{-8} \cdot z^3 \cdot ft + 8.190 \cdot 10^{-4} ft^2 \cdot z^2 - 6.867 \cdot 10^{-1} ft^3 \cdot z + 1.920 \cdot 10^2 ft^4 & \text{otherwise} \end{cases}$$

**Tower Frequency and Period Calculations**

$$M := \int_0^{Height} \left( \frac{\gamma_{concrete}}{g} \right) \cdot \left( A_{tower}(z) \right) \cdot (y(z))^2 dz + \frac{P_{turbine}}{g} \cdot y(Height)^2$$ Mass variable

$$k := \int_0^{Height} E_{hsc} \cdot \left( I_{col}(z) + I_{pan}(z) \right) \cdot \left( y_2(z) \right)^2 dz$$ Stiffness variable

$$k = 5.182 \cdot \frac{kip}{in}$$

$$\omega_{rad} := \sqrt{\frac{k}{M}} = 2.05 \cdot \frac{1}{s}$$ Tower Frequency (rad/second)

$$\omega_{scc} := \frac{\omega_{rad}}{2 \cdot \pi} = 0.326 \cdot \frac{1}{s}$$ Tower Frequency (cycles/second)

# Ultimate Moment Capacity of the UHUP-HPT Tower
## 0-Degree Loading, Low Relaxation Bonded Tendons

### Geometric and Material Properties

$f_{uhpc} := 26ksi$ — Compressive strength of UHPC

$E_{uhpc} := 7449.5ksi$ — Elastic modulus of UHPC

$\varepsilon_{cu} := .004\frac{in}{in}$ — HSC compressive strain limit

$\gamma_c := 155\frac{lbf}{ft^3}$ — Unit weight of HSC

$f_{pu} := 270ksi$ — Ultimate capacity of steel tendons

$E_s := 28500ksi$ — Elastic modulus of steel tendons

$f_{sco} := .6666 f_{pu} = 179.982ksi$ — Applied tendon stress from post-tensioning

$\gamma_D := 1.2$ — Dead load factor

$A_{col} := 374.22in^2$ — Single column area at the base

$D_{base} := 228in$ — Tower diameter at the base

$D_{column} := 25.5in$ — Column diameter at the base

$P_{top} := 314.1kip$ — Dead load at the tower top

$A_{centerduct} := 22.48in^2$ — Area of the center duct in the columns

$A_{radial1duct} := 7.99in^2$ — Area of two of the radial ducts in the columns

$A_{radial2duct} := 4.83in^2$ — Area of remaining two radial ducts in the columns

$P_{width} := 91.92in$ — Width of the panel at the base of the tower

$P_{thickness} := 3in$ — Thickness of the panel

$N_{Center} := 35$ — Number of strands in the center duct

$N_{Radial1} := 12$ — Number of strands in two of the radial ducts

$N_{Radial2} := 3$ Number of strands in the remaining two radial ducts

$A_{strand} := 0.217in^2$ Area of the steel strand

$N_{column} := N_{Center} + 2 \cdot (N_{Radial1} + N_{Radial2})$ Total number of strands in each column at the tower base

$A_{stot} := A_{strand} \cdot [N_{Center} + 2 \cdot (N_{Radial1} + N_{Radial2})] = 14.105 \cdot in^2$ Total tendon area per column

$f_{psTension} := 268.652ksi$ $f_{psMiddle} := 267.136ksi$ $f_{psCompression} := 65.982ksi$

Note: The three values listed above, are part of the iterative procedure used to determine the ultimate capacity. They represent the tendon stress in each column group also presented below.

$\sigma_{ColumnC} := \frac{(N_{column} \cdot A_{strand} \cdot f_{psCompression})}{A_{col}} = 2.487 \cdot ksi$ Column stress in the compression group

$\sigma_{ColumnAB} := \frac{(N_{column} \cdot A_{strand} \cdot f_{sco})}{A_{col}} = 6.784 \cdot ksi$ Column stress in the tension group

$\epsilon_d := \frac{\sigma_{ColumnAB}}{E_{uhpc}} = 9.106 \times 10^{-4}$ Decompression strain of the columns

$$y(x) := (0.85 \cdot f_{uhpc}) \cdot (4.603 \cdot 10^{-3} x^3 - 8.577 \cdot 10^{-1} \cdot x^2 + 4.856 \cdot 10^{1} \cdot x - 6.164 \cdot 10^{1}) + .85 \cdot f_{uhpc} \cdot (6.933 \cdot x$$
$$- (f_{psCompression} + f_{psTension} + f_{psMiddle}) \cdot \frac{A_{strand}}{in^2} \cdot (2 \cdot N_{column})$$

Note: The above equation represents the equilibrium equation for the tower, which is used to determine the neutral axis at the base of the tower.

$p := root(y(x), x, -200, 200) = 16.336$

$a := p \cdot 1in$ Depth of equivalent rectangular stress block

$a = 16.336 \cdot in$

$\beta_1 := .65$ Rectangular stress block distribution for HSC

$c := \frac{a}{\beta_1} = 25.132 \cdot in$ Bending neutral axis depth at base of tower

$$\varepsilon_{sM} := \left| \varepsilon_{cu} - \frac{\varepsilon_{cu}}{c} \cdot \frac{\left( \frac{D_{base}}{2} \cdot \sqrt{3} + D_{column} \right)}{2} \right| = 0.014 \cdot \frac{in}{in}$$

Strain caused by bending in center tendon group

$$\varepsilon_{sT} := \left| \varepsilon_{cu} - \frac{\varepsilon_{cu}}{c} \cdot \left( \frac{D_{base}}{2} \cdot \sqrt{3} + \frac{D_{column}}{2} \right) \right| = 0.029 \cdot \frac{in}{in}$$

Strain caused by bending in tension tendon group

Note: The previous two equations assume a linear strain distribution at the base of the tower. Neither tendon approaches the approximate rupture strain of 0.05 in/in.

$$\varepsilon_{pe} := \frac{f_{sco}}{E_s} = 6.315 \times 10^{-3} \cdot \frac{in}{in}$$

$$\varepsilon_{psT} := \varepsilon_{pe} + \varepsilon_d + \varepsilon_{sT} = 0.03668 \cdot \frac{in}{in}$$

Final strain of tension tendon at ultimate moment

$$\varepsilon_{psM} := \varepsilon_{pe} + \varepsilon_d + \varepsilon_{sM} = 0.02097 \cdot \frac{in}{in}$$

Final strain of center tendon at ultimate moment

$$\varepsilon_{psC} := \varepsilon_{pe} - \varepsilon_{cu} = 2.31516 \times 10^{-3} \cdot \frac{in}{in}$$

Final strain of compression tendon at ultimate moment

$$f_{psT} := \begin{cases} 28500ksi \cdot \varepsilon_{psT} & \text{if } |\varepsilon_{psT}| \le 0.0086 \\ \left( 270ksi - \frac{.04ksi}{\varepsilon_{psT} - .007} \right) & \text{if } \varepsilon_{psT} > 0.0086 \end{cases} = 268.652 \cdot ksi$$

Tension tendon stress

$$f_{psM} := \begin{cases} 28500ksi \cdot \varepsilon_{psM} & \text{if } |\varepsilon_{psM}| \le 0.0086 \\ \left( 270ksi - \frac{.04ksi}{\varepsilon_{psM} - .007} \right) & \text{if } \varepsilon_{psM} > 0.0086 \end{cases} = 267.136 \cdot ksi$$

Center tendon stress

$$f_{psC} := \begin{cases} 28500ksi \cdot \varepsilon_{psC} & \text{if } \varepsilon_{psC} \le 0.0086 \\ \left( 270ksi - \frac{.04ksi}{\varepsilon_{psC} - .007} \right) & \text{if } \varepsilon_{psC} > 0.0086 \end{cases} = 65.982 \cdot ksi$$

Compresion tendon stress

$$y_{bar} := \frac{\left[ \frac{(3-\sqrt{3})}{2} \cdot \left( \frac{D_{column}}{2} \right)^2 \cdot \left( \frac{D_{column}}{2} \right) \cdot 2 + P_{thickness} \cdot P_{width} \cdot \left( \frac{D_{column}}{2} \right) + 2 \left( a - D_{column} \cdot .75 - I \right.\right.}{\frac{(3-\sqrt{3})}{2} \cdot \left( \frac{D_{column}}{2} \right)^2 \cdot 2 + 2 \cdot \left( a - D_{column} \cdot .75 - P_{thi} \right.}$$

Note: The above equation is used to determine the centroid of the concrete area in compression. This will in turn be used for finding the ultimate moment capacity. The equation exceeds the width limitation of the sheet, and therefore, is only patially displayed. The resulting value is 17.74 inches from the extreme compression fiber.

$$jd_T := \frac{D_{base}}{2}\cdot\sqrt{3} + \frac{D_{column}}{2} - y_{bar} = 197.581\cdot in$$ Length of moment arm to tension tendons

$$jd_M := \frac{\frac{D_{base}}{2}\cdot\sqrt{3}}{2} + \frac{D_{column}}{2} - y_{bar} = 98.854\cdot in$$ Length of moment arm to center tendons

$$T_T := 2\cdot N_{column}\cdot A_{strand}\cdot\left(f_{psT}\right) = 7.579\times 10^{3}\cdot kip$$ Tendon force in tension group

$$T_M := 2\cdot N_{column}\cdot A_{strand}\cdot\left(f_{psM}\right) = 7.536\times 10^{3}\cdot kip$$ Tendon force in center group

$$M_{initial} := \left(T_T\cdot jd_T + T_M\cdot jd_M\right) = 186863.654\cdot ft\cdot kip$$ Ultimate moment capacity

Note: The above capacity does not include P-Delta effects, which will reduce the total capacity. See below for further analysis.

## Subtract P-Delta Effect

### UCUP-HPT Ultimate Moment Capacity at Base

$M_{Base} := 186863.65\text{ft}\cdot\text{kip}$ $M_{110} := 130323.63\text{ft}\cdot\text{kip}$ $M_{220} := 96107.87\text{ft}\cdot\text{kip}$ $M_{Top} := 49322.79\text{ft}\cdot\text{kip}$

Note: The above moment demand values at four seperate tower elevations were obtained from seperate spreadsheets using the same process as outlined above.

$Z_{bot} := 0\text{ft}$ $Z_{110} := 110\text{ft}$ $Z_{220} := 220\text{ft}$ $Z_{top} := 319.55\text{ft}$

$$M_{cst}(z) := \begin{cases} M_{Base} - \dfrac{(M_{Base} - M_{110})}{(Z_{110} - Z_{bot})}\cdot z & \text{if } 0\text{ft} \le z < 110\text{ft} \\ M_{110} - \dfrac{(M_{110} - M_{220})}{(Z_{220} - Z_{110})}\cdot(z - Z_{110}) & \text{if } 110\text{ft} \le z < 220\text{ft} \\ M_{220} - \dfrac{(M_{220} - M_{Top})}{(Z_{top} - Z_{220})}\cdot(z - Z_{220}) & \text{otherwise} \end{cases}$$

Note: The above set of equations is used to estimate the moment demand at any elevation, z, for the purposes of including P-delta effects in the ultimate moment capacity. Below, six seperate equations are shown that describe the moment of inertia of both the columns and panels.

$$I_{col}(z) := \begin{cases} 8.882\cdot10^{-16}\cdot z^3\cdot\text{ft} + 5.173\cdot10^{-3}\cdot z^2\cdot\text{ft}^2 - 3.8155\cdot z\cdot\text{ft}^3 + 7.0755\cdot10^2\cdot\text{ft}^4 & \text{if } Z_{bot} \le z < Z_{110} \\ -9.3844\cdot10^{-6}\cdot z^3\cdot\text{ft} + 9.760\cdot10^{-3}\cdot\text{ft}^2\cdot z^2 - 4.4406\text{ft}^3\cdot z + 7.4182\cdot10^2\text{ft}^4 & \text{if } Z_{110} \le z < Z_{220} \\ -3.4339\cdot10^{-6}\cdot z^3\cdot\text{ft} + 4.4103\cdot10^{-3}\text{ft}^2\cdot z^2 - 2.4967\text{ft}^3\cdot z + 5.2574\cdot10^2\text{ft}^4 & \text{otherwise} \end{cases}$$

$$I_{pan}(z) := \begin{cases} -1.068\cdot10^{-5}\cdot z^3\cdot\text{ft} + 1.090\cdot10^{-2}\cdot z^2\cdot\text{ft}^2 - 3.700\cdot z\cdot\text{ft}^3 + 4.17\cdot10^2\cdot\text{ft}^4 & \text{if } Z_{bot} \le z < Z_{110} \\ -3.556\cdot10^{-7}\cdot z^3\cdot\text{ft} + 8.768\cdot10^{-4}\cdot\text{ft}^2\cdot z^2 - 7.2\cdot10^{-1}\text{ft}^3\cdot z + 1.967\cdot10^2\text{ft}^4 & \text{if } Z_{110} \le z < Z_{220} \\ -3.256\cdot10^{-8}\cdot z^3\cdot\text{ft} + 8.190\cdot10^{-4}\text{ft}^2\cdot z^2 - 6.867\cdot10^{-1}\text{ft}^3\cdot z + 1.920\cdot10^2\text{ft}^4 & \text{otherwise} \end{cases}$$

$$\Delta_{flex}(z_1) := \int_0^{z_1} \frac{M_{cst}(z)\cdot(z_1 - z)}{(E_{uhpc}\cdot I_{col}(z) + E_{uhpc}\cdot I_{pan}(z))}\,dz$$

Equation used to describe tower displacement as a function of height

$$Wt(z) := \begin{cases} \gamma_c \cdot \left(2.7756 \cdot 10^{-17} \cdot z^2 - 1.7764 \cdot 10^{-15} \cdot z \cdot ft + 1.559 \cdot 10^{1} ft^2\right) & \text{if } 0ft \le z < Z_{110} \\ \gamma_c \cdot \left(6.7658 \cdot 10^{-5} \cdot z^2 - 8.3896 \cdot 10^{-2} ft \cdot z + 2.4405 \cdot 10^{1} ft^2\right) & \text{if } Z_{110} \le z < Z_{220} \\ \gamma_c \cdot \left(2.4578 \cdot 10^{-5} \cdot z^2 - 4.3437 \cdot 10^{-2} ft \cdot z + 1.8255 \cdot 10^{1} ft^2\right) & \text{otherwise} \end{cases}$$

Note: The above set of equations describe the weight of the columns as a function of height

$$M_{pd}(z_1, z_2) := \int_{z_2}^{z_1} \Delta_{flex}(z) \cdot Wt(z)\, dz$$

P-delta moment demand generated by column weight

$$H_{panel} := \begin{pmatrix} 15ft \\ 45ft \\ 75ft \\ 100ft \\ 130ft \\ 160ft \\ 185ft \\ 210ft \\ 240ft \\ 270ft \\ 305ft \\ 310ft \end{pmatrix} \quad Wt_{panel} := \begin{pmatrix} 50.73kip \\ 45.34kip \\ 33.67kip \\ 29.92kip \\ 38.39kip \\ 26.33kip \\ 25.42kip \\ 24.52kip \\ 32.72kip \\ 30.79kip \\ 24.49kip \\ 0kip \end{pmatrix}$$

Total panel weight discretized into ten foot elevation intervals

$$M_{pdpanel} := \sum_{i=0}^{11} \left(\Delta_{flex}\left(H_{panel_i}\right) \cdot Wt_{panel_i}\right) = 1146.194 \cdot ft \cdot kip$$

P-delta moment generated by panels

$$\phi := 0.9$$

$$M_{pdtop} := \left[\gamma_D \cdot \left(P_{top}\right)\right] \cdot \Delta_{flex}(319.55ft) = 4871.265 \cdot ft \cdot kip$$

P delta moments generated by head mass

$$M_n := M_{initial} - M_{pdtop} - M_{pd}(319.55ft, 0ft) - M_{pdpanel}$$

$$M_n = 179081.54 \cdot ft \cdot kip$$

Nominal moment capacity

Resistance factor

$$M_u := \phi \cdot M_n = 161173.39 \cdot ft \cdot kip$$

Ultimate moment capacity at the base of the HCHP-HPC tower

## Ultimate Capacity at 110'

Note: The same procedures used to determine the ultimate moment capacity at the base of the tower including P-delta effects, is used for the remaining elevations. Because these are locations of post-tensioning tendon cut-offs, the moment capacity directly above and below the designated elevation has been determined.

$$M_{pd110}(z_1, z_2) := \int_{z_2}^{z_1} \Delta_{flex}(z_1) \cdot Wt(z)\, dz$$

$$M_{pdpanel110} := \sum_{i=3}^{11} \left[ \left( \Delta_{flex}\left(H_{panel_i}\right) - \Delta_{flex}(110ft) \right) \cdot Wt_{panel_i} \right] = 865.561 \cdot ft \cdot kip$$

$$M_{pdtop110} := \gamma_D \cdot P_{top} \cdot \left( \Delta_{flex}(319.55ft) - \Delta_{flex}(110ft) \right) = 4456.522 \cdot ft \cdot kip$$

$$M_{n110} := M_{est}(110ft) - M_{pdtop110} - M_{pd110}(319.55ft, 110ft) - M_{pdpanel110}$$

$$M_{n110} = 120589.89 \cdot ft \cdot kip$$

$M_{blw110} := \phi \cdot M_{n110} = 108530.9 \cdot ft \cdot kip$ Ultimate moment demand directly below 110'

$M_{abv110} = 118640.640 \cdot kip$ Ultimate moment demand above 110', not including P-delta effects. (From seperate sheet)

$$M_{above110} := M_{abv110} - M_{pdtop110} - M_{pd110}(319.55ft, 110ft) - M_{pdpanel110}$$

$M_{uabove110} := \phi \cdot M_{above110} = 98016.21 \cdot ft \cdot kip$ Ultimate moment demand directly above 110'

## Ultimate Capacity at 220'

$$M_{pd220}(z_1, z_2) := \int_{z_2}^{z_1} \Delta_{flex}(z_1) \cdot Wt(z)\, dz$$

$$M_{pdbrace220} := \sum_{i=7}^{11} \left[ \left( \Delta_{flex}\left(H_{panel_i}\right) - \Delta_{flex}(220ft) \right) \cdot Wt_{panel_i} \right] = 283.403 \cdot ft \cdot kip$$

$$M_{pdtop220} := \gamma_D \cdot P_{top} \cdot \left( \Delta_{flex}(319.55ft) - \Delta_{flex}(220ft) \right) = 2879.807 \cdot ft \cdot kip$$

$$M_{n220} := M_{cst}(220ft) - M_{pdtop220} - M_{pd220}(319.55ft, 220ft)$$

$$M_{n220} = 91564.07 \cdot ft \cdot kip$$

$M_{u220} := \phi \cdot M_{n220} = 82407.66 \cdot ft \cdot kip$ Ultimate moment demand directly below 220'

$M_{abv220} := 59123.65ft \cdot kip$ Ultimate moment demand above 110', not including P-delta effects. (From seperate sheet)

$$M_{above220} := M_{abv220} - M_{pdtop220} - M_{pd220}(319.55ft, 220ft)$$

$M_{uabove220} := \phi \cdot M_{above220} = 49120.96 \cdot ft \cdot kip$ Ultimate moment demand directly above 110'

## Ultimate Capacity at Tower Top

$$M_{ntop} := M_{cst}(319.55ft) = 49322.79 \cdot ft \cdot kip$$

$M_{utop} := \phi \cdot M_{ntop} = 44390.51 \cdot ft \cdot kip$ Ultimate moment demand at tower top